Experimental and Simulation Study on Novel Adsorbents for Carbon Capture, Oxygen Sorption, and Methane Recovery

by

Mai Xu

A Dissertation Presented in Partial Fulfillment
of the Requirement for the Degree
of Doctor of Philosophy

Approved March 2020 by the
Graduate Supervisory Committee:

Shuguang Deng, Chair
MaryLaura Lind
Jerry Y.S. Lin
Matthew D. Green
Dong-Kyun Seo

ARIZONA STATE UNIVERSITY

May 2020

ABSTRACT

Global warming resulted from greenhouse gases emission has received widespread attention. Meanwhile, it is required to explore renewable and environmentally friendly energy sources due to the severe pollution of the environment caused by fossil fuel combustion. In order to realize a substantial adsorption process to resolve the environmental issues, the development of new adsorbents with improved properties has become the most critical issue. This dissertation presents the work of four individual but related studies on systematic characterization and process simulations of novel adsorbents with superior adsorption properties.

A perovskite oxide material, $La_{0.1}Sr_{0.9}Co_{0.9}Fe_{0.1}O_{3-\delta}$ (LSCF1991), was investigated first for high-temperature air separation. The oxygen sorption/desorption behavior of LSCF1991 was studied by thermogravimetric analysis (TGA) and fixed-bed breakthrough experiments. A parametric study was performed to design and optimize the operating parameters of the high-temperature air separation process by pressure swing adsorption (PSA). The results have shown great potential for applying LSCF1991 to the high-temperature air separation due to its excellent separation performance and low energy requirement.

Research on using nanostructured zeolite NaX (NZ) as adsorbents for CO_2 capture was subsequently conducted. The CO_2/N_2 adsorption characterizations indicated that the NZ samples lead to enhanced adsorption properties compared with the commercial zeolites (MZ). From the two-bed six-step PSA simulation, NZ saved around 30% energy over MZ for CO_2 capture and recovery while achieving a higher CO_2 purity and productivity.

A unique screening method was developed for efficient evaluation of adsorbents for PSA processes. In the case study, 47 novel adsorbents have been screened for coal bed methane (CBM) recovery. The adsorbents went through scoring-based prescreening, PSA simulation, and optimization. The process performance indicators were correlated with the adsorption selectivity and capacities, which provides new insights for predicting the PSA performance.

A new medium-temperature oxygen sorbent, $YBaCo_4O_{7+\delta}$ (YBC114), was investigated as an oxygen pumping material to facilitate solar thermochemical fuel production. The oxygen uptake and release attributes of YBC114 were studied by both TGA and a small-scale evacuation test. The study proved that the particle size has a significant effect on the oxygen pumping behavior of YBC114, especially for the uptake kinetics.

ACKNOWLEDGMENTS

First and foremost, I want to express my sincere gratitude to my Ph.D. advisor, Dr. Shuguang Deng, for providing consistent support and encouragement during the journey of my Ph.D. His passion for science, sharp research acumen, and hard-working spirit have always inspired me to strive for extra and make my own mark. I am also grateful to him for motivating me to actively participate in several collaborative research projects, inside and outside the department, helping me to acquire new skill sets. I will always carry with his guidance and spirit in my future career.

I would like to thank my dissertation committee members: Dr. Marylaura Lind, Dr. Jerry Lin, Dr. Matthew D. Green, and Dr. Dong-Kyun Seo for their technical assistance and guidance. I sincerely appreciate their time and effort in reviewing my dissertation and proposals. Their comments and suggestions have polished my research plans.

I must express my gratitude to our department staff: Fred Pena, lab manager, for giving us a safe research environment and good protection; Albert Thompson, technical support, for giving us IT support and software maintenance; Tiffany Wingerson, advising manager, for all the guidance and suggestions throughout my Ph.D. program.

I also wish to thank all of my colleagues in Dr. Deng's group. In particular, Dr. Jun Wang, Dr. Tapaswy Muppaneni, Dr. Xilei Lyu, Dr. Ying Xie, Dr. Fan Liu, Dr. Youhua Fan, Dr. Ting Tan, Chengxi Lu, and Kodanda Phani Raj Dandamudi, for their valuable advice, kindly cooperation, and helpful assistance. We established very good friendships and had a pleasant experience at Arizona State University.

Additionally, I would like to express my gratitude to other research associates: Dr. Ivan Ermanoski and Dr. Ellen B. Stechel for their guidance on building vacuum systems and analyzing the oxygen pumping related experimental data and modeling; Ananya Chowdhury and support team, in PSE gPROMS, for their assistance of software operation and debugging simulation codes; Tim Sullivan, from Swagelok Southwest, for his suggestions on the design of gas delivery system.

Finally, I would like to express my deepest gratitude to my parents for putting absolute trust in me and giving me so much freedom and unconditional love. I could not have reached this stage without their support and encouragement.

This work was partially supported by the US Department of Energy (DE-FE0024075) and the new faculty startup funds from the Fulton Schools of Engineering at Arizona State University. ASU LightWorks® (Seed Grant) is also acknowledged. I acknowledge the use of facilities within the Eyring Materials Center at Arizona State University supported in part by NNCI-ECCS-1542160.

TABLE OF CONTENTS

Page

CHAPTER Page

LIST OF TABLES

Table Page

Table Page

LIST OF FIGURES

Figure Page

Figure Page

Figure Page

Figure Page

Chapter 1 : Introduction, Motivations, and Research Objectives

1.1 Background

Global warming resulted from greenhouse gases emission has been an issue of great concern. The concentration of greenhouse gases in the atmosphere has been continuously increasing over the last few decades due to the strong energy dependence of fossil fuels. Among the greenhouse gases, carbon dioxide is considered the main contributor to global warming due to its huge emission amount. Annual energy-related CO_2 emissions in the U.S. have reached 5,269 million metric tons in 2018 according to the Energy Information Administration (EIA), which contributes to more than 80 percent of the U.S. greenhouse gas emissions. As shown in Figure 1.1, global CO_2 emissions have increased exponentially since the industrial revolution. In 2014 global CO_2 emissions were approximately two times higher than the 1980s. Thus, reducing anthropogenic CO_2 emission and controlling CO_2 concentration are critical global environmental issues.

Though various CO_2 capture technologies have been proposed, chemical absorption with amine solutions is currently the most popular method for CO_2 capture from the flue gas in power plants. Amine solvents, despite their wide use in industry have seveal downsides: significant energy requirement due to solvent regeneration, degradation and equipment corrosion, environmental impacts due to solvent emissions, and the large absorber volume. One possible alternative to traditional amine solvents is adsorption using solid sorbents. Solid adsorbents are promising candidates tfor CO_2 capture due to theirease of regeneration, stability, and low cost.

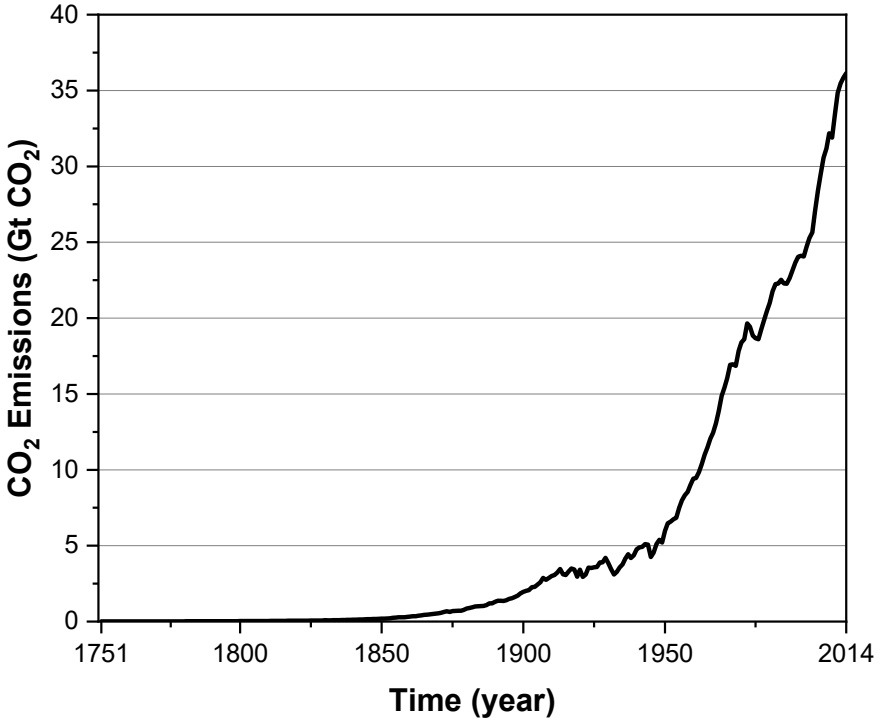

Figure 1.1. Worldwide CO_2 emissions[1].

The energy crisis is one of the biggest challenges for the world due to the increasing demand for energy in addition to the short life of fossil fuels. The EIA projects that world energy consumption will grow by approximately 50% between 2018 and 2050[2]. Currently, about 78% of the total energy consumption is from fossil fuel such as oil, coal, and natural gas. Consuming excess fossil fuels has caused significant damage on the environment. For example, global warming, air pollution, extinction of animals, and food shortage. Moreover, fossil fuels are not renewable. The estimated remaining fossil fuel depletion times for oil,

coal, and gas is approximately 48, 111, and 50 years, respectively[3]. In order to meet the global energy needs, renewable and environmentally friendly energy sources are required.

Among several alternative renewable energy sources, methane is one of the most promising energy sources due to its high heating values of 55.7 kJ/g and widespread availability. However, most methane gas streams, such as biogas, coalbed gas, and natural gas, contain impurities like N_2 and CO_2, which can corrode the pipelines and significantly reduce the combustion heat. It is, therefore, necessary to separate the impurities from the methane gas sources before they can be efficiently used as an energy source.

Besides the CO_2 capture and CH_4 recovery, air separation (N_2/O_2) is also an important chemical engineering process, as it produces oxygen for various applications. Oxygen can be used for steelmaking, coal gasification, and hydrothermal biomass gasification. Air separation can also be combined with the carbon capture and sequestration techniques to produce oxygen-enriched gas for oxy-combustion. Nitrogen with a low oxygen concentration that is produced during the process can be used to protect certain chemicals or foods from contact with air.

1.2 Gas Separation and Purification by Adsorption Processes

Gas separation and purification is an essential part of many industrial processes, such as carbon capture, methane recovery and oxygen production. In order to achieve efficient and economical gas separation, massive efforts have been devoted. Traditionally, gas separations can be achieved by cryogenic distillation that is commonly used in the

large-scale air separation process. The major concerns of cryogenic distillation are huge energy consumption and capital investment. Membrane technology is also commonly used for gas separation, such as biogas upgrading and CO_2 capture[4,5]. A membrane is a dense filter that can separate the components in gas feed, most often based on molecular size[6]. Membrane separation is good for bulk gas separations, but generally not an effective option for cases with either a low feed concentration or high product purity requirement. Absorption is a well-developed technology that often used in CO_2 capture or other separation applications. The process used liquid or solid material (solvents) to physically or chemically absorb the components. The major problem with absorption processes is the high regeneration cost, environmental impacts due to solvent emissions, and the large absorber volume.

Compared with other separation techniques, adsorption stands out to be an attractive operation due to its relatively low cost, ease to regenerate, high efficiency and excellent stability[7]. The adsorption process is based on the selective retention of the gas molecules in the pores or on the surface of the adsorbent[8]. The selective retention may be caused by differences either in the adsorption equilibrium or kinetics.

Two generic cycle concepts that are known as temperature swing adsorption (TSA) and pressure swing adsorption (PSA) are employed to perform the adsorption and desorption steps in conjunction with a variety of other complimentary steps[9]. Gas purification applications for removing trace impurities from a gaseous mixture primarily use TSA processes with some exceptions (e.g. gas drying), while bulk gas separation applications use PSA processes exclusively[10]. The PSA process is an industrial unit

operation for separating gas mixtures by repeatedly changing the ambient pressure. The pressure of the system swings between high pressure in adsorption and low pressure in desorption in a cyclic manner. Compared with TSA technology, the PSA process is more flexible, efficient, and energy-saving. PSA technology has been widely applied in various fields as summarized in Table 1.1.

Table 1.1. A brief overview of PSA applications reported in open literature.

PSA application	References
CO_2 capture from industrial flue gas and CO_2 sequestration	11,12
Methane recovery from biogas, syngas, coalbed gas, and natural gas	13–17
Air purification/ O_2 production	18,19
NO_x removal from exhaust gas	20
SO_2 recovery	21
H_2 production	22
Air drying	23
CO purification	24

A PSA system usually comprises of two or more adsorbent-filled beds interconnected to each other via a network of switch valve, which in turn controls the simultaneous operation of product purification and adsorbent regeneration steps. Therefore, a multiple bed assembly is used to ensure a constant supply of the product, while the other

bed is in the regeneration mode. The most commonly used PSA cycle in practice is the Skarstrom cycle that was originally employed for equilibriumdue based air drying applications[25]. The cycle involves two beds performing four basic steps as shown in Figure 1.2. The counter-current purge is provided by drawing off a product side stream undergoing adsorption step, making the assembly self-sufficient in terms of any input from the external sources.

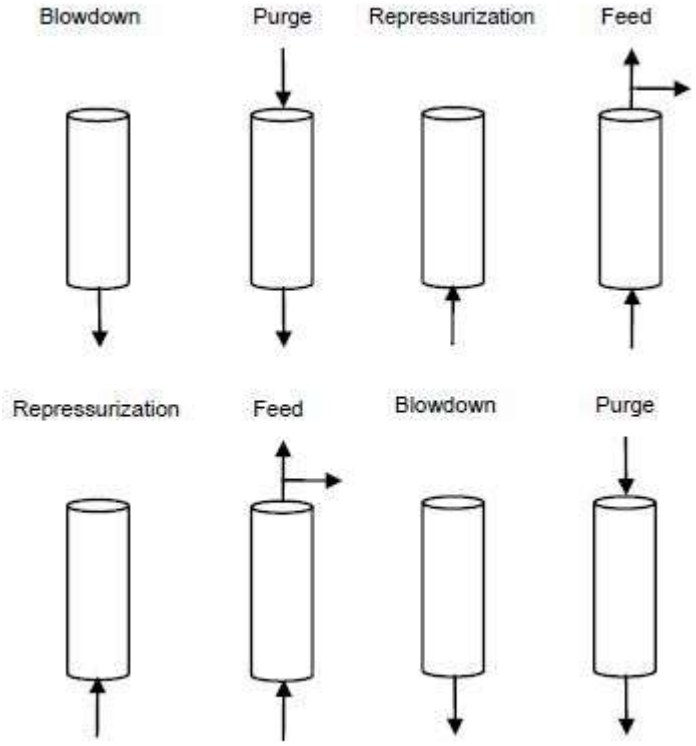

Figure 1.2. Two-bed, four-step Skarstrom cycle[25].

1.3 Problem Statement

The key challenge in the adsorption separation technique is to find a suitable solid adsorbent material with large adsorption capacity, high selectivity, excellent stability, and good reusability[26]. Various porous materials have been investigated including zeolite molecular sieve[27], porous organic polymers[28], porous carbon[29], and metal-organic frameworks (MOFs)[30,31]. However, conventional materials either suffer from unsatisfactory adsorption capacities or very high fabrication cost[7]. The limitations from conventional adsorbents make the adsorption process less effective for large scale industrial applications. Thus, it is necessary to develop novel adsorbents that are of low cost, easy to regenerate, high adsorption capacity and excellent selectivity. In order to meet the above requirements, adsorbents should be prepared to have a large surface area, suitable pore size distribution, large pore volume, sufficient attraction sites, and stability. The surface area, pore size, and volume are decided by pore structures, which could be adjusted by synthesis methods, reaction conditions (i.e. reaction temperature and time). The stability of the adsorbent is dominated by the materials and adsorbent structures.

On the other side, the fast development of adsorbents (i.e. increasing number of MOFs) made it very difficult to screen and select adsorbent with the conventional method. A new approach is needed for efficient and quick evaluation of adsorbents for their process performance. Novel adsorbents are typically synthesized in a small amount where adsorption isotherms, porosity, and surface area can be measured. However, a much larger adsorbent amount is required to perform breakthrough and lab-scale PSA experiments. Therefore, numerical modeling and simulation play a critical role in adsorbent evaluation.

Process simulation also allows us to design and optimize the PSA process with the novel adsorbents. To compete with other mature technologies, the PSA process should be targeted to produce products at high purity, recovery, and productivity while minimizing energy consumption during the process.

1.4 Trends of Adsorbent Development

Conventionally, the approach of the development of new adsorbents is mostly experimentally based. Typically, researchers first synthesized the adsorbents, characterized the adsorbents, and searched for applications based on the adsorption properties of the adsorbents. At the next stage, larger quantities of adsorbents were synthesized to perform column breakthrough experiments and adsorption process pilot tests. Process simulation was applied at the very late stage before the large-scale production of adsorbents. In the current work, we addressed an emerging approach of adsorbent development that is more efficient and economical than the conventional method. Instead of searching applications of the adsorbents, we design the adsorbents based on the application with molecular simulation. After that, the breakthrough behavior and process performance can also be predicted. If the process performance of the adsorbents meets the requirements of the application, we will then synthesize, characterize, and perform column breakthrough experiments. One significant advantage of the new approach is that it screens the adsorbent materials at the early stage so that we can save the cost and time for the synthesis and characterizations involved during the adsorbent design process. The procedures of the conventional and emerging approaches of adsorbent development are detailed described in

Figure 1.3. The experimental procedures are in the red box, and the simulation procedures are in the blue box. We can conclude that simulation plays a more and more critical role in the development of adsorbent material and the adsorption process. The current work will benefit the transition to the new approach of adsorbent development.

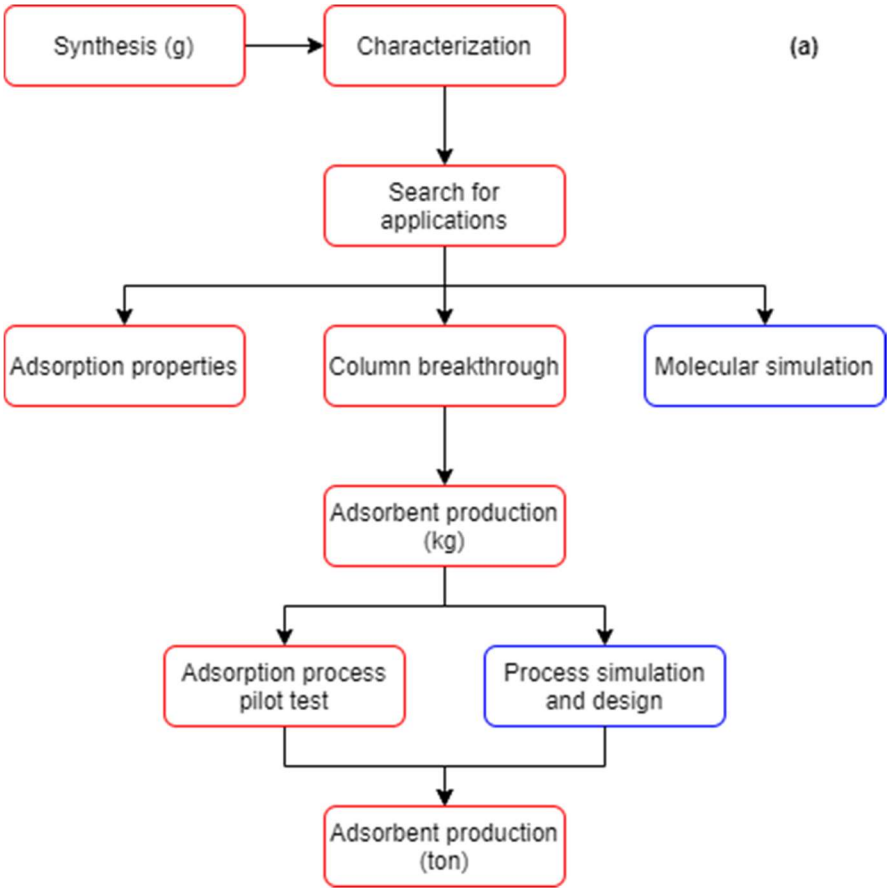

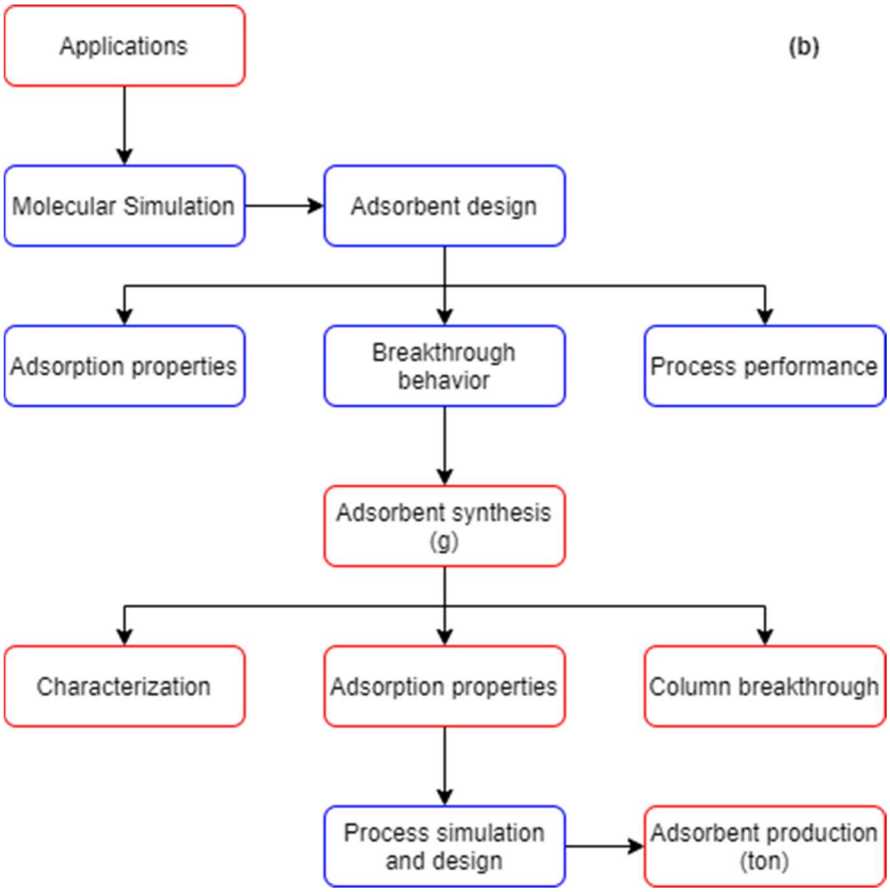

Figure 1.3. (a) The conventional approach and (b) the emerging approach for adsorbent material development

1.5 Research Objectives and Significance

The objective of this research can be separated into two parts. The first objective is to develop new adsorbents and processes to address various gas separation process, i.e. CO_2 capture, oxygen production, and methane recovery. The novel adsorbents are required to be of low cost, easy to regenerate, high adsorption capacity and excellent selectivity. This goal will be pursued via optimizing the synthesis route (i.e. reaction temperature and

time) and the ratios of each raw component. The second objective is to demonstrate an efficient process simulation-based approach for adsorbent evaluation. The process performance of novel adsorbents can be evaluated by comparing the product purity, recovery, productivity, and energy consumption of the process. This evaluation is more accurate than conventional screening by adsorption capacity and selectivity. The process simulation is also capable of design and optimization of the operating parameters of the process, providing an economic comparison with other mature gas separation technologies.

Chapter 2 : Mathematical Model for Adsorption Process Simulation

2.1 Adsorption Bed Dynamic Modeling

2.1.1 Adsorption Isotherm

An adsorption isotherm mathematically defines the relationship between the concentration of the molecules of a given species in the gas phase with its concentration in the adsorbed phase, under equilibrium conditions, and constant temperature. A variety of isotherms have been studied and employed in previous studies. The bestadsorption isotherm to use in a certain situation depends upon both the gas and solid system under consideration. This is beacuase the equilibrium adsorbed phase concentration of a given component strongly depends partial pressure in the gas phase of the given component, temperature, and the electrostatic interaction between the molecules with the adsorbent and the other species at the adsorption sites.

2.1.1.1 Henry's Law

At sufficiently low concentration, the adsorption equilibrium relationship generally approaches a linear form called Henry's Law.

$$q_i = Kp_i \tag{2.1}$$

where K is the Henry's constant, q_i is the adsorbed amount of component i, p_i refers to the partial pressure of component i. Henry's constant is temperature-dependent, and the temperature effect is described by the van't Hoff equation:

$$K = K_0 e^{-\frac{\Delta H}{RT}} \tag{2.2}$$

where ΔH is the enthalpy change on adsorption. Since adsorption is an exothermic process, ΔH is negative and the Henry's constant therefore decreases with increasing temperature.

2.1.1.2 Langmuir Isotherm

The Langmuir isotherm is the most important and widely used adsorption model for correlating and predicting adsorption equilibrium capacity of different adsorbate molecules on a variety of adsorbents. Each adsorption site is assumed to accommodate one and only one molecule or atom (monolayer) and the adsorbent surface is assumed to be homogeneous. The Langmuir equation is described below:

$$q_i = q_{s,i} \frac{b_i p_i}{1 + b_i p_i} \tag{2.3}$$

where b_i is the equilibrium parameter, p_i is the partial pressure for component i, $q_{s,i}$ is the maximal adsorbed equilibrium amount for component i. $q_{s,i}$ represents a fixed number of surface sites, and thus is assumed to be a temperature independent constant. b_i is assumed to be temperature dependent and follows the von't Hoff equation defined below:

$$b_i = b_0 e^{-\frac{\Delta H}{RT}} \tag{2.4}$$

2.1.1.3 Freundlich and Langmuir-Freundlich Isotherms

Freundlich and Langmuir-Freundlich (Sips) isotherms are two widely used empirical isotherm equations to account for the surface heterogeneity.

The Freundlich equation is described below:

$$q_i = b_i p_i^{\frac{1}{n_i}} \tag{2.5}$$

The Freundlich equation includes the distribution of affinity among the surface adsorption site. The larger the n value, the more nonlinear is the adsorption isotherm. It should also be noted that the Freundlich equation does not reduce to Henry's Law in a low concentration scenario.

Sips isotherm model is a combination of Langmuir and Freundlich models that exhibits greater flexibility and represents over a wide range of conditions, the Sips equation can be written as:

$$q_i = q_{s,i} \frac{b_i {p_i}^{1/n_i}}{1 + b_i {p_i}^{1/n_i}} \tag{2.6}$$

2.1.2 Adsorption Kinetics

Adsorption takes place at the adsorption site inside the adsorbent particle. The rate of mass transfer of the gaseous molecules of a multi-component mixture, from the bulk phase to the actual adsorption site, plays a significant role in the overall separation dynamics. The actual mass transfer rates not only depend on the gaseous species affinity

for the adsorbent material, but also on the adsorbent physical internal structure. The physical internal structure of the adsorbent governs the physical path that gaseous molecules follow from the bulk phase to the actual adsorption site. In order to describe the adsorption kinetics and to determine the intracrystalline diffusivity on adsorbents, a pore diffusion model was derived according to Ruthven[8]. Neglecting the heat transfer between particle and surrounding, the diffusion in spherical coordinate is written as:

$$\frac{\partial q}{\partial t} = \frac{1}{r^2}\frac{\partial}{\partial r}\left(r^2 D_c \frac{\partial q}{\partial r}\right) \tag{2.7}$$

where r is the radius of the equivalent sphere, D_c is the intracrystalline diffusivity, q(r,t) is the adsorbed amount at time t and radial position r. For constant diffusivity at a given pressure, the solution of the above equation can be given by:

$$\frac{m_t}{m_\infty} = 1 - \frac{6}{\pi^2}\sum_{n=1}^{\infty}\frac{1}{n^2}\exp\left(\frac{-\pi^2 D_c t}{{r_c}^2}\right) \tag{2.8}$$

where $\frac{m_t}{m_\infty}$ is the fraction adsorption uptake, r_c is the crystal size. If the fraction uptake is greater than 70%, equation (2.8) can be simplified as the following equation:

$$1 - \frac{m_t}{m_\infty} \approx \frac{6}{\pi^2}\exp\left(\frac{-\pi^2 D_c t}{{r_c}^2}\right) \tag{2.9}$$

If the fraction uptake is lower than 85%, equation (2.8) can be simplified as the following equation:

$$\frac{m_t}{m_\infty} \approx \frac{6}{\sqrt{\pi}}\sqrt{\left(\frac{D_c}{{r_c}^2}\right)t} - 3\left(\frac{D_c t}{{r_c}^2}\right) \tag{2.10}$$

Though incorporating the system of equations to capture mass transfer resistance mentioned above is expected to yield a rigorous model, computation solution of such a formulation for multi-bed, multi-step PSA assembly can be a challenging task. In the past PSA modeling studies, the linear driving force (LDF) model, which approximated the actual intra-particle diffusion rate with a semi-empirical lumped expression has been very widely used[32–34]. The LDF model can be described by the following equation:

$$\frac{\partial \mathrm{q_i}}{\partial \mathrm{t}} = \mathrm{K_{p,i}}(\mathrm{q_i^*} - \mathrm{q_i}) \tag{2.11}$$

where $\mathrm{K_{p,i}}$ is the mass transfer coefficient that can be obtained by correlating the experimental kinetic data.

The underlying assumption[35–37] for the applicability of this model is that the PSA cycle time stays considerably higher than the diffusional time constant for the given gas-solid system. For the case of very fast PSA cycles such as rapid pressure swing adsorption (RPSA), the additional corrective terms need to be considered to maintain its validity.

2.1.3 Mass Balance

The continuity equations for the gas phase mass balance describe how species are transported through the bed in the axial direction. The effects of axial convection, dispersion, and transport to the adsorbed phase can be calculated using the following equations[25]:

$$\varepsilon_{tot}\frac{\partial C_i}{\partial \mathrm{t}} = -\varepsilon_b \frac{\partial}{\partial z}\left(D\frac{\partial C_i}{\partial \mathrm{z}}\right) - \frac{\partial C_i v}{\partial \mathrm{z}} + \rho_\mathrm{b} \cdot \frac{\partial \mathrm{q_i}}{\partial \mathrm{t}} \tag{2.12}$$

where ε_{tot} is the total void fraction, including intra- an inter-particle void space, C_i is the molar concentration of component i in the gas phase, ε_b is the void fraction in the bed (bed porosity), D is the mass axial dispersion coefficient, v is the superficial velocity of the gas phase, ρ_b is the density of bed, and q_i is the specific amount of component i adsorbed on the solid phase.

Generally, dispersive effects are prevalent in both radial and axial directions for cylindrical geometry. However, for the adsorption column with a large length to diameter ratio, the radial dispersion effect is negligible as compared to the dispersion in the axial direction. The axial dispersion coefficient is calculated based on the correlation raised by Wakao and Funazkri[38]:

$$\frac{\varepsilon_b D}{D_m} = 20 + 0.5ScRe \tag{2.13}$$

Here, Sc and Re are the dimensionless groups Schmidt and Reynold numbers, respectively.

$$Sc = \frac{\mu}{\rho_{gas} D_m} \tag{2.14}$$

$$Re = \frac{\rho_{gas} U d_p}{\mu} \tag{2.15}$$

2.1.4 Energy Balance

The continuity equation for the energy transport of the gas phase, accounts for the effects of axial convection, dispersion, and the contribution of the energy contained in the adsorbed phase, is given by the following equation:

$$\frac{\partial \tilde{u}}{\partial t} = \varepsilon_b \frac{\partial}{\partial z}\left(\rho D \frac{\partial h}{\partial z}\right) - \frac{\partial v \rho h}{\partial z} + \frac{1}{1000}\frac{\partial}{\partial z}\left(\lambda_{eff}\frac{\partial T}{\partial z}\right) - \frac{4}{d_b}\frac{1}{1000}k_{T,b-w}(\mathrm{T} - T_w) \quad (2.16)$$

where $\tilde{u}$ is the energy density per unit volume of bed, ρ is the mass density of the gas phase, h is the specific enthalpy of the gas phase, λ_{eff} is the effective thermal conductivity, $k_{T,b-w}$ is the heat transfer coefficient from the gas phase to the bed wall, T is the gas temperature, T_w is the bed wall temperature, d_b is bed diameter.

Since the thermal equilibrium between adsorbents and the bulk flow is assumed, the temperature in the gas phase is equal to that of the solid phase. The energy density per unit volume of bed is given by the following equation:

$$\tilde{u} = \varepsilon_b(\rho h - 10^2 P) + \rho_b\left(\sum_{\forall i \in C} q_i h_{ad,i}(T) + C_{p,ads}(T - T_{ref})\right) \quad (2.17)$$

where P is pressure in the unit of bar, $h_{ad,i}(T)$ is molar specific enthalpy of component i at the bed temperature, $C_{p,ads}$ is the heat capacity of the adsorbent, T_{ref} is the reference temperature.

The molar specific enthalpy can be determined from the pure component enthalpy at a reference state, the heat of adsorption, and the change in the heat capacity of the adsorbed species using the following equation:

$$h_{ad,i}(T) = h_i^{\emptyset}(T) + \Delta H_{ad,i} + \Delta C_{p,ad,i}\left(T - T_{ref}\right) \tag{2.18}$$

where $h_i^{\emptyset}(T)$ is the pure component enthalpy at the bed temperature, $\Delta H_{ad,i}$ is the heat of adsorption for component i, $\Delta C_{p,ad,i}$ is the change in the heat capacity of the adsorbed species from reference condition to bed conditions for component i.

The effective thermal conductivity can be determined from the Specchia correlation:

$$\lambda_{eff} = \varepsilon_b \lambda + (1 - \varepsilon_b) \frac{1}{\frac{0.22{\varepsilon_b}^2}{\lambda} + \frac{2}{3}\lambda_{ads}} \tag{2.19}$$

where λ is the thermal conductivity of the gas mixture, λ_{ads} is the thermal conductivity of adsorbent material.

2.1.5 Momentum Balance

Pressure variations inside the bed play an essential role at every stage of a PSA cycle. The pressure drop for the gas flow in packed beds is determined from the Ergun equation[39]:

$$\left(\frac{\partial P}{\partial z}\right)_t = -\frac{150\mu}{d_p^2}\frac{(1-\varepsilon_b)^2 v}{{\varepsilon_b}^3} - \frac{1.75\rho}{d_p}\frac{(1-\varepsilon_b)}{{\varepsilon_b}^3} v^2 \tag{2.20}$$

where μ is the dynamic viscosity of the gas, d_p is the diameter of the pellet particles.

2.1.6 Isosteric Heat of Adsorption

Isosteric heat of adsorption represents the affinity between adsorbates and adsorbents in adsorption. By fitting the adsorption isotherms measured at different temperatures and applying a variant of the Clausius-Clapeyron equation[38], the isosteric heat of adsorption can be calculated. The equation to calculate isosteric heat of adsorption is defined as:

$$Q_{st} = RT^2 \left(\frac{\partial lnP}{\partial T}\right)_q \tag{2.21}$$

where Q_{st} is the isosteric heat of adsorption, T is the temperature, P is the pressure, R is the gas constant.

2.1.7 Ideal Adsorbed Solution Theory (IAST) Calculations

If the adsorbed phase is thermodynamically ideal, the Ideal adsorbed solution theory (IAST) of Myers and Prausnitz[40] can be used to derive the equilibrium relationships for an adsorbed mixture directly from the pure-component isotherms. The adsorption selectivity of component 1 over component 2 in a binary mixture is defined by:

$$S = \frac{q_1/q_2}{p_1/p_2} \tag{2.22}$$

where q_1 and q_2 are the absolute component loadings of the adsorbed phase in the mixture. For non-ideal adsorbed solution systems, the vacancy solution theory could be applied to

provide a more general method for the prediction of binary or multi-component equilibria from single-component data[41].

2.2 Model Validation

2.2.1 Validation with Experimental PSA Data

In this work, the process model was validated by comparing the computated values to experimental PSA data provided from the Western Research Institute (WRI) for a high-temperature air separation process. The simulated maximum and minimum oxygen concentration during a cycle after reaching the cyclic steady state (CSS) was compared with experimental data (maximum and minimum oxygen marked in Figure 2.1). In Figure 2.2, the blue points stand for the simulation data and the red points stand for the experimental data. It was found that the simulation fit well with the experimental PSA data. The average percentage error was 10.1% for minimum oxygen concentration and 6.1% for maximum oxygen concentration.

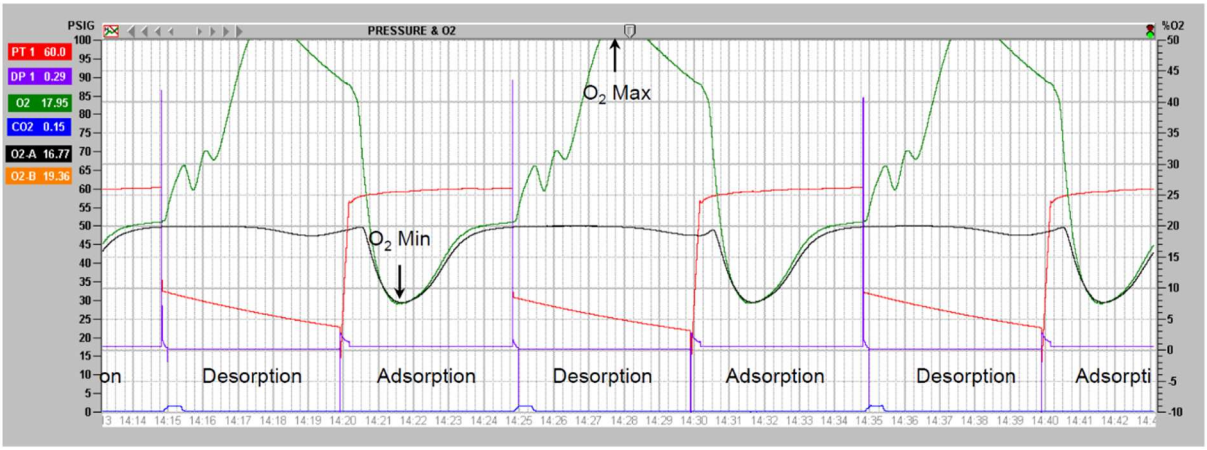

Figure 2.1. Experimental oxygen profile for cycles after reaching CSS.

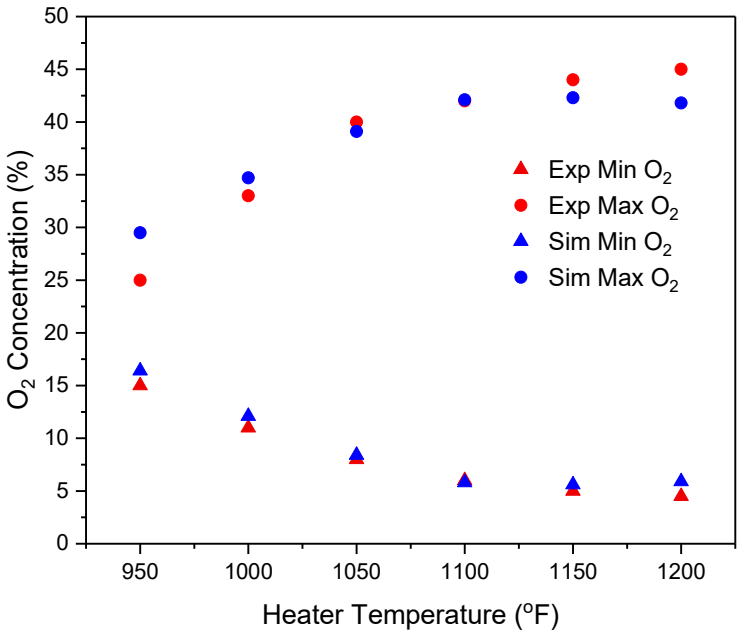

Figure 2.2. Experimental and simulated minimum and maximum oxygen concentration of product gas.

2.2.2 Validation with Air Separation Process from Literature

The process model was also validated by comparing with published data for a classical O_2/N_2 PSA system from Ruthven and Farooq[42]. The process used a nitrogen selective adsorbent, zeolite 5A, to produce a high purity oxygen product. The operating conditions and parameters for the process are given in Table 2.1. Figure 2.3 compares the experimental and simulation data for oxygen purity and recovery in the product. The simulation data fit well with the experimental data, and the overall trends as a function of cycle time are similar. The average percentage error of oxygen purity is 4.48%, and the average percentage error of oxygen recovery is 7.3%.

Table 2.1. Summary of operating conditions and parameters for the PSA process in Ruthven's work[42].

Parameters	Value
Adsorbent particles	Linde 5A
Average diameter, d_p (cm)	0.07
Bulk density, ρ_p (g/cm3)	1.574
Adsorption bed	
Length, L (cm)	35
Internal diameter, i.d. (cm)	3.5
Bed porosity, ε	0.4
Gas properties	
Flow rate of feeding gas (air), Q_f (mmol/s)	1.12

Feeding pressure, P_a (atm)	1.48
Flow rate of purging gas (CO_2), Q_p (mmol/s)	0.05
Purging pressure, P_d (atm)	1
Cycle time	
Total cycle time, tc (s)	100-250
Adsorption time (s)	0.2 tc
Desorption time (s)	0.2 tc
Pressurization time (s)	0.3 tc
Depressurization time (s)	0.3 tc
Adsorption equilibrium and kinetics	
Equilibrium constant K_a (O_2)	4.7
Equilibrium constant K_b (N_2)	14.8
Kinetic constant k_a (O_2) (1/s)	62
Kinetic constant k_b (N_2) (1/s)	20

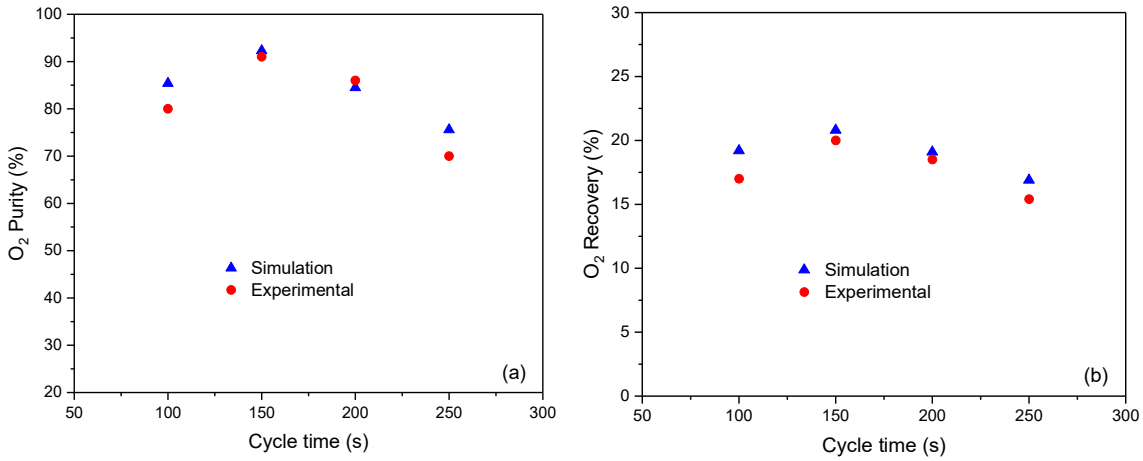

Figure 2.3. Experimental and simulated oxygen (a) purity and (b) recovery in the product as a function of cycle time.

2.2.3 Validation with CO_2 Capture Process from Literature

The simulation model was further validated with a one-bed four-step VPSA process for CO_2 capture from the flue gas using zeolite 13X from Ko's work[43]. The difference between the simulated and reported values of significant process performance indicators are acceptable, as shown in Table 2.2.

Table 2.2. Comparison of simulation results with literature regarding the product purity and productivity of a two-bed six-step VPSA process for CO_2 capture[43].

	CO_2 Purity	CO_2 Recovery	N_2 Purity	N_2 Recovery
Case 1				
Data reported from literature	88.94	96.60	99.45	99.65
Simulated data	88.67	94.81	99.65	98.63

Deviation	-0.27	-2.09	0.20	0.76
Case 2				
Data reported from literature	90.00	93.81	98.90	98.16
Simulated data	89.50	93.21	99.09	97.86
Deviation	-0.5	-0.6	0.19	-0.3

Chapter 3: High-Temperature Air Separation with Perovskite Oxide Sorbents

3.1 Introduction

The production of oxygen by air separation is an essential chemical engineering process. So far, the cryogenic distillation method has been widely used as an industrial production process of high-purity nitrogen and oxygen. Nevertheless, this method is more suitable for a large production scale due to its high energy cost[44,45]. Zeolites adsorbents, with their merits of low energy consumption and low investment, have been recently used in commercial pressure swing adsorption (PSA)[19,42,46]. However, most zeolite adsorbents separate air by adsorbing nitrogen, not oxygen. Larger quantities of adsorbents will be required because the amount of nitrogen in the air is nearly four times that of oxygen[47]. Besides, oxygen can hardly be separated from argon in the air under normal conditions by most zeolite adsorbents due to their weak or nonpolar nature and comparable polarizabilities[19]. The final product is a mixture of oxygen and argon, and the purity is limited to ~95%[48,49]. Thus, new adsorbent materials with superior adsorption properties and higher efficiency are desired to meet the industrial demand.

A novel high-temperature sorbent-based air separation process has drawn intense attention owing to the unique oxygen storage property of the perovskite oxide sorbents. As reported by Lin's group[50,51], perovskite oxides exhibit some crucial characteristics that might overcome the drawbacks of zeolite adsorbents. These characteristics include a large oxygen adsorption capacity, a high oxygen adsorption rate, and an infinite selectivity of oxygen over nitrogen or other gas species. Moreover, the high-temperature air separation

process will be more suitable for some high-temperature applications than previous air separation processes like cryogenic distillation or conventional PSA process based on zeolites[52]. Oxy-combustion is one example, where fuel is combusted with oxygen or oxygen-enriched gas instead of air to produce exhaust primarily of CO_2 and water vapor. The process substantially reduces NO_x emissions and makes it easier for CO_2 capture and sequestration[53]. At present, cryogenic air separation is the default technology for oxy-fuel power plants. However, its high energy consumption reduces the total plant efficiency by 8% to 12%[54]. The novel high-temperature air separation process based on perovskite oxide sorbents is perceived as the best alternative to cryogenic air separation as the high-temperature oxygen-enriched gas product can be combined with a combustion process very efficiently[55].

Perovskite oxides are a group of metal oxides having the general formula ABO_3[56]. Oxygen nonstoichiometry occurs in perovskite oxides with A- and B-site cations partially substituted by another cation with a lower oxidation state. The oxygen content in perovskite oxides varies continuously as a function of oxygen partial pressure and temperature, through the creation and destruction of oxygen nonstoichiometry in the crystal lattice. The transition of oxygen nonstoichiometry, represented as δ, between the fully oxidized state and reduced state in perovskite oxides, is shown in Equation 3.1. Oxygen is stored in the oxide lattice during the sorption step and releases to form oxygen nonstoichiometry during the desorption step.

$$\mathrm{AB}O_3 \leftrightarrow \mathrm{AB}O_{3-\delta} + \frac{\delta}{2} O_2 \tag{3.1}$$

Among the group of perovskite oxide materials, $La_{0.1}Sr_{0.9}Co_{0.9}Fe_{0.1}O_{3-\delta}$ (LSCF1991) has been reported[56–58] to exhibit large oxygen sorption capacity and relatively high oxygen adsorption and desorption rate. Moreover, Yin et al. proved[59] the presence of an endothermic disorder-order phase transition of oxygen nonstoichiometry during the exothermic adsorption step for LSCF1991. By taking advantage of the synergic effects of these two, the heat effects of the oxygen adsorption process can be lowered to reduce the operational cost of high-temperature air separation further. LSCF1991 was therefore selected as the representative adsorbent for high-temperature air separation in this work.

Recent work[56,60–62] has shown the potential for applying the PSA technique in the high-temperature air separation process by conducting thermogravimetric analysis (TGA) and fixed-bed breakthrough experiment with perovskite oxide sorbents. The PSA process is an industrial unit operation for separating gas mixtures by repeatedly changing the ambient pressure. The pressure of the system swings between high pressure in adsorption and low pressure in desorption in a cyclic manner. Despite there being many investigations that were performed on the dynamics of oxygen adsorption and desorption of different kinds of perovskite oxide adsorbents, the performance of PSA operations on high-temperature air separation has been rarely studied as yet. In addition, the operating conditions of this high-temperature PSA process are desired to be preliminarily designed and optimized before running the process in an actual pilot plant, which is both costly and time-consuming. The current study is demonstrated to determine the feasibility of producing oxygen-enriched gas via the PSA technique with the novel perovskite oxide

adsorbent, and to optimize the operating parameters of this PSA process by a process simulation study.

A great deal of research[50,63–66] regarding PSA simulations has been reported over the past couple of decades. To simulate the PSA process, a couple of partial differentials and algebraic equations (PDAEs)[9] distributed over time and space needs to be formulated, including mass, energy, and momentum conservation equations as well as transport and equilibrium equations. The set of nonlinear PDAEs is repeatedly solved with different initial and boundary conditions defining the steps of the PSA process. The optimal operating conditions for the PSA process were determined by studying the product purity and recovery under different conditions.

In this study, the LSCF1991 sorbents were prepared and pelletized using a pellet press. The mechanical properties of the solid pellets at different sintering temperatures were tested to determine the suitable sintering conditions. The oxygen storage ability of LSCF1991 sorbents was investigated by measuring the oxygen nonstoichiometry at different oxygen partial pressures and temperatures by TGA. Besides, the breakthrough experiments by sorption of oxygen on the LSCF1991 sorbents were performed in a fixed bed, as it simulated a small scale industrial air separation process and analyzed the separation performance. A PSA process simulation package was developed in Matlab. The simulation model was validated by comparing with the experimental data from fixed-bed experiments as well as the simulated result from another commercial software, ProSim DAC. Process simulations have been performed for high-temperature air separation under different operating conditions. The effect of adsorption and desorption pressure, feed and

purge gas flow rates, desorption duration, and the total cycle time on oxygen purity and recovery have been studied to optimize the operating parameters.

3.2 Experimental Section

The sorbent powder of LSCF1991 was synthesized by a liquid citrate method[67]. To prepare the sorbent powder, a stoichiometric mixture of $La(NO_3)_3 \cdot 6H_2O$, $Sr(NO_3)_2$, $Co(NO_3)_2 \cdot 6H_2O$, and $Fe(NO_3)_3 \cdot 9H_2O$ and 20% excess citric acid were dissolved in deionized water. The solution was then condensed and polymerized at 130 °C for 8 hours. The resulting gel-like solution was heated to 400 °C to remove organic content and was finally sintered at 1250 °C in the air for 20 hours. The prepared powder sorbents were ground in an agate mortar and mixed with a few drops of propylene carbonate emulsion as the binder. The ground sample was compressed with a pellet press to prepare pellet sorbents with a rod shape (3 mm diameter, 5-10 mm length). The resulting pellets were sintered at 500 - 1000 °C for 2 hours in the air, with a ramping rate of 5 °C /min.

The structure of the material was examined by high-resolution X-ray diffractometry (XRD, Panalytical X'pert Pro). The diffraction spectra were collected in the range of 2θ = 20 – 80 degrees. The mechanical properties of LSCF1991 pellets were determined by testing their crush strength and attrition resistance. The mechanical properties of the adsorbents are significant for their industrial applications. The crush strength of the pellets was tested by Instron universal mechanical property testing system. An increasing axial compressive load was forced on the sample until the sample deformed or fractured. The

attrition and abrasion resistance of the pellets was tested using a standard test method ASTM D4058[68]. The attrition testing units include a cylindrical drum with a single baffle, a motor, and a standard sieve. The pellets were rotated for 30 minutes at a rate of 60 rpm in the drum. Fines produced by attrition and abrasion in the test were sieved through the standard sieve. The attrition rate was calculated as follows:

$$\text{Loss on attrition} = \frac{A - B}{A} \tag{3.2}$$

where A is the original weight of the sample, and B is the weight of the sample on sieve after rotations. Mechanical failure of adsorbents may result in various problems of a PSA unit, such as blockage, the unacceptably high-pressure drop across the adsorption bed, and the maldistribution of fluid flow caused by fragments and fine particles[69]. The LSCF1991 pellets were sintered at different temperatures from 500 °C to 1000 °C to study the relationship between sintering temperature and mechanical properties.

The oxygen nonstoichiometry of the LSCF1991 sample was determined by the thermal gravimetric analyzer (TA Instrument, SQT 600). The initial oxygen vacancy of LSCF1991, δ_0, was obtained by reducing fresh LSCF 1991 sample in a 10% H_2/ 90% He flow at 850 °C. The value of δ_0 was calculated from the stoichiometry of the reduction reaction, the reaction equation, and the expression to calculate δ_0 is represented below[56]:

$$La_{0.1}Sr_{0.9}Co_{0.9}Fe_{0.1}O_{3-\delta} \rightarrow 0.05La_2O_3 + 0.9SrO + 0.9Co + 0.1Fe + \left(\frac{1.95 - \delta}{2}\right)O_2 \tag{3.3}$$

$$\delta_0 = \frac{1.95M_O - 3xM_O - x[0.1M_{La} + 0.9M_{Sr} + 0.9M_{Co} + 0.1M_{Fe}]}{(1-x)M_O} \tag{3.4}$$

where M_i is the atomic weight of element i, and x is the weight loss percentage after the reduction. With the calculated δ_0 value, the oxygen nonstoichiometry δ at different temperatures and oxygen partial pressures can be determined from the weight loss with respect to the fresh sample. The different partial oxygen pressures can be achieved under a flow of air/He mixture controlled by mass flow controllers. For each experiment, the sorbent amount is about 20 mg, and the flow rate is controlled at 100 ml/min. The oxygen storage capacity at a given pressure can be obtained from the oxygen nonstoichiometry at that condition and the reference condition with the following expression:

$$q = -\frac{\delta(P_{O_2}) - \delta_0}{2M_w} \tag{3.5}$$

where M_w is the molecular weight of LSCF1991 adsorbent.

The dynamic behavior of a packed adsorbent bed was studied to determine the feasibility of this new air separation process. The overall pattern of the dynamic behavior is generally determined by the adsorption equilibrium and may be strongly modified by kinetic effects. This dynamic behavior can be represented by a breakthrough curve, which is the outlet product concentration profile.

Figure 3.1 shows the schematic diagram of the fixed-bed experiment setup used in this work, including a gas delivery system, a fixed-bed column, a tube furnace, an oxygen analyzer, and a data recording system. The adsorption column is an alumina tube of 0.5 inch inner diameter and 0.625 inch outer diameter. The mass of the adsorbent packed in the column was about 10 grams for each experiment. Silica grains (Ceradyne Inc.) were used to fill the rest space of the column. Ultra-zero grade air (Praxair) and industrial grade

nitrogen (Praxair, 99.995%) were used during sorption and desorption, respectively. The flow rates of air and nitrogen were controlled by two mass flow controllers, and both were set at 30 mL/min to provide adequate oxygen concentration of the effluent in the experiments. During the sorption and desorption process, the oxygen concentration of the effluent was measured by an oxygen analyzer (Systech Illinois, ZR 800). The data was recorded each second on a PC connected to the oxygen analyzer.

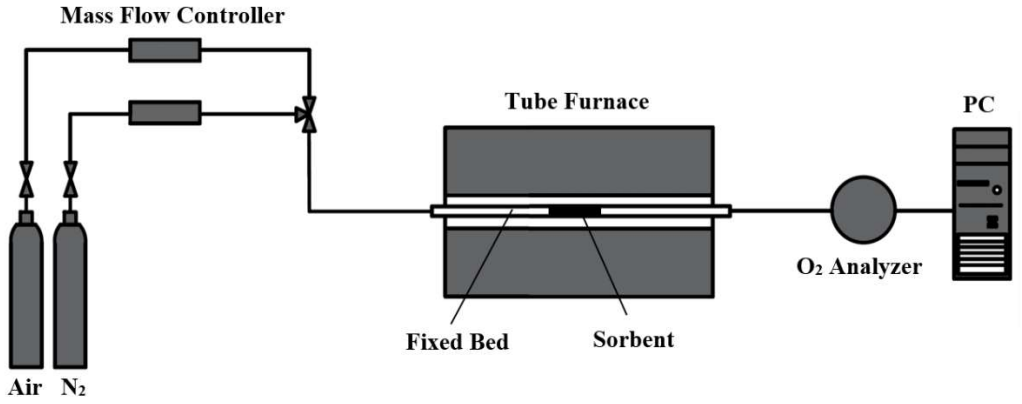

Figure 3.1. Schematic diagram of the fixed-bed setup for air separation on LSCF1991 pellets.

3.3 PSA Model and Simulation

The operation of the high-temperature air separation process is based on swings in oxygen partial pressure. There are four steps in this cyclic process: (1) Pressurization with feed air, (2) Adsorption with feed, (3) Depressurization, and (4) Purge with sweep gas to make the product. Oxygen partial pressure is lowered during the purge step to give sufficient driving force for oxygen desorption. The process flow diagram (PFD) of the PSA

process is shown in Figure 3.2. Carbon dioxide was used as the purge gas for this work to obtain an oxygen-enriched carbon dioxide stream for oxy-fuel combustion application.

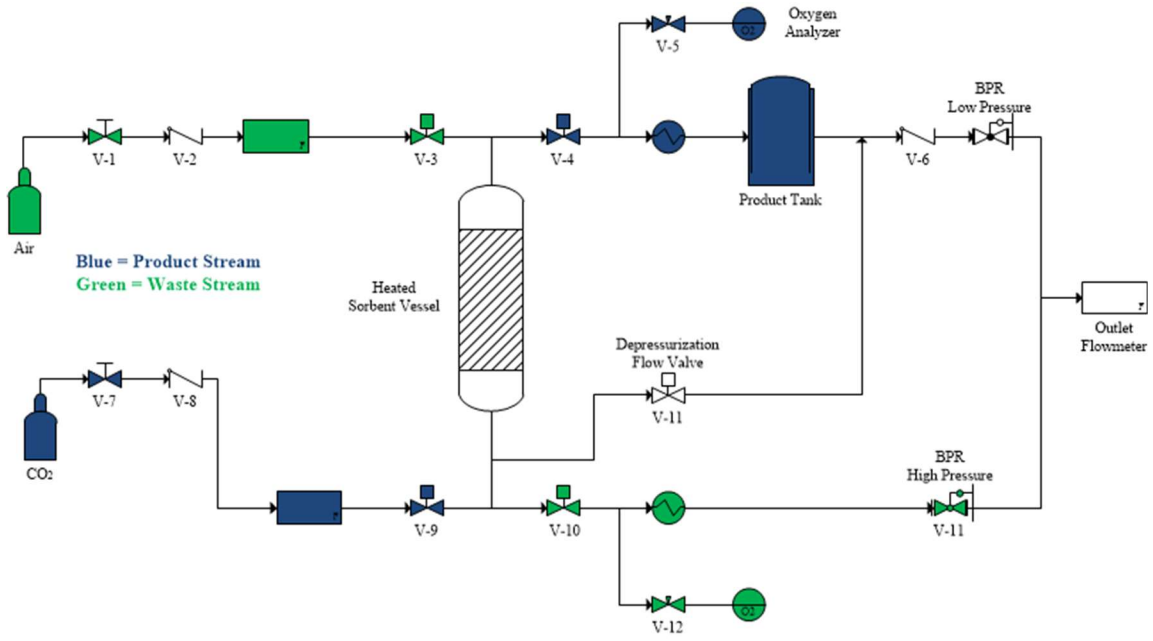

Figure 3.2. Graphical overview of the PSA system in the present work.

A PSA process simulation program for the high-temperature air separation using perovskite oxides was written in Matlab. The simulation methodology originated from Chai's simulation work[70,71] on single sorption or desorption step of oxygen on LiX zeolite adsorbents. The simulation program in this work added pressurization and depressurization steps in the PSA process for a more realistic simulation. Besides, each step of the PSA process was connected by the boundary conditions to simulate the PSA repeating cycles.

3.3.1 Simulation Assumptions

The following assumptions were applied in this study:

a. The gas-phase behaves as an ideal gas.

b. The system is isothermal.

c. There is no radial variation in gas concentration, temperature, and pressure.

d. The flow pattern is represented by the axial dispersed plug flow model.

e. Ignore the existence of argon. Assume the oxygen/nitrogen ratio of air is 21:79.

f. The porosity of the bed and adsorbent pellet is assumed to be uniform along the bed.

g. The diffusion and mass transfer effects are represented by the LDF model with a single lumped mass transfer coefficient.

h. A semi-empirical equation is used to describe oxygen adsorption behaviors.

3.3.2 Mathematical Model Equations

The equations describing the overall PSA cyclic operations are as follows.

Gas-phase mass balance for component i[72]:

$$\varepsilon\frac{\partial(y_i\rho_g)}{\partial t}-\varepsilon D_L\frac{\partial^2(y_i\rho_g)}{\partial z^2}+\frac{\partial(Qy_i)}{\partial z}+(1-\varepsilon)\rho_p\cdot\frac{\partial q_i}{\partial t}=0 \qquad (3.6)$$

where ε is the porosity of the bed, y_i is the molar fraction of component i in the bulk gas, ρ_g $[= \frac{P}{RT}]$ is the gas phase density, D_L is the mass axial dispersion coefficient, Q is the mass flux of the gas, ρ_p is the density of the adsorbent particle, and q_i is the specific amount of component i adsorbed on the solid phase.

The mass axial dispersion coefficient D_L in Equation 3.6 was estimated based on Wakao and Ruthven's estimation[8,73]:

$$D_L = 0.7D_m + 0.5\frac{d_p Q}{\varepsilon \rho_g} \tag{3.7}$$

where D_m is the molecular diffusivity, d_p is the diameter of the particle.

The molecular diffusivity was estimated by Fuller, Schettler and Giddings correlation[74]:

$$D_m = \frac{1.00 \times 10^{-3} \cdot T^{1.75} \sqrt{\frac{1}{M_A} + \frac{1}{M_B}}}{P[(\sum V_A)^{\frac{1}{3}} + (\sum V_B)^{\frac{1}{3}}]^2} \tag{3.8}$$

where M_A and M_B are the molecular weights for each component of the binary mixture, $\sum V_A$ and $\sum V_B$ are the values derived from the summation of molecular diffusion volumes for the two species.

The adsorption rate for component i was described by LDF model[75]:

$$\frac{\partial q_i}{\partial t} = K_{p,i}(q_i^* - q_i) \tag{3.9}$$

where $K_{p,i}$ is the effective mass transfer coefficient, q_i^* is the amount of component i adsorbed at equilibrium. The value of $K_{p,i}$ can be estimated by fitting the experimental kinetic data.

Column pressure drop was described by Ergun equation[76]:

$$\left(\frac{\partial P}{\partial z}\right)_t = -\frac{150\mu}{d_p^2\rho_g}\frac{(1-\varepsilon)^2}{\varepsilon^3}Q - \frac{1.75M_g}{d_p\rho_g}\frac{(1-\varepsilon)}{\varepsilon^3}Q^2 \tag{3.10}$$

where μ is the viscosity of the gas, ρ_g (=P/RT) is the gas density, M_g is the molecular weight of gas.

The oxygen nonstoichiometry of the LSCF1991 sorbent was predicted by a semi-empirical equation reported by Yang[77]. The semi-empirical equation has been proved to accurately predict oxygen nonstoichiometry on perovskite ceramics with respect to oxygen partial pressure and temperature.

$$\delta = \frac{3K{P_{O_2}}^n}{1+K{P_{O_2}}^n} \tag{3.11}$$

where K and n are the constants that only depends on temperature.

The oxygen adsorption isotherm was then obtained by comparing oxygen nonstoichiometry at a given oxygen partial pressure and the reference state:

$$q = -\frac{\delta(P_{O_2}) - \delta_0}{2M_w} = -\frac{\frac{3K{P_{O_2}}^n}{1+K{P_{O_2}}^n} - \delta_0}{2M_w} \tag{3.12}$$

Simulations of pressurization and depressurization steps were developed by a modified equation using the Ergun equation, mass conservation equation and Darcy equation[78]. The equations that describe pressure profile with respect to time during the pressurization and depressurization steps are as follows.

For a gas which is not adsorbed,

$$\left(\frac{\partial \mathrm{P}}{\partial \mathrm{t}}\right)_{\mathrm{z}} = -\frac{\kappa}{\mu\varepsilon} \times \left\{\frac{\partial}{\partial \mathrm{z}}\left[\mathrm{P}\left(\frac{\partial \mathrm{P}}{\partial \mathrm{z}}\right)_{\mathrm{t}}\right]\right\} \tag{3.13}$$

For an adsorbable gas,

$$\left(\frac{\partial \mathrm{P}}{\partial \mathrm{t}}\right)_{\mathrm{z}} = -\frac{\kappa}{\mu\big((1-\varepsilon)\rho \mathrm{f}'(\mathrm{p}) + \varepsilon\big)} \times \left\{\frac{\partial}{\partial \mathrm{z}}\left[\mathrm{P}\left(\frac{\partial \mathrm{P}}{\partial \mathrm{z}}\right)_{\mathrm{t}}\right]\right\} \tag{3.14}$$

where μ is the viscosity of the gas, κ is bed permeability, f'(p) is the gradient of adsorption isotherm with respect to pressure.

Value of κ is estimated by Kozeny-Carman equation[79,80]:

$$\kappa = \frac{\varepsilon^3}{Ko(1-\varepsilon)^2\left(\frac{6}{d_p}\right)^2} \tag{3.15}$$

where Ko is the Kozeny constant, which is 5 for fixed beds[81].

The initial and boundary conditions for the set of PDEs are described below:

Initial conditions:

$$\mathrm{y_i}(\mathrm{z}, 0) = 0; \quad \mathrm{P}(\mathrm{z}, 0) = \mathrm{P_0} \tag{3.16}$$

Boundary conditions for the pressurization step:

$$\mathrm{y_i}(0,\mathrm{t}) = y_{i,feed};\ \frac{\partial \mathrm{y_i}}{\partial z}(\mathrm{L},\mathrm{t}) = 0;\ \mathrm{P}(0,\mathrm{t}) = \mathrm{P_a};\ \frac{\partial \mathrm{P}}{\partial z}(\mathrm{L},\mathrm{t}) = 0 \tag{3.17}$$

Boundary conditions for the adsorption step:

$$\mathrm{y_i}(0,\mathrm{t}) = y_{i,feed};\ \frac{\partial \mathrm{y_i}}{\partial z}(\mathrm{L},\mathrm{t}) = 0;\ \mathrm{P}(0,\mathrm{t}) = \mathrm{P_a};\ \frac{\partial \mathrm{P}}{\partial z}(\mathrm{L},\mathrm{t}) = 0 \tag{3.18}$$

Boundary conditions for the depressurization step:

$$\frac{\partial \mathrm{y_i}}{\partial z}(0,\mathrm{t}) = 0;\ \frac{\partial \mathrm{y_i}}{\partial z}(\mathrm{L},\mathrm{t}) = 0;\ \mathrm{P}(0,\mathrm{t}) = \mathrm{P_d};\ \frac{\partial \mathrm{P}}{\partial z}(\mathrm{L},\mathrm{t}) = 0 \tag{3.19}$$

Boundary conditions for the desorption step:

$$\frac{\partial \mathrm{y_i}}{\partial z}(0,\mathrm{t}) = 0;\ \mathrm{y_i}(\mathrm{L},\mathrm{t}) = y_{i,purge};\ \mathrm{P}(0,\mathrm{t}) = \mathrm{P_d};\ \frac{\partial \mathrm{P}}{\partial z}(\mathrm{L},\mathrm{t}) = 0 \tag{3.20}$$

where $\mathrm{P_0}$ is the initial pressure in the adsorption bed, $\mathrm{P_a}$ is the adsorption pressure and $\mathrm{P_d}$ is the desorption pressure. Moreover, the final concentration and pressure of each step will equal the initial concentration and pressure of the next step.

The performance indicators of the PSA process (oxygen purity, recovery, and productivity) for one cycle at steady state are calculated with the following expressions:

$$O_2\ Purity = \frac{\int_0^{t_{des}} Q_{exit,des} * y_{O_2,exit,des}\, dt}{\int_0^{t_{des}} Q_{exit,des}\, dt} \tag{3.21}$$

$$O_2\ Recovery = \frac{\int_0^{t_{des}} Q_{exit,des} * y_{O_2,exit,des}\, dt}{\int_0^{t_{ads}} Q_{feed,ads} * y_{O_2,feed,ads} dt} \tag{3.22}$$

$$O_2\ Productivity = \frac{\int_0^{t_{des}} Q_{exit,des} * y_{O_2,exit,des}\, dt}{t_{cycle} * mass\ of\ adsorbent} \tag{3.23}$$

where t_{ads}, t_{des} is the duration of adsorption and desorption step, , t_{cycle} is the duration of one PSA cycle, $Q_{exit,des}$ and $y_{O_2,exit,des}$ are the exit gas mass flux and exit O_2 molar fraction during the desorption step, $Q_{feed,ads}$ and $y_{O_2,feed,ads}$ are the feeding gas mass flux and feeding O_2 molar fraction during the adsorption step.

A summary of the isotherm and model parameters for the PSA process are listed in Table 3.1 and Table 3.2. Other operational parameters for the PSA process can be found in Table 3.4. The isotherm constants K and n were determined by fitting experimental oxygen nonstoichiometry data using the nonlinear regression method.

Table 3.1. Regressed values of isotherm parameters K and n at different temperatures.

Temperature (°C)	K (atm^{-n})	n
500	0.0693	-0.1082
600	0.0854	-0.0844
700	0.1001	-0.0672
800	0.1082	-0.06095

Table 3.2. Model parameters for the PSA process.

Parameter	Value
$\sum V_{O_2}\ (cm^3/mol)$	16.6
$\sum V_{CO_2}\ (cm^3/mol)$	26.9
$D_m\ (cm^2/s)$	0.628
$D_L\ (cm^2/s)$	0.44
μ (g/cm/s)	$3.547*10^{-4}$
$\kappa\ (cm^2)$	$5.07*10^{-5}$
γ_{air}	1.39
γ_{CO2}	1.26
η_b	0.8
η_v	0.8

3.3.3 Numerical Methods

The PDAEs of continuous-time and spatial domain can be converted into differential-algebraic equations (DAEs) of time-domain only via the method of lines (MOL)[82] by discretizing all the spatial derivative terms. The DAEs can then be solved by an inbuilt function ode15s in Matlab.

The most convenient method to discretize the convective terms in the PDAEs is the linear approximation method. However, the linear discretizing method has its limitations.

It is not accurate enough at lower orders while introducing non-physical oscillation solutions at higher orders. As Godunov's published work[83] proved, linear methods cannot provide non-oscillatory solutions higher than first order.

Therefore, a nonlinear approximation method using flux conserving formulation and superbee flux limiter[84] was employed to discretize the convective terms. The superbee flux limiter can switch between the high and low-resolution schemes flux formulation. It allows the use of high order approximation at smooth solutions while limiting its use at high gradient regions, thus preventing nonphysical oscillation and numerical dispersion[71].

3.4 Results and Discussions

3.4.1 Material Characterization

The PXRD pattern of the LSCF-1991 sample is shown in Figure 3.3. It shows a typical perovskite phase structure. The mechanical properties of the sorbent samples were determined by measuring their crush strength and attrition rate. The testing results are shown in Figure 3.4. With different sintering temperatures, the crush strength increases with sintering temperature while the attrition rate decreases with sintering temperature. The temperature effect on the improvement of mechanical properties is more obvious when the sintering temperature is above 800 °C. At 1000 °C, the crush strength of the LSCF1991 pellets achieves the largest value (596.39 N) and the attrition rate reaches the lowest value (9.61 %). The same measurements were also performed on several commercial zeolite granule samples with similar particle sizes for comparison. The average crush strength and

attrition rate of zeolite samples are 77.75N and 11.6%, respectively. The LSCF1991 pellet samples that sintered at 1000 °C were therefore considered to have an adequate mechanical strength to be applicable for the PSA process.

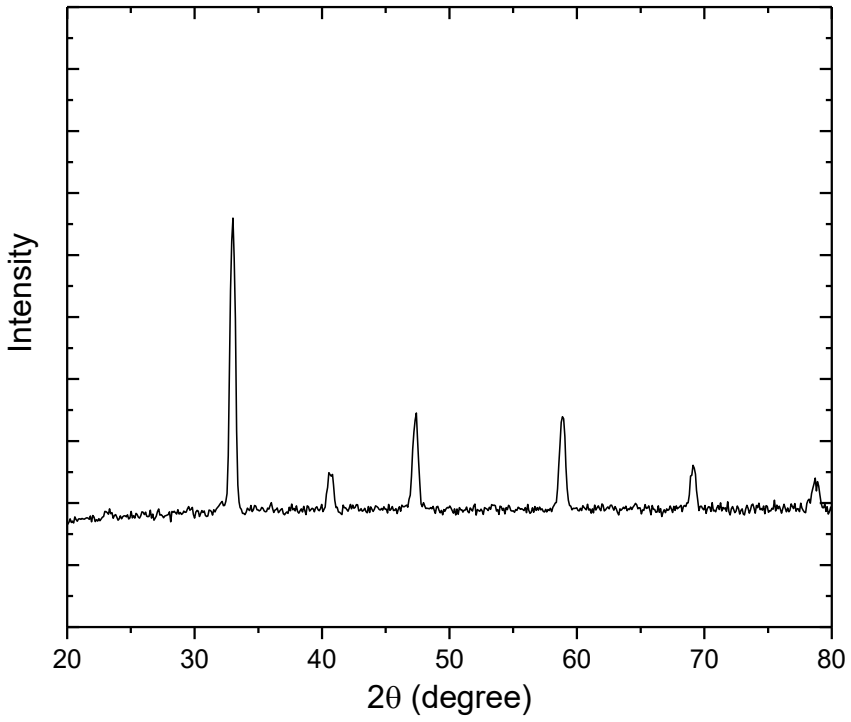

Figure 3.3. PXRD spectra of LSCF1991 sample.

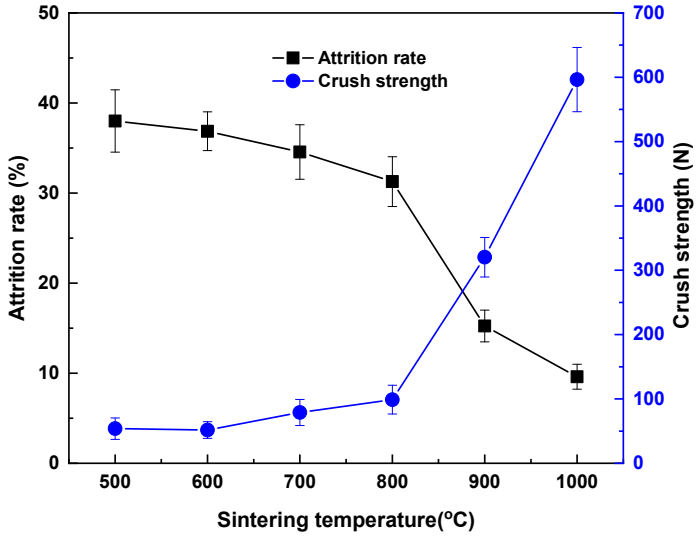

Figure 3.4. Mechanical properties of LSCF1991 pellets at different sintering temperatures.

3.4.2 Oxygen Nonstoichiometry and Adsorption Isotherm on LSCF1991

The oxygen nonstoichiometry of LSCF1991 was calculated with Equation 3.11. With the regressed values of K and n listed in Table 3.2, the simulated oxygen nonstoichiometry of LSCF1991 was obtained and compared with experimental isotherm data in Figure 3.5. It was found that the calculation results from Equation 3.11 agree well with the experimental values at all temperatures. With the calculated oxygen nonstoichiometry values, the adsorption amount of oxygen can be obtained by Equation 3.12. The oxygen isotherm of LSCF1991 from both experimental and simulated oxygen nonstoichiometry values are shown in Figure 3.6.

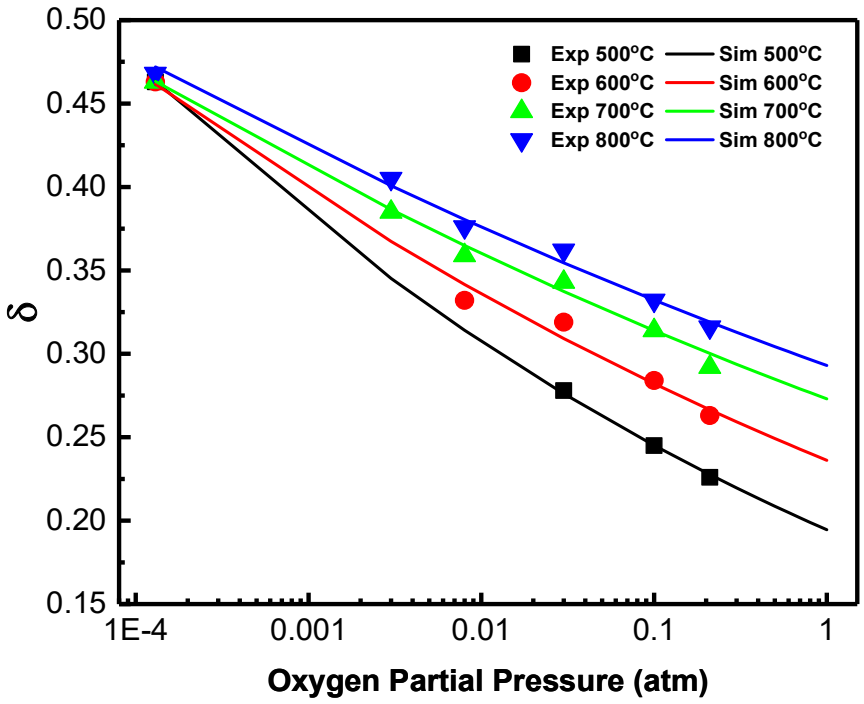

Figure 3.5. Experimental and simulated oxygen nonstoichiometry at different temperatures.

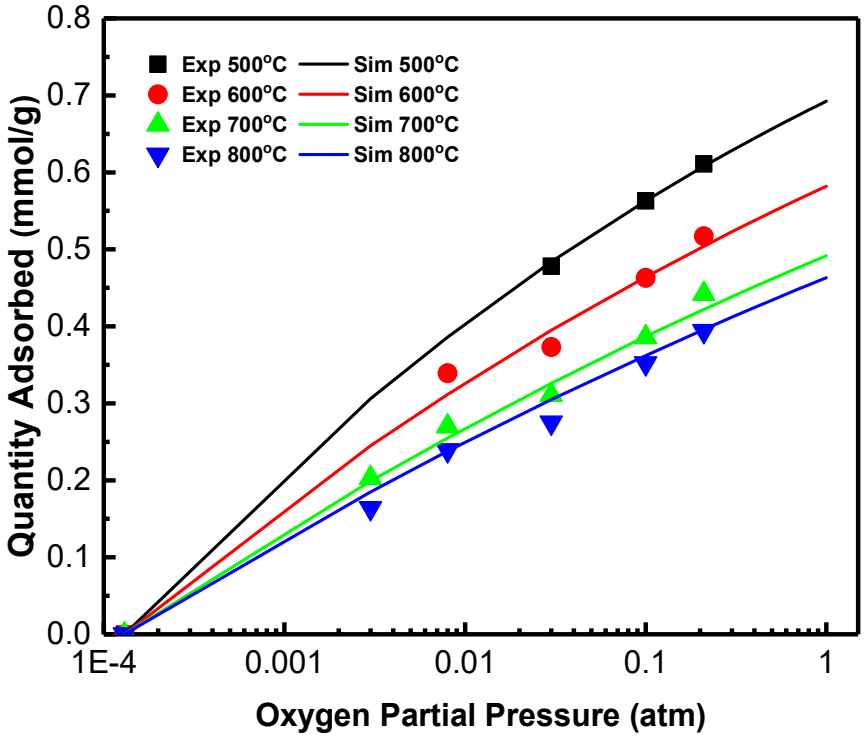

Figure 3.6. Experimental and simulated oxygen adsorption isotherms on LSCF1991.

3.4.3 Oxygen Adsorption and Desorption Kinetics on LSCF1991

Oxygen adsorption and desorption kinetics of LSCF1991 were measured by the TGA unit from 500 to 800 °C. The LDF model was used to simulate the dynamic behavior of oxygen adsorption and desorption. The experimental adsorption and desorption kinetic curves, as well as the corresponding simulated curves by the LDF model at different temperatures are shown in Figure 3.7, where the adsorbed amount of oxygen was represented by the weight change of the adsorbent. In Figure 3.7(b), the desorption rate has a sudden increase at around 20 minutes for all the temperatures. This phenomenon can be caused by the order-disorder phase transition according to previous research[67], which

observed a faster desorption rate of LSCF1991 than other perovskite oxide adsorbents without the phase transition. Although the LDF model doesn't fit the desorption kinetic curve well due to the sudden rate increase caused by the phase transition, the mass transfer coefficient still represents the average rate of desorption. The calculated mass transfer coefficients for oxygen adsorption and desorption on LSCF1991 are given in Table 3.3. The values will be used in Equation 3.9 for the adsorption bed model.

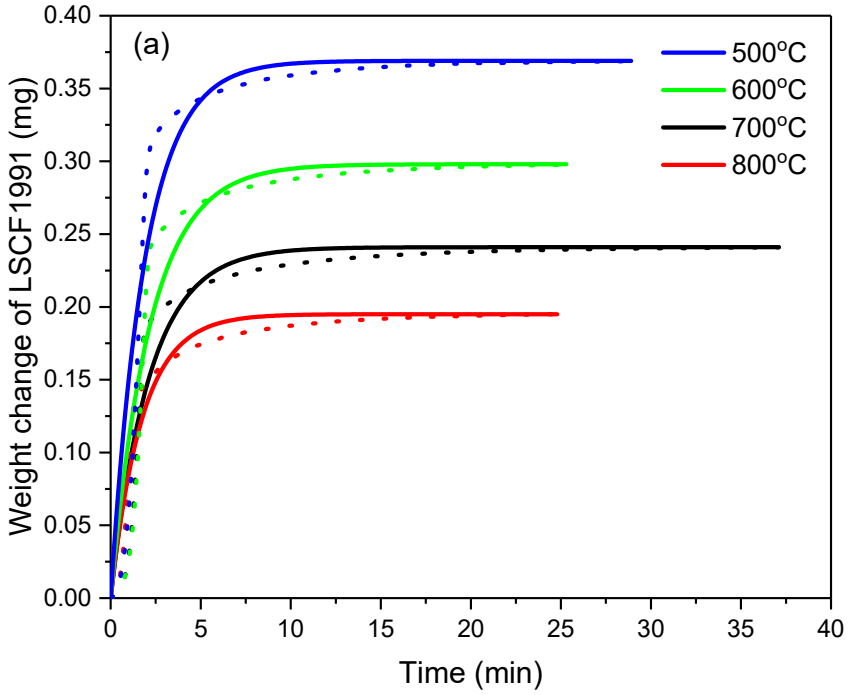

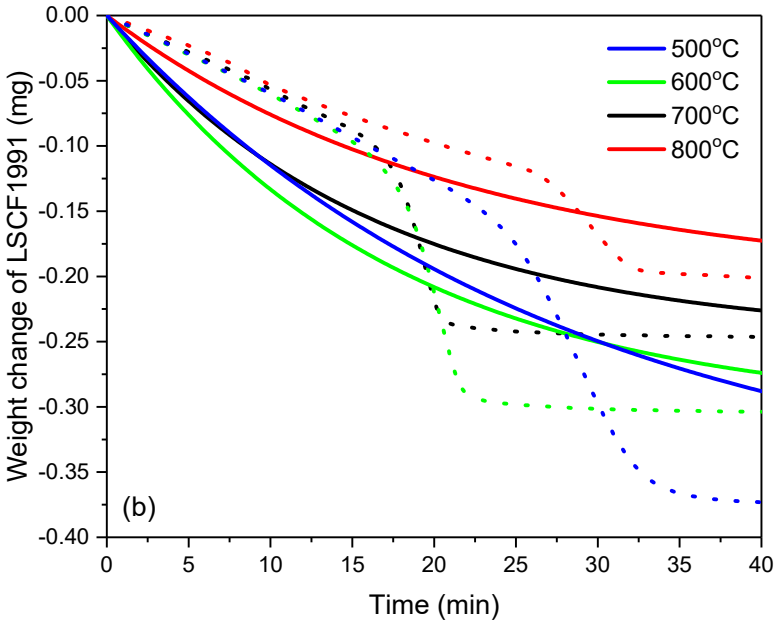

Figure 3.7. Weight change of LSCF1991 in TGA for oxygen (a) adsorption, and (b) desorption (dotted curve: experimental; solid curve: simulation).

Table 3.3. Mass transfer coefficients of oxygen adsorption and desorption on LSCF1991.

Temperature (°C)	$k_{O_2,sorption}\ (1/s)$	$k_{O_2,desorption}\ (1/s)$
500	0.523	0.0465
600	0.454	0.0576
700	0.463	0.0618
800	0.574	0.0464

3.4.4 Experimental and Simulated Breakthrough Curves

The adsorption and desorption breakthrough curves for oxygen on LSCF1991 pellets at different temperatures are represented in Figure 3.8(a) and (b), respectively. The adsorption breakthrough point can be achieved earlier when increasing the temperature due to the decreasing adsorption capacity, while the slope of the adsorption breakthrough curves at different temperatures are similar. For desorption, the oxygen concentration tends to drop slightly faster at a higher temperature, which is unfavorable for producing high purity oxygen product.

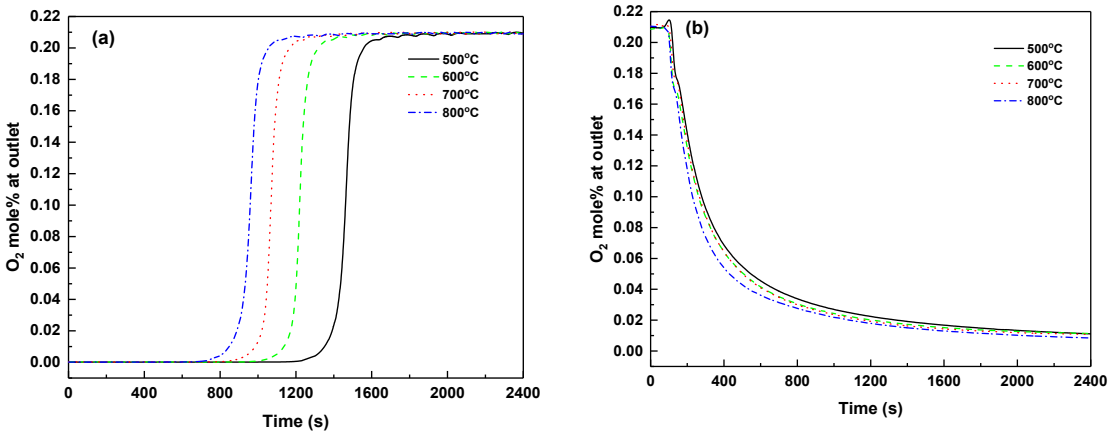

Figure 3.8. Fixed-bed breakthrough curves of LSCF1991 pellets from 500 °C to 800 °C during (a) adsorption and (b) desorption.

To validate the process simulation model, the simulated adsorption breakthrough curves for oxygen on LSCF1991 pellets at 500 °C and 600 °C were compared with the experimental data as well as the simulated results from ProSim DAC, which is shown in

Figure 3.9(a) and (b). From both figures, the simulated breakthrough curve from Matlab matches better with the experimental value compared with the simulation results from ProSim DAC. Because the Matlab programs are highly customized and can be more accurately simulate a specific adsorption process. The Matlab simulations were repeated for desorption breakthrough experiments as well; the experimental and simulated desorption breakthrough curves are presented in Figure 3.10.

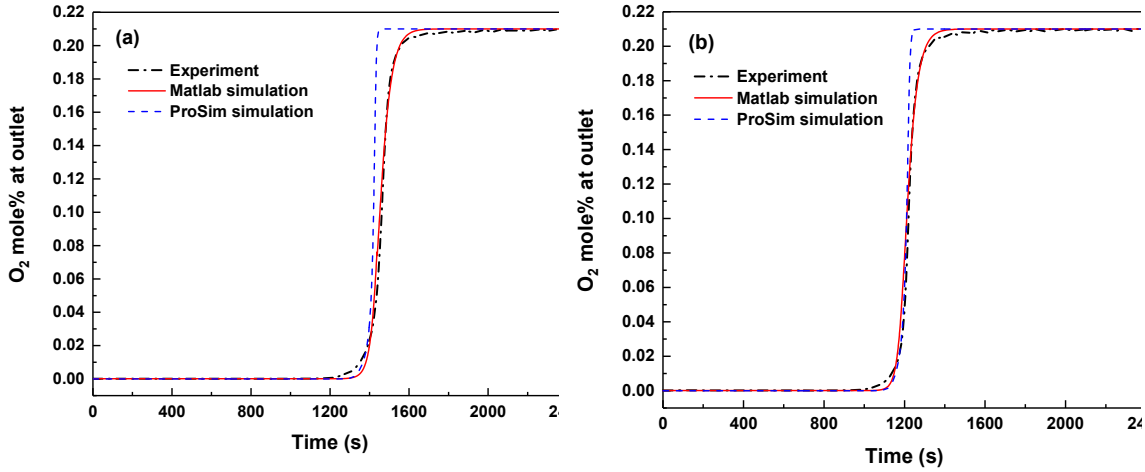

Figure 3.9. Experimental and simulated adsorption breakthrough curves of LSCF1991 pellets at (a) 500 °C, and (b) 600 °C.

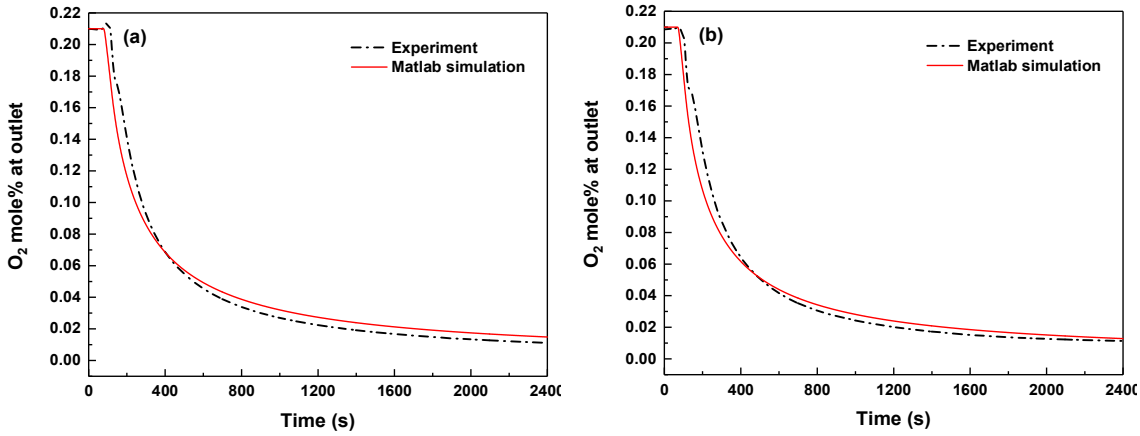

Figure 3.10. Experimental and simulated desorption breakthrough curves of LSCF1991 pellets at (a) 500 °C, and (b) 600 °C.

3.4.5 Parametric Study of PSA Process

A parametric study was performed in this work to clarify the effect of individual parameters on the PSA process performance through the Matlab PSA simulation. The parameters include adsorption and desorption pressure, flow rates of feed gas and purge gas, desorption duration, and cycle time. The base case parameters for the PSA process were displayed in Table 3.4. Once the base case parameters were determined, only one parameter was changed each time to analyze its effect. The performance of the PSA process was evaluated by oxygen purity, recovery, and productivity based on the last five cycles among the 20 cycles to ensure the system reached the cyclic steady state (CSS).

Table 3.4. Base case parameters for the PSA process.

Parameters	Value
Adsorbent particles	
Average diameter, d_p (cm)	0.3
Bulk density, ρ_p (g/cm3)	1.574
Adsorption bed	
Length, L (cm)	30.48
Internal diameter, i.d. (cm)	2.54
Bed porosity, ε	0.35
Gas properties	
Flow rate of feeding gas (air), Q_f (mmol/s)	2.08
Feeding pressure, P_a (atm)	1.36
Flow rate of purging gas (CO_2), Q_p (mmol/s)	0.409
Purging pressure, P_d (atm)	0.136
Cycle time	
Adsorption time (s)	295
Desorption time (s)	295
Pressurization time (s)	5
Depressurization time (s)	5

The effect of adsorption and desorption pressure on oxygen purity, recovery, and productivity were investigated by increasing the base case adsorption pressure and decreasing the base case desorption pressure, respectively. From Figure 3.11(a), oxygen purity, recovery, and productivity increase rapidly initially, then gradually slow down with the increasing adsorption pressure. The process indicators tend to achieve constant values when the adsorption pressure is large. This is because the oxygen adsorption capacity of the material increases with pressure. With a higher pressure, more oxygen will be adsorbed during the adsorption step. As a result, more oxygen will be released as well. The slow down phenomenon can be accounted for the logarithmic type of adsorption isotherm. From Figure 3.11(b), generally oxygen purity, recovery, and productivity increase when reducing the desorption pressure. Because the adsorber will hold less oxygen with lower desorption pressure. Since the desorption pressure investigated here is very low, larger simulation error may occur from the adsorption isotherm model. However, the trend of variation of these performance indicators is still representable.

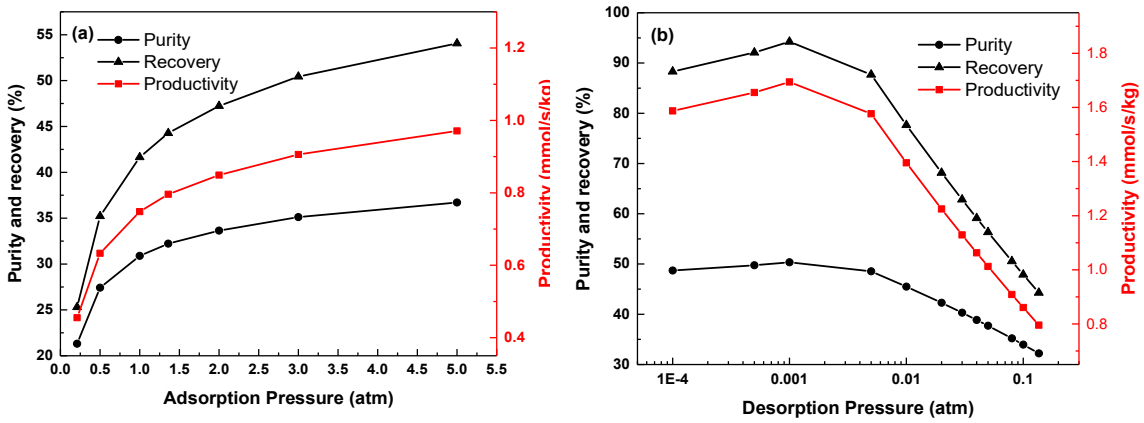

Figure 3.11. Oxygen purity and recovery as a function of (a) adsorption pressure, and (b) desorption pressure.

The effect of feed gas and purge gas flow rates on oxygen purity, recovery, and productivity were studied by varying the feed gas and purge gas flow rates, respectively. From Figure 3.12(a), oxygen purity and productivity increase and then become constant while recovery keeps decreasing when feed gas flow rate increases. The bed is not able to be saturated during the given cycle time at a lower feed gas flow rate, resulting in relatively low oxygen purity. However, if the feed gas flow rate is large enough to saturate the adsorption bed, the purity and productivity of oxygen will not change anymore. Further increasing the feed gas flow rate will only waste the feedstock and decrease oxygen recovery. As seen from Figure 3.12(b), oxygen purity goes up when reducing the purge gas flow rate, but the recovery and productivity follow the reverse trend. Since oxygen was produced during the desorption step, the only impurity in the product was the purge gas. Even though the amount of recovered oxygen will be reduced when reducing the flow rate

of purge gas, the loss of recovered oxygen was much less compared with the loss of purge gas, which results in higher oxygen percentage. Oxygen recovery and productivity are lowered because of the reduction of the total recovered oxygen amount.

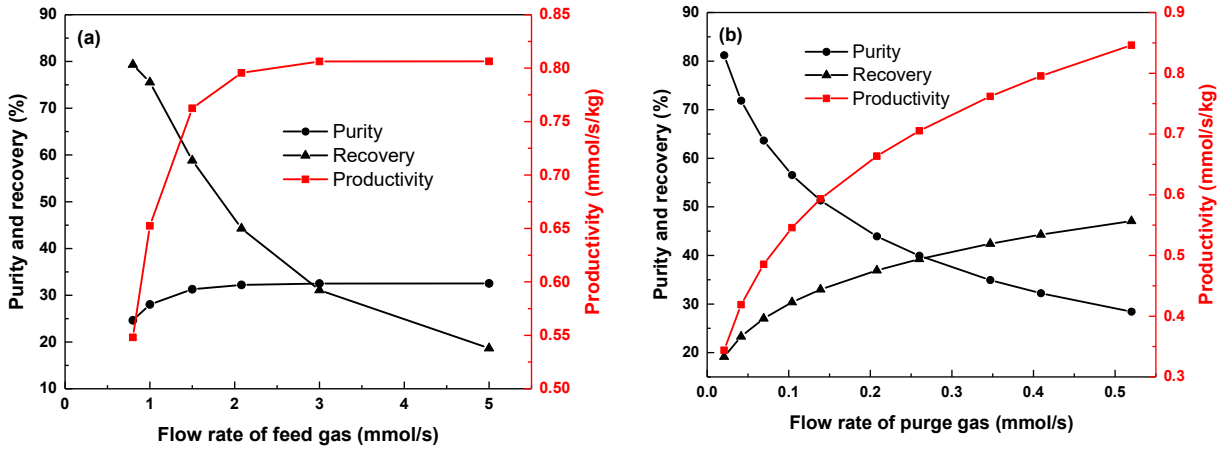

Figure 3.12. Oxygen purity, recovery, and productivity as a function of (a) feed gas flow rate, and (b) purge gas flow rate.

The effect of desorption duration was studied while keeping the total cycle time constant. As shown in Figure 3.13, oxygen purity decreases while recovery and productivity decrease with the decrease of desorption duration. The trend of oxygen purity is due to the oxygen concentration decreasing with time during the desorption step. With shorter desorption duration, higher oxygen purity can thus be obtained. However, recovery and productivity decrease at the same time. Because the increased oxygen purity cannot make up the loss of desorption time to produce oxygen. Thus, the desorption duration of a

cycle should be determined to balance the desired oxygen purity, high oxygen recovery, and productivity.

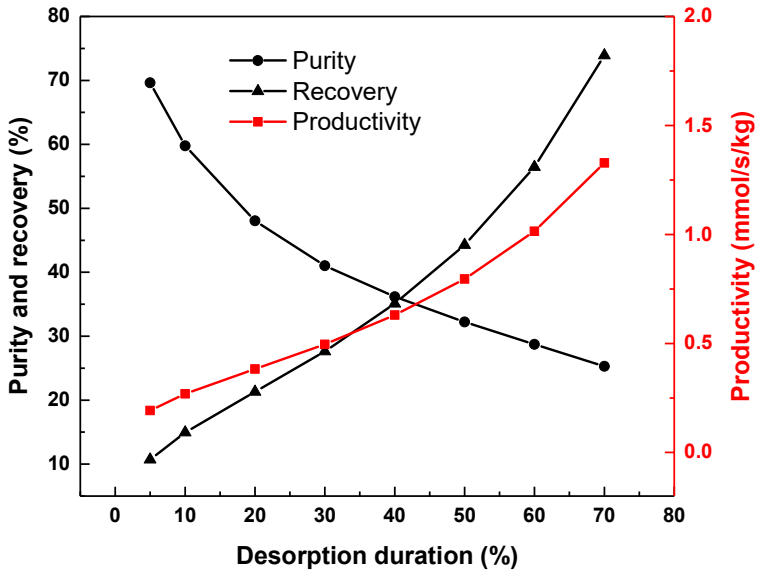

Figure 3.13. Effect of desorption duration on oxygen purity, recovery, and productivity.

While analyzing the effect of cycle time on oxygen purity, recovery, and productivity, the pressurization and depressurization time were kept constant as 5 seconds, and the ratio of the operation time of adsorption and desorption steps in a cycle was kept constant as well. Figure 3.14(a) and (b) show the effect of cycle time at different ratios of adsorption and desorption duration. It can be observed that within a specific range, decreasing the total cycle time will increase oxygen purity, recovery, and productivity. However, at a lower cycle time range, further decrease in the cycle time will reduce all the performance indicators. This can be explained that the variation of cycle time can affect

PSA performance in two ways. Even though the reduction of desorption time increases the average oxygen purity considering that oxygen concentration always decreases with time during desorption, the amount of oxygen stored in the adsorbents during adsorption step will also drop when the adsorber is not saturated with oxygen due to insufficient adsorption time. The optimum cycle time for the highest oxygen purity, recovery, and productivity depend on other operating parameters. As shown in Figure 3.14, the value of optimum cycle time is around 60 seconds and 120 seconds when the ratio of adsorption and desorption time is 1:1 and 1:4, respectively.

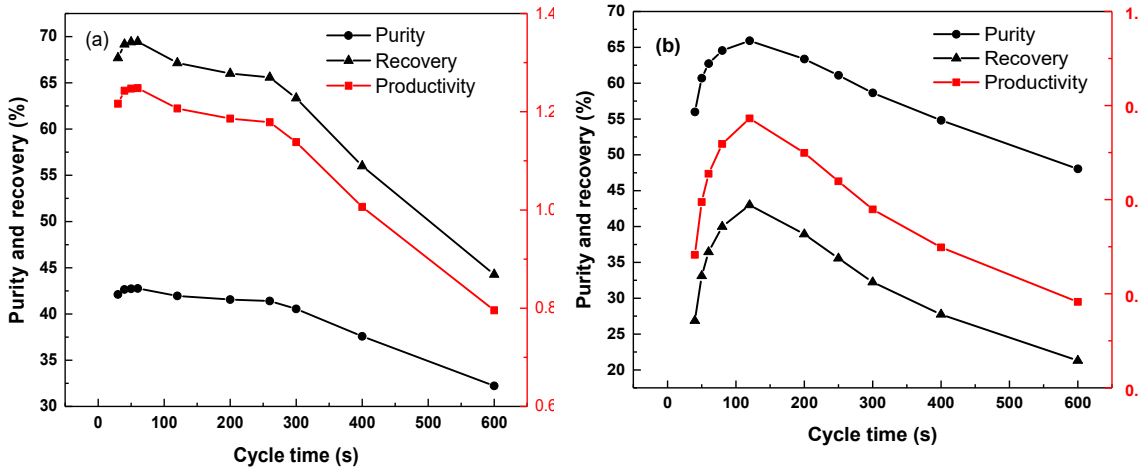

Figure 3.14. Effect of cycle time on oxygen purity, recovery, and productivity when the ratio of adsorption and desorption duration is (a) 1:1, and (b) 1:4.

As discussed above, adsorption and desorption pressure, flow rates of feed gas and purge gas, the time distribution of adsorption and desorption, and the total cycle time have

different effects on oxygen purity, recovery, and productivity. It can also be concluded that oxygen purity, recovery, and productivity can hardly to be maximized at the same time, since some of the parameters, like purge gas flow rate and desorption duration, have reverse effects on different PSA performance indicators. To optimize the operational parameters for the PSA process, a target oxygen concentration needs to be determined first. In this study, the target oxygen purity was set at 98%, and the corresponding optimum set of parameters are shown in Table 3.5. With the optimum parameters, oxygen purity of 98.21%, recovery of 74.05%, and productivity of 1.22 mmol/s/kg were achieved. The pressure and gas molar profile at the outlet of the adsorption bed of a PSA cycle under the above conditions is shown in Figure 3.15. The obtained oxygen purity, recovery, and productivity values are much higher than the corresponding values of the PSA process with several conventional zeolites, as shown in Table 3.6. In addition, the oxygen purity can be further improved by reducing the desorption duration of the purge gas flow rate at the loss of oxygen recovery and productivity.

Table 3.5. Optimal values of operational parameters for PSA.

Parameters	Value
Adsorption pressure (atm)	3
Desorption pressure (atm)	0.01
Flow rate of feed gas (mmol/s)	2
Flow rate of purge gas (mmol/s)	0.01

Cycle time	
Pressurization (s)	5
Adsorption (s)	139
Depressurization (s)	5
Desorption (s)	91

Table 3.6. Comparison of oxygen purity, recovery, and productivity for air separation with different adsorbents.

Adsorbents	O_2 purity (%)	O_2 recovery (%)	O_2 productivity (mmol/s/kg)
LSCF1991	98.21	74.05	1.22
NaX zeolite[85]	95.6	53.4	0.227[b]
LiX zeolite[85]	95.9	64.5	0.23[b]
Ag-Li-X zeolite[86]	~90	24	-
Zeolite 5A[87]	94.5[a]	44.5	0.24[b]
Zeolite 5A[64]	95.5	27.1	-

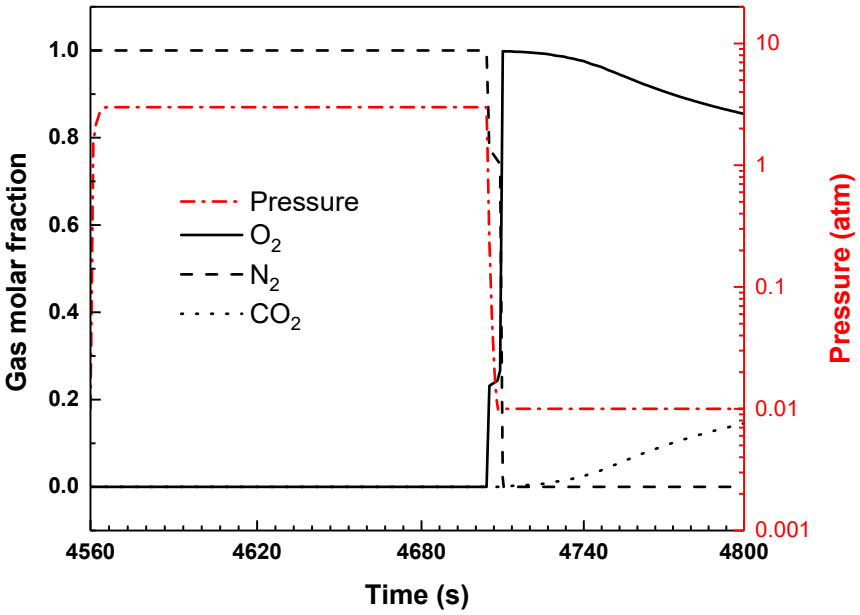

Figure 3.15. Pressure and gas molar fraction profile of a PSA cycle under the optimum condition.

In the numerical process simulation, the adsorption bed was separated into 13 sections in the axial direction. The beginning of the bed, where z/L = 0, was assumed to be the feed position. The end of the bed, where z/L = 1, was assumed to be the purge position since desorption was done counter-currently. The oxygen mole fraction profile along the adsorption bed at the last cycle under the base condition and the optimal condition was plotted in Figure 3.16. Each curve describes an oxygen concentration profile with time at a specific location of the adsorption bed. It can be concluded that the oxygen concentration under the optimum condition is much improved compared with the one under base condition.

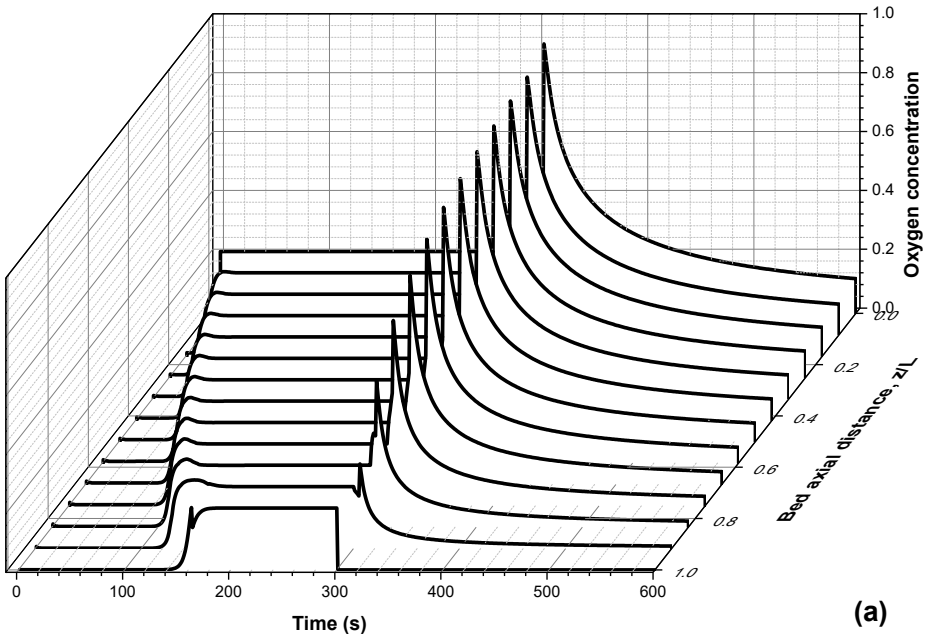

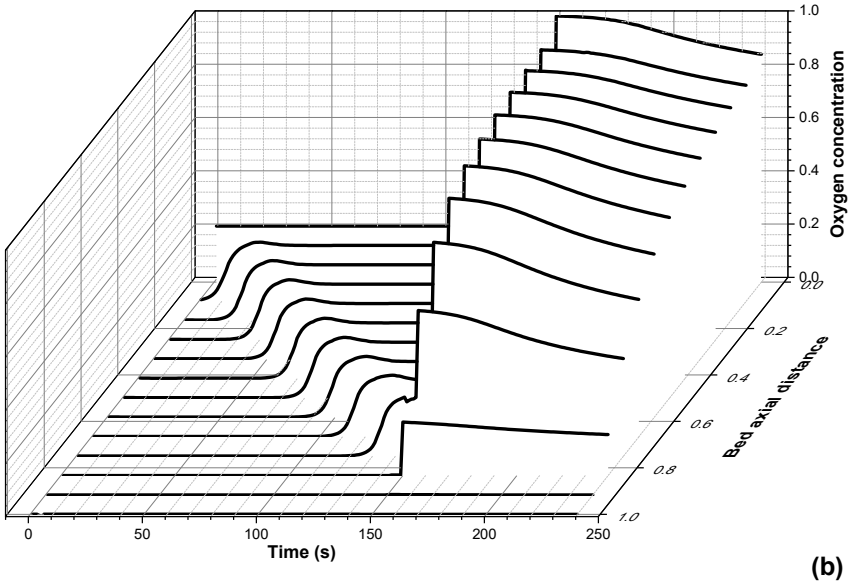

Figure 3.16. The oxygen mole fraction profile in the adsorption bed at the last cycle under (a) the base condition, and (b) the optimum condition.

3.4.6 Energy Consumption

To confirm whether the high-temperature air separation method is energy saving or not, we estimated the energy consumption of the process based on the optimal conditions obtained. It is assumed that the heating needs for the adsorption and desorption are essentially eliminated due to close coupling with high temperature integrated gasification combined cycle (IGCC) and oxy-combustion processes. The primary energy contributors of the process are the air blower that provided high-pressure air and the vacuum pump that provided the low pressure for desorption. The expression to calculate the power consumption per unit of produced oxygen is shown below:

$$Power\ consumption\ per\ unit\ of\ oxygen = \frac{\begin{matrix}\int_0^{t_{pre}+t_{ads}} \frac{\dot{n}_{feed} RT}{\eta_b} \frac{\gamma}{\gamma-1} [(\frac{P_{out,b}}{P_{in,b}})^{\frac{\gamma-1}{\gamma}} - 1]\, dt \\ + \int_0^{t_{dep}+t_{des}} \frac{\dot{n}_{purge} RT}{\eta_v} \frac{\gamma}{\gamma-1} [(\frac{P_{out,v}}{P_{in,v}})^{\frac{\gamma-1}{\gamma}} - 1]\, dt\end{matrix}}{mass\ of\ oxygen\ produced\ per\ cycle} \tag{3.24}$$

where t_{pre}, t_{ads}, t_{dep}, t_{des} is the duration of pressurization, adsorption, depressurization and desorption step, $\dot{n}_{feed}$ and $\dot{n}_{purge}$ are the molar flow rate of feed gas and purge gas, k is the polytropic constant, $P_{in,b}$ and $P_{out,b}$ are the suction pressure and discharge pressure for the air blower, $P_{in,v}$ and $P_{out,v}$ are the suction pressure and discharge pressure for the vacuum pump, η_b and η_v is the efficiency of the blower and vacuum pump. The values of corresponding parameters can be found in Table 3.2.

The calculated power consumption for the high-temperature air separation process is 171.8 kWh/ton O_2, which is about 23% lower than the cryogenic distillation method (223

kWh/ton O_2) and about 33% lower than the conventional PSA process (255 kWh/ton O_2) [88]. Besides, the productivity of the high-temperature air separation process is around five times larger than that of the PSA process with zeolites due to the large adsorption capacity of LSCF1991 (as shown in Table 3.6). For the same production scale, the adsorber for the new process is about 1/5 the size of the conventional PSA process, and a lower quantity of sorbents are required, which results in additional financial benefit.

3.5 Conclusions

Mechanical property tests show that LSCF1991 pellets tend to have stronger crushing strength and attrition resistance when increasing the sintering temperature. The pellet samples that sintered at 1000 °C were considered to have adequate mechanical strength to be applied for PSA processes by comparing with commercial zeolite pellets. Oxygen nonstoichiometry at different temperatures and oxygen partial pressures for LSCF1991 was predicted by a semi-empirical equation, the calculation results matched well with the experimental TGA measurements. The simulated breakthrough curve from Matlab showed a better fit than ProSim DAC compared with the experimental breakthrough values. The Matlab simulation package was further used to optimize the operating parameters of the PSA process by study their effects on oxygen purity and recovery. Since some of the parameters like purge gas flow rate and desorption duration will increase oxygen purity at the cost of reducing oxygen recovery, oxygen purity and recovery can hardly be maximized simultaneously. An optimum set of parameters were determined for a target oxygen purity of 98%. Under the optimal conditions, oxygen purity

of 98.21% and recovery of 74.05% was achieved. The obtained purity and recovery values are much higher than the corresponding values of the PSA process with several conventional zeolites. Additionally, the energy consumption of the new process is lower than both the cryogenic distillation method and the conventional PSA process. The simulation results have shown great potential for applying the PSA technique in the high-temperature air separation process by perovskite oxide adsorbents due to its excellent separation performance and low energy requirement.

Notations

A: Initial sample weight for attrition test (g)

B: Sample weight after attrition test (g)

d_p: Diameter of adsorbent particle (cm)

D_L: Axial dispersion coefficient (cm^2/s)

D_m: Molecular dispersion coefficient (cm^2/s)

i.d.: Bed internal diameter (cm)

K: Constant of oxygen nonstoichiometry correlation (atm^{-n})

$K_{p,i}$: Effective mass transfer coefficient of i compound (1/s)

Ko: Kozeny constant

L: Bed length (cm)

M_g: Molecular weight of gas (g/mmol)

M_i: Atomic/molecular weight of element/molecule i (g/mmol)

M_w: Molecular weight of LSCF1991 (g/mmol)

n: Constant of oxygen nonstoichiometry correlation

P: Pressure (atm)

P_0: Initial pressure of the bed (atm)

P_a: Adsorption pressure (atm)

P_d: Desorption pressure (atm)

P_i: Partial pressure of i compound (atm)

q_i: Partial concentration of i compound in the adsorbed phase (mmol/g)

q_i^*: Partial concentration at the solid interface of i compound (mmol/g)

Q: Mass flux of gas (mmol/cm^2/s)

Q_f: Flow rate of feed gas (mmol/s)

Q_p: Flow rate of purge gas (mmol/s)

$Q_{feed,ads}$: Feeding gas mass flux (mmol/cm^2/s)

$Q_{exit,des}$: Exit gas mass flux (mmol/cm^2/s)

t: Time (s)

t_{pre}: Duration of pressurization step (s)

t_{ads}: Duration of adsorption step (s)

t_{dep}: Duration of depressurization step (s)

t_{des}: Duration of desorption step (s)

t_{cycle}: Duration of a PSA cycle (s)

T: Temperature (K)

$\sum V_i$: Molecular diffusion volumes of component I (cm^3/mol)

x: weight loss percentage of LSCF sample after reduction (%)

y_i: Mole fraction of component i

$y_{O_2,feed,ads}$: Feeding oxygen molar fraction during adsorption step

$y_{O_2,exit,des}$: Exit oxygen molar fraction during desorption step

z: Bed axial distance (cm)

Greek letters:

δ: Oxygen vacancy (Oxygen nonstoichiometry)

δ_0: Oxygen vacancy at the reference state

ρ_p: Density of the adsorbent particle (g/cm^3)

ρ_g: Gas density ($mmol/cm^3$)

ε: Porosity of the adsorbent bed

μ: Dynamic viscosity of gas (g/cm/s)

κ: Bed permeability (cm^2)

γ: Adiabatic index

η_b, η_v: Efficiency of blower and vacuum pump

Chapter 4: Evaluation and Optimization of VPSA processes with Nanostructured Zeolite NaX for Post-Combustion CO_2 Capture

4.1 Introduction

Global warming resulted from greenhouse gases emission has been an issue of great concern. The concentration of greenhouse gases in the atmosphere has been continuously increasing over the last few decades due to the strong energy dependence of fossil fuels. Among the greenhouse gases, carbon dioxide is considered the main contributor to global warming due to its huge emission amount. Thus, reducing anthropogenic CO_2 emission and controlling CO_2 concentration have become one of the most urgent global environmental issues. The carbon capture and storage technology (CCS) requires the reduction of carbon emissions primarily from large stationary points, such as coal-based plants. It is necessary to separate CO_2 from N_2 in post-combustion emissions before full utilization of CO_2[89].

Traditionally, CO_2 capture can be achieved by absorption with amine commonly used in large-scale carbon removal from the flue gas. The process is efficient but has high energy costs due to the high-temperature requirement for regeneration. Adsorption stands out to be an attractive operation over amine capture due to its relatively low cost, flexible operating and more efficient regeneration[90]. Two generic cycle concepts, temperature swing adsorption (TSA) and pressure swing adsorption (PSA), are employed to carry out the essential adsorption and desorption steps in conjunction with a variety of other complimentary steps[9]. PSA is an industrial unit operation for separating gas mixtures where

the preferred gas component is adsorbed at high pressure and then desorbed at an atmospheric pressure repeatedly. PSA has been widely applied for carbon capture due to its simplicity, high efficiency, and low energy requirement[8,44]. Vacuum pressure swing adsorption (VPSA) is an emerging technology that applies pressurized gas to the adsorption process as well as a vacuum during the desorption stage. VPSA is more efficient than PSA processes when dealing with flue gas due to the low partial pressure of CO_2 and high partial pressure of N_2 in the flue gas stream[91].

Many conventional adsorbents have been used for N_2/CO_2 separation, such as zeolites, activated carbons and modified mesoporous silica[92–94]. However, the adsorption selectivity of CO_2 to N_2 and adsorption capacity of CO_2 are not high enough as current commercial adsorbents, which makes the adsorption process less competitive with other CO_2 capture methods like absorption and membrane separation. The key challenge in CO_2 capture by adsorption technique is to find a suitable solid adsorbent material with excellent separation performance, as the adsorbent plays a critical role in the overall process performance[95]. An ideal adsorbent for CO_2 capture should have a high CO_2 adsorption capacity, a large pore dimension that enables fast mass transfer, a decent CO_2 selectivity over N_2, and good stability[26]. New research has found that nanostructured zeolite NaX is particularly promising as CO_2 capture materials. For example, Pham et al. [96] found the decrease in the particle size of zeolite crystals from microscale to nanoscale leads to a significant increase in specific surface area, thus providing more active sites for adsorption of CO_2. Jiang et al.[97] have reported that the synthesized T-type zeolite showed higher adsorption capacities than micro-level T-type zeolite for the separation of CO_2/N_2.

Eskandari et al.[98] demonstrated that the reduction of the particle size increases the adsorption capacity for carbon dioxide as well as the adsorption selectivity on the X type zeolite particles.

Although progress has been made on the development of nanostructured zeolite as CO_2 capture adsorbent material, most work only reported the basic properties of the material such as adsorption isotherms, porosity, density and surface areas. More work is required to analyze the novel adsorbent through lab-scale breakthrough experiments as well as process modeling to determine the feasibility of the material for practical applications. In addition, to apply the nanostructured zeolites for CO_2 capture by VPSA, the operating conditions of the VPSA process is desired to be preliminarily designed and optimized before running the process in an actual pilot plant, which is both costly and time-consuming.

A large number of experimental and simulation studies have been reported for post-combustion CO_2 capture from the flue gas mixture by employing the VPSA technique[99–106]. It is clear that product purity, recovery, productivity, and energy consumption are four important performance indicators of the VPSA process, and they varied as the operating conditions changed. In addition, the performance of the VPSA process depends on the CO_2 concentration of the flue gas. To obtain over 90% CO_2 purity with a recovery of 90% for CO_2 capture from a flue gas containing 15% of CO_2, a deep vacuum (<0.05 bar) is often required. However, the deep vacuum involves multistage pump units which will dramatically increase the capital cost and energy consumption, which becomes the major obstacle of applying the CO_2 capture process by adsorption to the power plants[107]. There is a great need to employ an advanced adsorbent for the VPSA process for CO_2 capture,

and to optimize the process to lower the energy consumption while meeting CO_2 purity and recovery target.

Current work first presents a material study for a group of nanostructured zeolite NaX samples prepared with different binder ratios and sintering temperatures. The porosity properties, mechanical properties, adsorption isotherm, kinetics, IAST selectivity, and column dynamics for the group of nanostructured zeolite NaX samples are compared. Simulation and optimization studies of a two-bed six-step VPSA process were then performed in gPROMs environment for post-combustion CO_2 capture from dry flue gas using the optimal nanostructured zeolite NaX and a commercial microsized zeolite NaX. The objective is to minimize the energy consumption of the VPSA process for the specified CO_2 purity and recovery target by altering the operating conditions.

4.2 Experimental

4.2.1 Synthesis of Nanostructured Zeolite NaX

Detailed synthetic methodologies and characterization of the nanostructured zeolites will be published separately. The powder sample was synthesized by firstly preparing an aluminosilicate precursor mixture with the composition of $3.0Na_2O$: $1.0Al_2O_3$: $4.0SiO_2$: $32.4H_2O$. The mixture was prepared by dissolving 4.555 g of NaOH pellets (Sigma Aldrich) and 11.711g of water glass (Sigma Aldrich) in deionized water (DI water) (8.190 g), followed by the addition of 5.735 g of metakaolin (MetaMax®, BASF). The mixture was stirred with a mechanical mixer (RW 60 digital mixer, IKA) at 800 rpm for

40 min, producing a visually homogeneous and free-flowing dispersion. After the addition of 15 ml of canola oil (J.M. Smucker Company, Crisco®), the mixture was stirred for another 10 min and then transferred to 50 mL polypropylene tubes. After tightly capping the tubes, the mixture was heated at 90°C for 36 h. The product, exhibiting a paste consistency, was washed with hot DI water multiples times. The final product was collected after vacuum filtration with cold DI water until the pH of the filtrates reached 8 approximately. The product was then dried in a lab oven at 90°C overnight.

The resulting powder sample was ground in an agate mortar and mixed with bentonite clay binder (Nature's oil) and a few drops of DI water to form the paste. Since the mass ratio of the clay binder can significantly affect the mechanical and adsorption properties of the zeolites, a high binder ratio (20 wt.%) and a low binder ratio (10 wt.%) was used in this work. The mixed paste was then filled to a die and compressed with a pellet press (Parr Instrument Company) to prepare pellet sorbents with a rod shape (3 mm diameter, 5-10 mm length). The resulting pellets were sintered at 200 °C for 1 hour and then heated to 400 or 500 °C for 2 hours in the N_2, with a ramping rate of 5 °C /min.

4.2.2 Material Characterization

The structure of the material was examined by a powder X-ray diffractometry (XRD, Siemens D-5000) with CuKα radiation. To examine the crystal structure and size of the nanostructured zeolite samples, scanning electron microscopy (SEM) images of the nanostructured zeolite samples were taken using an XL30 Environmental FEG (FEI) with

15 kV acceleration voltage and a spot size of 3. Transmission electron microscopy (TEM) images were taken by an ARM200F (JEOL) with 200 kV acceleration voltage.

The mechanical properties of the group of nanostructured zeolite pellets were determined by testing their crush strength and attrition resistance, as they are very important for industrial applications of the adsorbents. Mechanical failure of adsorbents may result in various problems of a PSA unit, such as blockage, the unacceptably high-pressure drop across the adsorption bed, and the maldistribution of fluid flow caused by fragments and fine particles[108]. The crush strength of the pellets represents the maximum compressive load the adsorbents pellets can bear, and it was tested by Instron universal mechanical property testing system. The attrition and abrasion resistance of the pellets was tested using a standard test method ASTM D4058[68]. The attrition testing units include a cylindrical drum with a single baffle, a motor, and a standard sieve. The pellets were rotated for 30 minutes at a rate of 60 rpm in the drum. Fines produced by attrition and abrasion in the test were sieved through the standard sieve. The attrition rate was calculated as the weight loss percentage of the sample.

The adsorbents were also characterized for their pore textural properties with a Micromeritics ASAP 2020 adsorption apparatus. Prior to the measurement, the samples were degassed at 300 °C for 12 hours under vacuum. The Brunauer-Emmett-Teller (BET) surface area was calculated with nitrogen adsorption isotherms at 77K in the relative pressure range from 0.05 to 0.3. The specific surface area of micropores and the micropore volume were calculated by applying the t-plot method with the Harkins and Jura thickness equation in the thickness range of 0.35 to 0.50 nm. The external surface area was

determined as the difference between total surface area obtained by BET equation and surface area of micropores calculated by t-plot method. The total pore volume was obtained from the amount of nitrogen adsorbed at a relative pressure of 0.98.

4.2.3 Adsorption Measurement

The adsorption isotherms of N_2 and CO_2 at 25 °C and gas pressure up to 800 mmHg were measured volumetrically in the Micromeritics ASAP 2020 adsorption apparatus. The temperature was achieved by using a Dewar with a circulating jacket connected to a thermostatic bath with a precision of ±0.01 °C. The degas procedure was repeated for all samples at 300 °C for 12 hours before the measurement.

Adsorption kinetics data of N_2 and CO_2 on the nanostructured zeolite samples were measured in the Micromeritics ASAP 2020 adsorption unit by injecting a single dose of gas. The dose amount of CO_2 was fixed at 50 cm^3 (maximum dose of the unit) while the dose amount of N_2 was fixed at 10 cm^3. After introducing the gas into the adsorption system, the changes in gas pressure with time were recorded and converted into transient adsorption uptakes as a function of time. Still, the degassing procedure was repeated for all samples at 300 °C for 12 hours before the measurement.

The adsorption breakthrough curves of the fixed-bed packed with new adsorbents were measured to study the separation performance. The experimental fixed-bed setup used in this work includes a gas delivery system, a fixed-bed column, a tube furnace, and a gas chromatograph (GC, Agilent 7820). The adsorption column is a stainless-steel tube with a

length of 22 inches and an inner diameter of 0.25 inch. The mass of the adsorbent packed in the column was about 5 grams for each experiment. Silica grains (Ceradyne Inc.) were used to fill the rest space of the column. Helium (Praxair, 99.999%) was introduced to the adsorption bed prior to each experiment at 300 °C for 12 hours to degas the system. After the degassing, the mixture of nitrogen (Praxair, 99.999%) and carbon dioxide (Praxair, 99.9%) was continuously introduced at 10 ml/min until a breakthrough was obtained. The flow rate of the gases was controlled by the mass flow controllers from Alicat Scientific. The concentration of each component in the effluents was analyzed by the GC.

4.3 Mathematical Model and Simulation

4.3.1 Model Assumptions and Equations

In the current study, the VPSA processes were simulated and optimized by a modeling framework developed in gPROMs. gPROMs permits a detailed description of the complex phenomena taking place inside adsorption columns. The model relies on a coupled set of partial differential and algebraic equations (PDAEs) for mass, energy and momentum balance, as well as isotherm equations, transport and physical properties of the gas mixture and boundary conditions according to the operating step. In order to simplify the simulation process, the following assumptions are adopted in this study.

a. The gas-phase behaves as an ideal gas.

b. Thermal equilibrium between adsorbents and the bulk flow.

c. There is no radial variation in gas concentration, temperature, and pressure.

d. The flow pattern is represented by the axial dispersed plug flow model.

e. The porosity of the bed and adsorbent pellet is assumed to be uniform along the bed.

f. The diffusion and mass transfer effects are represented by the linear driving force (LDF) model with a single lumped mass transfer coefficient.

g. The pressure drop along the bed was calculated by using the Ergun equation.

The continuity equations for the gas phase mass balance describe how species are transported through the bed in the axial direction. The effects of axial convection, dispersion, and transport to the adsorbed phase can be calculated using the following equations[95]:

$$\varepsilon_{tot}\frac{\partial C_i}{\partial \mathrm{t}} = -\varepsilon_b\frac{\partial}{\partial z}\left(D\frac{\partial C_i}{\partial \mathrm{z}}\right) - \frac{\partial C_i v}{\partial \mathrm{z}} + \rho_\mathrm{b}\cdot\frac{\partial \mathrm{q_i}}{\partial \mathrm{t}} = 0, \quad \forall \mathrm{i} \in \mathrm{C} \tag{4.1}$$

where ε_{tot} is the total void fraction, including intra- an inter-particle void space, $\mathrm{C_i}$ is the molar concentration of component i in the gas phase, ε_b is the void fraction in the bed (bed porosity), D is the mass axial dispersion coefficient, v is the superficial velocity of the gas phase, ρ_b is the density of bed, and $\mathrm{q_i}$ is the specific amount of component i adsorbed on the solid phase.

The boundary conditions (assuming the flow direction is from feed to the product side of the bed) are given by the following equations:

$$\frac{F^{in}{w_i}^{in}}{A} = Mw_i\left(vC_i - \varepsilon_b D\frac{\partial C_i}{\partial \mathrm{z}}\right), \quad \forall \mathrm{i} \in \mathrm{C}, \quad \mathrm{z} = 0 \tag{4.2}$$

$$\varepsilon_b D \frac{\partial C_i}{\partial \mathrm{z}} = 0, \quad \forall \mathrm{i} \in \mathrm{C}, \quad \mathrm{z} = \mathrm{L} \tag{4.3}$$

where F^{in} is the mass flow rate at the entrance of the adsorption bed, ${w_i}^{in}$ is the mass fraction of component i at the entrance of the adsorption bed, A is the cross-sectional area of the bed, Mw_i is the molecular weight for component i, L is the bed length.

The continuity equation for the energy transport of the gas phase, which includes the effects of axial convection, dispersion and the contribution of the energy contained in the adsorbed phase, is given by the following equation:

$$\frac{\partial \tilde{u}}{\partial t} = \varepsilon_b \frac{\partial}{\partial z}\left(\rho D \frac{\partial h}{\partial \mathrm{z}}\right) - \frac{\partial v \rho h}{\partial z} + \frac{1}{1000}\frac{\partial}{\partial z}\left(\lambda_{eff}\frac{\partial T}{\partial z}\right) - \frac{4}{d_b}\frac{1}{1000}k_{T,b-w}(\mathrm{T} - T_w) \tag{4.4}$$

where $\tilde{u}$ is the energy density per unit volume of bed, ρ is the mass density of gas phase, h is the specific enthalpy of gas phase, λ_{eff} is the effective thermal conductivity, $k_{T,b-w}$ is the heat transfer coefficient from the gas phase to the bed wall, T is the gas temperature, T_w is the bed wall temperature, d_b is bed diameter.

The boundary conditions (assuming the flow direction is from feed to product side of the bed) are given by the following equations:

$$\frac{F^{in}h^{in}}{A} = \mathrm{v}\rho\mathrm{h} - \varepsilon_b D \rho \frac{\partial h}{\partial \mathrm{z}} - \frac{1}{1000}\left(\lambda_{eff}\frac{\partial T}{\partial z}\right), \quad \mathrm{z} = 0 \tag{4.5}$$

$$\frac{\partial T}{\partial z} = 0, \quad z = L \tag{4.6}$$

where h^{in} is the mass specific enthalpy at the entrance of the adsorption bed.

Since thermal equilibrium between adsorbents and the bulk flow is assumed, the temperature in the gas phase is equal to that of the solid phase. The energy density per unit volume of bed is given by the following equation:

$$\tilde{u} = \varepsilon_b(\rho h - 10^2 P) + \rho_b \left(\sum_{\forall i \in C} q_i h_{ad,i}(T) + C_{p,ads}\left(T - T_{ref}\right) \right) \tag{4.7}$$

where P is pressure in the unit of bar, $h_{ad,i}(T)$ is molar specific enthalpy of component i at the bed temperature, $C_{p,ads}$ is the heat capacity of the adsorbent, T_{ref} is the reference temperature.

The molar specific enthalpy can be determined from the pure component enthalpy at a reference state, the heat of adsorption and the change in the heat capacity of the adsorbed species using the following equation:

$$h_{ad,i}(T) = h_i^{\emptyset}(T) + \Delta H_{ad,i} + \Delta C_{p,ad,i}\left(T - T_{ref}\right) \tag{4.8}$$

where $h_i^{\emptyset}(T)$ is the pure component enthalpy at the bed temperature, $\Delta H_{ad,i}$ is the heat of adsorption for component i, $\Delta C_{p,ad,i}$ is the change in the heat capacity of the adsorbed species from reference condition to bed conditions for component i.

The effective thermal conductivity can be determined from the Specchia correlation:

$$\lambda_{eff} = \varepsilon_b \lambda + (1 - \varepsilon_b) \frac{1}{\frac{0.22{\varepsilon_b}^2}{\lambda} + \frac{2}{3}\lambda_{ads}} \tag{4.9}$$

where λ is the thermal conductivity of the gas mixture, λ_{ads} is the thermal conductivity of adsorbent material.

The pressure drop for the gas flow in packed beds is determined from the Ergun equation[39]:

$$\left(\frac{\partial P}{\partial z}\right)_t = -\frac{150\mu}{d_p^2}\frac{(1-\varepsilon_b)^2 v}{{\varepsilon_b}^3} - \frac{1.75\rho}{d_p}\frac{(1-\varepsilon_b)}{{\varepsilon_b}^3}v^2 \tag{4.10}$$

where μ is the dynamic viscosity of gas, d_p is the diameter of the pellet particle.

The boundary condition for this equation is given below:

$$\mathrm{P} = P_{in}, \;\; z = 0 \tag{4.11}$$

where P_{in} is the pressure at the feed end of the adsorption bed.

The mass transfer from the gas phase to the solid phase for component i is described by the LDF model[19,109]:

$$\frac{\partial \mathrm{q_i}}{\partial \mathrm{t}} = k_i(\mathrm{q_i^*} - \mathrm{q_i}), \quad \forall \mathrm{i} \in \mathrm{C} \tag{4.12}$$

where k_i is the mass transfer coefficient for the LDF model, $\mathrm{q_i^*}$ is the amount of component i adsorbed at equilibrium. The value of the mass transfer coefficient k_i can be estimated by fitting the experimental kinetic data.

The adsorption equilibrium is predicted by the Langmuir-Freundlich isotherm:

$$\mathrm{q_i^*} = q_{s,i}\frac{(b_i p_i)^{\frac{1}{n_i}}}{1+(b_i p_i)^{\frac{1}{n_i}}}, \quad \forall \mathrm{i} \in \mathrm{C} \tag{4.13}$$

where b_i is the equilibrium parameter, n_i is Freundlich exponent for component i, p_i is the partial pressure for component i, $q_{s,i}$ is the maximal adsorbed equilibrium amount for component i.

Both equilibrium parameter b_i and Freundlich exponent n_i are functions of temperature:

$$q_{s,i} = q_{s1,i} + q_{s2,i}\left(T - T_{ref}\right), \quad \forall \mathrm{i} \in \mathrm{C} \tag{4.14}$$

$$b_i = b_{1,i} e^{b_{2,i}\left(\frac{1}{T} - \frac{1}{T_{ref}}\right)}, \quad \forall \mathrm{i} \in \mathrm{C} \tag{4.15}$$

$$n_i = n_{1,i} + n_{2,i}\left(T - T_{ref}\right), \quad \forall \mathrm{i} \in \mathrm{C} \tag{4.16}$$

The gas phase dispersion in the axial flow direction can be estimated based on Wakao and Ruthven's estimation[8,110]:

$$\frac{\varepsilon_b D_i}{D_{m,i}} = 20 + 0.5 * SC_i * \mathrm{Re} \tag{4.17}$$

where $\mathrm{D_{m,i}}$ is the molecular diffusivity for component i, SC_i is Schmidt number based on molecular diffusivity of component i, Re is the Reynolds number

The Schmidt and Reynolds numbers are given by the following equations:

$$SC_i = \frac{\mu}{\rho D_{m,i}}, \quad \forall \mathrm{i} \in \mathrm{C} \tag{4.18}$$

$$\mathrm{Re} = \frac{v \rho d_p}{\mu} \tag{4.19}$$

The molecular diffusivity is given by the following equation:

$$D_{m,i} = \frac{1 - x_i}{\sum_{j=1}^{n} \frac{x_j}{D_{i,j}} - \frac{x_i}{D_{i,i}}} \tag{4.20}$$

where $D_{i,j}$ is the binary diffusivity for component i with component j, $D_{i,i}$ is the self diffusivity for component i.

The energy consumption of the process is defined as the summation of energy required for compression and evacuation of the gas streams. The energy consumption for compressing the gas streams in a compressor is given by the following equation:

$$E_c = \frac{\dot{n}_{in} R T_{in}}{\eta_c} \frac{\gamma}{\gamma - 1} [(\frac{P_{out,c}}{P_{in,c}})^{\frac{\gamma-1}{\gamma}} - 1] \tag{4.21}$$

where E_c is the energy consumption of the compressor, $\dot{n}_{in}$ is the molar flow rate of the feed stream of the compressor, T_{in} is the temperature of feed stream of the compressor, γ is the specific heat capacity ratio, $P_{in,c}$ and $P_{out,c}$ are the pressure of inlet stream and leaving stream of the compressor, η_c is the isentropic compression efficiency of the compressor.

The energy consumption for evacuation of gas streams in a vacuum pump is provided by the following equation:

$$E_v = \frac{\dot{n}_{in} R T_{in}}{\eta_v} \frac{\gamma}{\gamma - 1} [(\frac{P_{in,v}}{P_{out,v}})^{\frac{\gamma-1}{\gamma}} - 1] \tag{4.22}$$

where E_c is the energy consumption of the vacuum pump, $\dot{n}_{in}$ is the molar flow rate of the feed stream of the vacuum pump, T_{in} is the temperature of feed stream of the vacuum pump,

$P_{in,v}$ and $P_{out,v}$ are the suction pressure and discharge pressure of the vacuum pump, η_v is the isentropic evacuation efficiency of the vacuum pump.

The performance indicators of VPSA process (product purity, recovery, productivity, and energy consumption) are defined by the following expressions:

$$\text{Product } Purity = \frac{mole\ of\ component\ in\ the\ product}{Total\ moles\ of\ the\ product} \tag{4.23}$$

$$Product\ Recovery = \frac{moles\ of\ component\ in\ the\ product}{moles\ of\ component\ in\ the\ feed} \tag{4.24}$$

$$Product\ Productivity = \frac{moles\ of\ component\ in\ the\ product}{time \cdot mass\ of\ adsorbent} \tag{4.25}$$

$$energy\ consumption = \text{sum of energy required for all compression and vacuum sources} \tag{4.26}$$

It should be noted that all the performance indicators are obtained at cyclic steady-state conditions when the indicators are constant over time. Also, the product refers to the heavy extract (CO_2) in this study.

4.3.2 Process Description

The raw flue gas stream is obtained from coal-fired power plants that typically contains N_2, CO_2, H_2O and minor impurities such as SO_x and NO_x. In the current study, it can be assumed that the feedstock is pretreated to remove H_2O, SO_x, and NO_x, and contains only N_2 and CO_2 components. The ratio of N_2 and CO_2 in the pretreated dry flue gas is assumed to be 85% and 15%, respectively.

The VPSA cycle applied in this work consists of two beds with six operating steps, including a pressurization with the light product step (PLP), an adsorption step (AD), a depressurizing pressure equalization step (DPE), a blowdown step (BD), an evacuation step (EVAC), and a pressurizing pressure equalization step (PPE). Two pressure equalization steps were employed to reduce overall energy consumption. The cycle sequence of two beds during each operating step of the VPSA process is shown in Figure 4.1.

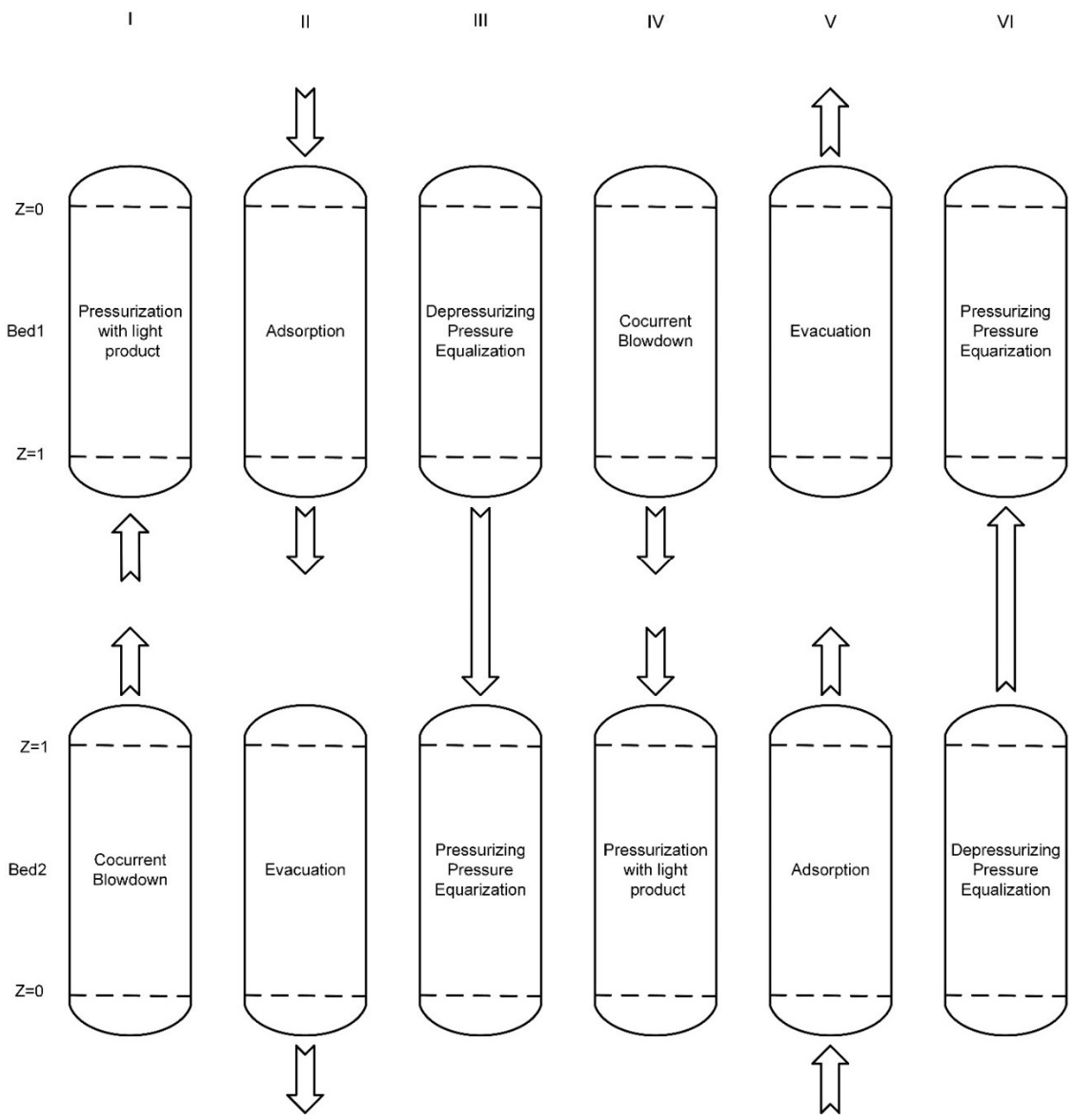

Figure 4.1. Cycle sequence of operating steps for the two-bed six-step VPSA system.

4.3.3 Formulation of the Optimization

The dynamic optimization problem is formulated to investigate the effect of feed pressure, feed flow rate, blowdown pressure, evacuation pressure, and length to diameter

ratio on the overall process performance. The objective of this study is to minimize the energy consumption for specified requirements in product purity and recovery by varying the above variables. It's important to note that cycle time and operating durations are kept constant during the optimization due to the need for synchronization of multi-bed configuration. Based on the information above, the optimization is formulated below:

$$\text{min. energy consumption}$$

$$\text{s. t.}$$

$$\text{Product purity } \geq 92\%$$

$$\text{Product recovery } \geq 90\%$$

$$0.01 \text{ bar} \leq P_{evac} \leq 0.3 \text{ bar}$$

$$0.3 \text{ bar} \leq P_{blowdown} \leq 1 \text{ bar} \qquad (4.27)$$

$$1 \text{ bar} \leq P_{feed} \leq 2 \text{ bar}$$

$$0.2\ m^3/h \leq F_{feed} \leq 6\ m^3/h$$

$$2.53 \leq L/D \leq 28.28$$

$$\text{General bed model equations}$$

4.3.4 Numerical Methods

The bed model equations are implemented in gPROMs modeling environment. The resulting mathematical model consists of a set of partial differential and algebraic equations

that can be converted into differential-algebraic equations (DAEs) only via the method of lines (MOL)[111]. This method is based on the discretization of the original equation set with respect to all the spatial domain, so the remaining equations contain time domain only. The centered finite difference method (CFDM) of the second order is used to discretize the spatial domain into 50 discretization points. The DAEs can then be solved with the DAE solver DASOLV.

The optimization problem is solved using gPROMS/gOPT tool. The solution of the optimization problem requires both a DAE solver that integrates the DAEs to determine the objective function and constraints and a nonlinear programming problem (NLP) solver to optimize the decision variables. In this study, the SRQPD algorithm is adopted to solve the NLP for the optimization, which implements a reduced sequential quadratic programming algorithm. Given the initial estimates, DASOLV and SRQPD will be repeatedly called until the objective function converges to the optimization tolerance (e.g. 0.001).

4.4 Results and Discussion

4.4.1 Material Synthesis and Characterization

The structural and textural properties of the nanostructured zeolite (NZ) were studied by taking TEM, SEM images and PXRD analysis with the powdered sample (without binder material). The TEM and SEM images of nanostructured zeolite are shown in Figure 4.2. The TEM images indicate that the aggregates consist of nanosized plate-like

crystallites showing well-developed lattice fringes. The SEM images confirm the aggregate form in nature and exhibit round-shaped pores on the aggregate. The PXRD spectra of NZ and commercial zeolite NaX is shown in Figure 4.3. The PXRD pattern of the NZ sample matches well with the commercial NaX in terms of Bragg peak position and relative intensities, which indicate the nanostructured NaX is indeed zeolite NaX. The average crystallite size was determined by applying Scherrer's equation[112] to [1 1 1], [3 3 1], and [5 3 3] reflection peaks for the NZ. The calculated crystallite size is 19.3 nm, confirming the zeolite sample has nanosized crystallites.

The NZ pellets were prepared by adding 10 wt.% or 20 wt.% bentonite clay as the binder and sintered at 400 or 500 °C. The resulting pellet samples were named NZL-400, NZL-500, NZH-400, NZH-500 (L and H represent a low and high ratio of binder material), determined by the mass ratio of binder and sintering temperature.

The nitrogen adsorption experiment at 77K was performed to study the porosity properties of the group of NZ pellets. The porosity of commercial microsized zeolite NaX pellets (Alfa Aesar) (MZ) was also analyzed for comparison. As shown in Figure 4.4, all the NZ samples exhibited isotherms of type I and type IV combination with a hysteresis loop at high relative pressure, indicating the presence of both micropores and mesopores. In comparison, the MZ sample exhibited a type I isotherm, indicating the material was mainly microporous. The results were further confirmed in the pore distribution profile shown in Figure 4.5, as well as the high external surface area and mesoporous volume of NZs shown in Table 4.1. The hierarchical porous structure of NZ is beneficial for adsorption mass transfer, according to our previous work[113]. Among the NZ samples, the

low binder ratio group (NZL-400 and NZL-500) has larger specific surface areas and pore volumes than the low binder ratio group (NZH-400 and NZH-500). In comparison, the effect of sintering temperature on the porosity of the material is not that significant. NZH-400 only exhibits a slightly larger surface area and pore volume than NZH-500 and the porosity properties of NZL-400 and NZL-500 are almost the same.

The mechanical strength of the group of NZ pellets is displayed in Table 4.2. The results show that NZ pellets that prepared with a higher ratio of binder material and a higher sintering temperature have stronger mechanical properties. However, temperature is obviously a more significant factor compared to the binder ratio. The sintering temperature increase from 400 to 500 °C almost doubled the crushing strength and reduced the attrition rate by more than half, while the enhancement of mechanical properties by the increased binder ratio is roughly 20%. For material that sintered at 500 °C, both mechanical properties are comparable with the commercial MZ pellets, indicating they can be used in actual adsorption operations.

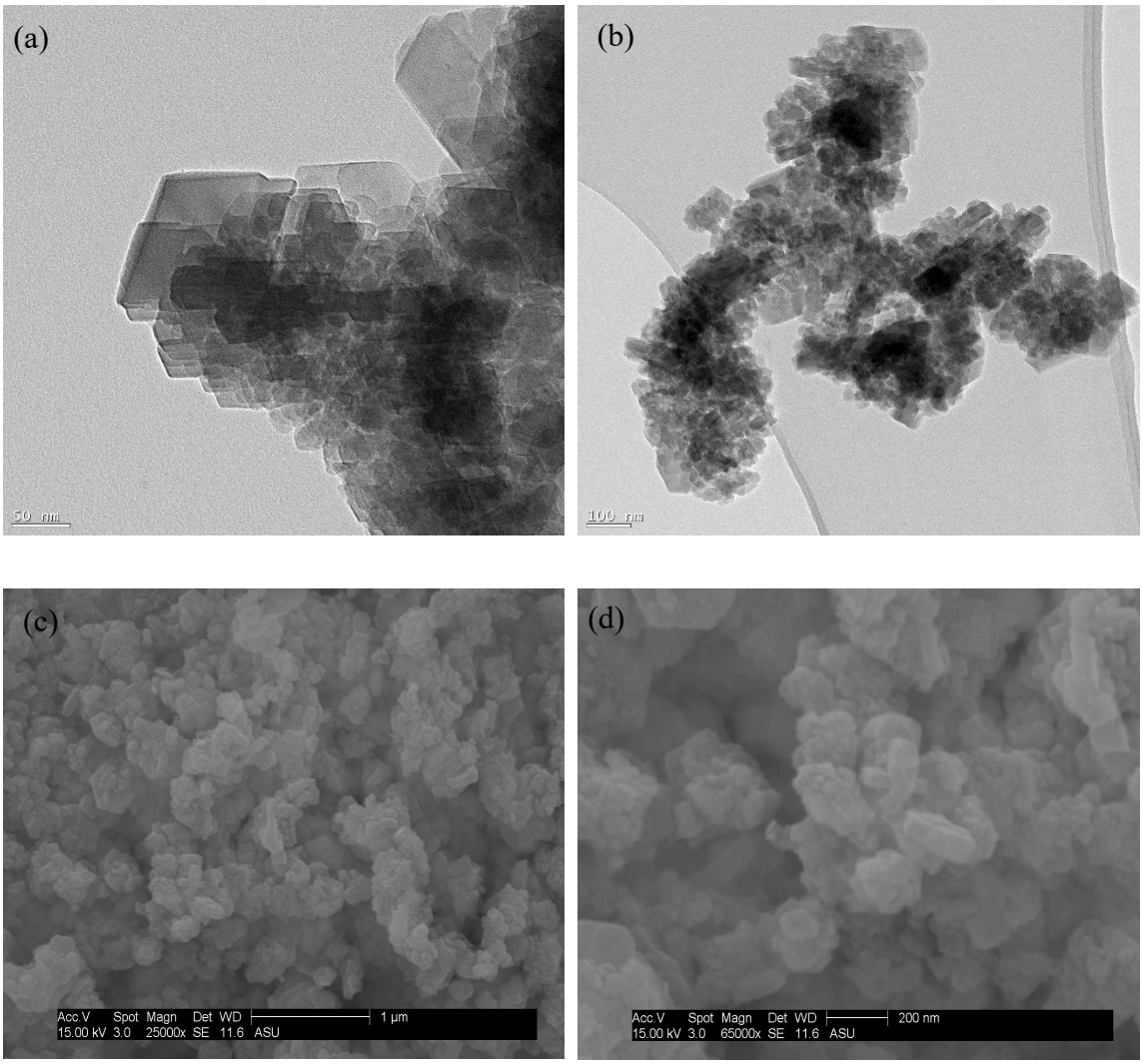

Figure 4.2.TEM ((a) and (b)) and SEM ((c) and (d)) images of NZ.

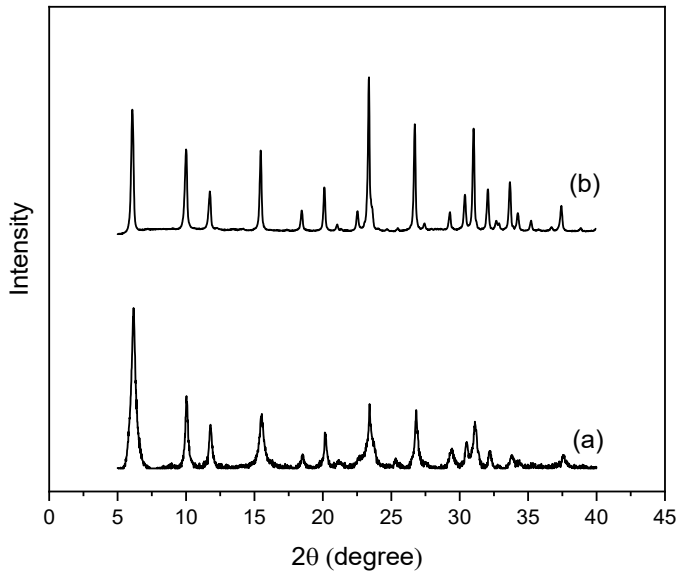

Figure 4.3. PXRD pattern of (a) NZ and (b) Commercial zeolite NaX.

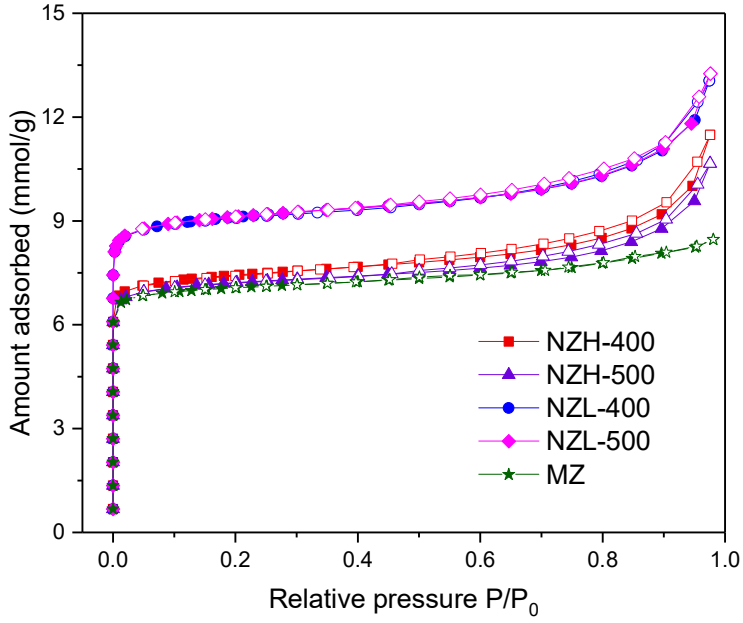

Figure 4.4. N_2 adsorption (filled symbol) - desorption (open symbol) isotherms of NZs and MZ at 77K.

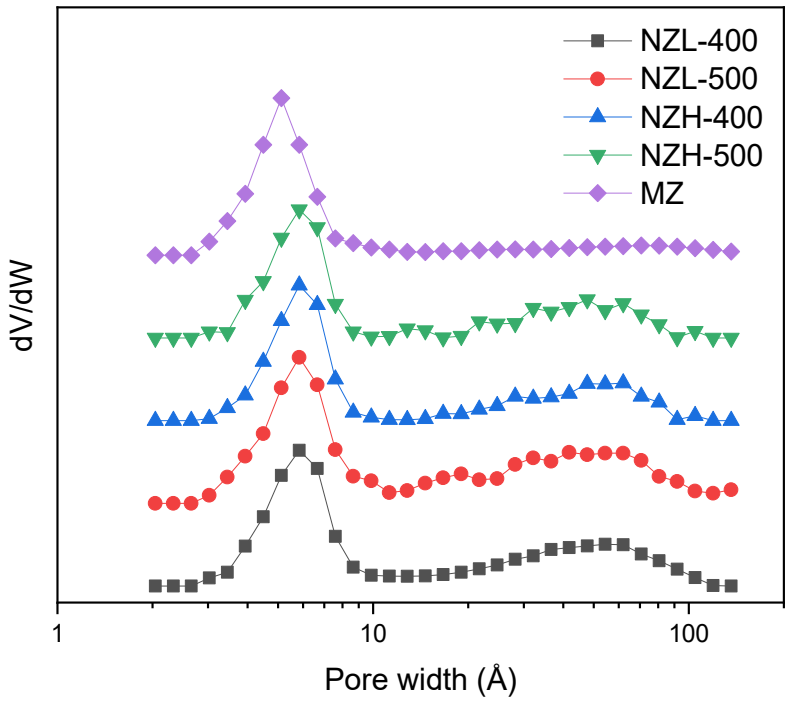

Figure 4.5. Pore distributions of NZs and MZ.

Table 4.1. Porosity properties of nanostructured and microsized zeolite NaX.

	S_{BET} (m^2/g)	S_{micro} (m^2/g)	S_{ext} (m^2/g)	V_{total} (cm^3/g)	V_{micro} (cm^3/g)	V_{meso} (cm^3/g)
MZ	518.66	481.83	36.83	0.349	0.318	0.031
NZL-400	672.09	586.60	85.49	0.459	0.279	0.180
NZL-500	670.11	585.69	84.42	0.453	0.278	0.175
NZH-400	546.99	473.93	73.06	0.398	0.226	0.172
NZH-500	530.16	465.52	64.64	0.370	0.222	0.148

Table 4.2. Mechanical properties of zeolite NaX pellets.

Samples	NZL-400	NZL-500	NZH-400	NZH-500	MZ
Crushing strength (MPa)	3.46 ± 0.83	7.12 ± 1.66	4.11 ± 1.03	8.94 ± 1.59	8.54 ± 1.61
Attrition loss (wt. %)	24.28 ± 3.21	11.24 ± 1.95	20.87 ± 2.51	9.12 ± 1.30	9.61 ± 1.22

4.4.2 Adsorption Isotherm of N_2 and CO_2 on NZ

Single component gas adsorption and desorption isotherms of N_2 and CO_2 were measured by an ASAP-2020 adsorption apparatus, as shown in Figure 4.6. As indicated from the isotherm figures, isotherms of N_2 adsorption are almost linear within the measured pressure range, while CO_2 adsorption isotherm is curved and gradually reaches a saturation point. Generally, the CO_2 adsorption capacities of different samples were displayed in the following trend: NZL-400 ≈ NZL-500 > NZH-400 > NZH-500 > MZ. While the CO_2 adsorption capacity of NZL-400 and NZL-500 are similar, NZL-500 has lower N_2 adsorption capacities than NZL-400, which results in a higher CO_2 to N_2 adsorption selectivity. The sips model fitting parameters are listed in Table 4.3.

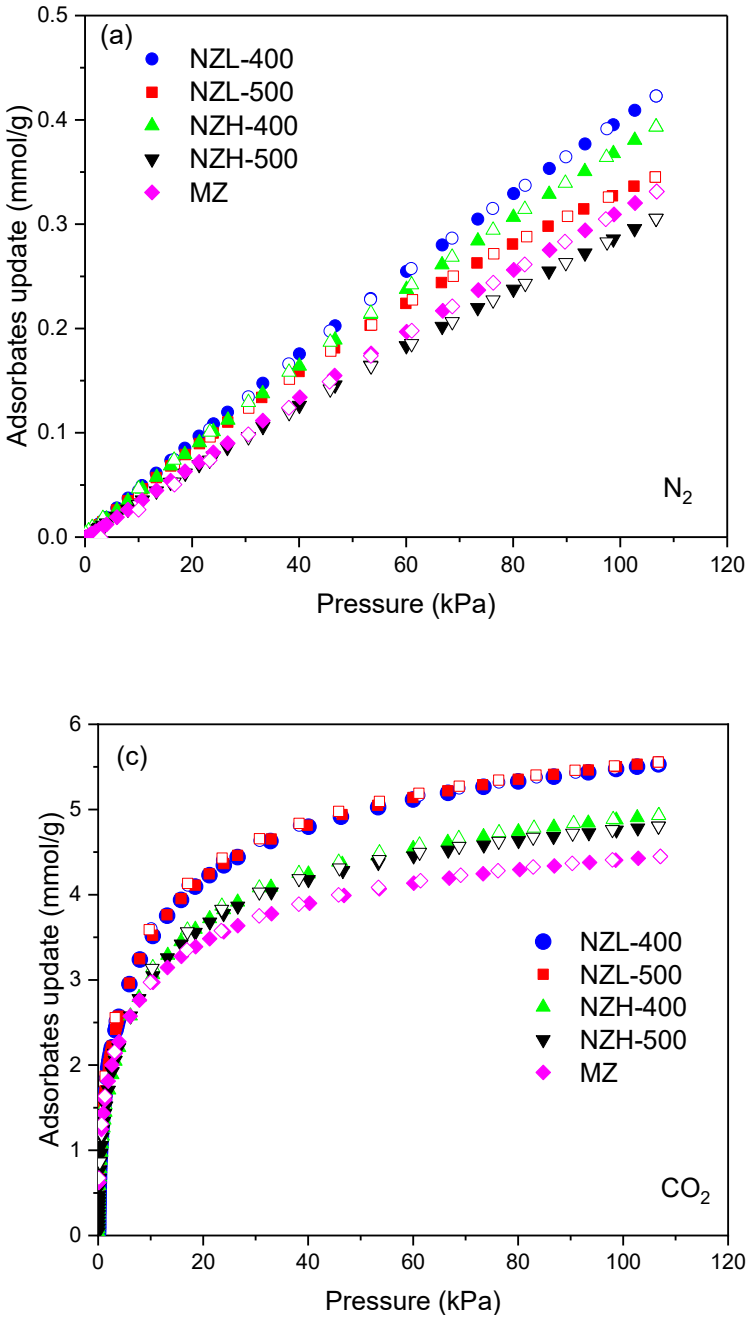

Figure 4.6. Adsorption isotherms for NZs at 298 K of (a) N_2, (b) CO_2 (filled symbols: adsorption; open symbols: desorption).

Table 4.3. Sips isotherm constants of N_2 and CO_2 adsorption on NZ samples at 298 K.

Samples		MZ	NZL-400	NZL-500	NZH-400	NZH-500
N_2	$q_{s,i}$ (mmol/g)	1.92	3.05	1.06	2.53	2.26
	b_i (1/kPa)	0.0021	0.0016	0.0040	0.0018	0.0015
	n_i	0.96	1.01	0.97	1.00	1.01
CO_2	$q_{s,i}$ (mmol/g)	5.79	6.99	7.04	6.27	6.03
	b_i (1/kPa)	0.11	0.10	0.10	0.09	0.12
	n_i	2.03	1.78	1.77	1.74	1.74

4.4.3 IAST Selectivity

Ideal adsorbed solution theory (IAST) of Myers and Prausnitz[40] was applied to investigate the adsorption selectivity of CO_2 over N_2 on the NZ samples, which allows us to analyze the potential of NZs for carbon removal from flue gas (N_2/CO_2 mixture). In this study, the IAST calculations were performed by a Python package called pyIAST[114]. The IAST calculation results of 85%N_2/15%CO_2 for different NZ samples at 298 K and various total pressures were shown in Figure 4.7. Among the zeolite samples, NZL-500 obtained the highest CO_2 selectivity over N_2, and all the NZs exhibited a higher CO_2 selectivity compared with the commercial MZ. At 298K and 100kPa, the calculated selectivity values and CO_2 adsorption capacities of NZs are much higher than the corresponding values of many other benchmark zeolite and MOF adsorbents, as shown in Table 4.4. The results

strongly supported the fact that nanostructured zeolite NaX is a potential adsorbent for effective selective capture of CO_2 from N_2.

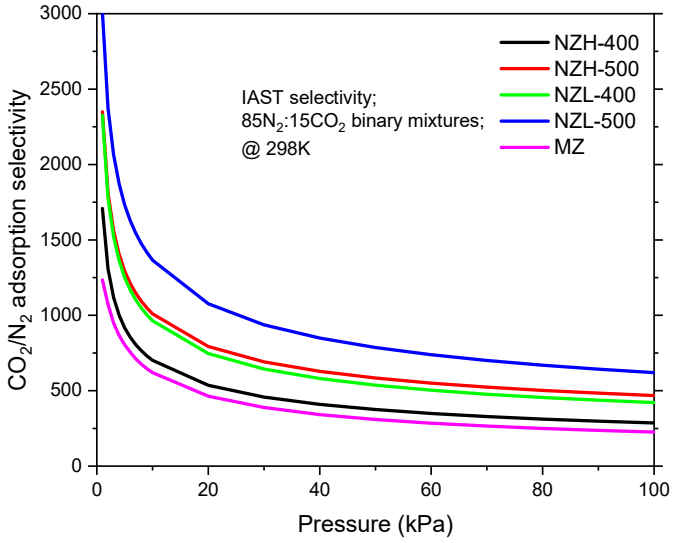

Figure 4.7. IAST selectivities for a binary mixture of 15%CO_2/85%N_2 at 298 K.

Table 4.4. Comparison of IAST selectivities of 50%CO_2/50%N_2 and CO_2 adsorption capacity on NZs and other potential CO_2 adsorbents at 298K and 100 kPa.

CO_2 Adsorbents	IAST selectivities of CO_2/N_2 (50%/50%)	CO_2 capacity (mmol/g)
MZ	226.00	4.45
NZL-400	421.35	5.53
NZL-500	619.99	5.56
NZH-400	285.92	4.93
NZH-500	468.02	4.80

Zeolite 13X[115]	180	4.25
ZIF-8[115]	11	0.82
Zeolite 5A[116]	240.56	4.73
BPL AC[115]	25	2.2
MOF-74-Mg[117]	182	6.03
rht-MOF[118]	25	3.35
MOF-5[116]	17.5	0.91
MOF-177[116]	17.73	1.7
UTSA-16[119]	350	-
ZIF-78[120]	50	2.68

4.4.4 Adsorption Kinetics of CO_2 on NZ

To investigate the CO_2 adsorption mass transfer performance of NZs, we collected adsorption kinetic data of CO_2 for all the NZs at 298 K by the Micromeritic ASAP 2020 adsorption unit using the ROA package and compared with the commercial MZ. As shown in Figure 4.8, under a given dose of CO_2 stream, NZs adsorb CO_2 faster than MZ. Among the NZ samples, NZH-400 and NZL-400 showed the fastest mass transfer for CO_2 adsorption. The mass transfer enhancement of NZs can be attributed to their hierarchical porous structure and improved molecular diffusion[121]. Besides, the nanostructure is also

beneficial for intracrystalline diffusion as the diffusion time decreases with the crystal dimension of zeolites[122].

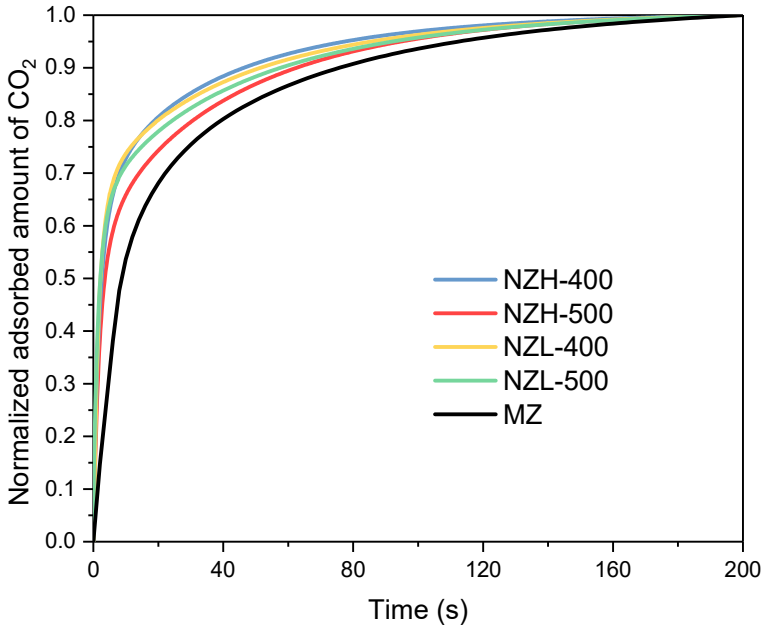

Figure 4.8. Adsorption kinetics of CO_2 on NZs and MZ.

Table 4.5. Mass transfer coefficients of CO_2 on MZ and different NZ samples.

Samples	MZ	NZL-400	NZL-500	NZH-400	NZH-500
$k_{CO_2}\ (1/s)$	0.016	0.120	0.102	0.116	0.073

4.4.5 Column Dynamics

From the previous measurements, it is found that NZL-500 has both good mechanical strength and excellent separation performance of CO_2 from N_2, it's therefore selected for the following fixed-bed adsorption experiments and corresponding simulations. The purpose of the set of breakthrough experiments is to mimic a small-scale CO_2 removal process and to confirm whether or not the simulation model set up in gPROMs can accurately simulate the adsorption process of gas mixtures on the zeolite samples. Breakthrough experiments were also performed for MZ under the same experimental condition for comparison. By taking into account the adsorption equilibrium and kinetics of different gas species on zeolite samples and applying the experimental operating conditions, the breakthrough curves were simulated and compared with the experimental result, as shown in Figure 4.9. Apparently, NZL-500 has a longer breakthrough time of CO_2 compared with the MZ sample, which indicates a larger CO_2 adsorption capacity of NZL-500. The N_2 adsorption breakthrough profile looks similar for these two samples. Additionally, the simulated results are in good agreement with the experimental data at all different studied conditions for all the gases. The same model parameters (excluding bed sizing and operating parameters) will thus be used for the following VPSA simulations.

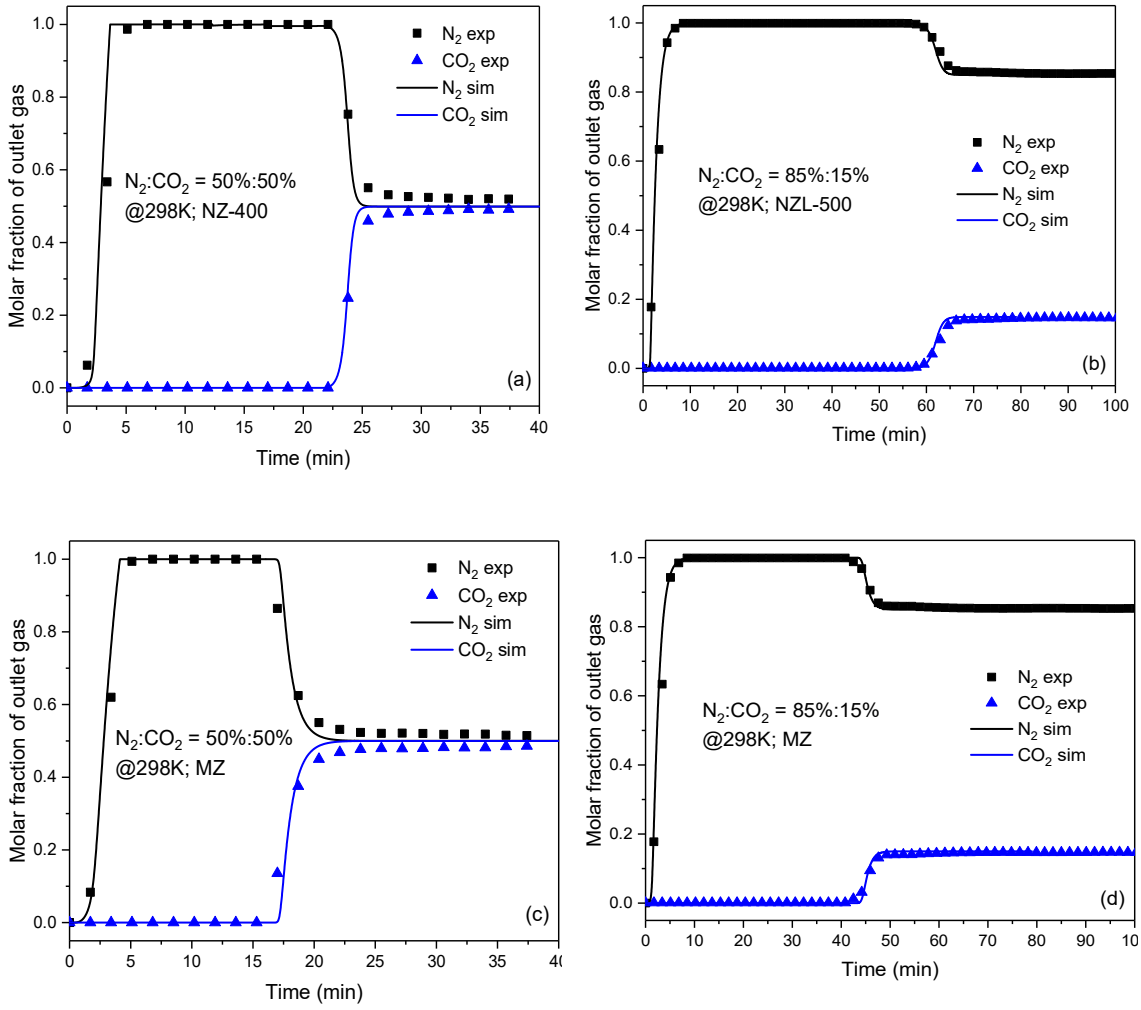

Figure 4.9. Experimental and simulated breakthrough curves for separation of (a) equimolar N_2/CO_2 and (b) 85% N_2/15% CO_2 of NZL-500, (c) equimolar N_2/CO_2 and (b) 85% N_2/15% CO_2 of MZ in a fixed bed at 298 K and 1 bar (dotted line for the experimental data, solid line for the simulation results).

4.4.6 VPSA Simulation

In the current study, NZL-500 is chosen as the novel adsorbent material in the VPSA capture unit, and the performance is compared with the commercial adsorbent MZ. The physical properties of the adsorbents and characteristics of the adsorption bed are summarized in Table 4.6. The operating parameters at the base case are displayed in Table 4.7. These parameters will be used as the initial guesses for the optimization problem.

Table 4.6. Characteristics of adsorbents and adsorption bed of VPSA simulation for carbon capture.

Parameters	Values	Values
Adsorbent	NZL-500	MZ
Type	Pellet	Pellet
Average diameter, d_p (cm)	0.15	0.15
Bulk density, ρ_b (g/cm3)	0.694	1.159
Heat capacity of the adsorbent, $C_{p,ads}$ (J/g/K)	0.641	0.504
Adsorbent thermal conductivity, λ_{ads} (W/m/K)[43]	1	1
Particle porosity, α	0.35	0.28
Adsorption bed		
Length, L (cm)	50	50
Internal diameter, D_{bi} (cm)	5	5
Bed porosity, ε_b	0.32	0.32

Heat capacity of the column, $C_{p,w}$ (J/g/K)[43]	0.90	0.90
Heat transfer coefficient, h ($W/cm^2/K$)[43]	$3.8*10^{-3}$	$3.8*10^{-3}$
Other parameters		
CO_2 mass transfer coefficient (1/s)	0.102	0.016
N_2 mass transfer coefficient (1/s)	0.845	0.639
Dispersion coefficient (m^2/s)	$1.3*10^{-5}$	$1.3*10^{-5}$

Table 4.7. Operating parameters of the VPSA process at the base case.

Parameters	Values
Feed pressure, P_{feed} (bar)	2
Blowdown pressure, P_{bd} (bar)	1
Evacuation pressure, P_{evac} (bar)	0.15
Feed flow rate, F_{feed} (m^3/h)	2.24
Length to diameter ratio, L/D	10
Cycle time (s)	200
PLP duration (s)	10
AD duration (s)	50
DPE duration (s)	10
BD duration (s)	10
EVAC duration (s)	50
PPE duration (s)	10

Due to the need for synchronization of multi-bed configuration, the effect of cycle time on VPSA process performance is investigated independently. Among the operating steps, the adsorption/evacuation (AD-EVAC) duration is critical for the VPSA process performance. The effect of AD-EVAC duration on CO_2 purity, recovery, productivity, and the energy consumption of the process is therefore studied. The duration of PLP-BD and PPE-DPE do not affect the overall process performance much and will keep fixed at 10 seconds.

Figure 4.10 and Figure 4.11 show the effect of AD-EVAC duration on the performance indicators for NZL-500. Results show that CO_2 product purity increases with the increase of AD-EVAC duration. However, the increase in AD-EVAC duration causes higher retention of the CO_2 product in the column, resulting in decreased product recovery and productivity. Since the product purity and recovery can still be improved by other operating parameters, the AD-EVAC duration is chosen to minimize the energy consumption of the process, which is at 50 seconds. Figure 4.12 and Figure 4.13 show the effect of AD-EVAC duration on the performance indicators for MZ. The overall trend for all the performance indicators is similar to NZL-500. However, compared with the process with NZL-500, the values of product purity, recovery, and productivity of process with MZ are lower while the energy consumption is higher, indicating MZ is less favorable for carbon capture with VPSA process. The optimal AD-EVAC duration for the minimized energy consumption of the process with MZ is also 50 seconds.

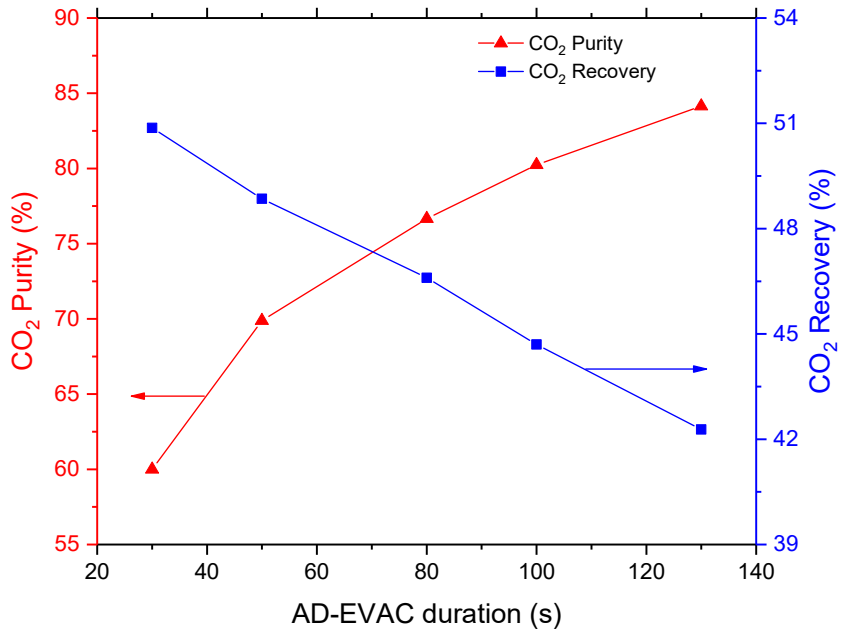

Figure 4.10. Effect of AD-EVAC duration on CO_2 purity and recovery for NZL-500.

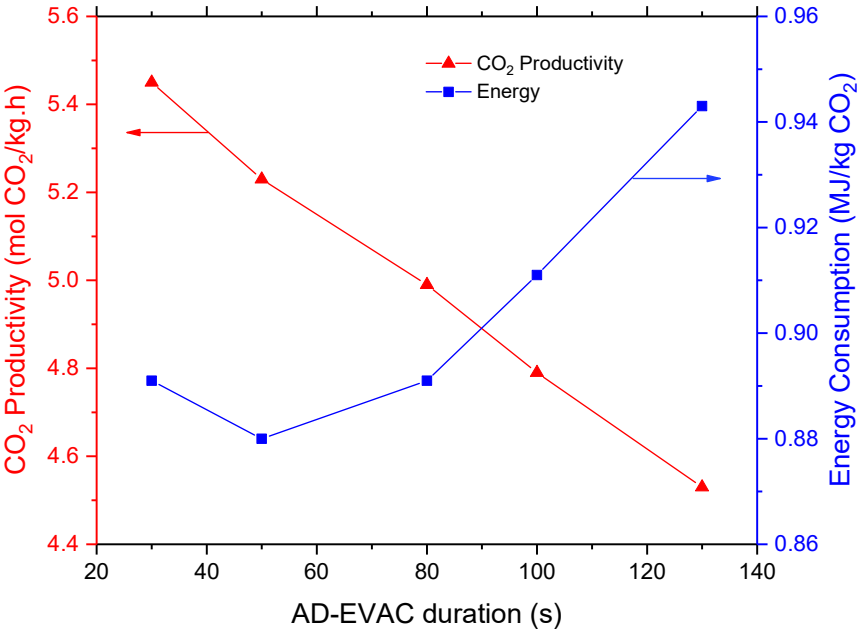

Figure 4.11. Effect of AD-EVAC duration on CO_2 productivity and energy consumption for NZL-500.

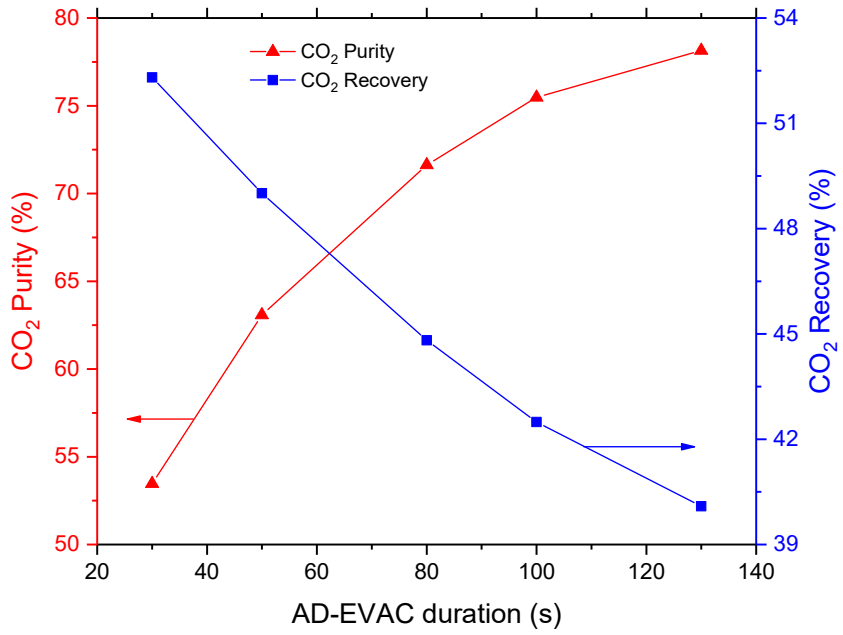

Figure 4.12. Effect of AD-EVAC duration on CO_2 purity and recovery for MZ.

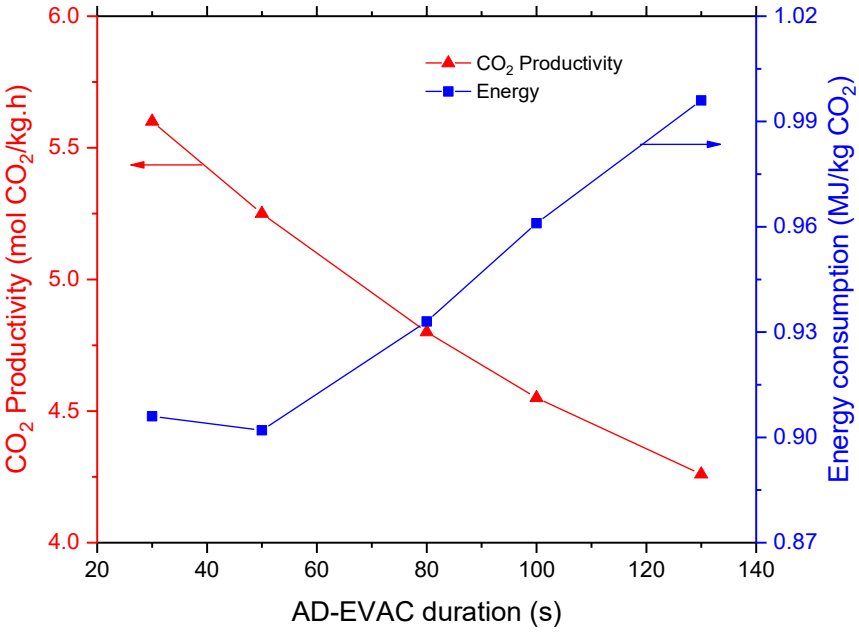

Figure 4.13. Effect of AD-EVAC duration on CO_2 productivity and energy consumption for MZ.

After determining the cycle time of the process, optimization was then performed to minimize the energy consumption for specified minimum requirements in CO_2 purity and recovery. The optimization results for processes employing NZL-500 and MZ are summarized in Table 4.8. The results reveal that the specified target of 92% in CO_2 purity and 90% in CO_2 recovery is met for both adsorbents. However, MZ requires both a higher feeding pressure and lower blowdown and evacuation pressures to achieve the specified target compared with NZL-500, resulting in higher energy consumption. As a result, the energy consumption for the process is around 30% lower when working with NZL-500. Considering that the evacuation pressure of the process with MZ is 0.048, which is at the deep vacuum level that needs multiple stages of pumping, the actual energy saving is even more. The difference can be attributed to the difference in the CO_2 adsorption equilibrium and kinetics for each adsorbent. Also, the obtained CO_2 product purity for the process with NZL-500 (95.06%) is much higher than the process with MZ (92.95%).

Under the optimal conditions, the pressure profiles during a VPSA cycle of the two adsorption beds for both adsorbents are presented in Figure 4.14; the numbers above the figures indicate each operating step that illustrated in Figure 4.1. The CO_2 concentration of the product stream at the cyclic steady-state for both adsorbents is presented in Figure 4.15. Apparently, NZL-500 has a larger CO_2 concentration of the product stream compared with MZ, resulting in the higher CO_2 product purity.

Table 4.8. Optimization results for VPSA process employing NZL-500 and MZ.

Decision variables	NZL-500	MZ
AD-EVAC duration (s)	50	50
PLP-BD duration (s)	10	10
PPE-DPE duration (s)	10	10
P_{feed} (bar)	1.485	1.944
P_{bd} (bar)	0.56	0.37
P_{evac} (bar)	0.103	0.048
F_{feed} (m^3/h)	1.98	1.49
L/D	7.156	11.01
CO_2 purity (%)	95.06	92.95
CO_2 Recovery (%)	90.00	90.00
CO_2 Productivity (mol CO_2/kg/h)	10.35	9.96
Energy (MJ/kg CO_2)	0.464	0.658

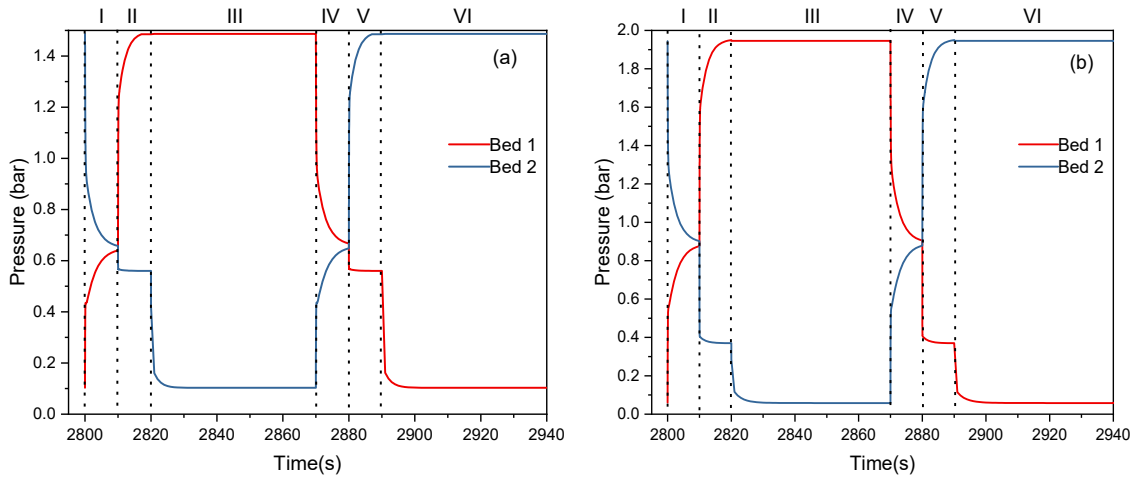

Figure 4.14. Pressure profiles in a VPSA cycle for (a) NZL-500, and (b) MZ.

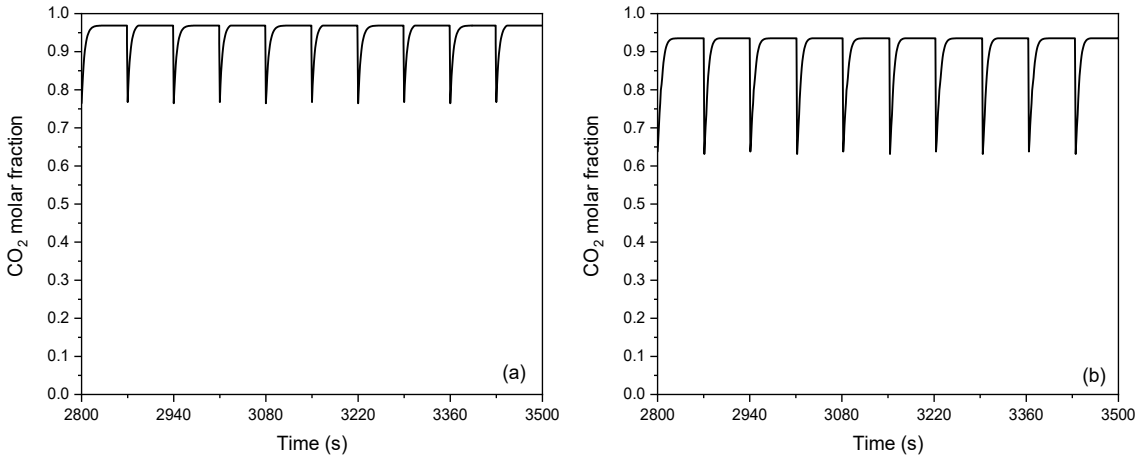

Figure 4.15. CO_2 concentration of the product stream at the cyclic steady state for (a) NZL-500, and (b) MZ.

4.4. Conclusion

In this study, a group of nanostructured zeolite NaX pellets was prepared with different binder ratios and different sintering temperatures. The comparison of porosity properties, mechanical properties, adsorption isotherm, adsorption kinetics, and adsorption

IAST selectivity of CO_2 over N_2 showed that NZL-500 has the best performance among all the samples. Additionally, the results indicate the NZs lead to a higher CO_2 adsorption capacity, enhanced mass transfer rate for CO_2 adsorption, and better separation performance of an N_2/CO_2 mixture compared with the commercial MZ.

As a next step, a VPSA process for CO_2 capture from flue gas is simulated and optimized. The simulation model has been validated with both breakthrough experimental data and reported data from the literature. Both NZL-500 and MZ were selected for the optimization that employed with a two-bed six-step cycle configuration with two pressure equalization steps to save the energy cost. The objective of the optimization is to minimize the energy consumption of the VPSA process while meeting the specified minimum CO_2 purity and recovery target. The optimization results show that the energy consumption of the process with NZL-500 is around 30% lower than that of the process with MZ while achieved higher CO_2 purity and productivity. This is due to the more moderate conditions (e.g. higher blowdown pressure, higher evacuation pressure, and lower feeding pressure) the process required to meet specified CO_2 purity and recovery target. In short, the optimization results have shown great potential for employing nanostructured zeolite NaX by VPSA process for CO_2 capture from the flue gas with low CO_2 concentrations, as a CO_2 purity of over 95% and a recovery of 90% was obtained with a practical vacuum level (>0.1 bar). Lower vacuum levels or multi-stage operations may be possible to achieve products with higher purity.

Notations:

A: Cross-sectional area of the adsorption bed (m^2)

b_i: Equilibrium parameter of Sips isotherm for component i (1/bar)

C_i: Molar concentration of component i in the gas phase ($kmol/m^3$)

$C_{p,ads}$: Heat capacity of the adsorbent (kJ/kg/K)

$\Delta C_{p,ad,i}$: Change in the heat capacity of the adsorbed species from reference condition to bed conditions for component i (kJ/kg/K)

d_b: Diameter of adsorption bed (m)

d_p: Diameter of adsorbent particle (m)

D: Mass axial dispersion coefficient (m^2/s)

$D_{m,i}$: Molecular diffusivity for component i (m^2/s)

$D_{i,j}$: Binary diffusivity for component i with component j (m^2/s)

$D_{i,i}$: Self diffusivity for component i (m^2/s)

E_c: Energy consumption of the compressor (kJ/s)

E_v: Energy consumption of the vacuum pump (kJ/s)

F^{in}: Mass flow rate at the entrance of the adsorption bed (kg/s)

h: Specific enthalpy of gas phase (kJ/kg)

h^{in}: Mass specific enthalpy at the entrance of the adsorption bed (kJ/kg)

$h_{ad,i}$(T): Molar specific enthalpy of component i at the bed temperature (kJ/kmol)

h_i^{ϕ}(T): Pure component enthalpy at the bed temperature (kJ/kg)

$\Delta H_{ad,i}$: Heat of adsorption for component i (kJ/kg)

$k_{T,b-w}$: Heat transfer coefficient from the gas phase to the bed wall ($W/m^2/K$)

k_i: Mass transfer coefficient of i compound (1/s)

L: Bed length (m)

M_g: Molecular weight of gas (kg/kmol)

M_i: Atomic/molecular weight of element/molecule i (kg/kmol)

Mw_i: Molecular weight of component i (kg/kmol)

n_i: Freundlich exponent of component i

$\dot{n_{in}}$: Molar flow rate of the feed stream of compressor/ vacuum pump (kmol/s)

P: Pressure (bar)

P_{in}: Pressure at the feed end of the adsorption bed (bar)

P_i: Partial pressure of i compound (bar)

$P_{in,c}$: Pressure of inlet stream of the compressor (bar)

$P_{out,c}$: Pressure of leaving stream of the compressor (bar)

$P_{in,v}$: Pressure of inlet stream of the vacuum pump (bar)

$P_{out,v}$: Pressure of leaving stream of the vacuum pump (bar)

q_i: Specific amount of component i adsorbed on solid phase (kmol/kg)

q_i^*: Amount of i compound adsorbed at equilibrium (kmol/kg)

$q_{s,i}$: Maximal adsorbed equilibrium amount for component i (kmol/kg)

t: Time (s)

T: Gas temperature (K)

T_{in}: Temperature of the feed stream of the compressor/ vacuum pump (K)

T_w: Bed wall temperature (K)

T_{ref}: Reference temperature (K)

$\tilde{u}$: Energy density per unit volume of bed (kJ/m^3)

v: Superficial velocity of the gas phase (m/s)

w_i^{in}: Mass fraction of component i at the entrance of the adsorption bed

z: Bed axial distance (m)

Greek letters:

ρ: Mass density of gas phase (kg/m^3)

ρ_b: Density of the bed (kg/m^3)

ρ_p: Density of the adsorbent particle (kg/m^3)

ε_b: Porosity of the adsorbent bed

ε_{tot}: Total void fraction, including intra- and inter- particle void space

λ: Thermal conductivity of the gas (W/m/K)

λ_{ads}: Thermal conductivity of adsorbent material (W/m/K)

λ_{eff}: Effective thermal conductivity (W/m/K)

γ: Specific heat capacity ratio

η_c, η_v: Isentropic efficiency of compressor and vacuum pump

$\forall i \in C$: For all chemical species involved in the system

Chapter 5: Efficient Screening of Novel Adsorbents for Coalbed Methane Recovery

5.1 Introduction

Coalbed methane (CBM) is a form of the gas mixture extracted from underground coal mining. As the major energy content of CBM, methane (CH_4) delivers roughly twice the energy of coal for the same amount of carbon dioxide (CO_2) release[123]. CBM is therefore commonly considered as a clean and efficient alternative energy source. However, significant quantities of coalbed gas may not be efficiently used because the presence of nitrogen (N_2) in the mixture lowers the overall energy content. It is, therefore, necessary to recover CH_4 from CBM before the energy contained can be utilized.

It is well known that the separation of CH_4/N_2 is a challenging task because of their similarly physicochemical properties[124]. Traditionally, CH_4/N_2 separation can be achieved by the cryogenic distillation method. Although the process is efficient for the separation, its enormous energy consumption and substantial investment could be the biggest drawback. Membrane separation though offered a lower cost than traditional cryogenic distillation; it is difficult to achieve a sufficient selectivity to develop an effective separation for CBM because CH_4 and N_2 are of similar molecular sizes[125]. Adsorption stands out to be an attractive alternative due to its relatively low cost, flexible operating, and efficient regeneration[105]. The process of adsorption arises due to the presence of unbalanced forces at the surface of adsorbents so that the gas molecules are attracted and retrained when they come in contact with the surface[126]. Some generic cycle concepts are known as temperature swing adsorption (TSA), pressure swing adsorption (PSA) and

vacuum pressure swing adsorption (VPSA) are employed to carry out the essential adsorption and desorption steps in conjunction with a variety of other complimentary steps[9]. VPSA is an emerging technology that applies pressurized gas to the adsorption process as well as a vacuum during the desorption stage. VPSA is more efficient than PSA processes when dealing with CBM due to the low partial pressure of CH_4 and high partial pressure of N_2 in the CBM stream[127].

The key challenge in CBM recovery by adsorption technique is to find a suitable solid adsorbent material with good separation performance, as the adsorbent plays a critical role in the overall process performance[25]. Many materials have been studied as potential adsorbents for CBM recovery, including activated carbons (ACs)[128–136], zeolites[137–141], and metal-organic frameworks (MOFs)[117,140,142,143]. However, it is still unclear how the reported adsorbent properties such as adsorption isotherms related to process performance which is measured by purity, recovery, energy consumption and throughput. An effective screening method is therefore required. Consider that experimental evaluation of the adsorbents is both resource and time intensive to be practically feasible for screening, hence the evaluation of novel materials by simulation is computationally demanding[144].

For adsorption screening purposes, a variety of criteria have been used for the separation process in the previous literature. For example, adsorption selectivity is one of the most used criteria for screening suitable adsorbents for the separation process. The adsorption selectivity of component i of a gas mixture over another component j is a function of the equilibrium gas phase pressure (P), temperature (T), and mole fraction (y_i) of component i. which defined by the following equation[145]:

$$S_{ij} = \frac{n_i y_j}{n_j y_i} \tag{5.1}$$

where n_i is the specific equilibrium amount of component i adsorbed from the gas mixture at P, T, and y_i. The adsorption selectivity plays a crucial role in determining the performance of adsorptive gas separation process, as it is a measure of the competitiveness of adsorption between components of a gas mixture. Another criterion that often used for adsorbent evaluation is the adsorption capacity. The absolute adsorption capacity has been reported extensively for different materials. But rather than a single point loading, working capacity might be a better measure as it represents the loading difference between the high and low operating pressures corresponding to the adsorption and desorption, which is more relevant to the actual separation process. Taking account of both adsorption selectivity and working capacity, Rage and Yang[146] proposed a composite dimensionless parameter (S) for selecting the adsorbents for the VPSA process of a binary mixture. The definition of S is given by the following equation:

$$S = \frac{WC_1}{WC_2}\alpha_{12} \tag{5.2}$$

where WC_1 and WC_2 are the working capacities of components 1 and 2, respectively. α_{12} is the ratio of Henry's constant of component 1 and component 2. Besides the lumped factor, breakthrough simulation has also been used for screening adsorbents for various adsorptive separation process[147,148], where the breakthrough time is related to working capacity and the ratio of breakthrough time is related to adsorption selectivity.

Though all the previous factors are related to the process performance to some extent, they are only suitable for prescreening the adsorbents because several factors such as pressure drop, energy consumption, gas phase, and solid phase concentration distribution along the adsorption bed are not considered. Also, for CBM recovery, regeneration is the most important step as the CH_4 product is produced in the regeneration. Most previous criteria focused more on the adsorption process. To accurately assess the process performance of different adsorbents and to resolve the dilemma on how to weigh the selectivity and capacity characteristics, a detailed process simulation of the VPSA process is required. VPSA simulation has been extensively used for applications like air separation and CO_2 capture[87,100,101,103,104,106,149,150]. Most comments on VPSA simulation is its extensive calculation and long simulation time. However, for screening purposes, we are more focused on comparing the process performance of different adsorbents. The model can be simplified by making some suitable assumptions and simulation time can be much reduced.

In this study, we aimed to develop a new method for efficient evaluation of adsorbents for VPSA processes. Most previous screening methods[146,151,152] inspected materials solely by their adsorption capacity or selectivity, which were often inaccurate and misleading. The new screening method should be robust, comprehensive, while also simple to implement. To reduce the total amount of simulation time, we firstly prescreened the studied materials with their adsorption selectivity and S factor. A unique scoring system was built to rank the materials properly. The prescreened adsorbents were then simulated in a simplified VPSA model for efficient screening, and optimized to determine the optimal

operating conditions. The process performance was evaluated by comparing the product purity, recovery, productivity, and energy consumption of the process. With this screening methodology, we identified the best adsorbents for CH_4 production at different conditions and found the adsorbent properties most related to process performance. This screening method is general to any VPSA process even though the example used in the case study is VPSA for CBM recovery.

5.2. Mathematical Model of the VPSA Process for Screening

5.2.1 Model Assumptions and Equations

In the current study, the VPSA processes were simulated by a modeling framework developed in gPROMs. In order to simplify the simulation process and reduce the simulation time, the following assumptions were adopted for the model.

a. The gas phase behaves as an ideal gas.

b. Isothermal operation.

c. There is no radial variation in gas concentration, temperature, and pressure.

d. The flow pattern is represented by the axial dispersed plug flow model.

e. The porosity of the bed and adsorbent pellet is assumed to be uniform along the bed.

f. The diffusion and mass transfer effects are represented by a linear driving force (LDF) model with a single lumped mass transfer coefficient.

g. The pressure drop along the bed was calculated by using the Ergun equation.

The model equations and boundary conditions are provided as follows.

The continuity equations for the gas phase mass balance describe how species are transported through the bed in the axial direction. The effects of axial convection, dispersion, and transport to the adsorbed phase can be calculated using the following equations[25]:

$$\varepsilon_{tot}\frac{\partial C_i}{\partial \mathrm{t}} = -\varepsilon_b\frac{\partial}{\partial z}\left(D\frac{\partial C_i}{\partial \mathrm{z}}\right) - \frac{\partial C_i v}{\partial \mathrm{z}} + \rho_\mathrm{b}\cdot\frac{\partial \mathrm{q_i}}{\partial \mathrm{t}} = 0, \quad \forall \mathrm{i} \in \mathrm{C} \tag{5.3}$$

where ε_{tot} is total void fraction, including intra- an inter-particle void space, $\mathrm{C_i}$ is the molar concentration of component i in the gas phase, ε_b is the void fraction in the bed (bed porosity), D is the mass axial dispersion coefficient, v is the superficial velocity of the gas phase, ρ_b is the density of bed, and $\mathrm{q_i}$ is the specific amount of component i adsorbed on solid phase.

The boundary conditions (assuming the flow direction is from feed to product side of the bed) are given by the following equations:

$$\frac{F^{in}{w_i}^{in}}{A} = Mw_i\left(vC_i - \varepsilon_b D\frac{\partial C_i}{\partial \mathrm{z}}\right), \quad \forall \mathrm{i} \in \mathrm{C}, \quad \mathrm{z} = 0 \tag{5.4}$$

$$\varepsilon_b D\frac{\partial C_i}{\partial \mathrm{z}} = 0, \quad \forall \mathrm{i} \in \mathrm{C}, \quad \mathrm{z} = \mathrm{L} \tag{5.5}$$

where F^{in} is the mass flow rate at the entrance of the adsorption bed, ${w_i}^{in}$ is the mass fraction of component i at the entrance of the adsorption bed, A is the cross-sectional area of the bed, Mw_i is the molecular weight for component i, L is the bed length.

The pressure drop for the gas flow in packed beds is determined from the Ergun equation[39]:

$$\left(\frac{\partial P}{\partial z}\right)_t = -\frac{150\mu}{d_p^2}\frac{(1-\varepsilon_b)^2 v}{{\varepsilon_b}^3} - \frac{1.75\rho}{d_p}\frac{(1-\varepsilon_b)}{{\varepsilon_b}^3}v^2 \tag{5.6}$$

where μ is the dynamic viscosity of gas, d_p is the diameter of the pellet particle.

The boundary condition for this equation is given below:

$$\mathrm{P} = P_{in}, \;\; z = 0 \tag{5.7}$$

where P_{in} is the pressure at the feed end of the adsorption bed.

The mass transfer from the gas phase to the solid phase for component i is described by an LDF model[19,109]:

$$\frac{\partial \mathrm{q_i}}{\partial \mathrm{t}} = k_i(\mathrm{q_i^*} - \mathrm{q_i}), \quad \forall \mathrm{i} \in \mathrm{C} \tag{5.8}$$

where k_i is the mass transfer coefficient for the LDF model, $\mathrm{q_i^*}$ is the amount of component i adsorbed at equilibrium.

The adsorption equilibrium can be predicted by the Langmuir isotherm:

$$\mathrm{q_i^*} = q_{s,i}\frac{b_i p_i}{1 + b_i p_i}, \quad \forall \mathrm{i} \in \mathrm{C} \tag{5.9}$$

where b_i is the equilibrium parameter, p_i is the partial pressure for component i, $q_{s,i}$ is the maximal adsorbed equilibrium amount for component i.

The energy consumption of the process is defined as the summation of energy required for compression and evacuation of the gas streams. The energy consumption for compressing the gas streams in a compressor is given by the following equation:

$$E_c = \frac{\dot{n}_{in} R T_{in}}{\eta_c} \frac{\gamma}{\gamma - 1} \left[\left(\frac{P_{out,c}}{P_{in,c}} \right)^{\frac{\gamma - 1}{\gamma}} - 1 \right] \tag{5.10}$$

where E_c is the energy consumption of the compressor, $\dot{n}_{in}$ is the molar flow rate of the feed stream of the compressor, T_{in} is the temperature of the feed stream of the compressor, γ is the specific heat capacity ratio, $P_{in,c}$ and $P_{out,c}$ are the pressure of the inlet and leaving stream of the compressor, η_c is the isentropic compression efficiency of the compressor.

The energy consumption for the evacuation of gas streams in a vacuum pump is provided by the following equation:

$$E_v = \frac{\dot{n}_{in} R T_{in}}{\eta_v} \frac{\gamma}{\gamma - 1} \left[\left(\frac{P_{in,v}}{P_{out,v}} \right)^{\frac{\gamma - 1}{\gamma}} - 1 \right] \tag{5.11}$$

where E_c is the energy consumption of the vacuum pump, $\dot{n}_{in}$ is the molar flow rate of the feed stream of the vacuum pump, T_{in} is the temperature of the feed stream of the vacuum pump, $P_{in,v}$ and $P_{out,v}$ are the suction pressure and discharge pressure of the vacuum pump, η_v is the isentropic evacuation efficiency of the vacuum pump.

The performance indicators of the VPSA process (product purity, recovery, productivity, and energy consumption) are defined by the following expressions:

$$\text{Product } Purity = \frac{mole\ of\ the\ desirable\ component\ in\ the\ product}{Total\ moles\ of\ the\ product} \tag{5.12}$$

$$Product\ Recovery = \frac{moles\ of\ the\ desirable\ component\ in\ the\ product}{moles\ of\ the\ desirable\ component\ in\ the\ feed} \quad (5.13)$$

$$Product\ Productivity = \frac{moles\ of\ the\ desirable\ component\ in\ the\ product}{time \cdot mass\ of\ adsorbent} \quad (5.14)$$

$$energy\ consumption = sum\ of\ energy\ required\ for\ all\ compression\ and\ vacuum\ sources \quad (5.15)$$

It should be noted that all the performance indicators are obtained at cyclic steady-state conditions when the indicators are constant over time. Also, the desirable component refers to the heavy extract (CH_4) in this study.

5.2.2 Process Description

The raw CBM stream is obtained from coal beds that typically contain N_2, CH_4 and minor impurities such as CO_2 and C2 to C5 hydrocarbons. In the current study, it can be assumed that the feedstock is pretreated to remove CO_2 and the amount of C2 to C5 hydrocarbons is ignorable. The ratio of N_2 and CH_4 in the CBM is assumed to be 70% and 30%, respectively.

The VPSA cycle applied in this work consists of two beds with six operating steps, including a pressurization with the light product step (PLP), an adsorption step (AD), a depressurizing pressure equalization step (DPE), a blowdown step (BD), an evacuation step (EVAC), and a pressurizing pressure equalization step (PPE). Two pressure equalization steps were employed to reduce overall energy consumption. The cycle

sequence of two beds during each operating step of the VPSA process is shown in Figure 5.1.

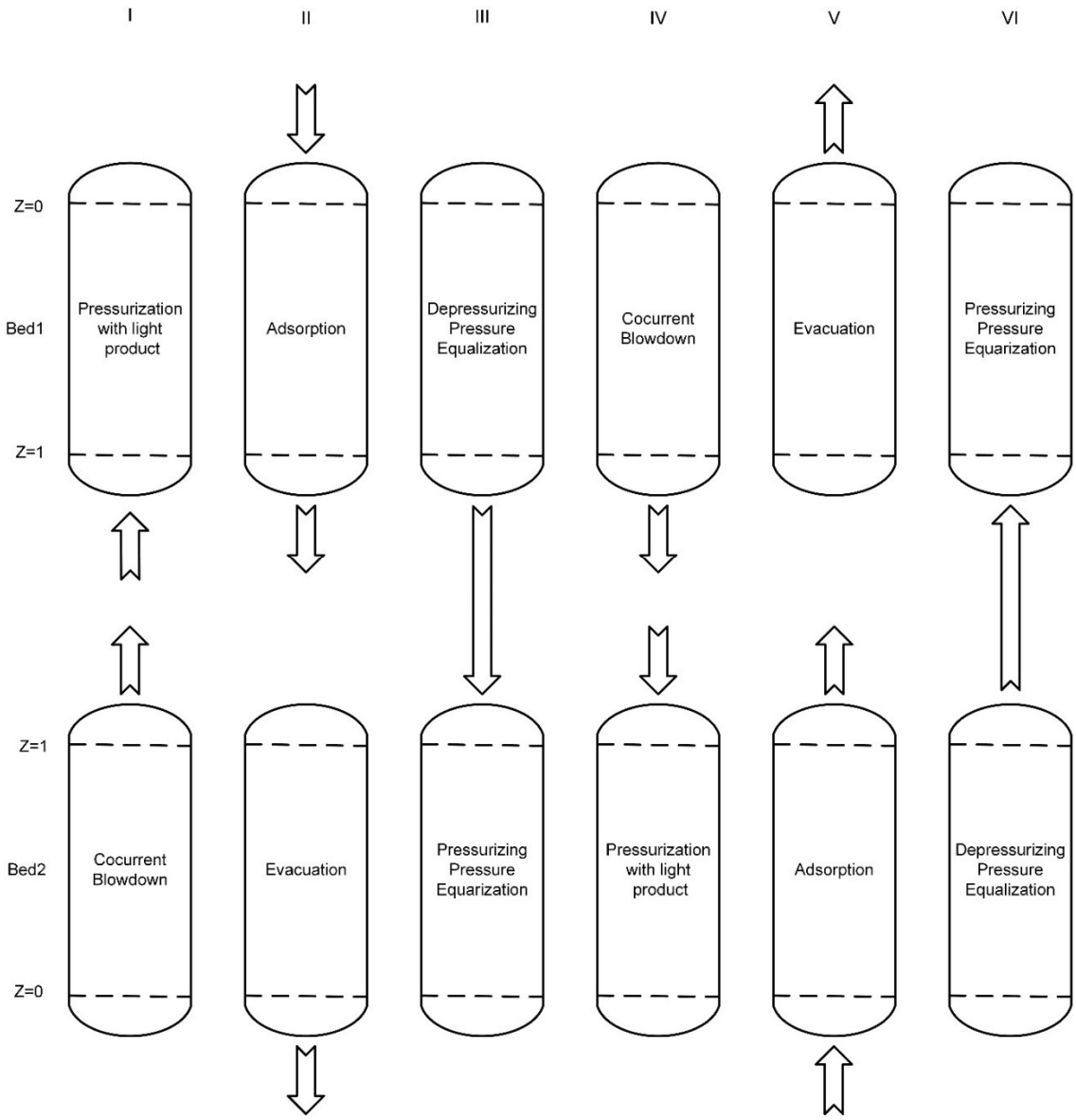

Figure 5.1. Cycle sequence of operating steps for the two-bed six-step VPSA system.

5.3 Results and Discussion

5.3.1 Adsorbent Selection

Adsorbent properties are the most influential aspects of CBM recovery performance of a given VPSA cycle. CH_4/N_2 separation by adsorption is majorly operated with equilibrium-based adsorbents, such as zeolites, ACs, and MOFs. These adsorbents have stronger surface interactions with CH_4 than N_2 to separate the components. The current study selected 47 novel adsorbents that have potential to be used in the CBM recovery process. The reported studies regarding these adsorbents are yet at a lab-scale, and their process performance in the real VPSA application is still unknown. Therefore, the new screening approach was utilized to evaluate and compare the process performance of different adsorbents. The details and references of the materials can be found in Table 5.1.

Table 5.1. Description of adsorbents for the current screening work

Material type	Sample name	Description	Reference
Zeolites	Zeolite 5A	Zeolite 5A	[140]
	Zeolite 13X	Zeolite 13X (Na exchanged)	[115]
	Silicalite-1-H	Hierarchical pure silica zeolite	[113]
	Silicalite-1-M	Microporous pure silica zeolite	[113]
ACs	OMC	Ordered mesoporous carbon	[134]

NAC-600	Nitrogen-doped porous carbons	132
NAC-700		
NAC-800		
OAC-0	Hydroquinone and quinone-grafted porous activated carbons	131
OAC-1		
OAC-2		
PF-600 KOH	Polyfuran derived microporous carbons	130
PF-800 KOH		
PF-600 $ZnCl_2$		
PF-800 $ZnCl_2$		
NAPC-1-6	N-doped algae-derived porous carbons	153
NAPC-2-6		
NAPC-3-6		
Meso-carbon	Mesoporous carbon	154
sOMC	Ordered mesoporous carbon with soft template	134
OTS-1-550	Ultramicroporous biomass-derived carbons	129
OTS-2-650		
OTS-3-750		
OTSS-3-350	Ultra-high surface area and nitrogen-rich porous carbons	136
OTSS-2-450		
OTSS-1-550		

	SNMC-1-600		
	SNMC-2-600	N-doped microporous carbon with SFRH polymer	133
	SNMC-3-600		
	AAC-1		
	AAC-1W		
	AAC-2	MOF-derived porous carbons	143
	AAC-2W		
	AAC-3		
	SA-1-600		
	SA-1-700		
	SA-1-800	High N-content porous carbons prepared from shrimp-shells	135
	SA-2-600		
	SA-2-700		
	SA-2-800		
	Zif-8	Zeolitic imidazolate frameworks	115
	Cu-MOF	Ultramicroporous copper MOF	142
	MOF-177	MOF-177	140
MOFs	MOF-5	MOF-5	140
	MOF-74-1		
	MOF-74-2	Mg-MOF-74	117
	MOF-74-3		

5.3.2 Prescreening Study

As we have 47 different adsorbents for screening, it would be time-consuming for simulating all of them in the VPSA model. For efficient evaluation, some evaluation criteria described earlier were adopted for prescreening. In this work, the CH_4/N_2 adsorption selectivity and the dimensionless adsorption selection parameter S were selected for the comparison of different adsorbent materials as they represented both adsorption selectivity and working capacity. To obtain the values of these factors, the adsorption equilibrium data would be required first. A single-site Langmuir adsorption isotherm has been selected for CH_4 and N_2 adsorption due to its easy form and good approximation, the equation has been listed in Equation 5.13 in mathematical model section. The isotherm parameters were obtained by fitting experimental adsorption data from literature and summarized in Table 5.2.

Ideal adsorbed solution theory (IAST) of Myers and Prausnitz[40] was applied to investigate the adsorption selectivity of CH_4 over N_2 for different adsorbent materials. In this study, the IAST calculations were performed by a Python package called pyIAST[114]. Since the CH_4 molar fraction varies with both time and bed location during the VPSA operations, IAST adsorption selectivity at different CH_4/N_2 ratios was studied while the total pressure kept constant at 1 bar. The calculation of S requires working capacities and Henry's constants of CH_4 and N_2, as defined in Equation 5.2. The working capacity is defined as the component capacity difference at adsorption and desorption conditions. The total pressure of adsorption and desorption of the VPSA process are assumed to be 1 bar and 0.01 bar, respectively. The CBM feed is assumed to be a binary mixture that contains

30% of CH_4 and 70% of N_2. We also assumed that the N_2 capacity at the desorption step is negligible due to the low molar fraction of N_2 in the product. Hence, the working capacity of CH_4 is calculated by the difference of adsorption capacity of CH_4 at 0.3 bar and 0.01 bar, while the working capacity of N_2 equals to the adsorption capacity of N_2 at 0.7 bar. Henry's constants can be calculated from the product of two Langmuir parameters ($q_{s,i} \times b_i$) that summarized in Table 5.2. The results of IAST predicted CH_4/N_2 adsorption selectivity at various component fractions and S of all screening adsorbents are shown in Table 5.3.

Table 5.2. Adsorption isotherms of CH_4 and N_2 on various adsorbents at 298K.

	CH_4		N_2	
Sample	q_{sat} mol g^{-1}	b bar^{-1}	q_{sat} mol g^{-1}	b bar^{-1}
OMC	1.711	1.448	1.555	0.332
Zeolite 5A	5.081	0.338	4.266	0.55
MOF-177	2.004	0.92	2.061	0.233
MOF-5	0.363	1.324	9.506	0.0335
NAC-600	4.9	0.353	2.9	0.178
NAC-700	5.2	0.306	4.2	0.114
NAC-800	4.9	0.233	3.6	0.098
OAC-0	3.323	0.586	2.45	0.176
OAC-1	2.638	0.865	1.544	0.229

OAC-2	2.173	0.578	1.348	0.204
PF-600 KOH	2.658	1.026	2.077	0.291
PF-800 KOH	2.954	1.03	1.961	0.362
PF-600 $ZnCl_2$	3.301	0.582	3.442	0.116
PF-800 $ZnCl_2$	3.409	0.611	2.51	0.199
NAPC-1-6	1.792	1.277	1.609	0.294
NAPC-2-6	3.366	0.605	3.205	0.166
NAPC-3-6	1.662	0.719	1.269	0.135
Cu-MOF	0.804	1.34	0.580	0.27
Silicalite-1-H	2.606	0.326	1.523	0.154
Silicalite-1-M	2.857	0.302	1.707	0.144
Meso-carbon	1.76	1.368	1.478	0.357
sOMC	2.758	0.475	2.099	0.173
OTS-1-550	2.236	0.964	1.067	0.441
OTS-2-650	3.928	0.71	2.055	0.31
OTS-3-750	5.763	0.27	3.146	0.136
OTSS-3-350	2.286	0.675	1.323	0.256
OTSS-2-450	2.187	0.721	1.468	0.251
OTSS-1-550	3.586	0.702	2.35	0.276
SNMC-1-600	3.325	0.769	1.633	0.38
SNMC-2-600	5.277	0.42	2.863	0.202

SNMC-3-600	5.151	0.294	3.111	0.145
MOF-74-1	10.15	0.15	2.58	0.36
MOF-74-2	7.37	0.18	7.47	0.14
MOF-74-3	9.61	0.15	7.54	0.14
Zeolite 13X	1.739	0.292	0.437	0.597
Zif-8	3.357	0.0090	2.282	0.0465
AAC-1	1.325	1.071	1.039	0.291
AAC-1W	14.146	0.085	1.022	0.235
AAC-2	1.704	0.94	3.479	0.092
AAC-2W	2.442	0.681	3.009	0.405
AAC-3	0.402	0.503	0.657	0.132
SA-1-600	3.294	0.653	1.805	0.291
SA-1-700	4.806	0.46	2.538	0.196
SA-1-800	5.206	0.331	2.908	0.158
SA-2-600	2.281	0.48	2.533	0.132
SA-2-700	4.165	0.406	2.088	0.275
SA-2-800	4.778	0.36	2.771	0.166

Table 5.3. IAST predicted adsorption selectivity at various molar ratios of CH_4/N_2 and the S index of the screening adsorbents.

Sample	5%	10%	15%	20%	30%	50%	S
Cu-MOF	0.379	0.807	1.293	1.848	3.223	7.767	16.421
NAPC-3-6	0.374	0.794	1.266	1.801	3.114	7.381	18.018
OAC-1	0.359	0.767	1.232	1.765	3.092	7.528	15.760
OTS-1-550	0.271	0.583	0.942	1.357	2.409	6.014	8.741
OTSS-3-350	0.254	0.541	0.867	1.238	2.158	5.201	8.376
NAPC-1-6	0.259	0.548	0.872	1.238	2.131	5.013	8.346
PF-600 ZnCl2	0.253	0.533	0.846	1.198	2.052	4.781	8.778
AAC-1	0.255	0.542	0.868	1.235	2.13	5.057	8.226
OAC-2	0.251	0.533	0.851	1.214	2.106	5.032	8.369
OMC	0.257	0.543	0.864	1.227	2.113	4.969	8.080
OTS-2-650	0.249	0.532	0.853	1.222	2.141	5.212	7.910
AAC-2	0.249	0.522	0.822	1.155	1.951	4.427	8.534
SA-1-700	0.246	0.523	0.837	1.194	2.077	4.987	8.139
Meso-carbon	0.247	0.524	0.836	1.189	2.055	4.863	7.541
OAC-0	0.244	0.517	0.823	1.171	2.021	4.782	8.024
PF-600 KOH	0.246	0.521	0.831	1.183	2.046	4.856	7.684
SNMC-1-600	0.239	0.512	0.824	1.182	2.08	5.107	7.180
PF-800 KOH	0.24	0.511	0.819	1.169	2.037	4.903	7.213

OTSS-2-450	0.235	0.5	0.799	1.138	1.973	4.708	7.281
SA-1-600	0.231	0.492	0.788	1.126	1.966	4.749	6.948
PF-800 ZnCl2	0.226	0.478	0.763	1.084	1.872	4.43	6.894
SNMC-2-600	0.212	0.45	0.719	1.025	1.777	4.246	6.142
OTSS-1-550	0.215	0.456	0.728	1.038	1.8	4.297	6.108
SA-1-800	0.205	0.435	0.693	0.987	1.706	4.052	5.868
SA-2-800	0.204	0.433	0.691	0.983	1.701	4.038	5.815
NAPC-2-6	0.202	0.427	0.679	0.962	1.651	3.861	5.700
OTS-3-750	0.198	0.419	0.669	0.951	1.642	3.891	5.536
MOF-177	0.201	0.425	0.675	0.955	1.637	3.813	5.516
Silicalite-1-H	0.197	0.418	0.667	0.948	1.638	3.881	5.467
sOMC	0.194	0.411	0.654	0.929	1.6	3.767	5.266
Silicalite-1-M	0.191	0.404	0.643	0.914	1.578	3.732	5.137
NAC-700	0.184	0.389	0.619	0.878	1.51	3.544	4.865
NAC-600	0.183	0.388	0.619	0.881	1.521	3.606	4.714
AAC-1W	0.183	0.385	0.611	0.864	1.478	3.428	5.004
SNMC-3-600	0.182	0.386	0.615	0.874	1.507	3.56	4.712
NAC-800	0.173	0.365	0.581	0.824	1.416	3.322	4.323
SA-2-600	0.171	0.361	0.573	0.811	1.387	3.228	4.222
SA-2-700	0.166	0.354	0.564	0.802	1.383	3.331	3.804
Zeolite ZIF-8	0.151	0.318	0.506	0.717	1.231	2.881	3.359

AAC-3	0.118	0.248	0.392	0.555	0.946	2.189	2.127
Zeolite 13X	0.124	0.265	0.426	0.61	1.069	2.613	2.040
MOF-74-1	0.098	0.207	0.33	0.47	0.813	1.933	1.332
AAC-2W	0.072	0.153	0.242	0.343	0.587	1.366	0.890
MOF-74-3	0.073	0.154	0.245	0.347	0.595	1.389	0.811
MOF-74-2	0.067	0.141	0.224	0.317	0.543	1.267	0.693
MOF-5	0.051	0.108	0.171	0.242	0.416	0.973	0.682
Zeolite 5A	0.04	0.084	0.134	0.19	0.325	0.757	0.278

The objective of the prescreening work is to select the top 10 adsorbents from 47 adsorbents in respect to the IAST adsorption selectivity and the S index. As we have six adsorption selectivity data at different component molar ratios but only 1 data for S, a corrected ranking score is defined to balance these two factors. The ranking score is defined as the summation of both the rankings of adsorption selectivity at various component molar ratios and the ranking of S, but the S ranking will be multiplied to a weight of 6. The calculation formula of the ranking score is shown below:

$$Ranking\ Score = \sum Individual\ ranking\ of\ IAST\ adsorption\ selectivity + 6 * ranking\ of\ S\ index \quad (5.16)$$

The Adsorbents were ranked based on the ranking score from smallest to largest, the ranking score and sequence can be found in Table 5.4. Adsorbents that ranked the top

10 among the 47 adsorbents were selected for the next screening stage. The adsorption isotherm parameters of CH_4 and N_2 of the top 10 adsorbents are shown in Table 5.5. The results of calculated IAST adsorption selectivity and S of the prescreened adsorbents are shown in Table 5.6.

Table 5.4. Ranking scores of the screening adsorbents based on IAST adsorption selectivity and the S index.

Sample	5%	10%	15%	20%	30%	50%	S	Total	Rank
Cu-MOF	1	1	1	1	1	1	12	18	1
NAPC-3-6	2	2	2	2	2	3	6	19	2
OAC-1	3	3	3	3	3	2	18	35	3
OTS-1-550	4	4	4	4	4	4	30	54	4
OTSS-3-350	8	8	7	6	5	6	42	82	5
NAPC-1-6	5	5	5	5	7	10	54	91	6
PF-600 ZnCl2	9	9	11	11	14	17	24	95	7
AAC-1	7	7	6	7	8	8	60	103	8
OAC-2	10	10	10	10	10	9	48	107	9
OMC	6	6	8	8	9	12	72	121	10
OTS-2-650	12	11	9	9	6	5	84	136	11
AAC-2	11	14	17	18	20	21	36	137	12
SA-1-700	14	13	12	12	12	11	66	140	13

Meso-carbon	13	12	13	13	13	14	96	174	14
OAC-0	16	16	16	16	17	16	78	175	15
PF-600 KOH	15	15	14	14	15	15	90	178	16
SNMC-1-600	18	17	15	15	11	7	114	197	17
PF-800 KOH	17	18	18	17	16	13	108	207	18
OTSS-2-450	19	19	19	19	18	19	102	215	19
SA-1-600	20	20	20	20	19	18	120	237	20
PF-800 ZnCl2	21	21	21	21	21	20	126	251	21
SNMC-2-600	23	23	23	23	23	23	132	270	22
OTSS-1-550	22	22	22	22	22	22	138	270	23
SA-1-800	24	24	24	24	24	24	144	288	24
SA-2-800	25	25	25	25	25	25	150	300	25
NAPC-2-6	26	26	26	26	26	28	156	314	26
OTS-3-750	28	28	28	28	27	26	162	327	27
MOF-177	27	27	27	27	29	29	168	334	28
Silicalite-1-H	29	29	29	29	28	27	174	345	29
sOMC	30	30	30	30	30	30	180	360	30
Silicalite-1-M	31	31	31	31	31	31	186	372	31
NAC-700	32	32	32	33	33	34	198	394	32
NAC-600	33	33	33	32	32	32	204	399	33
AAC-1W	34	35	35	35	35	35	192	401	34

SNMC-3-600	35	34	34	34	34	33	210	414	35
NAC-800	36	36	36	36	36	37	216	433	36
SA-2-600	37	37	37	37	37	38	222	445	37
SA-2-700	38	38	38	38	38	36	228	454	38
Zeolite ZIF-8	39	39	39	39	39	39	234	468	39
AAC-3	41	41	41	41	41	41	240	486	40
Zeolite 13X	40	40	40	40	40	40	246	486	41
MOF-74-1	42	42	42	42	42	42	252	504	42
AAC-2W	44	44	44	44	44	44	258	522	43
MOF-74-3	43	43	43	43	43	43	264	522	44
MOF-74-2	45	45	45	45	45	45	270	540	45
MOF-5	46	46	46	46	46	46	276	552	46
Zeolite 5A	47	47	47	47	47	47	282	564	47

Table 5.5. Adsorption isotherms of CH_4 and N_2 on the top 10 adsorbents at 298K from the prescreening study.

	CH_4		N_2	
Sample	q_{sat} mol g^{-1}	b bar^{-1}	q_{sat} mol g^{-1}	b bar^{-1}
Cu-MOF	0.804	1.34	0.580	0.270
NAPC-3-6	1.66	0.719	1.27	0.135

OAC-1	2.64	0.865	1.54	0.229
OTS-1-550	2.24	0.964	1.07	0.441
OTSS-3-350	2.29	0.675	1.32	0.256
NAPC-1-6	1.79	1.28	1.61	0.294
PF-600 ZnCl2	3.30	0.582	3.44	0.116
AAC-1	1.33	1.07	1.04	0.291
OAC-2	2.17	0.578	1.35	0.204
OMC	1.71	1.45	1.56	0.332

Table 5.6. IAST predicted adsorption selectivity and the S index for the top 10 adsorbents from the prescreening study.

Sample	IAST selectivity						S
	5%	10%	15%	20%	30%	50%	
Cu-MOF	0.379	0.807	1.29	1.85	3.22	7.77	16.4
NAPC-3-6	0.374	0.794	1.27	1.80	3.11	7.38	18.0
OAC-1	0.359	0.767	1.23	1.77	3.09	7.53	15.8
OTS-1-550	0.271	0.583	0.942	1.36	2.41	6.01	8.74
OTSS-3-350	0.254	0.541	0.867	1.24	2.16	5.20	8.38
NAPC-1-6	0.259	0.548	0.872	1.24	2.13	5.01	8.35
PF-600 ZnCl2	0.253	0.533	0.846	1.12	2.05	4.78	8.78

AAC-1	0.255	0.542	0.868	1.24	2.13	5.06	8.23
OAC-2	0.251	0.533	0.851	1.21	2.11	5.03	8.37
OMC	0.257	0.543	0.864	1.23	2.11	4.97	8.08

5.3.3 VPSA Simulation for Adsorbent Screening

For running the VPSA simulation, many inputs would be required, such as adsorbent physical properties, adsorption equilibrium, and kinetic parameters, adsorption bed characteristics, and operating parameters. It is a challenging work to find the values of all these parameters since all we got is the adsorption isotherm data from the literature of screening materials. In current work, since most of the prescreened adsorbents are ACs, we assumed that all the adsorbents have the same physical properties. Also, the separation of N_2/CH_4 is based on the adsorption equilibrium difference between N_2 and CH_4. The effect of adsorption kinetic difference between the adsorbents is therefore assumed to be insignificant. The values of physical properties and adsorption kinetic constants are taken from a VPSA simulation for CBM recovery with a typical AC[127]. The characteristics of the adsorbents and adsorption bed are listed in Table 5.7. Two sets of VPSA simulations are performed for the 10 different adsorbents. Case one is at a regular pressure while case two is at a high pressure during the adsorption step, while all other operating conditions are kept constant. The specific operating conditions can be found in Table 5.8. The CH_4 working capacities of the ten adsorbents calculated in two cases are displayed in Table 5.9.

Table 5.7. Characteristics of adsorbents and adsorption bed of VPSA simulations.

Parameters	Values
Adsorbent	
Average diameter, d_p (cm)	0.240
Bulk density, ρ_b (g/cm3)	0.232
Particle porosity, α	0.350
Adsorption bed	
Length, L (cm)	50
Internal diameter, D_{bi} (cm)	5
Bed porosity, ε_b	0.320
Other parameters	
CH_4 mass transfer coefficient (1/s)	1.28
N_2 mass transfer coefficient (1/s)	3.02
Dispersion coefficient (m^2/s)	$1.60*10^{-5}$

Table 5.8. Operating conditions of VPSA processes in two cases.

Parameters	Case 1	Case 2
Feed pressure, P_{feed} (bar)	1	3
Blowdown pressure, P_{bd} (bar)	1	1
Evacuation pressure, P_{evac} (bar)	0.15	0.15

Feed flow rate, F_{feed} (m^3/h)	2.24	2.24
Length to diameter ratio, L/D	10	10
Cycle time (s)	60	60
PLP duration (s)	5	5
AD duration (s)	20	20
DPE duration (s)	5	5
BD duration (s)	5	5
EVAC duration (s)	20	20
PPE duration (s)	5	5

Table 5.9. CH_4 working capacity of the top 10 adsorbents at two base cases.

Adsorbents	CH_4 working capacity at case 1 (mmol/g)	CH_4 working capacity at case 2 (mmol/g)
Cu-MOF	0.22	0.429
NAPC-3-6	0.283	0.641
OAC-1	0.521	1.132
OTS-1-550	0.48	1.017
OTSS-3-350	0.37	0.849
NAPC-1-6	0.474	0.936
PF-600 ZnCl2	0.472	1.116
AAC-1	0.308	0.636

OAC-2	0.309	0.731
OMC	0.494	0.944

The product purity, recovery, and productivity of VPSA processes with different adsorbents are compared in two cases in Table 5.10. The purity and recovery of the adsorbents are also marked in the plot in Figure 5.2. Obviously, all the performance indicators improved from case 1 to case 2, because the higher adsorption pressure gives a larger adsorption capacity of CH_4. Among the 10 adsorbents, Cu-MOF and NAPC-3-6 exhibit much higher product purity but relatively low product recovery compared with other adsorbents. Meanwhile, these two adsorbents also have the highest IAST adsorption selectivity and the highest S parameter among all the adsorbents, while the working capacities are relatively low. In terms of recovery and productivity, OAC-1 showed the best performance for both. OAC-1 also has the third-highest product purity among all the adsorbents (only lower than Cu-MOF and NAPC-3-6). From Table 5.6 and Table 5.9, we can observe that OAC-1 has the largest working capacity, and its S parameter and IAST selectivity are only lower than Cu-MOF and NAPC-3-6. The results strongly indicate that the S parameter and IAST selectivity might be relevant to product purity, and working capacity might be relevant to product recovery. To verify this conjecture, we studied the effect of working capacity on product recovery, as well as the effect of S and IAST selectivity on product purity.

The trend of product recovery with working capacity is shown in Figure 5.3. For both regular and high-pressure cases, adsorbents with larger working capacity also exhibit

higher product recovery in the VPSA process, which is consistent with previous observation. The effect of S and IAST selectivity on product purity is also studied, which is shown in Figure 5.4 and Figure 5.5, respectively. For this study, the value of IAST selectivity is taken as the average for all different component compositions in Table 5.6. The product purity ranking of the adsorbents seems unpredictable with the given S ranking or the IAST selectivity ranking. However, the top three adsorbents from S ranking and selectivity ranking still have higher product purity than the other seven adsorbents. As a result, we can conclude that high adsorption selectivity is still a requirement to obtain ultra-high product purity, though it might not be sufficient.

As for the screening, we have compared the purity, recovery, and productivity of VPSA processes at two base cases with the 10 prescreened adsorbents. But as for now, we haven't discussed anything about the energy consumption of the process, which is indeed an important factor to be considered in real industrial operations. It is therefore interesting to know how much energy each adsorbent cost while meeting the specified purity and recovery target. Due to the complexity of optimization, we only selected three adsorbents that exhibited the best process performance at the two base cases to the next stage. Cu-MOF and NAPC-3-6 were selected due to their ultra-high product purity. OAC-1 is the other candidate that has the largest product recovery and productivity among the samples, while the product purity is only lower than Cu-MOF and NAPC-3-6.

Table 5.10. Process indicators of VPSA process with the top 10 adsorbents in two cases.

	Case 1			Case 2		
Sample	Purity (%)	Recovery (%)	Productivity (mol CH_4/kg/h)	Purity (%)	Recovery (%)	Productivity (mol CH_4/kg/h)
Cu-MOF	89.0	42.2	4.53	95.3	80.3	8.61
NAPC-3-6	91.3	56.1	5.50	95.3	86.7	9.29
OAC-1	86.1	76.7	8.22	90.9	96.4	10.3
OTS-1-550	82.0	74.2	7.95	87.9	96.2	10.3
OTSS-3-350	83.9	63.1	6.76	90.1	91.2	9.77
NAPC-1-6	80.4	74.0	7.93	86.6	93.5	10.0
PF-600 ZnCl2	82.3	73.9	7.91	88.4	92.7	9.93
AAC-1	83.3	54.7	5.86	90.8	85.3	9.14
OAC-2	84.9	55.5	5.95	91.4	87.8	9.41
OMC	79.4	75.9	8.13	85.5	93.6	10.0

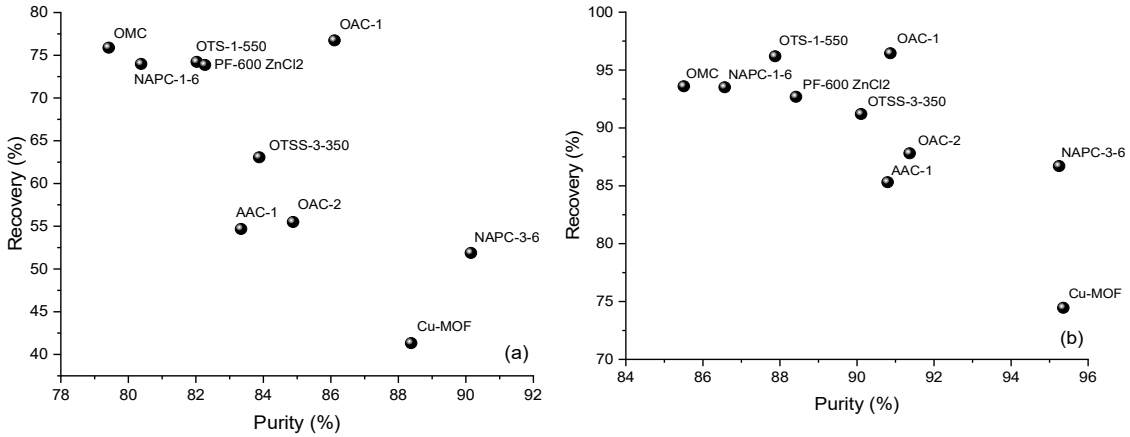

Figure 5.2. Product purity and recovery of the VPSA process at (a) case 1 and (b) case 2 for 10 different adsorbents.

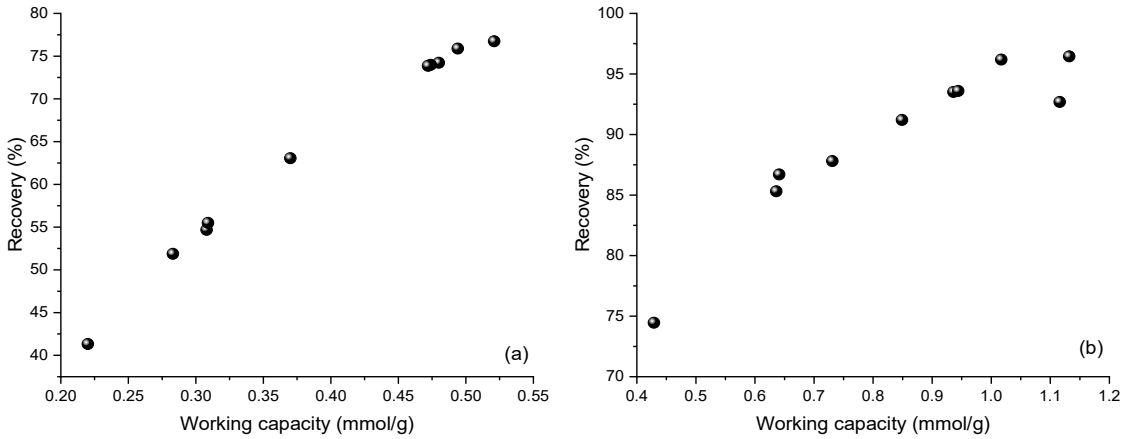

Figure 5.3. Effect of working capacity on the product recovery of the VPSA process at (a) case 1 and (b) case 2 for 10 different adsorbents.

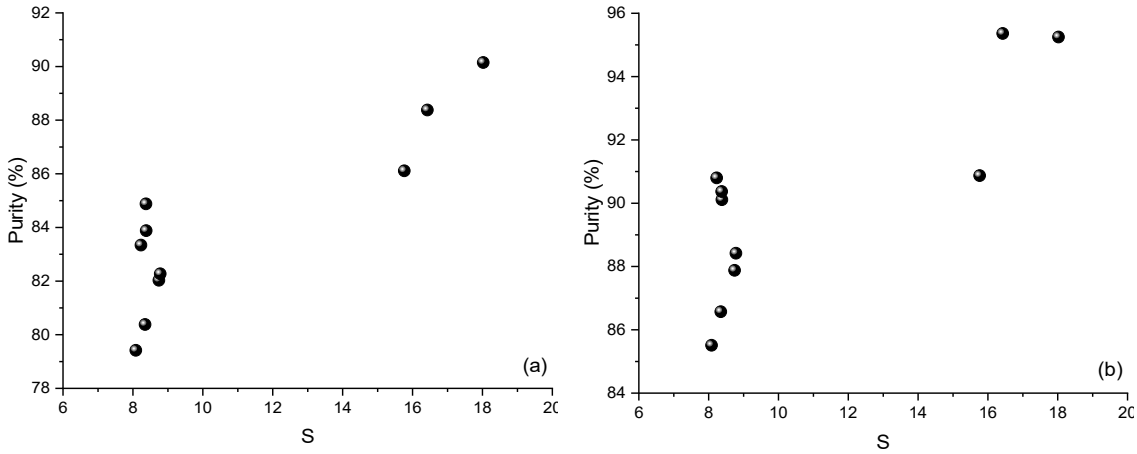

Figure 5.4. Effect of S parameter on the product purity of the VPSA process at (a) case 1 and (b) case 2 for 10 different adsorbents.

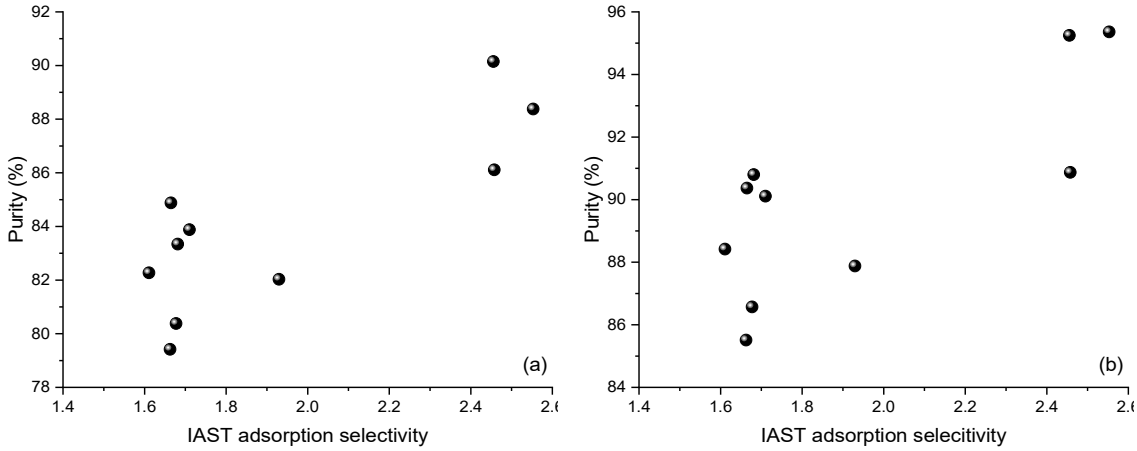

Figure 5.5. Effect of IAST selectivity on the product purity of the VPSA process at (a) case 1 and (b) case 2 for 10 different adsorbents.

5.3.4 Process Optimization

Before the optimization, we firstly studied the effects of several essential process variables on performance indicators, including product purity, recovery, productivity, and

energy consumption, to help determine the range constraints of the variables. Each variable was altered individually, while other conditions were kept constant. The effect of evacuation pressure on the performance indicators is shown in Figure 5.6. Obviously, for all the three adsorbents, product purity, recovery, and productivity can be improved by evacuating at a lower pressure. This is reasonable as the working capacity of CH_4 is very sensitive to the evacuation pressure. Meanwhile, the deeper vacuum would require more energy consumption of the VPSA process. As for the effect of feed flow rate shown in Figure 5.7, increasing the feed flow rate tends to increase product purity and productivity but decreases the recovery. The energy cost also increases with the feed flow rate, but the energy consumption difference at the lower flow rate range is not that significant. The other factor that has been studied is the adsorption pressure, which is shown in Figure 5.8. As we expected, all of the product purity, recovery, and productivity increases with the adsorption pressure due to the increasing working capacity of CH_4. But this increasing effect tends to slow down at a certain pressure and begin to stabilize. The energy consumption decreases initially while increasing the adsorption pressure because of the dramatically increased productivity, but then start to increase due to the higher cost of compression work. The product purity and recovery of the three adsorbents at the varying conditions still exhibited similar characteristics shown at the two base cases, where Cu-MOF and NAPC-3-6 have higher product purity, and OAC-1 has the highest product recovery and productivity.

The dynamic optimization problem is then formulated to investigate the optimal evacuation pressure, feed flow rate, and adsorption pressure at two different targets of

product purity and recovery of the VPSA process for CBM recovery. The objective for the optimization is to minimize the energy consumption for target 1 (95% purity and 90% recovery) or target 2 (98% purity and 90% recovery) by varying the above variables. The cycle time and operating durations are kept constant during the optimization due to the need for synchronization of multi-bed configuration. Based on the information above, the optimization is formulated below:

$$\text{min. energy consumption}$$

$$\text{s. t.}$$

$$\text{Product purity } \geq 95\% \text{ for target 1 or } 98\% \text{ for target 2}$$

$$\text{Product recovery } \geq 90\%$$

$$0.01 \text{ bar} \leq P_{evac} \leq 0.3 \text{ bar} \tag{5.16}$$

$$1 \text{ bar} \leq P_{adsorption} \leq 8 \text{ bar}$$

$$0.01\ kmol/h \leq F_{feed} \leq 0.3\ kmol/h$$

$$\text{General bed model equations}$$

The optimization problem is solved using gPROMS/gOPT tool. The solution of the optimization problem requires both a DAE solver that integrates the DAEs to determine the objective function and constraints and a nonlinear programming problem (NLP) solver to optimize the decision variables. In this study, the SRQPD algorithm is adopted to solve the NLP for the optimization, which implements a reduced sequential quadratic programming algorithm. Given the initial estimates, DASOLV and SRQPD will be

repeatedly called until the objective function converges to the optimization tolerance (e.g. 0.001).

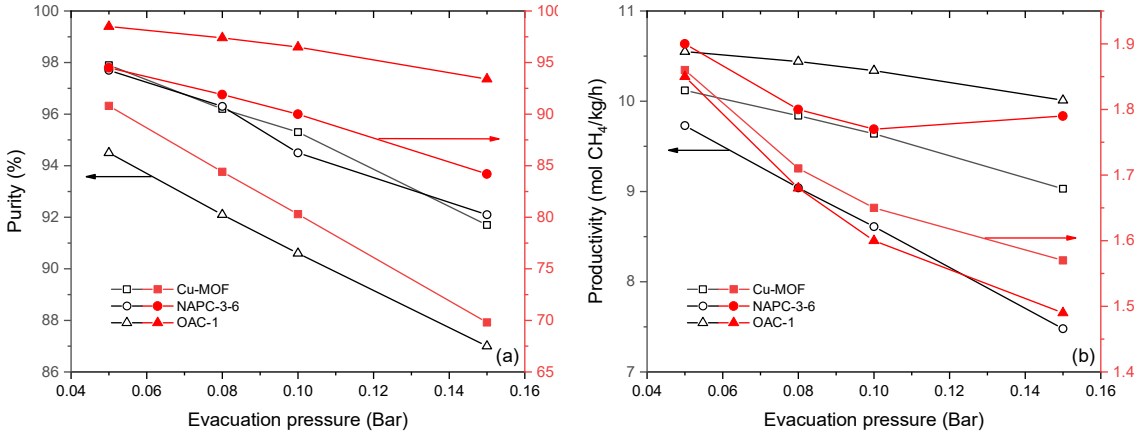

Figure 5.6. Effect of evacuation pressure on (a) product purity and recovery, (b) productivity and energy consumption for the top three adsorbents (Other conditions were kept at case 2).

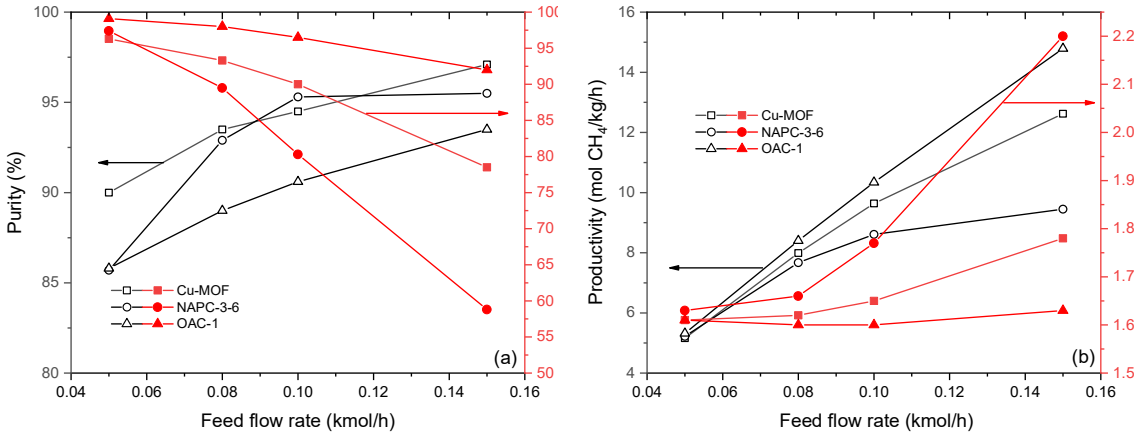

Figure 5.7. Effect of feed flow rate on (a) product purity and recovery, (b) productivity and energy consumption for the top three adsorbents (Other conditions were kept at case 2).

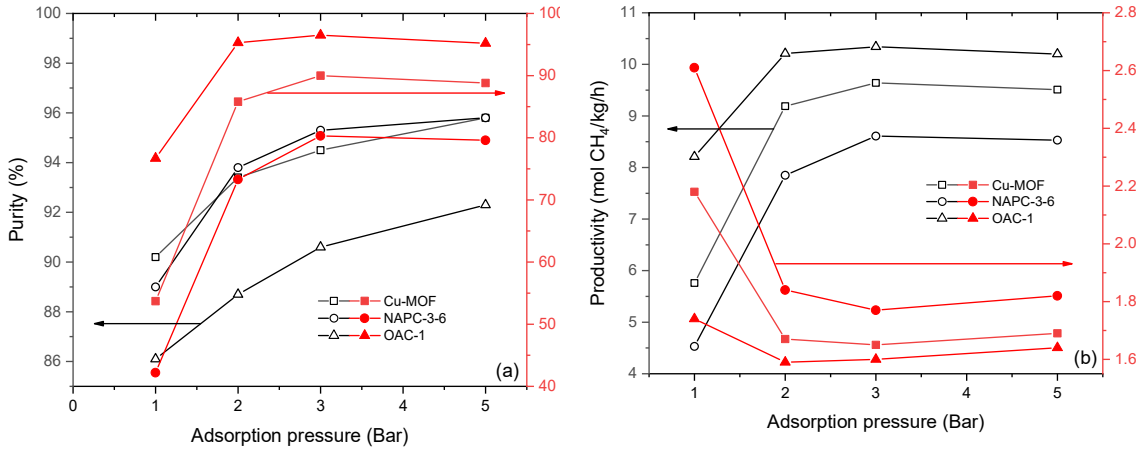

Figure 5.8. Effect of adsorption pressure on (a) product purity and recovery, (b) productivity and energy consumption for the top three adsorbents (Other conditions were kept at case 2).

The optimization results for target 1 (95% purity and 90% recovery) and target 2 (98% purity and 90% recovery) are summarized in Table 5.11 and Table 5.12, respectively. It is observed that all three adsorbents could achieve target 1 and target 2 at the optimized conditions. The adsorbent that consumed the lowest energy at the specified purity and recovery target was identified as the best adsorbent for such conditions. The results showed that OAC-1 consumed the lowest energy of 1.64 MJ/kg CH_4 at the lower purity target (target 1), and NAPC-3-6 had the lowest energy cost of 1.80 MJ/kg CH_4 at the higher purity target (target 2). The results indicated that the energy consumption was highly dependent on the evacuation pressure, as OAC-1 and NAPC-3-6 also exhibited the highest evacuation pressure at target 1 and target 2, respectively. Another finding is that the CH_4 productivity of OAC-1 is much higher than the other two adsorbents at both optimization cases. The

high CH_4 productivity should be correlated with the high feed flow rate at the specified purity and recovery condition, which is contributed to the large working capacity of OAC-1. As a result, the adsorbent selection will depend on the production scale and purity requirement of the application. OAC-1 is the best candidate for a large scale CH_4 production with a regular purity grade. NAPC-3-6 is a promising adsorbent for a small scale CH_4 production with a high purity requirement. Cu-MOF is also more suitable for high purity applications, but it is costlier than NAPC-3-6 due to its poor CH_4 working capacity.

Table 5.11. Optimized operating conditions and process performance of the top three adsorbents for target 1.

	Cu-MOF	NAPC-3-6	OAC-1
Evacuation pressure (bar)	0.0870	0.0953	0.102
Feed flow rate (kmol/h)	0.0761	0.0838	0.161
Adsorption pressure (bar)	3.41	3.14	3.80
CH_4 Purity (%)	95.0	95.0	95.0
CH_4 Recovery (%)	90.0	90.0	90.7
CH_4 Productivity (mol CH_4/kg/h)	7.20	6.81	15.6
Energy consumption (MJ/kg CH_4)	1.72	1.66	1.64

Table 5.12. Optimized operating conditions and process performance of the top three adsorbents for target 2.

	Cu-MOF	NAPC-3-6	OAC-1
Evacuation pressure (bar)	0.0631	0.0723	0.0544
Feed flow rate (kmol/h)	0.0945	0.110	0.214
Adsorption pressure (bar)	4.07	4.21	5.65
CH_4 Purity (%)	98.0	98.0	98.0
CH_4 Recovery (%)	90.0	90.0	90.5
CH_4 Productivity (mol CH_4/kg/h)	9.07	10.6	20.8
Energy consumption (MJ/kg CH_4)	1.85	1.80	1.93

5.4 Conclusion

A new screening method was developed and used to evaluate 47 adsorbents for their potential applications for CBM recovery. The adsorbents were firstly prescreened based on their CH_4/N_2 IAST adsorption selectivity and a composite S index that incorporating both adsorption selectivity and working capacity. A weighted ranking score that balances both factors was developed, and the adsorbents were ranked from smallest to largest score.

The top 10 adsorbents from prescreening were applied in a simplified VPSA simulation developed in gPROMs platform for efficient screening at two base cases. The CBM recovery performance was analyzed by comparing the product purity, recovery, and

productivity of VPSA processes with 10 adsorbents. It was observed that Cu-MOF and NAPC-3-6 exhibited the highest product purity, and OAC-1 showed the highest product recovery and productivity at the two base cases. We also found that the working capacity and adsorption selectivity have some correlations with the process performance. Adsorbents with larger working capacity exhibited higher product recovery in the VPSA process at the same operating conditions. Similarly, the top three adsorbents that exhibited the highest product purity have the highest adsorption selectivity as well. However, there was no apparent relationship between adsorption selectivity and product purity for the other seven adsorbents. It is therefore concluded that high adsorption selectivity is a requirement to obtain high product purity, but it might not be sufficient.

Three adsorbents that showed the best process performance at the two base cases were selected for the next process optimization stage. The optimization is targeted to minimize the energy consumption of the VPSA process while meeting the product purity and recovery requirement. The decision variables include the evacuation pressure, feed flow rate, and adsorption pressure. The sensitivity of each variable on the process performance was studied through a parametric study. We found that each operating parameter has a significant effect on the performance of the VPSA process. The optimization results show that OAC-1 is the best adsorbent for a low purity requirement, and NAPC-3-6 is the better choice for high purity requirements. Besides, OAC-1 has much larger CH_4 productivity than the other two adsorbents. The adsorbent selection will, therefore, depend on the production scale and purity requirement of the actual application. With the optimization results of three adsorbents, we also obtained the following optimal

conditions for CBM recovery. For producing CH_4 with 95% purity, the optimal adsorption and evacuation pressure appears to lie in the range of 3~4 bar and 0.08~0.1 bar, respectively. For producing CH_4 with 98% purity, the corresponding values ranged in 4~6 bar and 0.05~0.08 bar, respectively.

Notations:

A: Cross-sectional area of the adsorption bed (m^2)

b_i: Equilibrium parameter of Langmuir isotherm for component i (1/bar)

C_i: Molar concentration of component i in the gas phase ($kmol/m^3$)

d_b: Diameter of adsorption bed (m)

d_p: Diameter of adsorbent particle (m)

D: Mass axial dispersion coefficient (m^2/s)

E_c: Energy consumption of the compressor (kJ/s)

E_v: Energy consumption of the vacuum pump (kJ/s)

F^{in}: Mass flow rate at the entrance of the adsorption bed (kg/s)

k_i: Mass transfer coefficient of i compound (1/s)

L: Bed length (m)

Mw_i: Molecular weight of component i (kg/kmol)

$\dot{n_{in}}$: Molar flow rate of the feed stream of compressor/ vacuum pump (kmol/s)

P: Pressure (bar)

P_{in}: Pressure at the feed end of the adsorption bed (bar)

P_i: Partial pressure of i compound (bar)

$P_{in,c}$: Pressure of inlet stream of the compressor (bar)

$P_{out,c}$: Pressure of leaving stream of the compressor (bar)

$P_{in,v}$: Pressure of inlet stream of the vacuum pump (bar)

$P_{out,v}$: Pressure of leaving stream of the vacuum pump (bar)

q_i: Specific amount of component i adsorbed on solid phase (kmol/kg)

q_i^*: Amount of i compound adsorbed at equilibrium (kmol/kg)

$q_{s,i}$: Maximal adsorbed equilibrium amount for component i (kmol/kg)

t: Time (s)

T: Gas temperature (K)

T_{in}: Temperature of the feed stream of the compressor/ vacuum pump (K)

v: Superficial velocity of the gas phase (m/s)

w_i^{in}: Mass fraction of component i at the entrance of the adsorption bed

z: Bed axial distance (m)

Greek letters:

ρ: Mass density of gas phase (kg/m^3)

ρ_b: Density of the bed (kg/m^3)

ρ_p: Density of the adsorbent particle (kg/m^3)

ε_b: Porosity of the adsorbent bed

ε_{tot}: Total void fraction, including intra- and inter- particle void space

γ: Specific heat capacity ratio

η_c, η_v: Isentropic efficiency of compressor and vacuum pump

Chapter 6: Oxygen Pumping Characteristics of $YBaCo_4O_{7+\delta}$ for Solar Thermochemical Cycles

6.1 Introduction

The two-step metal oxide solar thermochemical cycle has received considerable attention as a promising technology for renewable fuel production[155,156]. The method is environmentally friendly compared with conventional fuel production approaches. It utilizes heat (e.g. solar-derived) to split water or carbon dioxide to produce fuels and chemical feedstock, such as hydrogen and carbon monoxide. Since the conversion from thermal to chemical energy is direct, the theoretical efficiency is high[157]. The generic two-step thermochemical cycle uses a redox active metal oxide, which repeatedly reduces and re-oxidizes during the redox cycle (equation 6.1-6.3). Many suitable redox active materials have been investigated[158–163]. Among them, cerium oxide has the best, albeit far from ideal performance[164–166].

$$\frac{1}{\delta}MO_x \rightarrow \frac{1}{\delta}MO_{x-\delta} + \frac{1}{2}O_2 \tag{6.1}$$

$$\frac{1}{\delta}MO_{x-\delta} + H_2O \rightarrow \frac{1}{\delta}MO_x + H_2 \tag{6.2}$$

$$\frac{1}{\delta}MO_{x-\delta} + CO_2 \rightarrow \frac{1}{\delta}MO_x + CO \tag{6.3}$$

Equation (6.1) describes the metal oxide reduction step, and Equations (6.2) and (6.3) illustrate water and carbon dioxide splitting steps, respectively, which is also re-oxidization of the metal oxide. During reduction, the metal oxide reduces at high temperature and low

p_{O2}, releasing oxygen. The reduced oxide is then re-oxidized to split water or carbon dioxide to generate hydrogen or carbon monoxide, respectively, during the splitting step.

A key technical challenge in the practical implementation of the two-step cycles is to create and maintain a low p_{O2} during the thermal reduction step. At a given temperature, a low p_{O2} increases the reduction extent of the redox material. To reduce the p_{O2}, current approaches include purging the reactor with an inert sweep gas, and vacuum pumping. However, both approaches are energy-intensive and require large capital cost[26,167–169]. A thermochemical oxygen pump is a novel method for oxygen removal which is both efficient and economically attractive compared with the conventional methods[170]. It uses another redox material to adsorb the oxygen released during the thermal reduction step. Unlike the redox material for splitting, the redox material for oxygen pumping reduces at much lower temperatures and higher p_{O2} and can create low p_{O2} with lower temperature re-oxidation. Theoretically, for a reactor that contains both the pumping material and redox material for splitting, no mechanical pump or sweeping gas would be required to lower p_{O2} during the thermal reduction step. A previous calculation has shown that the energy cost for such a system can be significantly smaller than the corresponding energy cost of a mechanical vacuum pump[167,171] and with appropriate heat integration no additional external energy inputs.

Pumping materials have been studied experimentally in previous works, such as CoO[167], $SrFeO_{3-\delta}$[172]. A key challenge of thermochemical pumping is the relatively high temperatures for oxygen uptake (400-600 °C) and regeneration (700-950 °C), which in turn increases the theoretical work of pumping. This process relies on the bulk transport of

oxygen, which typically limits oxygen uptake rates. To address these challenges, and minimize the pumping heat (e.g. per mole oxygen atom), Ermanoski and Stechel have proposed a chemisorption-based approach[173]. In this concept, oxygen capture occurs on a sorbent surface (via chemisorption), at or around ambient temperatures, with no expected bulk uptake. Desorption (activation) of the sorbent occurs at ~350 °C.

As a step toward the goal of ambient-temperature, kinetically fast pumping, we evaluated the $YBaCo_4O_{7+\delta}$ (YBC114) compound for a pumping application, due to its known oxygen uptake and release behavior. YBC114 was firstly reported by Valldor et al. in 2002[174], and has been studied for several potential applications such as oxygen storage material[175], oxygen sensor[176], and robust catalysts for H_2O_2 oxidation[177] and soot oxidation[178]. Previous studies have shown the compound is capable of capturing oxygen in a narrow temperature range of 200-325 °C (albeit higher than ambient) and release it over 400 °C[179–181], which are both much lower than other redox-active metal oxides explored for thermochemical pumping[53,182]. Initial air separation experiments also proved the material was efficient for oxygen removal in a medium-temperature range[183].

To evaluate and address kinetic limitations common in oxygen ion conductors, we prepared YBC114 in two different particle sizes. We studied YBC114 oxygen uptake and release for combinations of two parameters, temperatures and p_{O2}, in a thermogravimetric analyzer (TGA). To evaluate its *in-situ* oxygen pumping performance, we built a simple benchtop vacuum system—effectively a very basic oxygen vacuum pump.

In the following sections, we will first describe the experimental methodology in Section 6.2, followed by results and discussion in Section 6.3. A conclusion is then drawn in the last section.

6.2 Experimental

The experimental section begins with the synthesis methods for YBC114 in two different particle sizes. It will then illustrate the procedures of a couple of experiments to study both physical and chemical properties related to thermochemical pumping, including structural materials' characterization, TGA measurement, and the vacuum test.

6.2.1 Synthesis of YBC114

To study the effect of particle size on the uptake performance, we prepared the sorbent materials with two methods, so their particle size varied. YBC114 with larger particle size is denoted as YBC114-L. YBC114 with smaller particle size is denoted as YBC114-S. The procedures of each method are illustrated below.

The YBC114-L sample was prepared by a solid-state reaction method. Firstly, stoichiometric amounts of Y_2O_3 (Alfa Aesar, 99.995%), $BaCO_3$ (Alfa Aesar, 99.95%), and Co_3O_4 (Aldrich Chemistry, 99.5%) were mixed and milled with agate milling balls. The mixture was then sintered at 1000 °C in the air for 10 hours. After sintering, the powder was cooled back to room temperature rapidly and milled again.

The YBC114-S sample was synthesized with an EDTA sol-gel method. Firstly, stoichiometric amounts of Y_2O_3 (Alfa Aesar, 99.995%), $Ba(NO_3)_2$ (Acros Organics, 99+%), $Co(NO_3)_2 \cdot 6H_2O$ (Sigma-Aldrich, 99+%) were mixed and dissolved in excess HNO_3 solution (Acros Organics, 68-70%), followed by the addition of EDTA (Honeywell, 99+%). The molar ratio of EDTA and all the metal ions (M^+) is 1.5:1. The solution was then neutralized with $NH_3 \cdot H_2O$ (Thomas Scientific, 28% in water) until the PH of the solution was about 8. The solution was dried at a heating plate with stirring until it self-burned to fluffy ashes. The ashes were transferred to a muffle furnace and calcined at 1000 °C in the air for 10 hours. After sintering, the resulting samples were cooled back to room temperature rapidly and milled.

6.2.2 Structural Materials' Characterization

A powder X-ray diffractometry (PXRD, Siemens D-5000) with CuKα radiation was used to examine the structure of the material. The microstructure of YBC114 samples was observed by scanning electron microscopy (SEM, XL30 Environmental FEG) with a spot size of 3. A Micromeritics 3-Flex apparatus was used to measure the textural properties of the samples. Prior to the measurement, the samples were degassed at 400 °C for 12 hours under vacuum. The Brunauer-Emmett-Teller (BET) surface area was calculated with nitrogen adsorption isotherms at 77K in the relative pressure range from 0.05 to 0.3. The total pore volume was determined with a non-local density function theory model (NLDFT).

6.2.3 Thermogravimetric Measurement

A thermogravimetric analyzer (TGA, Netzsch TG 209 F1 Libra) was used to investigate the oxygen uptake and release characteristics. The mass of the sample for each measurement was 50-80 mg. All the samples were fully reduced at 400 °C in 20 ml/min nitrogen flow for 2 hours before the measurements. In the first experiment, the sample was heated from ambient temperature to 1000 °C with a heating rate of 1 °C/min in 20 ml/min airflow (Praxair, Ultra zero). The slow ramping rate was selected to guarantee the mass change at each temperature represented thermal equilibrium as close as possible. In the second set of experiments, temperature swing, varying both the uptake temperature and p_{O2}, was used to measure oxygen uptake. The uptake temperatures varied from 150 °C to 325 °C, fixing the recovery temperature at 400 °C. The measurements were performed in a mixed gas flow of oxygen (Matheson, UHP) and nitrogen (Matheson, UHP) with a total flow rate of 20 ml/min. The p_{O2} was controlled by adjusting the ratio of oxygen and nitrogen in the mixed gas flow. Finally, the cyclability of YBC114 samples was studied by recording the mass change of the materials for several temperature swing uptake-release cycles. The uptake and release temperatures for the cycling set of experiments are 275 °C and 400 °C, respectively, with p_{O2} fixed at 1 bar.

6.2.4 Evacuation Test

Evacuation tests were performed to investigate the oxygen pumping performance of the sorbents. Figure 6.1 shows the evacuation test setup. The YBC114 samples were

placed in a 10 ml alumina combustion boat (CoorsTek) and inserted into the middle of a tube furnace (Lindberg 59545). One end of the tube was connected to a pressure gauge (MKS), a vacuum pump (Edwards), and the oxygen source (Matheson, 99.999%), while the other end of the tube was mainly for inserting and removing the sample boat. The total volume of the vacuum chamber is estimated to be 0.35 L.

A leak test was first performed to ensure the vacuum level of the chamber can be well maintained. To recover the oxygen stored in the sorbents and remove gases in the system, the chamber was first evacuated at 400 °C for 1 hour. Oxygen was then introduced to the chamber to reach an atmospheric p_{O2}. The introduction and evacuation can be repeated several times to adjust the oxygen pressure until it equilibrates at 21.2 kPa. The chamber was then slowly cooled to 275 °C for oxygen pumping and the pressure of the system was recorded. A background experiment with the same operating procedures, without the sample boat, was also performed to remove the temperature effect on pressure.

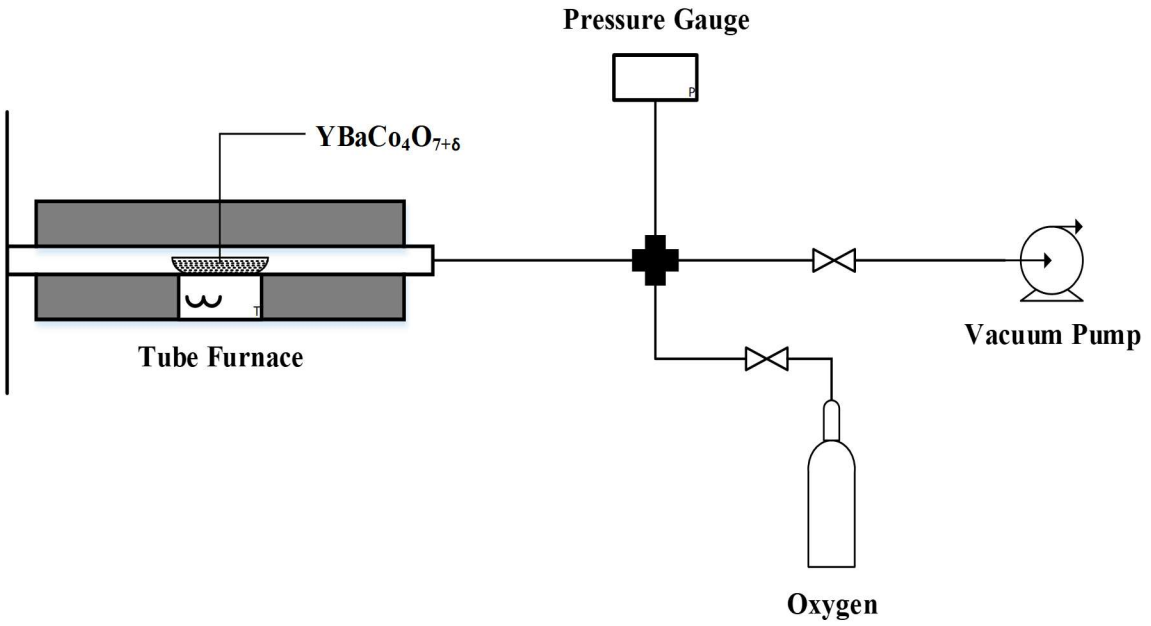

Figure 6.1. Schematic diagram of the evacuation test setup.

6.3 Results and Discussion

Figure 6.2 shows the PXRD patterns of YBC114-S and YBC114-L. It can be observed that the major peaks of YBC114-S are narrower than those for YBC114-L, indicating a smaller particle size. The average crystallite size was determined by applying Scherrer's equation[112]. The calculated crystallite size for YBC114-S and YBC114-L is 32.2 nm and 136.5 nm, respectively. Figure 6.3 shows SEM images of YBC114-S and YBC114-L. The photographs confirm that the particle size of YBC114-S is much smaller than YBC114-L. In addition, YBC114-S exhibits round-shaped pores between the particles, which can be beneficial for faster diffusion.

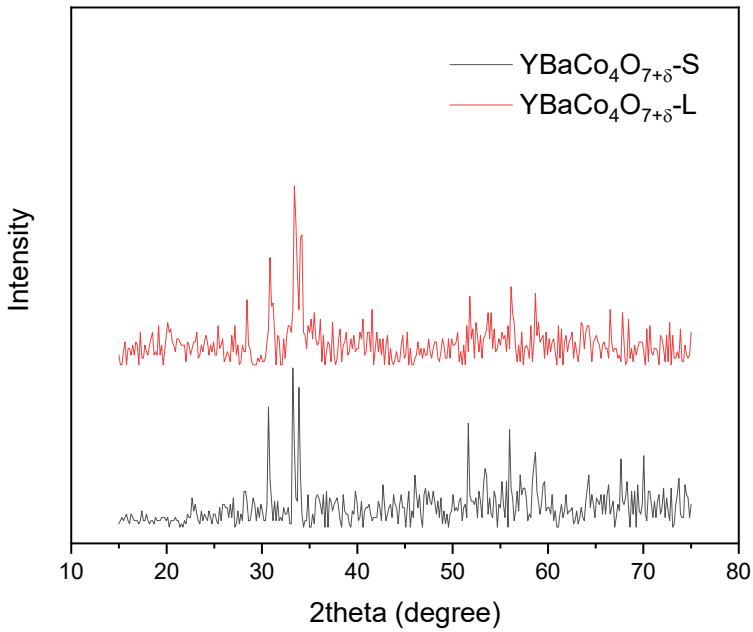

Figure 6.2. PXRD patterns of YBC114-S and YBC114-L.

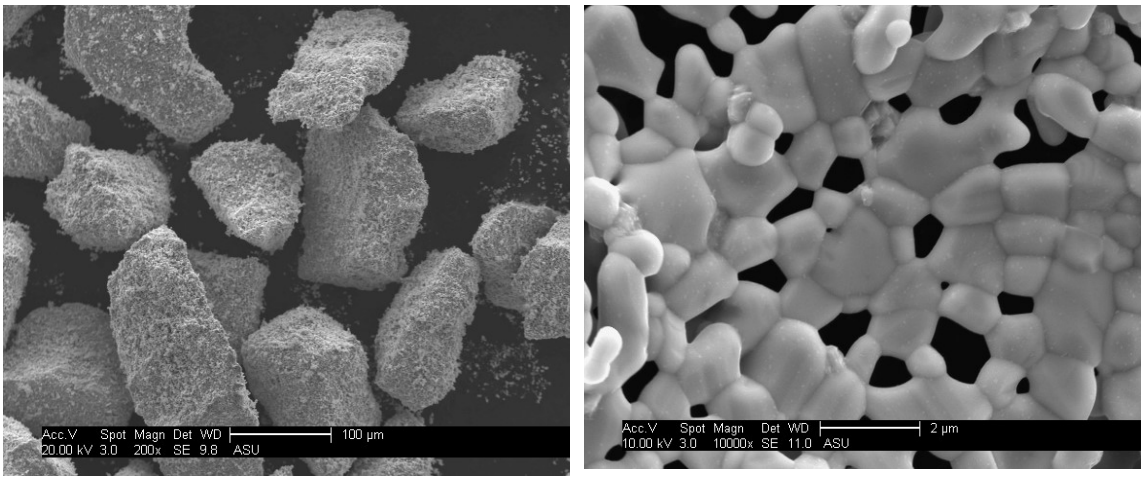

Figure 6.3. SEM images of (a) YBC114-L and (b) YBC114-S.

Figure 6.4 displays nitrogen adsorption and desorption isotherms of YBC114-S and YBC114-L. Both showed type III isotherms, which is typical for nonporous or macroporous materials. In addition, the nitrogen adsorption capacity of YBC114-S is much larger than YBC114-L. Table 6.1 summarizes the BET surface area and total pore volume calculated from the isotherms. Both samples showed relatively small surface areas and pore volumes compared with typical porous adsorbents. However, the values of both properties of YBC114-S were significantly larger than for YBC114-L, indicating more macropores between the particles. The results were also consistent with the observations from SEM images.

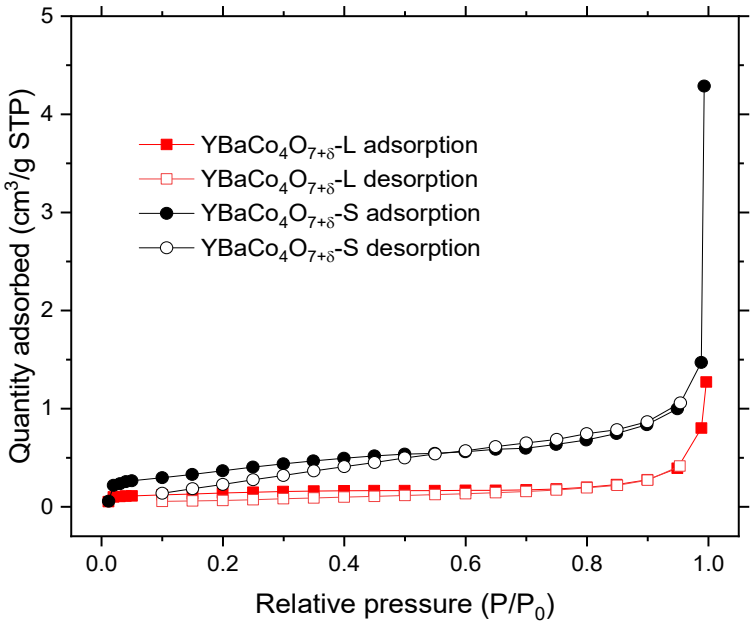

Figure 6.4. N_2 adsorption and desorption isotherm of YBC114-L and YBC114-S at 77 K.

Table 6.1. Porosity properties of YBC114-L and YBC114-S.

Samples	BET surface area (m^2/g)	Total pore volume (cm^3/g)
YBC114-L	0.480	0.0039
YBC114-S	2.42	0.018

Figure 6.5 shows the oxygen uptake and release behavior of YBC114 samples when slowly heating from ambient temperature to 1000 °C. The oxygen uptake is represented by the oxygen nonstoichiometry (δ), the number of oxygen atoms per unit cell of YBC114 in excess of seven. The relationship between δ and the mass change percentage measured from TGA can be determined with the following equation:

$$\delta = \frac{\frac{Mass\ change\ \%}{M_O}}{\frac{100\ \%}{M_{YBaCo_4O_{7+\delta}}}} \tag{6.4}$$

where M_O is the atomic mass of oxygen atom, and $M_{YBaCo_4O_{7+\delta}}$ is the molecular weight of YBC114. It can be seen that both YBC114 samples capture oxygen in the temperature ranges of 200-350 °C or 650-800 °C. The high uptake temperature range is normal oxygen uptake similar to other redox materials. YBC114 is unique, however, for its ability to capture oxygen at a lower temperature range, which could reduce the energy demand for oxygen pumping relative to other materials. We should also note that YBC114-S is able to capture both more oxygen and at a faster rate than YBC114-L for both temperature ranges, which could be attributed to the effect of particle size.

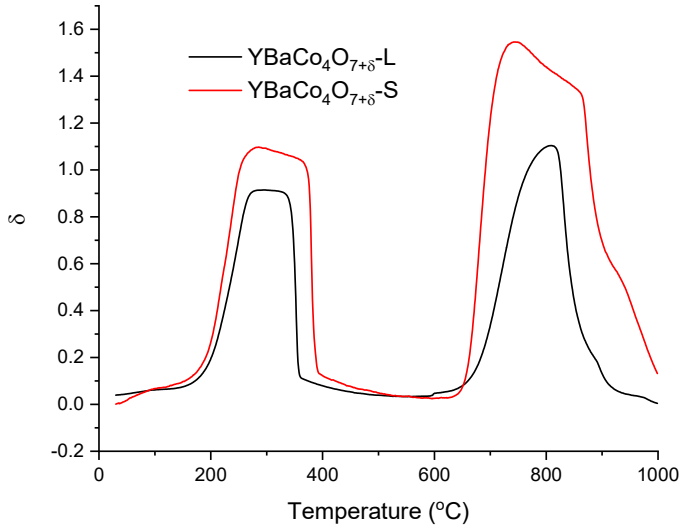

Figure 6.5. Temperature screening from ambient temperature to 1000 °C of YBC114 samples with airflow.

The oxygen uptake of YBC114-L and YBC114-S at various temperatures were then analyzed and displayed as δ in Figure 6.6. It should be noted that all the uptake data were measured after 1 hour of oxygen sorption. Therefore, the displayed δ values depend on both uptake equilibrium and kinetics. With the increase of temperature, the oxygen uptake initially increased and then decreased, which showed a similar trend with a previous study on the temperature effect of oxygen capacities of YBC114[183]. The optimal temperature for the highest oxygen uptake for 1 hour of oxygen sorption is between 250 °C and 275 °C. The unique peak feature can be explained by the structure change of YBC114 that takes place at the transition point at 300 °C[184]. Also found is that YBC114-S generally exhibits

a larger oxygen uptake than YBC114-L, especially at low to medium p_{O2}. The largest δ value obtained from YBC114-L and YBC114-S is 1.14 and 1.2, respectively.

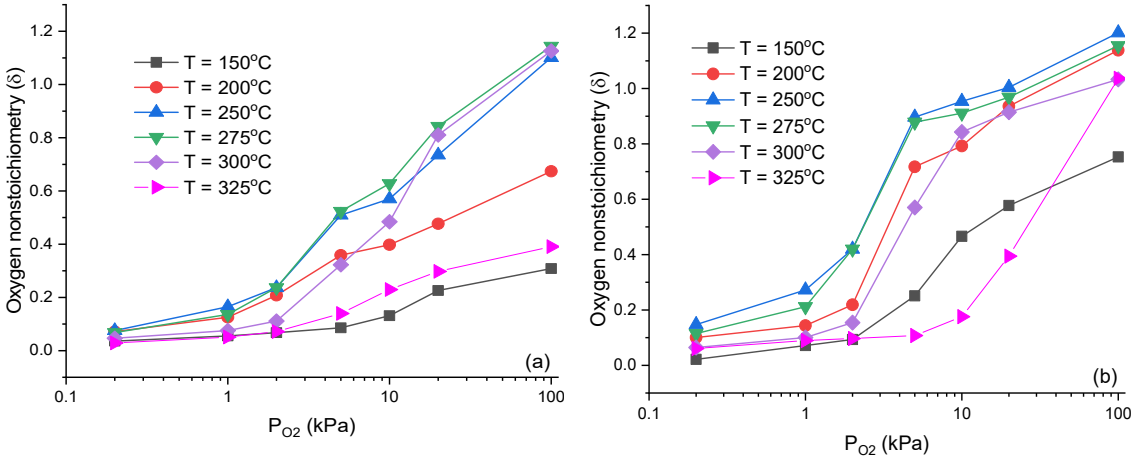

Figure 6.6. Oxygen uptake after 1 hour of oxygen sorption of (a) YBC114-L and (b) YBC114-S at varying temperatures and p_{O2}s.

The oxygen uptake rate of YBC114-L and YBC114-S are also compared at varying temperatures or varying oxygen partial pressure, as shown in Figure 6.7 and Figure 6.8, respectively. When varying the uptake temperatures, the p_{O2} was kept at 21 kPa (using airflow). While studying the effect of p_{O2} on the uptake kinetics, the uptake temperature was held fixed at 275 °C. As the slope of the uptake curves suggested, the initial uptake rate of oxygen increased with both p_{O2} and temperature. However, at higher temperatures, the uptake rate was then limited due to decreased uptake capacity. As a result, both samples exhibited the best oxygen uptake performance in a temperature range from 250 °C to

300 °C. Furthermore, it is evident as well as expected that YBC114-S showed faster oxygen uptake than YBC114-L, for all cases measured.

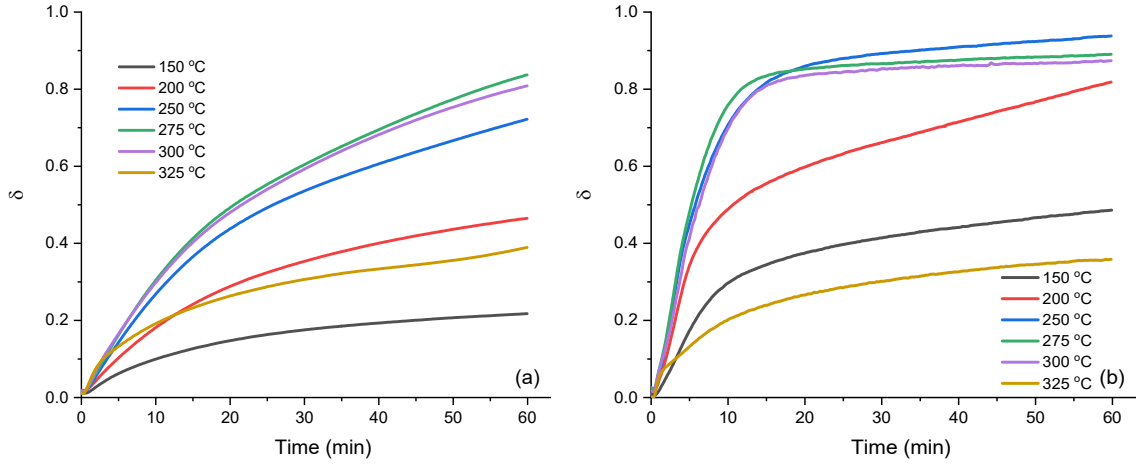

Figure 6.7. Oxygen uptake kinetics of (a) YBC114-L and (b) YBC114-S at varying temperatures.

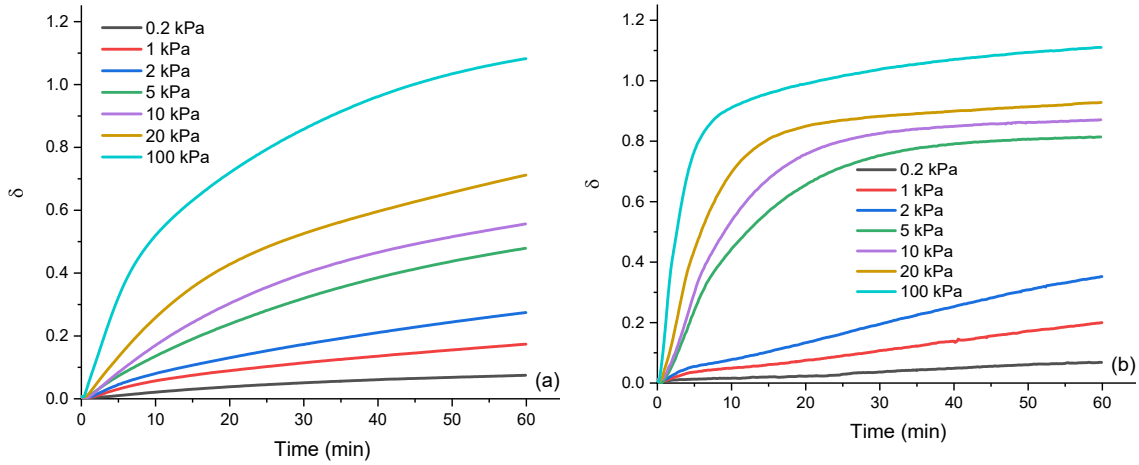

Figure 6.8. Oxygen uptake kinetics of (a) YBC114-L and (b) YBC114-S at varying partial pressures.

To further study the uptake kinetics, a pseudo-first order kinetic model was applied. The equation of the pseudo-first order kinetic model is:

$$\frac{d\delta}{dt} = k(\delta^* - \delta) \tag{6.5}$$

where k is the rate constant of pseudo-first order sorption, δ^* represents the oxygen loading at sorption equilibrium. The values of k and δ^* are determined by nonlinear regressions of the experimental kinetic data, as shown in Table 6.2. The kinetic data involved for the investigation are at varying temperatures while p_{O2} is held at 20 kPa. We found that the values of δ^* at various temperatures follow the trend of oxygen uptake shown in Figure 6.5. We also observe that the rate constant of YBC114-S is larger than YBC114-L at all the temperatures, indicating a faster uptake rate. It also shows that the rate constant increases with temperature.

Table 6.2. Kinetic model parameters of YBC114-L and YBC114-S at various temperatures and p_{O2} = 20 kPa.

Temperature (°C)	k*10^2 (1/min)		δ^*	
	YBC114-L	YBC114-S	YBC114-L	YBC114-S
150	1.42	2.37	0.43	0.78
200	2.12	3.35	0.70	1.06
250	3.05	5.22	0.94	1.19
275	3.41	5.77	1.00	1.15
300	4.29	6.40	0.89	1.09
325	4.67	6.99	0.45	0.41

Based on the correlation between the sorption rate constant and temperature, we calculated the activation energy by the integrated Arrhenius equation:

$$lnk = -\frac{E_a}{RT} + lnA \tag{6.6}$$

where k is the rate constant, E_a is the activation energy, A is the pre-exponential factor. Both parameters can be determined by plotting lnk vs 1/T with a linear fit. We observe that the correlation factor, R-Square, is over 0.99 for the linear fitting of the Arrhenius equation on both sorbents, as shown in Figure 6.9. The results reveal that the sorption process is in accordance with pseudo-first order kinetic model. The activation energy is then calculated

by the slope of the fitting line. The obtained activation energy for oxygen sorption of YBC114-L and YBC114-S is 14.9 and 13.5 kJ/mol O, respectively. The results confirm that YBC114-S has a faster oxygen sorption rate.

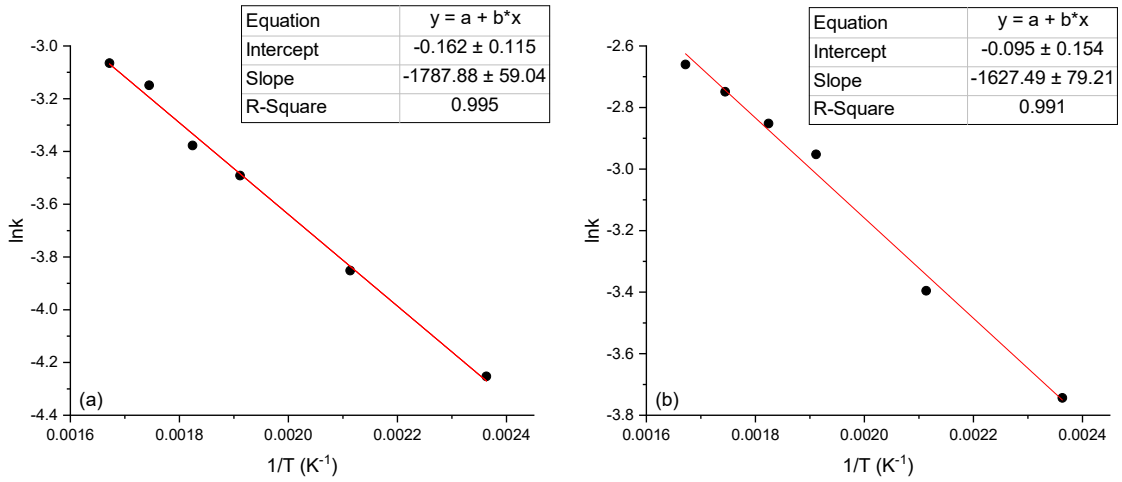

Figure 6.9. The linear fitting of Arrhenius equation for (a) YBC114-L and (b) YBC114-S.

The oxygen release properties of YBC114 samples were also studied at different temperatures, as shown in Figure 6.10. It's observed that both YBC114 samples release oxygen efficiently at 375 °C and 400 °C, and the recovery rate of YBC114-S was slightly faster as expected. Nevertheless, the release rate became much slower at 350 °C. It is, therefore, preferable to maintain the recovery temperature over 375 °C.

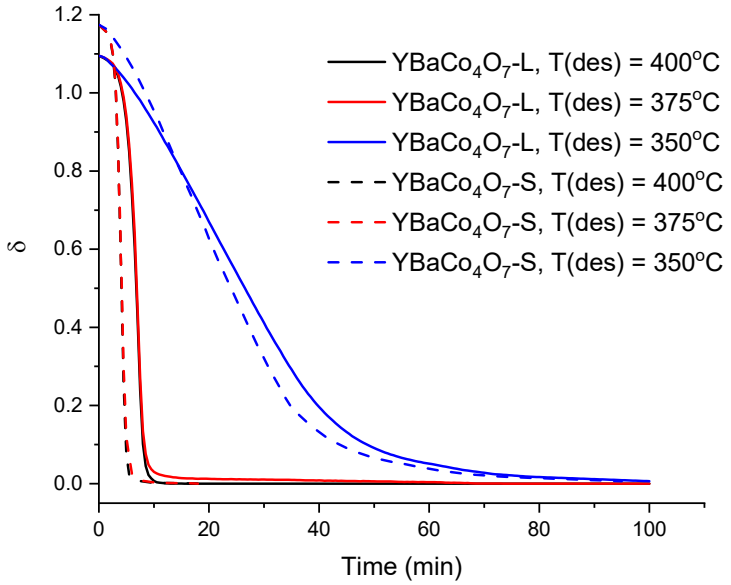

Figure 6.10. Oxygen release profiles of YBC114-L and YBC114-S at different temperatures.

Finally, the cyclability of YBC114 samples was studied by recording the mass change of the materials in several temperature swing uptake-release cycles. The uptake and release temperatures for this set of experiments were 275 °C and 400 °C, respectively, as shown in Figure 6.11 (b). The p_{O2} was held fixed at 1 bar. The mass change percentage of YBC114-S and YBC114-L during the cyclic process was recorded, illustrated in Figure 6.11 (a). Both YBC114-S and YBC114-L showed good cyclability. No significant oxygen uptake capacity or kinetics differences were observed between the two samples, as both the uptake temperature and p_{O2} are set at the optimal conditions for maximized oxygen uptake. The oxygen uptake loss for YBC114-L and YBC114-S after 10 cycles was around 6.0% and 3.7%, respectively. We also note that YBC114-S was fully oxidized at the start,

while YBC114-L was only partially oxidized. The oxidation occurred during the cooling process from sintering temperature down to ambient temperature. Since both samples were prepared with the same cooling process, the oxidation difference also indicates that YBC114-S exhibits a faster oxygen uptake rate than that of YBC114-L.

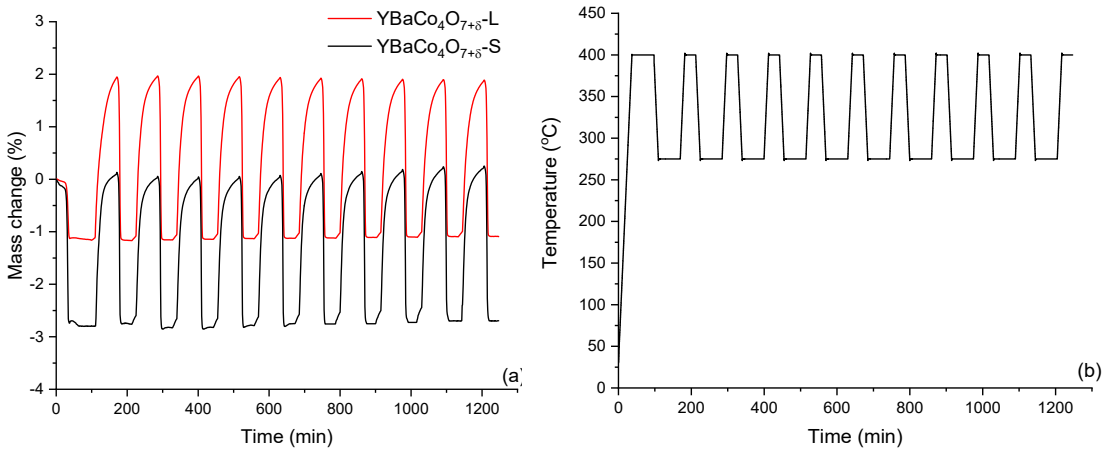

Figure 6.11. Temperature swing uptake-release cycles with recordings of (a) mass change percentage and (b) temperature profile.

The oxygen pumping performance of YBC114 samples was determined by the evacuation test introduced above. The chamber pressure was recorded during cooling from 400 °C to 275 °C, which was controlled in a tube furnace, so the oxygen in the chamber can be captured by the sorbents. The initial oxygen pressure was set at 21.2 kPa to represent the p_{O2} of air. In the first set of experiments, the pumping performance of YBC114-L and YBC114-S were compared with a sorbent mass of 2 grams and 5 grams, respectively, as shown in Figure 6.12. As is evident in the figure, both YBC114-S cases pump oxygen

faster and deeper than YBC114-L, consistent with the TGA measurements. It is also apparent that 2g of sorbents are insufficient to capture enough oxygen to establish low p_{O2}. The final achieved vacuum levels for the case of 5g of YBC114-L and of YBC114-S are ~1 kPa and ~0.5 kPa, respectively.

The pumping performance of YBC114-S was then investigated further at various conditions by altering the cooling rate or sorbent mass. Figure 6.13 shows a comparison between pressure (red curves) and temperature (black curves) profiles during the cooling experiments. As the results suggest, the pressure drop rate or oxygen uptake rate increases with the sorbent mass, especially for the initial stage. The oxygen working capacity also increases with sorbent mass below 5 grams. However, when the sorbent mass exceeds 5 grams, additional sorbent shows no significant performance gains in the final vacuum level as the oxygen pumping at this stage is limited by the low p_{O2}. As for the effect of cooling rate, faster cooling accelerates oxygen uptake significantly, especially at the beginning of the cooling process because it brings the sorbents to the optimal uptake temperature faster. Nevertheless, the final obtained vacuum level does not appear to depend on the cooling rate.

To calculate the effective oxygen working capacity of YBC114-S, the total amount of oxygen in the system must first be determined. For this purpose, the test chamber without the sample boat at 21.2 kPa and 400 °C was cooled down to ambient temperature and held for 48 hours to ensure all oxygen inside the chamber equilibrated to ambient temperature. The estimated total moles of oxygen, assuming ideal gas, is ~2.25 mmol. Removing the background pressure drop, which stems from the temperature effect, is necessary to reflect

the pressure drop that exclusively stems from the oxygen uptake. The background pressure is linear with the equivalent gas temperature, again assuming ideal gas. With known test volume and total gas moles, the equivalent ideal gas temperature can be inferred with each background pressure point at the corresponding furnace temperature, as shown in Table 6.3. The amount of captured oxygen can then be inferred with the following equation:

$$n_{O_2,adsorbed} = \frac{V}{R}\left(\frac{P_i}{\overline{T_i}} - \frac{P_f}{\overline{T_f}}\right) \tag{6.7}$$

where V is the test volume of the vacuum chamber, R the gas constant, P_i and P_f the initial and final background pressures, $\overline{T_i}$ and $\overline{T_f}$ the initial and final equivalent ideal gas temperature.

The oxygen working capacity was then calculated for the case of 5 grams of YBC114-S, as it is the lowest sorbent mass to produce a good vacuum level. The calculated total oxygen amount captured for this case is ~2.19 mmol, which is 97.3% of the initial oxygen in the chamber. The working oxygen capacity per gram of YBC114-S is 0.44 mmol/g, or 0.12 if converted to δ. The calculated δ in the vacuum test is a little lower than the corresponding δ at the final pressure level (533 Pa) measured from TGA experiments, as δ is 0.11 and 0.21 at p_{O2}s of 200 Pa and 1000 Pa, respectively. This discrepancy is probably due to the small oxygen amount captured by the sorbents at 400 °C, which implies that a small portion of the oxygen is already captured at the beginning of the evacuation test. Nonetheless, the results from the evacuation tests showed excellent oxygen pumping performance and generally matched the results from the TGA experiments.

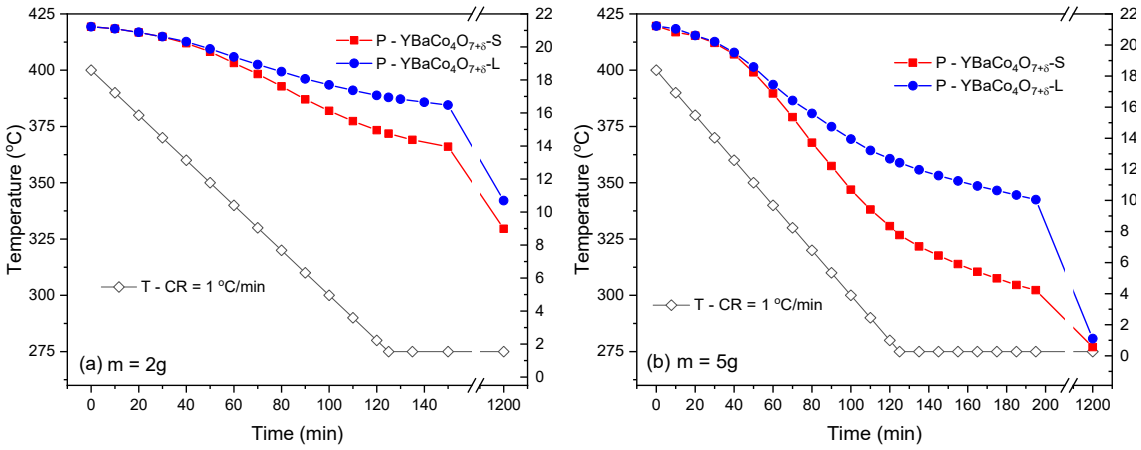

Figure 6.12. Pumping performance of YBC114-L and YBC114-S with (a) 2 grams of sorbent, and (b) 5 grams of sorbent.

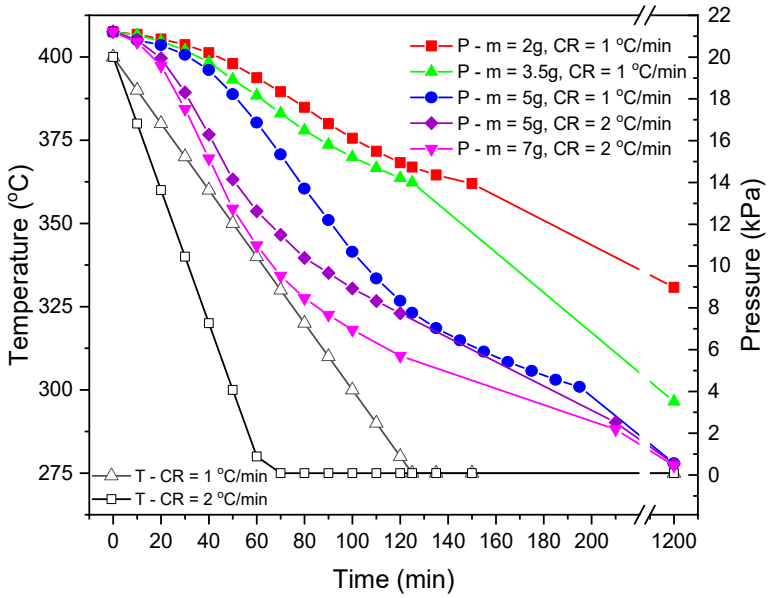

Figure 6.13. Pumping performance of YBC114-S with various sorbent mass and cooling rates.

Table 6.3. Background pressures and equivalent ideal gas temperatures at varying furnace temperatures.

Furnace Temperature (°C or K in parenthesis)	Pressure (kPa)	Equivalent ideal gas Temperature (K)
400 (673.15)	21.22	397.09
390 (663.15)	21.16	395.84
380 (653.15)	21.05	393.85
370 (643.15)	20.94	391.85
360 (633.15)	20.82	389.61
350 (623.15)	20.70	387.36
340 (613.15)	20.58	385.12
330 (603.15)	20.48	383.12
320 (593.15)	20.36	380.88
310 (583.15)	20.24	378.63
300 (573.15)	20.12	376.39
290 (563.15)	20.00	374.14
280 (553.15)	19.85	371.40
275 (548.15)	19.80	370.40

6.4 Conclusion

Performance measurements on YBC114 were conducted to assess its potential as an oxygen pumping material for solar thermochemical cycles, due to its unique medium temperature oxygen storage properties. YBC114 were prepared in different particle sizes with a solid reaction method and an EDTA sol-gel method, denoted as YBC114-S and YBC114-L, respectively. Both XRD, SEM, and BET analysis confirmed that the particle size of YBC114-S is smaller than YBC114-L. The uptake and release properties of YBC114 samples were measured at varying temperatures and p_{O2}s. Both YBC114-S and YBC114-L exhibit the best oxygen uptake performance in a temperature range from 250 °C to 300 °C and recovered oxygen efficiently at temperatures >375 °C. A key finding is that YBC114-S shows better oxygen uptake performance than YBC114-L in terms of both oxygen uptake capacity and kinetics, albeit not unexpectedly. The uptake capacity and kinetics of YBC114-S and YBC114-L are, nevertheless, similar at uptake-favorable conditions, e.g., with an uptake temperature of 275 °C and p_{O2} of 1 bar. However, when the uptake temperature was out of the optimal range or p_{O2} became lower, YBC114-S performed much better than YBC114-L for both oxygen uptake capacity and kinetics. As an oxygen pumping material, the material must have excellent pumping characteristics at different p_{O2} levels, as the p_{O2} decreases continuously during the uptake process. In addition, both YBC114-L and YBC114-S showed good cyclability during temperature swing uptake-release cycles. As a result, the oxygen capacity loss for YBC114-L and YBC114-S after 10 cycles was around 6.0% and 3.7%, respectively.

To investigate the oxygen pumping performance of YBC114 samples, a small vacuum setup was used. Comparisons for the pumping performance of YBC114-L and YBC114-S were made for two cases with different amounts of sorbents. For both cases, YBC114-S pumped oxygen faster and deeper than YBC114-L. The final achieved vacuum levels for the case of 5 grams of YBC114-L and YBC114-S were ~1 kPa and 0.5 kPa, respectively. The effect of sorbent mass and cooling rate were further investigated with YBC114-S. The comparison showed that the oxygen uptake accelerates by increasing either sorbent mass or cooling rate. The total pressure drop also increased with the sorbent mass initially but approached saturation with no significant improvements for >5 grams of sorbent. The oxygen working capacity of YBC114-S was inferred with 5 grams of sorbent, which implied that 97.3% of the initial oxygen amount was captured by the active material. The inferred working oxygen capacity per gram of YBC114-S is 0.44 mmol/g, or 0.12 if converted to δ. The results were consistent with measurements from TGA experiments.

Overall, we conclude that YBC114 is a promising material for oxygen pumping, having a large oxygen uptake capacity in a suitable temperature range. Nevertheless, challenges remain; for example, the kinetic rate of oxygen uptake still needs to be faster and ideally the uptake temperature still lower. The current study has demonstrated that by reducing the particle size of the material, the uptake kinetics improves significantly. Research in material development would be required to advance this concept to practice.

Chapter 7: Conclusions and Recommendations

7.1 Summary and Conclusions

To meet the growing energy needs of the world, while minimizing the environmental impact caused by CO_2 emissions, we need to reduce the CO_2 emission with carbon capture and explore renewable energy sources. Adsorption is a promising separation technique that could be applied to capture CO_2 from the flue gas or remove impurities from renewable energy sources. Conventional adsorbents do not meet the rigorous properties that are required to make adsorption economically feasible for the industry. To meet these demands novel adsorbents with large adsorption capacity, high selectivity, excellent stability, and good reusability should be synthesized. With this goal in mind, we developed various novel adsorbents and applied them for various industrial applications depending on their adsorption properties. A rigorous mathematical model was also developed to evaluate the process performance of the novel adsorbents. The model has been validated with several reported works on PSA processes. The process simulations allow us to investigate essential adsorbent design parameters such as the effect of adsorbent preparation conditions and operating parameters on the process performance; understand the correlation between process performance indicators and adsorption characteristics; design and optimize the operating parameters to minimize the energy cost.

The first novel adsorbent discussed in the dissertation is a ceramic sorbent, LSCF1991, for high-temperature oxygen production. One unique advantage of LSCF1991 is that it has an infinite selectivity of oxygen over nitrogen or other non-oxygen species,

which overcome the difficulty to generate high-purity oxygen. As LSCF1991 adsorbs oxygen by chemical adsorption, the adsorption capacity, kinetics, and energy consumption of the process should be the main objectives to optimize. From the TGA measurements at a temperature range from 500 °C to 800 °C, the optimal adsorption temperature of LSCF1991 is 500 °C. At this temperature, the oxygen adsorption capacity of LSCF1991 is approximately 0.6 mmol/g, and the overall mass transfer coefficient is 0.523 s^{-1} at an oxygen partial pressure of 0.21 kPa. A PSA process with LSCF1991 for cyclic oxygen adsorption and recovery was then simulated and optimized to identify the actual process performance of LSCF1991. The objective of the optimization is to maximize the oxygen recovery and productivity while meeting a target oxygen purity of 98%. Under the optimized conditions, oxygen purity of 98.21%, recovery of 74.05%, and productivity of 1.22 mmol/s/kg were achieved. The obtained purity, recovery, and productivity values are much higher than the reported corresponding values of the PSA process with conventional zeolites. Additionally, the energy consumption of the high-temperature air separation process with LSCF1991 is 171.8 kWh/ton O_2, which is about 23% lower than the cryogenic distillation method (223 kWh/ton O_2) and about 33% lower than the conventional PSA process (255 kWh/ton O_2).

In the next case study, we synthesized a group of nanostructured zeolite NaX (NZ) for post-combustion CO_2 capture. Compared with the commercial microsized zeolite (MZ), NZ has several advantages. Firstly, NZ has a higher surface area than MZ due to the smaller particle size, thus provide more active sites for CO_2 adsorption and increases the CO_2 adsorption capacity. The nanostructure is also beneficial for intracrystalline diffusion as

the diffusion time decreases with the crystal dimension of zeolites. Furthermore, the shape of N_2 isotherm at 77K (combination of type I and type IV), the high external surface area (more than twice of MZ) and high mesopore volume (around six times of MZ) of NZ sample confirmed the existence of the hierarchical porous structure, which could also contribute to the enhanced mass transfer of CO_2 adsorption. The effects of sintering temperature and binder ratio have been investigated to optimize the synthesis conditions. As a result, the NZ sample prepared at the optimized condition has a CO_2 capacity of 5.56 mmol/g and an IAST selectivity of 50% CO_2/50% N_2 of 620 at 298 K and 100 kPa, higher than commercial MZ and most other CO_2 adsorbents. A systematic and rigorous model was employed to a two-bed six-step VPSA system with NZ and MZ, where the key optimization objective is to minimize the energy consumption of the process while achieving a product purity of 95% and recovery of 90%, for separating 85% N_2, 15% CO_2 feed. The optimization results indicated NZ saved around 30% energy over the MZ for CO_2 capture and recovery while also achieving a higher CO_2 purity, recovery, and productivity.

The mathematical model developed could also be used to screen novel adsorbents for applying to the PSA process. The presented study screened 47 novel adsorbents for their potential for CBM recovery. However, the screening method is general enough to be applied to any PSA process. To be an excellent screening tool for novel adsorbents, the screening method should be robust, comprehensive, while also being efficient to implement. To achieve this target a prescreening step was added to significantly reduce the total screening time, while the rigorous PSA simulation ensured the quality and accuracy of the screening. The screening results showed that OAC-1 consumed the lowest energy of 1.64

MJ/kg CH_4 for target 1 (95% purity and 90% recovery), and NAPC-3-6 has the lowest energy cost of 1.8 MJ/kg CH_4 for target 2 (98% purity and 90% recovery). The results indicated that the energy consumption was highly dependent on the evacuation pressure because OAC-1 and NAPC-3-6 also exhibited the highest evacuation pressure at target 1 and target 2. Another finding is that the CH_4 productivity of OAC-1 is approximately twice the other two adsorbents at both optimization cases, which can be contributed to the large working capacity of CH_4. We can thus conclude that adsorbent selection depends on the production scale and purity requirement of the actual application. For example, OAC-1 is most suitable for producing large-scale and low-purity (95%) methane, NAPC-3-6 is the better choice for higher purity requirements. During the screening study, we also have some interesting findings regarding the correlations between adsorption characteristics and PSA process performance indicators. For example, product recovery has a linear dependence on the working capacity of adsorbents, while high adsorption selectivity is a prerequisite for high product purity.

Finally, a new medium-temperature oxygen adsorbent material, YBC114, was synthesized. Performance measurements on YBC114 were conducted to assess its potential as an oxygen pumping material to facilitate solar thermochemical fuel production. YBC114 was prepared with a solid reaction method (YBC114-L) and an EDTA sol-gel method (YBC114-S), respectively, to investigate the effect of particle size. From the TGA measurement, we found both samples exhibited the best oxygen uptake performance in a temperature range from 250 °C to 300 °C and recovered oxygen efficiently at temperature >375 °C. The YBC114 samples also showed excellent cyclability during a

TSA cycle. The oxygen capacity loss of YBC114-L and YBC114-S after 10 cycles was around 6.0% and 3.7%, respectively. A key finding is that YBC114-S shows better oxygen uptake performance than YBC114-L in terms of both oxygen uptake capacity and kinetics. A vacuum system was built to investigate the actual oxygen pumping performance of YBC114 samples. We found that YBC114-S pumped oxygen both faster and deeper than YBC114-L. The final achieved vacuum levels for the case of 5 grams of YBC114-L and YBC114-S were ~1 kPa and 0.5 kPa, respectively. The inferred working oxygen capacity per gram of YBC114-S in the vacuum system is 0.44 mmol/g, or 0.12 if converted to δ, which implied that 97.3% of the initial oxygen amount was adsorbed by the active material. The current study has demonstrated that by reducing the particle size of the material, the uptake kinetics improves significantly. Research in material development would be required to advance this concept to practice.

7.2 Recommendations for Future Work

In this dissertation, we studied two groups of adsorbents. The first group is porous materials, such as zeolites and ACs, which are utilized in CO_2 capture and methane recovery. The other group is ceramic materials, such as LSCF1991 and YBC114, which are applied for oxygen production and oxygen pumping, respectively. For both zeolite NaX and YBC114, we synthesized the nanostructured or nanosized particles to study the effect of particle size on their adsorption performance. The current study has demonstrated that the reduction of crystalline size or particle size improved the adsorption performance of the material significantly, especially for the adsorption kinetics. While the advanced

adsorption properties might be sufficient for physical adsorption, for chemical sorption (such as oxygen pumping) research in further material development would be required to make the process economically feasible. One possible solution is to develop a stable 2D adsorbent material with a high adsorption capacity and fast adsorption kinetics. Various synthesis methods including sol-gel, the mesoporous template could be employed to prepare 2D adsorbents. In the preparation methods, the raw precursors are dissolved in a suitable solvent, and the reaction is carried out in closed systems (control the thermodynamics and kinetics under pressure) for sufficient time to construct the 2D sheets.

For the modeling portion, the focus was on the evaluation of the novel adsorbents and the optimization of the PSA process at a defined bed structure and connections. For a more general case that could be used for industry, complex PSA operations with multiple interconnected beds and complicated operating procedures are often applied to maximize product purity, recovery, and productivity. Future studies should be carried out with different bed designs, so that the effect of the bed volume, the number of beds, and interconnections between the beds can be accounted for. In addition, the optimization routine could also be improved. Dynamic optimization usually spent half of the CPU time for sensitivity calculation. Due to the PSA inherent feature of achieving cyclic steady state (CSS), the optimization of the PSA process can be effectively employed without the need of calculating model sensitivities throughout the whole operation duration. The objective function and constraints sensitivities with respect to time are only required at the final time of the operation. Therefore, we can calculate the sensitivity information only at the end of the operation to accelerate the PSA optimization procedure.

REFERENCES

1. Boden, T. A., Marland, G. & Andres, R. J. Global, Regional, and National Fossil-Fuel CO2 Emissions. *Carbon Dioxide Inf. Anal. Center, Oak Ridge Natl. Lab. U.S. Dep. Energy, Oak Ridge, Tenn., U.S.A.* **53**, 1689–1699 (2015).

2. *Total Energy Annual Data - U.S. Energy Information Administration (EIA)*.

3. BP. *CO2 emissions – BP Statistical Review of World Energy 2019*. (2019).

4. Chen, X. Y., Vinh-Thang, H., Ramirez, A. A., Rodrigue, D. & Kaliaguine, S. Membrane gas separation technologies for biogas upgrading. *RSC Advances* **5**, 24399–24448 (2015).

5. Venna, S. R. & Carreon, M. A. Amino-functionalized SAPO-34 membranes for CO2/CH4 and CO2/N2 separation. *Langmuir* **27**, 2888–2894 (2011).

6. Bauer, F., Persson, T., Hulteberg, C. & Tamm, D. Biogas upgrading - technology overview, comparison and perspectives for the future. *Biofuels, Bioprod. Biorefining* **7**, 499–511 (2013).

7. Mondal, M. K., Balsora, H. K. & Varshney, P. Progress and trends in CO2 capture/separation technologies: A review. *Energy* **46**, 431–441 (2012).

8. Ruthven, D. M. (Douglas M. *Principles of adsorption and adsorption processes*. (Wiley, 1984).

9. Sircar, S. Pressure Swing Adsorption. *Ind. Eng. Chem. Res.* **41**, 1389–1392 (2002).

10. Sircar, S. Applications of Gas Separation by Adsorption for the Future. *Adsorpt. Sci. Technol.* **19**, 347–366 (2001).

11. Riboldi, L. & Bolland, O. Overview on Pressure Swing Adsorption (PSA) as CO2 Capture Technology: State-of-the-Art, Limits and Potentials. *Energy Procedia* **114**, 2390–2400 (2017).

12. Reynolds, S. P., Ebner, A. D. & Ritter, J. A. New Pressure Swing Adsorption Cycles for Carbon Dioxide Sequestration. *Adsorption* **11**, 531–536 (2005).

13. Grande, C. A. & Blom, R. Utilization of Dual-PSA Technology for Natural Gas Upgrading and Integrated CO2 Capture. *Energy Procedia* **26**, 2–14 (2012).

14. Regufe, M. J. *et al.* Syngas Purification by Porous Amino-Functionalized Titanium Terephthalate MIL-125. *Energy & Fuels* **29**, 4654–4664 (2015).

15. Syngas purification process. (2006).

16. Alonso-Vicario, A. *et al.* Purification and upgrading of biogas by pressure swing adsorption on synthetic and natural zeolites. *Microporous Mesoporous Mater.* **134**, 100–107 (2010).

17. Liu, C., Zhou, Y., Sun, Y., Su, W. & Zhou, L. Enrichment of coal-bed methane by PSA complemented with CO2 displacement. *AIChE J.* **57**, 645–654 (2011).

18. Jee, J.-G., Lee, J.-S. & Lee, C.-H. Air Separation by a Small-Scale Two-Bed Medical O 2 Pressure Swing Adsorption. *Ind. Eng. Chem. Res.* **40**, 3647–3658 (2001).

19. Hassan, M. M., Ruthven, D. M., Raghavan, N. S., Science, N. R.-C. E. & 1986, U. Air separation by pressure swing adsorption on a carbon molecular sieve. *Chem. Eng. Sci.* **41**, 1333–1343 (1986).

20. Kikkinides, E. S. & Yang, R. T. Simultaneous sulfur dioxide/nitrogen oxide (NOx) removal and sulfur dioxide recovery from flue gas by pressure swing adsorption. *Ind. Eng. Chem. Res.* **30**, 1981–1989 (1991).

21. Kikkinides, E. S. & Yang, R. T. Gas separation and purification by polymeric adsorbents: flue gas desulfurization and sulfur dioxide recovery with styrenic polymers. *Ind. Eng. Chem. Res.* **32**, 2365–2372 (1993).

22. Reddy, S. & Vyas, S. Recovery of Carbon Dioxide and Hydrogen from PSA Tail Gas. *Energy Procedia* **1**, 149–154 (2009).

23. Carter, J. W. & Wyszynski, M. L. The pressure swing adsorption drying of compressed air. *Chem. Eng. Sci.* **38**, 1093–1099 (1983).

24. Kasuya, F. & Tsuji, T. High purity CO gas separation by pressure swing adsorption. *Gas Sep. Purif.* **5**, 242–246 (1991).

25. Ruthven, D. M., Farooq, S. & Knaebel, K. S. *Pressure Swing Adsorption*. *New York: VCH Publishers* **1**, (1994).

26. Sivadas, D. L., Vijayan, S., Rajeev, R., Ninan, K. N. & Prabhakaran, K. Nitrogen-enriched microporous carbon derived from sucrose and urea with superior CO2 capture performance. *Carbon N. Y.* **109**, 7–18 (2016).

27. Rocha, L. A. M., Andreassen, K. A. & Grande, C. A. Separation of CO2/CH4 using carbon molecular sieve (CMS) at low and high pressure. *Chem. Eng. Sci.* **164**, 148–157 (2017).

28. Klumpen, C., Breunig, M., Homburg, T., Stock, N. & Senker, J. Microporous Organic Polyimides for CO2 and H2O Capture and Separation from CH4 and N2 Mixtures: Interplay between Porosity and Chemical Function. *Chem. Mater.* **28**, 5461–5470 (2016).

29. Lee, M. S., Park, M., Kim, H. Y. & Park, S. J. Effects of Microporosity and Surface Chemistry on Separation Performances of N-Containing Pitch-Based Activated Carbons for CO2/N2 Binary Mixture. *Sci. Rep.* **6**, (2016).

30. Safarifard, V. *et al.* Influence of the Amide Groups in the CO2/N2 Selectivity of a Series of Isoreticular, Interpenetrated Metal-Organic Frameworks. *Cryst. Growth Des.* **16**, 6016–6023 (2016).

31. Pan, Y. *et al.* Cation exchanged MOF-derived nitrogen-doped porous carbons for CO 2 capture and supercapacitor electrode materials. *J. Mater. Chem. A* **5**, 9544–9552 (2017).

32. Zhang, R. & Ritter, J. A. New approximate model for nonlinear adsorption and diffusion in a single particle. *Chem. Eng. Sci.* **52**, 3161–3172 (1997).

33. Sircar, S. & Hufton, J. R. Why does the linear driving force model for adsorption kinetics work? *Adsorption* **6**, 137–147 (2000).

34. Buzanowski, M. A. & Yang, R. T. Approximations for intraparticle diffusion rates in cyclic adsorption and desorption. *Chem. Eng. Sci.* **46**, 2589–2598 (1991).

35. Todd, R. S. & Webley, P. A. Limitations of the LDF/equimolar counterdiffusion assumption for mass transport within porous adsorbent pellets. *Chem. Eng. Sci.* **57**, 4227–4242 (2002).

36. Hsuen, H. K. An improved linear driving force approximation for intraparticle adsorption. *Chem. Eng. Sci.* **55**, 3475–3480 (2000).

37. Rodrigues, A. E. & Dias, M. M. Linear driving force approximation in cyclic adsorption processes: Simple results from system dynamics based on frequency response analysis. *Chem. Eng. Process. Process Intensif.* **37**, 489–502 (1998).

38. Wakao, N. & Funazkri, T. Effect of fluid dispersion coefficients on particle-to-fluid mass transfer coefficients in packed beds: Correlation of sherwood numbers. *Chem. Eng. Sci.* **33**, 1375–1384 (1978).

39. Ergun, S. & Orning, A. A. Fluid Flow through Randomly Packed Columns and Fluidized Beds. *Ind. Eng. Chem.* **41**, 1179–1184 (1949).

40. Myers, A. L. & Prausnitz, J. M. Thermodynamics of mixed-gas adsorption. *AIChE J.* **11**, 121–127 (1965).

41. Duong, D. D. *Adsorption analysis : equilibria and kinetics*. (Imperial College Press, 1998).

42. Ruthven, D. M. & Farooq, S. Air separation by pressure swing adsorption. *Gas Sep. Purif.* **4**, 141–148 (1990).

43. Ko, D., Siriwardane, R. & Biegler, L. T. Optimization of pressure swing adsorption and fractionated vacuum pressure swing adsorption processes for CO 2 capture. *Ind. Eng. Chem. Res.* **44**, 8084–8094 (2005).

44. Yang, R. T. *Gas separation by adsorption processes*.

45. Zhu, X., Sun, S., He, Y., Cong, Y. & Yang, W. New concept on air separation. *J. Memb. Sci.* **323**, 221–224 (2008).

46. Kostroski, K. P. & Wankat, P. C. High recovery cycles for gas separations by pressure-swing adsorption. *Ind. Eng. Chem. Res.* **45**, 8117–8133 (2006).

47. Jayaraman, A. & Yang, R. T. Stable oxygen-selective sorbents for air separation. *Chem. Eng. Sci.* **60**, 625–634 (2005).

48. Hao, P., Shi, Y., Li, S. & Liang, S. Oxygen sorption/desorption kinetics of SrCo0.8Fe0.2O3−δperovskite adsorbent for high temperature air separation. *Adsorption* **24**, 65–71 (2018).

49. Smith, A. R. & Klosek, J. A review of air separation technologies and their integration with energy conversion processes. *Fuel Process. Technol.* **70**, 115–134 (2001).

50. Farooq, S. & Ruthven, D. M. Numerical simulation of a kinetically controlled pressure swing adsorption bulk separation process based on a diffusion model. *Chem. Eng. Sci.* **46**, 2213–2224 (1991).

51. Yue-Sheng Lin, Donald L. MacLean, Y. Z. High temperature adsorption process.

52. Hashim, S. S., Mohamed, A. R. & Bhatia, S. Oxygen separation from air using ceramic-based membrane technology for sustainable fuel production and power generation. *Renewable and Sustainable Energy Reviews* **15**, 1284–1293 (2011).

53. Vieten, J. *et al.* Perovskite oxides for application in thermochemical air separation and oxygen storage. *J. Mater. Chem. A* **4**, 13652–13659 (2016).

54. Davison, J. Performance and costs of power plants with capture and storage of CO2. *Energy* (2007). doi:10.1016/j.energy.2006.07.039

55. Stadler, H. *et al.* Oxyfuel coal combustion by efficient integration of oxygen transport membranes. *Int. J. Greenh. Gas Control* (2011). doi:10.1016/j.ijggc.2010.03.004

56. Yang, Z., Lin, Y. S. & Zeng, Y. High-temperature sorption process for air separation and oxygen removal. *Ind. Eng. Chem. Res.* (2002). doi:10.1021/ie010736k

57. Yang, Z. & Lin, Y. S. Equilibrium of oxygen sorption on perovskite-type lanthanum cobaltite sorbent. *AIChE J.* (2003). doi:10.1002/aic.690490323

58. Guntuka, S., Banerjee, S., Farooq, S. & Srinivasan, M. P. A- and B-site substituted lanthanum cobaltite perovskite as high temperature oxygen sorbent. 1. thermogravimetric analysis of equilibrium and kinetics. in *Industrial and Engineering Chemistry Research* (2008). doi:10.1021/ie070859q

59. Yin, Q., Kniep, J. & Lin, Y. S. High temperature air separation by perovskite-type oxide sorbents-Heat effect minimization. *Chem. Eng. Sci.* (2008). doi:10.1016/j.ces.2008.09.004

60. Yang, Z. H. & Lin, Y. S. High-temperature oxygen sorption in a fixed bed packed with perovskite-type ceramic sorbents. *Ind. Eng. Chem. Res.* (2003). doi:10.1021/ie030313d

61. Yang, Q., Lin, Y. S. & Bülow, M. High temperature sorption separation of air for producing oxygen-enriched CO 2 stream. *AIChE J.* (2006). doi:10.1002/aic.10638

62. Yin, Q., Kniep, J. & Lin, Y. S. Oxygen sorption and desorption properties of Sr-Co-Fe oxide. *Chem. Eng. Sci.* **63**, 2211–2218 (2008).

63. Beeyani, A. K., Singh, K., Vyas, R. K., Kumar, S. & Kumar, S. Parametric studies and simulation of PSA process for oxygen production from air. *Polish J. Chem. Technol.* (2010). doi:10.2478/v10026-010-0013-2

64. Farooq, S., Ruthven, D. M. & Boniface, H. A. Numerical simulation of a pressure swing adsorption oxygen unit. *Chem. Eng. Sci.* (1989). doi:10.1016/0009-2509(89)85090-0

65. Jiang, L., Biegler, L. T. & Fox, V. G. Simulation and optimization of pressure-swing adsorption systems for air separation. *AIChE J.* **49**, 1140–1157 (2003).

66. Todd, R. S. & Webley, P. A. Mass-transfer models for rapid pressure swing adsorption simulation. *AIChE J.* (2006). doi:10.1002/aic.10948

67. Wu, H. C. & Lin, Y. S. Effects of Oxygen Vacancy Order-Disorder Phase Transition on Air Separation by Perovskite Sorbents. *Ind. Eng. Chem. Res.* (2017). doi:10.1021/acs.iecr.7b00461

68. Standard, A. D4058-96, 2001,"Standard Test Method for Attrition and Abrasion of Catalysts and Catalyst Carriers", ASTM Int'l. *West Conshohoken, PA. Viewed Feb* **19**, (2009).

69. David, E. Mechanical strength and reliability of the porous materials used as adsorbents/ catalysts and the new development trends. *Arch. Mater. Sci. Eng.* **73**, 5–17 (2015).

70. Chai, S. W. Experimental Simulation of Rapid Pressure Swing Adsorption for Medical Oxygen Concentrator and Numerical Simulation of the Critical Desorption-by-Purge Step. *Chem. Eng.* (2011).

71. Chai, S., Kothare, M. V. & Sircar, S. Numerical study of nitrogen desorption by rapid oxygen purge for a medical oxygen concentrator. *Adsorption* (2012). doi:10.1007/s10450-012-9384-4

72. Ruthven, D. M., Pressure, F. S. K. K. S., Farooq, S., Knaebel, K. S. & Pressure, F. S. K. K. S. *Pressure Swing Adsorption*. *New York: VCH Publishers* **1**, (1994).

73. Wakao, N., Kaguei, S. & Funazkri, T. Effect of fluid dispersion coefficients on particle-to-fluid heat transfer coefficients in packed beds. Correlation of nusselt numbers. *Chem. Eng. Sci.* (1979). doi:10.1016/0009-2509(79)85064-2

74. Fuller, E. N., Schettler, P. D. & Giddings, J. C. A new method for prediction of binary gas-phase diffusion coefficients. *Ind. Eng. Chem.* (1966). doi:10.1021/ie50677a007

75. Hassan, M. M., Raghavan, N. S. & Ruthven, D. M. Pressure swing air separation on a carbon molecular sieve-II. Investigation of a modified cycle with pressure equalization and no purge. *Chem. Eng. Sci.* (1987). doi:10.1016/0009-2509(87)80149-5

76. Ergun, S. & Orning, A. A. Fluid Flow through Randomly Packed Columns and Fluidized Beds. *Ind. Eng. Chem.* (1949). doi:10.1021/ie50474a011

77. Yang, Z. & Lin, Y. S. A semi-empirical equation for oxygen nonstoichiometry of perovskite-type ceramics. *Solid State Ionics* (2002). doi:10.1016/S0167-2738(02)00524-6

78. Hart, J., Battrum, M. J. & Thomas, W. J. Axial pressure gradients during the pressurization and depressurization steps of a PSA gas separation cycle. *Gas Sep. Purif.* (1990). doi:10.1016/0950-4214(90)80035-J

79. Kozeny, J. Uber kapillare Leitung der Wasser in Boden. *Sitzungsber. Akad. Wiss. Wien* (1927).

80. Alzaydi, A. FLOW OF GASES THROUGH POROUS MEDIA. (1977). doi:10.1016/0010-2180(57)90038-x

81. Rushton, A., Ward, A. S. & Holdich, R. G. *Solid-liquid filtration and separation technology*. *Solid-Liquid Filtration and Separation Technology* (2008). doi:10.1002/9783527614974

82. Schiesser, W. E. & Griffiths, G. W. *A compendium of partial differential equation models: Method of lines analysis with matlab*. *A Compendium of Partial Differential Equation Models: Method of Lines Analysis with Matlab* (2009). doi:10.1017/CBO9780511576270

83. Godunov, S. K. A difference method for numerical calculation of discontinuous solutions of the equations of hydrodynamics [English title page]. *Mat. Sb.* (1959).

84. Schiesser, W. & Griffiths, G. *Traveling Wave Analysis of Partial Differential Equations*. *Traveling Wave Analysis of Partial Differential Equations* (2012). doi:10.1016/C2009-0-64536-0

85. Rege, S. U. & Yang, R. T. Limits for Air Separation by Adsorption with LiX Zeolite. *Ind. Eng. Chem. Res.* (1997). doi:10.1021/ie9705214

86. Rama Rao, V., Farooq, S. & Krantz, W. B. Design of a two-step pulsed pressure-swing adsorption-based oxygen concentrator. *AIChE J.* (2010). doi:10.1002/aic.11953

87. Mendes, A. M. M., Costa, C. A. V. & Rodrigues, A. E. Oxygen separation from air by PSA: modelling and experimental results: Part I: isothermal operation. *Sep. Purif. Technol.* **24**, 173–188 (2001).

88. Krish Krishnamurthy, Divy Acharya & Frank Fitch. *Pilot-Scale Demonstration of a Novel, Low-Cost Oxygen Supply Process and its Integration with Oxy-Fuel Coal-Fired Boilers*. (2008). doi:10.2172/966357

89. Wang, J. *et al.* Effect of nitrogen group on selective separation of CO2/N2 in porous polystyrene. *Chem. Eng. J.* **256**, 390–397 (2014).

90. Arias, B. *et al.* Emerging CO2 capture systems. *Int. J. Greenh. Gas Control* **40**, 126–166 (2015).

91. Hasan, M. M. F., Baliban, R. C., Elia, J. A. & Floudas, C. A. Modeling, Simulation, and Optimization of Postcombustion CO $_2$ Capture for Variable Feed Concentration and Flow Rate. 2. Pressure Swing Adsorption and Vacuum Swing Adsorption Processes. *Ind. Eng. Chem. Res.* **51**, 15665–15682 (2012).

92. Pevida, C., Plaza, M., Arias, B., … J. F.-A. S. & 2008, undefined. Surface modification of activated carbons for CO2 capture. *Elsevier*

93. Yang, S. *et al.* Graphene-Based Porous Silica Sheets Impregnated with Polyethyleneimine for Superior CO $_2$ Capture. *Adv. Mater.* **25**, 2130–2134 (2013).

94. Su, F., Lu, C., Cnen, W., Bai, H. & Hwang, J. F. Capture of CO2 from flue gas via multiwalled carbon nanotubes. *Sci. Total Environ.* **407**, 3017–3023 (2009).

95. Ruthven, D. M., Farooq, S. & Knaebel, K. S. *Pressure Swing Adsorption; VCH: New York, 1994*. *There is no corresponding record for this reference*

96. Pham, T.-H., Lee, B.-K., Kim, J. & Lee, C.-H. Enhancement of CO2 capture by using synthesized nano-zeolite. *J. Taiwan Inst. Chem. Eng.* **64**, 220–226 (2016).

97. Jiang, Q. *et al.* Synthesis of T-type zeolite nanoparticles for the separation of CO2/N2 and CO2/CH4 by adsorption process. *Chem. Eng. J.* **230**, 380–388 (2013).

98. Anbia, M., Eskandari, A. & Jahangiri, mansoor. Effect of Particle Size of NaX Zeolite on Adsorption of CO2/CH4. *Int. J. Eng.* **29**, 1–7 (2016).

99. Zhang, J., Webley, P., Management, P. X.-E. C. and & 2008, undefined. Effect of process parameters on power requirements of vacuum swing adsorption technology for CO2 capture from flue gas. *Elsevier*

100. Zhang, J. & Webley, P. A. Cycle Development and Design for CO $_2$ Capture from Flue Gas by Vacuum Swing Adsorption. *Environ. Sci. Technol.* **42**, 563–569 (2008).

101. Ling, J., Ntiamoah, A., Xiao, P., Webley, P. A. & Zhai, Y. Effects of feed gas concentration, temperature and process parameters on vacuum swing adsorption performance for CO2 capture. *Chem. Eng. J.* **265**, 47–57 (2015).

102. Kikkinides, E. S., Yang, R. T. & Cho, S. H. *Concentration and Recovery of CO2 from Flue Gas by Pressure Swing Adsorption*. *Ind. Eng. Chem. Res* **32**, (1993).

103. Haghpanah, R., Nilam, R., Rajendran, A., Farooq, S. & Karimi, I. A. Cycle synthesis and optimization of a VSA process for postcombustion CO $_2$ capture. *AIChE J.* **59**, 4735–4748 (2013).

104. Haghpanah, R. *et al.* Multiobjective Optimization of a Four-Step Adsorption Process for Postcombustion CO $_2$ Capture Via Finite Volume Simulation. *Ind. Eng. Chem. Res.* **52**, 4249–4265 (2013).

105. Arias, B. *et al.* Emerging CO2 capture systems. *Int. J. Greenh. Gas Control* **40**, 126–166 (2015).

106. Zhang, W. *et al.* Process simulations of post-combustion CO2 capture for coal and natural gas-fired power plants using a polyethyleneimine/silica adsorbent. *Int. J. Greenh. Gas Control* **58**, 276–289 (2017).

107. Park, J.-H., Beum, H.-T., Kim, J.-N. & Cho, S.-H. Numerical Analysis on the Power Consumption of the PSA Process for Recovering CO $_2$ from Flue Gas. *Ind. Eng. Chem. Res.* **41**, 4122–4131 (2002).

108. Engineering, E. D.-A. of M. S. and & 2015, undefined. Mechanical strength and reliability of the porous materials used as adsorbents/catalysts and the new development trends. *amse.acmsse.h2.pl*

109. Hassan, M. M., Raghavan, N. S. & Ruthven, D. M. Pressure swing air separation on a carbon molecular sieve—II. Investigation of a modified cycle with pressure equalization and no purge. *Chem. Eng. Sci.* **42**, 2037–2043 (1987).

110. Wakao, N. & Funazkri, T. Effect of fluid dispersion coefficients on particle-to-fluid mass transfer coefficients in packed beds: Correlation of sherwood numbers. *Chem. Eng. Sci.* **33**, 1375–1384 (1978).

111. Schiesser, W. E. & Griffiths, G. W. *A compendium of partial differential equation models : method of lines analysis with Matlab*. (Cambridge University Press, 2009).

112. Patterson, A. L. The Scherrer Formula for X-Ray Particle Size Determination. *Phys. Rev.* **56**, 978–982 (1939).

113. Yang, J. *et al.* Enhanced mass transfer on hierarchical porous pure silica zeolite used for gas separation. *Microporous Mesoporous Mater.* **266**, (2018).

114. Simon, C. M., Smit, B. & Haranczyk, M. pyIAST: Ideal adsorbed solution theory (IAST) Python package. *Comput. Phys. Commun.* **200**, 364–380 (2016).

115. McEwen, J., Hayman, J.-D. & Ozgur Yazaydin, A. A comparative study of CO2, CH4 and N2 adsorption in ZIF-8, Zeolite-13X and BPL activated carbon. *Chem. Phys.* **412**, 72–76 (2013).

116. Saha, D., Bao, Z., Jia, F. & Deng, S. Adsorption of CO_2, CH_4, N_2O, and N_2 on MOF-5, MOF-177, and Zeolite 5A. *Environ. Sci. Technol.* **44**, 1820–1826 (2010).

117. Yao, Z. *et al.* Controlled synthesis of micro/nanoscale Mg-MOF-74 materials and their adsorption property. *Mater. Lett.* **223**, 174–177 (2018).

118. Luebke, R. *et al.* The unique rht-MOF platform, ideal for pinpointing the functionalization and CO_2 adsorption relationship. *Chem. Commun.* **48**, 1455–1457 (2012).

119. Xiang, S. *et al.* Microporous metal-organic framework with potential for carbon dioxide capture at ambient conditions. *Nat. Commun.* **3**, 954–959 (2012).

120. Banerjee, R. *et al.* Control of Pore Size and Functionality in Isoreticular Zeolitic Imidazolate Frameworks and their Carbon Dioxide Selective Capture Properties. *J. Am. Chem. Soc.* **131**, 3875–3877 (2009).

121. Na, K. *et al.* Directing zeolite structures into hierarchically nanoporous architectures. *science.sciencemag.org*

122. Pérez-Ramírez, J. Imagination has no limits. *Nat. Chem.* **4**, 250–251 (2012).

123. Li, J.-R., Sculley, J. & Zhou, H.-C. Metal–Organic Frameworks for Separations. *Chem. Rev.* **112**, 869–932 (2012).

124. Ruthven, D. M. Past progress and future challenges in adsorption research. *Ind. Eng. Chem. Res.* **39**, 2127–2131 (2000).

125. Bhadra, S. J. & Farooq, S. Separation of Methane–Nitrogen Mixture by Pressure Swing Adsorption for Natural Gas Upgrading. *Ind. Eng. Chem. Res.* **50**, 14030–14045 (2011).

126. Kalia, S. & Avérous, L. *Biodegradable and Biobased Polymers for Environmental and Biomedical Applications*. (2016). doi:10.1002/9781119117360

127. Yang, H., Yin, C., Jiang, B. & Zhang, D. Optimization and analysis of a VPSA process for N2/CH4 separation. *Sep. Purif. Technol.* **134**, 232–240 (2014).

128. Wang, J., Yang, J., Krishna, R., Yang, T. & Deng, S. derived porous carbons for CO 2 capture and gas. *J. Mater. Chem. A Mater. energy Sustain.* **4**, 19095–19106 (2016).

129. Zhang, Y. *et al.* Facile and controllable preparation of ultramicroporous biomass-derived carbons and application on selective adsorption of gas-mixtures. *Ind. Eng. Chem. Res.* **57**, 14191–14201 (2018).

130. Wang, J., Krishna, R., Wu, X., Sun, Y. & Deng, S. Polyfuran-Derived Microporous Carbons for Enhanced Adsorption of CO2 and CH4. *Langmuir* **31**, 9845–9852 (2015).

131. Wang, J., Krishna, R., Yang, J. & Deng, S. Hydroquinone and Quinone-Grafted Porous Carbons for Highly Selective CO2 Capture from Flue Gases and Natural Gas Upgrading. *Environ. Sci. Technol.* **49**, 9364–9373 (2015).

132. Wang, J., Krishna, R., Yang, J., Dandamudi, K. P. R. & Deng, S. Nitrogen-doped porous carbons for highly selective CO2 capture from flue gases and natural gas upgrading. *Mater. Today Commun.* **4**, 156–165 (2015).

133. Zhang, P. *et al.* A new choice of polymer precursor for solvent-free method: Preparation of N-enriched porous carbons for highly selective CO2 capture. *Chem. Eng. J.* **355**, 963–973 (2019).

134. Yuan, B. *et al.* Adsorption of CO2, CH4, and N2 on Ordered mesoporous carbon: Approach for greenhouse gases capture and biogas upgrading. *Environ. Sci. Technol.* **47**, 5474–5480 (2013).

135. Yang, F. *et al.* Synthesis of Porous Carbons with High N-Content from Shrimp Shells for Efficient CO2 Capture and Gas Separation. *ACS Sustain. Chem. Eng.* **6**, 15550–15559 (2018).

136. Zhang, Y. *et al.* Ultra-high surface area and nitrogen-rich porous carbons prepared by a low-temperature activation method with superior gas selective adsorption and outstanding supercapacitance performance. *Chem. Eng. J.* **355**, 309–319 (2019).

137. Li, P. & Handan Tezel, F. Adsorption separation of N2, O2, CO2 and CH4 gases by b-zeolite. *Microporous Mesoporous Mater.* **98**, 94–101 (2007).

138. McEwen, J., Hayman, J.-D. & Ozgur Yazaydin, A. A comparative study of CO2, CH4 and N2 adsorption in ZIF-8, Zeolite-13X and BPL activated carbon. *Chem. Phys.* **412**, 72–76 (2013).

139. Yang, J. *et al.* Enhanced mass transfer on hierarchical porous pure silica zeolite used for gas separation. *Microporous Mesoporous Mater.* **266**, 56–63 (2018).

140. Saha, D. & Bao, Z. Adsorption of CO2,CH4, N2O, and N2 on MOF-5 , MOF-177 , and Zeolite 5A. *Environ. Sci. Technol.* **44**, 1820–1826 (2010).

141. Cavenati, S., Grande, C. A., Lopes, F. V. S. & Rodrigues, A. E. Adsorption of small molecules on alkali-earth modified titanosilicates. *Microporous Mesoporous Mater.* **121**, 114–120 (2009).

142. Wu, X., Yuan, B., Bao, Z. & Deng, S. Adsorption of carbon dioxide, methane and nitrogen on an ultramicroporous copper metal-organic framework. *J. Colloid Interface Sci.* **430**, 78–84 (2014).

143. Wang, J., Yang, J., Krishna, R., Yang, T. & Deng, S. A versatile synthesis of metal-organic framework-derived porous carbons for CO2capture and gas separation. *J. Mater. Chem. A* **4**, 19095–19106 (2016).

144. Khurana, M. & Farooq, S. Adsorbent Screening for Postcombustion CO 2 Capture: A Method Relating Equilibrium Isotherm Characteristics to an Optimum Vacuum Swing Adsorption Process Performance. *Ind. Eng. Chem. Res.* **55**, 2447–2460 (2016).

145. Wu, C.-W. & Sircar, S. Comments on binary and ternary gas adsorption selectivity. *Sep. Purif. Technol.* **170**, 453–461 (2016).

146. Rege, S. & Yang, R. A simple parameter for selecting an adsorbent for gas separation by pressure swing adsorption. *Sep. Sci. Technol.* **36**, 3355–3365 (2001).

147. Krishna, R. & Van Baten, J. M. A comparison of the CO 2 capture characteristics of zeolites and metal-organic frameworks. *Sep. Purif. Technol.* **87**, 120–126 (2012).

148. Mason, J. A., Sumida, K., Herm, Z. R., Krishna, R. & Long, J. R. Evaluating metal-organic frameworks for post-combustion carbon dioxide capture via temperature swing adsorption. *Energy Environ. Sci.* **4**, 3030–3040 (2011).

149. Zhang, J., Webley, P. A. & Xiao, P. Effect of process parameters on power requirements of vacuum swing adsorption technology for CO2 capture from flue gas. *Energy Convers. Manag.* **49**, 346–356 (2008).

150. Jiang, L., Biegler, L. T. & Fox, V. G. Simulation and optimization of pressure-swing adsorption systems for air separation. *AIChE J.* **49**, 1140–1157 (2003).

151. Krishna, R. & Long, J. R. Screening Metal–Organic Frameworks by Analysis of Transient Breakthrough of Gas Mixtures in a Fixed Bed Adsorber. *J. Phys. Chem. C* **115**, 12941–12950 (2011).

152. Ackley, Mark William; Stewart, Alan barnard; Henzler, Gregory William; Leavitt, Frederick Wells; Notaro, Frank; Kane, M. S. US6027548A - PSA apparatus and process using adsorbent mixtures.

153. Wang, J. *et al.* Controllable synthesis of bifunctional porous carbon for efficient gas-mixture separation and high-performance supercapacitor. *Chem. Eng. J.* **348**, 57–66 (2018).

154. Yuan, B. *et al.* Adsorptive separation studies of ethane-methane and methane-nitrogen systems using mesoporous carbon. *J. Colloid Interface Sci.* **394**, 445–450 (2013).

155. Haile, S. M. Solar-Driven Thermochemical Dissociation of CO 2 and H 2 O Using Ceria Using g the Sun to Make Fuels. *Chem. Eng.* **330**, 1797–1802 (2011).

156. Marxer, D., Furler, P., Takacs, M. & Steinfeld, A. Solar thermochemical splitting of CO2into separate streams of CO and O2with high selectivity, stability, conversion, and efficiency. *Energy Environ. Sci.* **10**, 1142–1149 (2017).

157. Steinfeld, A. Solar thermochemical production of hydrogen—a review. *Sol. Energy* **78**, 603–615 (2005).

158. Steinfeld, A. Solar hydrogen production via a two-step water-splitting thermochemical cycle based on Zn/ZnO redox reactions. *Int. J. Hydrogen Energy* **27**, 611–619 (2002).

159. Allen, K. M., Coker, E. N., Auyeung, N. & Klausner, J. F. Cobalt Ferrite in YSZ for Use as Reactive Material in Solar Thermochemical Water and Carbon Dioxide Splitting, Part I: Material Characterization. *JOM* **65**, 1670–1681 (2013).

160. Ezbiri, M., Becattini, V., Hoes, M., Michalsky, R. & Steinfeld, A. High Redox Capacity of Al-Doped La $_{1-x}$ Sr $_{x}$ MnO $_{3-\delta}$ Perovskites for Splitting CO $_2$ and H $_2$ O at Mn-Enriched Surfaces. *ChemSusChem* **10**, 1517–1525 (2017).

161. McDaniel, A. H. *et al.* Sr- and Mn-doped LaAlO3−δ for solar thermochemical H2 and CO production. *Energy Environ. Sci.* **6**, 2424 (2013).

162. Call, F. *et al.* Thermogravimetric Analysis of Zirconia-Doped Ceria for Thermochemical Production of Solar Fuel. *Am. J. Anal. Chem.* **04**, 37–45 (2013).

163. Scheffe, J. R., Weibel, D. & Steinfeld, A. Lanthanum–Strontium–Manganese Perovskites as Redox Materials for Solar Thermochemical Splitting of H $_2$ O and CO $_2$. *Energy & Fuels* **27**, 4250–4257 (2013).

164. Marxer, D., Furler, P., Takacs, M. & Steinfeld, A. Solar thermochemical splitting of CO $_2$ into separate streams of CO and O $_2$ with high selectivity, stability, conversion, and efficiency. *Energy Environ. Sci.* **10**, 1142–1149 (2017).

165. Bhosale, R. R. *et al.* A decade of ceria based solar thermochemical H2O/CO2 splitting cycle. *Int. J. Hydrogen Energy* **44**, 34–60 (2019).

166. Abanades, S. & Flamant, G. Thermochemical hydrogen production from a two-step solar-driven water-splitting cycle based on cerium oxides. *Sol. Energy* **80**, 1611–1623 (2006).

167. Brendelberger, S., von Storch, H., Bulfin, B. & Sattler, C. Vacuum pumping options for application in solar thermochemical redox cycles – Assessment of mechanical-, jet- and thermochemical pumping systems. *Sol. Energy* **141**, 91–102 (2017).

168. Brendelberger, S., Roeb, M., Lange, M. & Sattler, C. Counter flow sweep gas demand for the ceria redox cycle. *Sol. Energy* **122**, 1011–1022 (2015).

169. Lin, M. & Haussener, S. Solar fuel processing efficiency for ceria redox cycling using alternative oxygen partial pressure reduction methods. *Energy* **88**, 667–679 (2015).

170. Brendelberger, S., Vieten, J., Roeb, M. & Sattler, C. Thermochemical oxygen pumping for improved hydrogen production in solar redox cycles. *Int. J. Hydrogen Energy* **44**, 9802–9810 (2019).

171. Bulfin, B. *et al.* Thermodynamics of CeO2 thermochemical fuel production. *Energy and Fuels* **29**, 1001–1009 (2015).

172. Brendelberger, S., Vieten, J., Vidyasagar, M. J., Roeb, M. & Sattler, C. Demonstration of thermochemical oxygen pumping for atmosphere control in reduction reactions. *Sol. Energy* **170**, 273–279 (2018).

173. Ermanoski, Ivan; Stechel, E. Thermally Driven Adsorption/Desorption Cycle for Oxygen Pumping in Thermochemical Fuel Production. *Submitt. to Sol. Energy*

174. Valldor, M. & Andersson, M. The structure of the new compound YBaCo4O7 with a magnetic feature. *Solid State Sci.* **4**, 923–931 (2002).

175. Parkkima, O., Yamauchi, H. & Karppinen, M. Oxygen Storage Capacity and Phase Stability of Variously Substituted YBC114. *Chem. Mater.* **25**, 599–604 (2013).

176. Măicăneanu, A. *et al.* Organics removal from aqueous solutions using suspended and immobilized Romanian bentonites. *Stud. Univ. Babes-Bolyai Chem.* 82–93 (2011).

177. Parkkima, O., Silvestre-Albero, A., Silvestre-Albero, J. & Karppinen, M. Oxygen-Nonstoichiometric YBC114 as a Catalyst in H2O2 Oxidation of Cyclohexene. *Catal. Letters* **145**, 576–582 (2015).

178. Tian, G. *et al.* An oxygen pool from YBaCo4O7-based oxides for soot combustion. *Catal. Sci. Technol.* **6**, 4511–4515 (2016).

179. Karppinen, M. *et al.* Oxygen Nonstoichiometry in YBaCo4O 7+δ : Large Low-Temperature Oxygen Absorption/Desorption Capability. (2006). doi:10.1021/cm0523081

180. Hao, H. *et al.* Oxygen adsorption properties of YBaCo4O7-type compounds. *Solid State Ionics* **177**, 631–637 (2006).

181. Tsipis, E. V., Khalyavin, D. D., Shiryaev, S. V., Redkina, K. S. & Núñez, P. Electrical and magnetic properties of YBC114. *Mater. Chem. Phys.* **92**, 33–38 (2005).

182. Agrafiotis, C., Roeb, M. & Sattler, C. Cobalt oxide-based structured thermochemical reactors/heat exchangers for solar thermal energy storage in concentrated solar power plants. in *ASME 2014 8th International Conference on Energy Sustainability, ES 2014 Collocated with the ASME 2014 12th International Conference on Fuel Cell Science, Engineering and Technology* **1**, (Web Portal ASME (American Society of Mechanical Engineers), 2014).

183. HAO, H., ZHAO, L., HU, J., HU, X. & HOU, H. Oxygen adsorption/desorption behavior of YBC114and its application to oxygen removal from nitrogen. *J. Rare Earths* **27**, 815–818 (2009).

184. Valkeapää, M. *et al.* In Situ and Ex Situ Monitoring of Oxygen Absorption in YBC114. *Chem. Lett.* **36**, 1368–1369 (2007).

APPENDIX A

LIST OF PUBLICATIONS

The preceding chapters are modified versions of the papers already published or accepted:

Chapter 3.

Xu, M.; Wu, H.C.; Lin, Y.S.; Deng, S. Simulation and optimization of pressure swing adsorption process for high-temperature air separation by perovskite sorbents. *Chem. Eng. J.* **354**, 62-74 (2018).

Chapter 4.

Xu, M.; Chen, S.; Seo, D.K.; Deng, S. Evaluation and optimization of VPSA processes with nanostructured zeolite NaX for post-combustion CO_2 capture. *Chem. Eng. J.* **371**, 693–705 (2019).

Chapter 5.

Xu, M.; Deng, S. Efficient screening of novel adsorbents for coalbed methane recovery. *J. Colloid Interface Sci.* **565**, 131–141 (2020).

Chapter 6.

Xu, M.; Ermanoski, I.; Stechel, B.S.; Deng, S. Oxygen pumping characteristics of $YBaCo_4O_7$ for solar thermochemical cycles. *Chem. Eng. J.* in press (2020).

LIST OF PUBLICATIONS

1. Xu, M.; Wu, H.C.; Lin, Y.S.; Deng, S. Simulation and optimization of pressure swing adsorption process for high-temperature air separation by perovskite sorbents. *Chem. Eng. J.* **354**, 62-74 (2018).
2. Yang, J.; Yuan, N; Xu, M; Liu, J; Li, J; Deng, S. Enhanced mass transfer on hierarchical porous pure silica zeolite used for gas separation. *Microporous Mesoporous Mater.* **266**, 56-63 (2018).
3. Zhang, Y.; Zhang, P.; Yu, W.; Wang, J.; Deng, Q.; Yang, J.; Zeng, Z.; Xu, M.; Deng, S. Facile and controllable preparation of ultramicroporous biomass- derived carbons and application on selective adsorption of gas-mixtures. *Ind. Eng. Chem. Res.* **57**, 14191–14201 (2018).
4. Xie, Y.; Ma, S.; Wang, Y.; Xu, M.; Lu, C; Xiao, L.; Deng, S. Controlled synthesis and luminescence properties of $CaMoO_4$: Eu^{3+}microcrystals. *Opt. Mater. (Amst)*. **77**, 13-18 (2018).
5. Xu, M.; Chen, S.; Seo, D.K.; Deng, S. Evaluation and optimization of VPSA processes with nanostructured zeolite NaX for post-combustion CO_2 capture. *Chem. Eng. J.* **371**, 693–705 (2019).
6. Lyu, X.; Xu, M.; Chen, X.; Xu, L.; Wang, J.; Deng, S. Beneficial Effect of Water on the Catalytic Conversion of Sugars to Methyl Lactate in Near-Critical Methanol Solutions. *Ind. Eng. Chem. Res.* **58**, 12451–12458 (2019).

7. Lyu, X.; Zhang, Z.; Okejiri, F.; Chen, H.; Xu, M.; Chen, X.; Deng, S. Simultaneous Conversion of C5 and C6 Sugars into Methyl Levulinate with the Addition of 1, 3, 5-Trioxane. *ChemSusChem.* **12**, 4400-4404 (2019).

8. Zhang, Y.; Zhang, P.; Yu, W.; Zhang, J.; Huang, J.; Wang, J.; Xu, M.; Deng, Q.; Zeng, Z.; Deng, S. Highly Selective and Reversible Sulfur Dioxide Adsorption on a Microporous Metal-organic Framework via Polar Sites. *ACS Appl. Mater. Interfaces.* **11**, 10680-10688 (2019).

9. Zhang, P.; Zhong, Y.; Ding, J.; Wang J.; Xu, M.; Deng, Q.; Zeng, Z.; Deng, S. A new choice of polymer precursor for solvent-free method: Preparation of N-enriched porous carbons for highly selective CO_2 capture. *Chem. Eng. J.* **355**, 963-973 (2019). doi:10.1016/j.cej.2018.08.219

10. Zhang, Y.; Liu, L.; Zhang, P.; Wang, J.; Xu, M.; Deng, Q.; Zeng, Z.; Deng, S. Ultra-high surface area and nitrogen-rich porous carbons prepared by a low-temperature activation method with superior gas selective adsorption and outstanding supercapacitance performance. *Chem. Eng. J.* **355**, 309-319 (2019). doi:10.1016/j.cej.2018.08.169

11. Chen, S.; Lu, C.; Liu, L.; Xu, M.; Wang, J; Deng, Q.; Zeng Z.; Deng, S. A hierarchical glucose-intercalated NiMn-G-LDH@$NiCo_2S_4$ core-shell structure as binder-free electrode for flexible all-solid-state asymmetric supercapacitors. *Nanoscale.* (2020).

12. Xu, M.; Deng, S. Efficient screening of novel adsorbents for coalbed methane recovery. *J. Colloid Interface Sci.* **565**, 131–141 (2020).

13. Xu, M.; Ermanoski, I.; Stechel, B.S.; Deng, S. Oxygen pumping characteristics of $YBaCo_4O_7$ for solar thermochemical cycles. *Chem. Eng. J.* in press (2020).

APPENDIX B

MATLAB PROGRAM FOR LAUNCHING PSA SIMULATION

```
% Clear previous files
clc
clear all
format short
%
% parameters shared with the ODE routine
%
global Mg1 Mg2 De1 De2 taup adsorptionORpurge
dYbardZbarDifferentialMethod rhog0 T0 ncall n noutstep dzbar tbar
epsilon epsilonbar tc tt k1 k2 rhob n10 n20 dp L ta td tp tdep y1feed
y10 Y0 Qa P0 Pa Pd Ta Pmax Pmin Tmax Tmin Tref Q0 MassAxial tbar tbara
tbarp tbardep tbard nouta noutp noutdep noutd noutcycle miu dtbara
dtbarp dtbardep dtbard
%
% Input data
PSA_inputs
%
% ODE integration
%
ncall = 0;
reltol = 1.0e-05;
abstol = 1.0e-05;
options = odeset('RelTol',reltol,'AbsTol',abstol);
%
% Cycle #1 pressurization
%
% Initial conditions for y1bar, n1bar, n2bar for i=1:n
%
for i = 1:n
    Y0(0*n+i) = y10*rhog0*L/(Qa*tt); % for Y1bar
    Y0(1*n+i) = (k1*rhob*L/Qa)*n10; % for n1bar
    Y0(2*n+i) = (k2*rhob*L/Qa)*n20; % for n2bar
    Y0(3*n+i) = P0/(Pmax-Pmin); % for Pbar
end
for i = 1
    Y0(3*n+1) = Pa/(Pmax-Pmin);
end
%
[t,Ys] = ode15s(@PSA_pressurization, tbarp, Y0, options);
%
for it = 1:noutp % time
   for i = 1:4*n % position
       Y(it,i) = Ys(it,i);
   end
end
%
% Cycle #1 adsorption
%
% Initial conditions for adsorption step
%
for i = 1:n
    Y0(0*n+i) = Y(noutp,0*n+i); % for Y1bar
    Y0(1*n+i) = Y(noutp,1*n+i); % for n1bar
    Y0(2*n+i) = Y(noutp,2*n+i); % for n2bar
```

```
    Y0(3*n+i) = Pa/(Pmax-Pmin); % for Pbar
end
%
[t,Ys] = ode15s(@PSA_adsorption, tbara, Y0, options);
%
for it = 1:(nouta-1) % time
    for i = 1:4*n % position
         Y(it+noutp,i) = Ys(it+1,i);
    end
end
%
% Cycle #1 depressurization
%
% Initial conditions for depressurization step
%
for i = 1:n
    Y0(0*n+i) = Y(noutp+nouta-1,0*n+i); % for Y1bar
    Y0(1*n+i) = Y(noutp+nouta-1,1*n+i); % for n1bar
    Y0(2*n+i) = Y(noutp+nouta-1,2*n+i); % for n2bar
    Y0(3*n+i) = Y(noutp+nouta-1,3*n+i); % for Pbar
end
Y0(3*n+n) = Pd/(Pmax-Pmin);
%
[t,Ys] = ode15s(@PSA_depressurization, tbardep, Y0, options);
%
for it = 1:(noutdep-1) % time
   for i = 1:4*n % position
       Y(it+noutp+nouta-1,i) = Ys(it+1,i);
   end
end
%
% Cycle #1 desorption
%
% Initial conditions for desorption step
%
for i = 1:n
    Y0(0*n+i) = Y(noutp+nouta+noutdep-2,0*n+i); % for Y1bar
    Y0(1*n+i) = Y(noutp+nouta+noutdep-2,1*n+i); % for n1bar
    Y0(2*n+i) = Y(noutp+nouta+noutdep-2,2*n+i); % for n2bar
    Y0(3*n+i) = Pd/(Pmax-Pmin); % for Pbar
end
%
[t,Ys] = ode15s(@PSA_desorption, tbard, Y0, options);
%
for it = 1:(noutd-1) % time
    for i = 1:4*n
        Y(it+nouta+noutp+noutdep-2,i) = Ys(it+1,i);
    end
end
%
% For cycles after the first cycle
%
for ic = 1:(cycle-1)
    %
```

```
    % pressurization
    %
    % Initial conditions for pressurization step
    for i = 1:n
        Y0(0*n+i) = Y((noutcycle-1)*ic+1,0*n+i); % for Y1bar
        Y0(1*n+i) = Y((noutcycle-1)*ic+1,1*n+i); % for n1bar
        Y0(2*n+i) = Y((noutcycle-1)*ic+1,2*n+i); % for n2bar
        Y0(3*n+i) = Y((noutcycle-1)*ic+1,3*n+i); % for Pbar
    end
    Y0(3*n+1) = Pa/(Pmax-Pmin);
    %
    [t,Ys] = ode15s(@PSA_pressurization, tbarp, Y0, options);
    %
    for it = 1:(noutp-1) % time
        for i = 1:4*n
            Y(it+ic*(noutcycle-1)+1,i) = Ys(it+1,i);
        end
    end
    %
    % Adsorption
    %
    % Initial conditions for adsorption step
    %
    for i = 1:n
        Y0(0*n+i) = Y((noutcycle-1)*ic+noutp,0*n+i); % for Y1bar
        Y0(1*n+i) = Y((noutcycle-1)*ic+noutp,1*n+i); % for n1bar
        Y0(2*n+i) = Y((noutcycle-1)*ic+noutp,2*n+i); % for n2bar
        Y0(3*n+i) = Pa/(Pmax-Pmin); % for Pbar
    end
    [t,Ys] = ode15s(@PSA_adsorption, tbara, Y0, options);
    for it = 1:(nouta-1) % time
        for i = 1:4*n
            Y(it+ic*(noutcycle-1)+noutp,i) = Ys(it+1,i);
        end
    end
    %
    % Depressurization
    %
    % Initial conditions for depressurization step
    %
     for i = 1:n
        Y0(0*n+i) = Y((noutcycle-1)*ic+noutp+nouta-1,0*n+i); % for
Y1bar
        Y0(1*n+i) = Y((noutcycle-1)*ic+noutp+nouta-1,1*n+i); % for
n1bar
        Y0(2*n+i) = Y((noutcycle-1)*ic+noutp+nouta-1,2*n+i); % for
n2bar
        Y0(3*n+i) = Y((noutcycle-1)*ic+noutp+nouta-1,3*n+i); % for Pbar
     end
     Y0(3*n+n) = Pd/(Pmax-Pmin);
     %
     %
    [t,Ys] = ode15s(@PSA_depressurization, tbardep, Y0, options);
    for it = 1:(noutdep-1) % time
```

```
        for i = 1:4*n
             Y(it+ic*(noutcycle-1)+nouta+noutp-1,i) = Ys(it+1,i);
        end
    end
    %
    % Desorption
    %
    % Initial conditions for desorption step
    %
    for i = 1:n
        Y0(0*n+i) = Y((noutcycle-1)*ic+nouta+noutp+noutdep-2,0*n+i); %
for Y1bar
        Y0(1*n+i) = Y((noutcycle-1)*ic+nouta+noutp+noutdep-2,1*n+i); %
for n1bar
        Y0(2*n+i) = Y((noutcycle-1)*ic+nouta+noutp+noutdep-2,2*n+i); %
for n2bar
        Y0(3*n+i) = Pd/(Pmax-Pmin); % for Pbar
    end
    [t,Ys] = ode15s(@PSA_desorption, tbard, Y0, options);
    for it = 1:(noutd-1) % time
        for i = 1:4*n
            Y(it+ic*(noutcycle-1)+nouta+noutp+noutdep-2,i) =
Ys(it+1,i);
        end
    end
    %
end
%
% One vector to three vectors
%
for it = 1:nout % time
    for i = 1:n % position
        Y1bar(it,i)=Y(it,0*n+i);
        n1bar(it,i)=Y(it,1*n+i);
        n2bar(it,i)=Y(it,2*n+i);
        Pbar(it,i) = Y(it,3*n+i);
        y1bar(it,i) = Y1bar(it,i)/(rhog0*L/(Qa*tt));
        Mg(it,i) = Mg1*y1bar(it,i)+Mg2*(1-y1bar(it,i));
    end
end
%
% Fix the boundary conditions
%
% ODE solver does take care of initial conditions at it = 1
%
for ic = 1:cycle
    for it = 2:(nouta+noutp-1) % time
        i = 1;
        y1bar(it+(noutcycle-1)*(ic-1),i) = y1a;
    end
    %
    for it = 2:(noutdep+noutd-1)
        i = n;
        y1bar(it+(noutcycle-1)*(ic-1)+nouta+noutp-2,i) = y1d;
```

```
    end
end
%
% Isobaric, Isothermal
%
for it = 1:nout
    for i=1:n
        thetabar(it,i) = (T0-Tref)/(Tmax-Tmin);
        rhogbar(it,i) = rhog0*L/(Qa*tt);
    end
end
%
% Formulate nleqmbar(i), n2eqmbar(i), Qbar(i), usbar(i) with inital and
% boundary conditions
%
for it = 1:nout
    for i = 1:n
        py = (y1bar(it,i))*((Pmax-Pmin)*Pbar(it,i)/1013250);
        if py < 0.00013
            n1eqmbar(it,i) = 0;
        else
       n1eqmbar(it,i) = -
(k1*rhob*L/Qa)*(3*0.069337*((y1bar(it,i))*((Pmax-
Pmin)*Pbar(it,i)/1013250))^(-
0.10825)/(1+0.069337*((y1bar(it,i))*((Pmax-
Pmin)*Pbar(it,i)/1013250))^(-0.10825))-0.4633)/2/193.842*1000;
        end
       n2eqmbar(it,i) = 0;
    end
end
%
for it = 1
    for i = 1:n
        Qbar(it,i) = Qa/Qa;
        usbar(it,i) = Qbar(it,i)/rhogbar(it,i);
    end
end
%
for ic = 1:cycle
    for it = 2:(nouta+noutp-1) % time
        for i = 1
            Qbar(it+(noutcycle-1)*(ic-1),i) = Qa/Qa;
            usbar(it+(noutcycle-1)*(ic-1),i) = Qbar(it+(noutcycle-
1)*(ic-1),i)/rhogbar(it+(noutcycle-1)*(ic-1),i);
        end
        for i = 2:n
            Qbar(it+(noutcycle-1)*(ic-1),i) = -
((n1eqmbar(it+(noutcycle-1)*(ic-1),i)-n1bar(it+(noutcycle-1)*(ic-
1),i))+(n2eqmbar(it+(noutcycle-1)*(ic-1),i)-n2bar(it+(noutcycle-1)*(ic-
1),i)))*dzbar+Qbar(it+(noutcycle-1)*(ic-1),i-1);
            usbar(it+(noutcycle-1)*(ic-1),i) = Qbar(it+(noutcycle-
1)*(ic-1),i)/rhogbar(it+(noutcycle-1)*(ic-1),i);
        end
    end
```

```
    for it = 2:(noutdep+noutd-1)
        for i = n
            Qbar(it+(noutcycle-1)*(ic-1)+nouta+noutp-2,i) = -Qd/Qa;
            usbar(it+(noutcycle-1)*(ic-1)+nouta+noutp-2,i) =
Qbar(it+(noutcycle-1)*(ic-1)+nouta+noutp-2,i)/rhogbar(it+(noutcycle-
1)*(ic-1)+nouta+noutp-2,i);
        end
        for i = n-1:-1:1
            Qbar(it+(noutcycle-1)*(ic-1)+nouta+noutp-2,i) =
+((n1eqmbar(it+(noutcycle-1)*(ic-1)+nouta+noutp-2,i)-
n1bar(it+(noutcycle-1)*(ic-1)+nouta+noutp-
2,i))+(n2eqmbar(it+(noutcycle-1)*(ic-1)+nouta+noutp-2,i)-
n2bar(it+(noutcycle-1)*(ic-1)+nouta+noutp-
2,i)))*dzbar+Qbar(it+(noutcycle-1)*(ic-1)+nouta+noutp-2,i+1);
            usbar(it+(noutcycle-1)*(ic-1)+nouta+noutp-2,i) =
Qbar(it+(noutcycle-1)*(ic-1)+nouta+noutp-2,i)/rhogbar(it+(noutcycle-
1)*(ic-1)+nouta+noutp-2,i);
        end
    end
end
%
% Calculate O2 purity
%
O2 = 0;
Product = 0;
for ic = 1:cycle
    for it = 1:((td+tdep)/tstep)
        yy1bar(it) = y1bar(it+(tc*(ic-1)+ta+tp)/tstep+1,1);
        QQdbar(it) = Qbar(it+(tc*(ic-1)+ta+tp)/tstep+1,1);
        c1bar(it) = yy1bar(it)*QQdbar(it);
    end
    t = tstep:tstep:((td+tdep)/tstep);
    O2 = O2 + trapz(t,c1bar);
    Product = Product + trapz(t,QQdbar);
end
Pu = O2/Product;
%
% Calculate O2 recovery
%
O2feed = 0;
for ic = 1:cycle
    for it = 1:((ta+tp)/tstep)
        QQabar(it) = Qbar(it+tc/tstep*(ic-1)+1,1);
    end
    t = tstep:tstep:((ta+tp)/tstep);
    O2feed = O2feed + trapz(t,QQabar)*y1a;
end
Re = -O2/O2feed;

% Calculate the amount of adsorbent (g)

m = A*L*rhob;
%
```

```
% Calculate O2 Productivity (mmol/sec/kg)
%
Pro = qa/m*1000*Re;
%
% Display selected output
%
fprintf('\n abstol = %8.1e  reltol = %8.1e\n', abstol, reltol);
fprintf('\n ncall = %4d\n', ncall);
%
% Display important parameters
%
fprintf('\n process step = %d     dYbardZbar differential method = %d',
adsorptionORpurge, dYbardZbarDifferentialMethod);
fprintf('\n P0 = %g atm     T0 = %g K    yN20 = %g    Q0 = %g
mmol/cm2/sec', P0/1013250, T0, (1-y10), Q0);
fprintf('\n ta = %g sec     ta = %g K    yN2feed = %g    Qa = %g
mmol/cm2/sec    Qa = %g mmol/sec', ta, ta, (1-y1a), Qa, Qa);
fprintf('\n dp = %g um     L = %g cm    D = %g cm', dp*10000, L, D);
fprintf('\n k1 = %g sec-1    k2 = %g sec-1    rhob = %g g/ml', k1, k2,
rhob);
fprintf('\n Adsorbent mass = %g g', m);
fprintf('\n O2 purity = %g    Oxygen Recovery = %g    Oxygen
productivity = %g mmol/sec/kg\n\n', Pu, Re, Pro);
%
% Plot numerical solutions vs independent variables (t,z)
%
z0 = 0.0;
zend = L;
z = linspace(z0,zend,n);

t0 = 0.0;
tend = tt;
t = linspace(t0,tend,nout);
%
if choose == 1 % start of choose == 1 : 2D subplots of y1, y2, n1, n2,
T, P
    %
    % Subplots of y1, y2, n1, n2, T, P
    %
    figure(1);

    subplot(2,2,1)
    plot(t,y1bar(:,(n+1)/2),'-r',t,(1-y1bar(:,(n+1)/2)),'-b'); % axis
tight
    h = legend('y_{O2}','y_{N2}',1);
    title('y_{O2} and y_{N2} vs. time at L/2');
    xlabel('time (sec)');
    ylabel('y_{O2} and y_{N2}')

    subplot(2,2,2)
    plot(t,(Qa/(k1*rhob*L)).*n1bar(:,(n+1)/2),'-
r',t,(Qa/(k2*rhob*L).*n2bar(:,(n+1)/2)),'-b'); % axis tight
    h = legend('n_{O2}','n_{N2}',1);
```

```
    title('n_{O2} and n_{N2} vs. time at L/2');
    xlabel('time (sec)');
    ylabel('n_{O2} and n_{N2} (mmol/g adsorbent')

    subplot(2,2,3)
    plot(t,Tref+(Tmax-Tmin).*thetabar(:,(n+1)/2)); % axis tight
    title('T vs. time at L/2');
    xlabel('time (sec)');
    ylabel('T (K)')

    subplot(2,2,4)
    plot(z,((Pmax-Pmin)/1013250).*Pbar(nout,:)); % axis tight
    title('P vs. bed axial position at tfinal');
    xlabel('Bed axial position, z (cm)');
    ylabel('P (atm)')
end % end of choose == 1
%
if choose == 2 % start of choose == 2 : Individual 2D plots
    %
    figure(2)
    plot(t,y1bar(:,n),'-r>',t,(1-y1bar(:,n)),'-
bs','LineWidth',2,'MarkerSize',3)
    legend('y_{O2}','y_{N2}');
    xlabel('Time, t (sec)','color','k','fontsize',10,'fontweight','b')
    ylabel('Gas phase mole fraction, y_{O2} and
y_{N2}','color','k','fontsize',10,'fontweight','b')
    title('Gas phase mole fraction vs. time at the last
cell','color','k','fontsize',12,'fontweight','b');
    axis([0 tt 0 1])
    grid on
    %
    figure(3)
    plot(t,y1bar(:,1),'-r>',t,(1-y1bar(:,1)),'-
bs','LineWidth',2,'MarkerSize',3)
    legend('y_{O2}','y_{N2}');
    xlabel('Time, t (sec)','color','k','fontsize',10,'fontweight','b')
    ylabel('Gas phase mole fraction, y_{O2} and
y_{N2}','color','k','fontsize',10,'fontweight','b')
    title('Gas phase mole fraction vs. time at the first
cell','color','k','fontsize',12,'fontweight','b');
    axis([0 tt 0 1])
    grid on
    %
    figure(4)
    y1outbar(1) = y1bar(1,n);
    for ic = 1:cycle
        for it = 1:((ta+tp)/tstep)
            y1outbar(it+(tc*(ic-1))/tstep+1) = y1bar(it+(tc*(ic-
1))/tstep+1,n);
        end
        for it = 1:((td+tdep)/tstep)
            y1outbar(it+(tc*(ic-1)+ta+tp)/tstep+1) = y1bar(it+(tc*(ic-
1)+ta+tp)/tstep+1,1);
```

```
        end
    end
    plot(t,y1outbar,'-r>','LineWidth',2,'MarkerSize',3)
    xlabel('Time, t (sec)','color','k','fontsize',10,'fontweight','b')
    ylabel('O2 mole fraction, y_{O2} and
y_{N2}','color','k','fontsize',10,'fontweight','b')
    title('O2 mole fraction vs. time at the
outlet','color','k','fontsize',12,'fontweight','b');
    axis([0 tt 0 1])
    grid on
    %
    % Amount adsorbed on adsorbent, n1 and n2, vs. time at L/2
    %
    figure(5)
    plot(t,(Qa/(k1*rhob*L)).*n1bar(:,n),'-
r>',t,(Qa/(k2*rhob*L)).*n2bar(:,n),'-bs','LineWidth',2,'MarkerSize',3);
    legend('n_{O2}','n_{N2}');
    title('Amount adsorbed on adsorbent vs. time at the last
cell','color','k','fontsize',12,'fontweight','b');
    xlabel('Time, t (sec)','color','k','fontsize',10,'fontweight','b');
    ylabel('Amount adsorbed on adsorbent, n_{O2} and n_{N2} (mmol/g
adsorbent)','color','k','fontsize',10,'fontweight','b')
    grid on
    %
    % Temperature, T, vs. time at L/2
    %
    figure(6)
    plot(t,(Tref+(Tmax-Tmin).*thetabar(:,(n+1)/2)),'LineWidth',2)
    xlabel('Time, t (sec)','color','k','fontsize',10,'fontweight','b')
    ylabel('Temperature, T
(K)','color','k','fontsize',10,'fontweight','b')
    title('Temperature vs. time
','color','k','fontsize',12,'fontweight','b');
    grid on
    %
    % Pressure, P, vs. time
    %
    figure(6)
    plot(t,((Pmax-Pmin)/1013250).*Pbar(:,(n+1)/2),'LineWidth',2)
    xlabel('Time, t (sec)','color','k','fontsize',10,'fontweight','b')
    ylabel('Pressure, P
(atm)','color','k','fontsize',10,'fontweight','b')
    title('Pressure vs.
time','color','k','fontsize',12,'fontweight','b');
    grid on
    %
end % end of choose == 2
%
if choose == 3 % start of choose == 3 : Surface plots of y1, y2, n1,
n2, T, P, rhog, Q, us
    %
    % Gas phase mole fraction, y1
    %
    figure(7)
```

```
    surf(z,t,y1bar,'edgecolor','none')
    colormap jet
    xlabel('Bed axial position, z
(cm)','color','k','fontsize',10,'fontweight','b')
    ylabel('Time, t (sec)','color','k','fontsize',10,'fontweight','b')
    zlabel('Gas phase mole fraction,
y_{O2}','color','k','fontsize',10,'fontweight','b')
    axis tight
    %
    % Gas phase mole fraction, y2
    %
    figure(8)
    surf(z,t,(1-y1bar),'edgecolor','none')
    colormap jet
    xlabel('Bed axial position, z
(cm)','color','k','fontsize',10,'fontweight','b')
    ylabel('Time, t (sec)','color','k','fontsize',10,'fontweight','b')
    zlabel('Gas phase mole fraction,
y_{N2}','color','k','fontsize',10,'fontweight','b')
    axis tight
    %
    % Amount adsorbed on adsorbent, n1
    %
    figure(9)
    surf(z,t,(Qa/(k1*rhob*L)).*n1bar,'edgecolor','none')
    colormap jet
    xlabel('Bed axial position, z
(cm)','color','k','fontsize',10,'fontweight','b')
    ylabel('Time, t (sec)','color','k','fontsize',10,'fontweight','b')
    zlabel('Amount adsorbed on adsorbent, n_{O2} (mmol/g
adsorbent)','color','k','fontsize',10,'fontweight','b')
    axis tight
    %
    % Temperature, T
    %
    figure(10)
    surf(z,t,(Tmin+(Tmax-Tmin).*thetabar),'edgecolor','none')
    colormap jet
    xlabel('Bed axial position, z
(cm)','color','k','fontsize',10,'fontweight','b')
    ylabel('Time, t (sec)','color','k','fontsize',10,'fontweight','b')
    zlabel('Temperature, T
(K)','color','k','fontsize',10,'fontweight','b')
    axis tight
    %
    % Pressure, P
    %
    figure(11)
    surf(z,t,((Pmax-Pmin)/1013250).*Pbar,'edgecolor','none')
    colormap jet
    xlabel('Bed axial position, z
(cm)','color','k','fontsize',10,'fontweight','b')
    ylabel('Time, t (sec)','color','k','fontsize',10,'fontweight','b')
```

```
    zlabel('Pressure, P
(atm)','color','k','fontsize',10,'fontweight','b')
    axis tight
    %
end % end of choose == 3
%
if choose == 4 % start of choose 4 : The contour plots
    %
    % Among nout points, take 5 time points spreading evenly between
    % [0,ta]
    %
    for m = 1:5
        it(m) = 1+(m-1)*(nout-1)/4;
    end
    % If nout = 101 ==> it = 1 26 51 76 101

    for m = 1:5
        time((m)) = t(it(m));
    end
    %
    % Adsorption/Desorption profiles
    %
    % particle diameter in micrometer
    dp = dp * 10000;

    if adsorptionORpurge == 111
        % O2 initially present in the bed
        O2ingas = epsilon*A*L*(y10)*rhog0; % mmoles O2
        O2insolid = A*L*rhob*n10; % mmoles O2
        TotalO2inbed0_mmolesO2 = O2ingas + O2insolid % mmoles O2

        % O2 remaining at every it, average over the whole bed i = 1:n
        for it = 1:nout
            ylacc(it) = 0;
            rhogbaracc(it) = 0;
            n1baracc(it) = 0;
            for i = 1:n
                ylacc(it) = y1bar(it,i) + ylacc(it);
                rhogbaracc(it) = rhogbar(it,i) + rhogbaracc(it);
                n1baracc(it) = n1bar(it,i)+n1baracc(it);
            end
            y1ave(it) = ylacc(it)/n;
            rhogave(it) = (Qa*ta/L)*rhogbaracc(it)/n;
            n1ave(it) = (Qa/(k1*rhob*L))*n1baracc(it)/n;
        end

        for it = 1:nout
            O2remainingas(it) = epsilon*A*L*y1ave(it)*rhogave(it); %
mmoles O2
            O2remaininsolid(it) = A*L*rhob*n1ave(it); % mmoles O2
            TotalO2remaininbed_mmolesO2(it) =
O2remainingas(it)+O2remaininsolid(it);
            % mmoles O2
```

```
            frac_O2_desorbed(it) = (TotalO2inbed0_mmolesO2 -
TotalO2remaininbed_mmolesO2(it))/TotalO2inbed0_mmolesO2;
        end

        frac_O2_desorbedv = frac_O2_desorbed';
    end

    if adsorptionORpurge == 222
        % N2 initially present in the bed
        N2ingas = epsilon*A*L*(1-y10)*rhog0; % mmoles N2
        N2insolid = A*L*rhob*n20; % mmoles N2
        TotalN2inbed0_mmolesN2 = N2ingas + N2insolid % mmoles N2

        % N2 remaining at every it, average over the whole bed i = 1:n
        for it = 1:nout
            y2acc(it) = 0;
            rhogbaracc(it) = 0;
            n2baracc(it) = 0;
            for i = 1:n
                y2acc(it) = (1-y1bar(it,i)) + y2acc(it);
                rhogbaracc(it) = rhogbar(it,i) + rhogbaracc(it);
                n2baracc(it) = n2bar(it,i)+n2baracc(it);
            end
            y2ave(it) = y2acc(it)/n;
            rhogave(it) = (Qa*ta/L)*rhogbaracc(it)/n;
            n2ave(it) = (Qa/(k2*rhob*L))*n2baracc(it)/n;
        end

        for it = 1:nout
            N2remainingas(it) = epsilon*A*L*y2ave(it)*rhogave(it); %
mmoles N2
            N2remaininsolid(it) = A*L*rhob*n2ave(it); % mmoles N2
            TotalN2remaininbed_mmolesN2(it) =
N2remainingas(it)+N2remaininsolid(it);
            % mmoles N2
            frac_N2_desorbed(it) = (TotalN2inbed0_mmolesN2 -
TotalN2remaininbed_mmolesN2(it))/TotalN2inbed0_mmolesN2;
        end

        frac_N2_desorbedv = frac_N2_desorbed';
    end
    %

    figure(12)
    plot(zbar,(y1bar(1,:)),zbar,(y1bar((nout-
1)*0.2+1,:)),zbar,(y1bar((nout-1)*0.4+1,:)),zbar,(y1bar((nout-
1)*0.6+1,:)),zbar,(y1bar((nout-
1)*0.8+1,:)),zbar,(y1bar(nout,:)),'LineWidth',2,'MarkerSize',3); %axis
tight

legend('tbar=0.0','tbar=0.2','tbar=0.4','tbar=0.6','tbar=0.8','tbar=1.0
',1);
```

```
    text(.02,1.05,['\fontsize{11}d_p = ',num2str(dp),'\mum ;
\fontsize{11}L =',num2str(L),' cm ; \fontsize{11}D = ', num2str(D),'
cm'])
    if adsorptionORpurge == 111
        title('Contour plot of oxygen mole
fraction','color','k','fontsize',12,'fontweight','b');
    end
    if adsorptionORpurge == 222
        title('Contour plot of oxygen mole
fraction','color','k','fontsize',12,'fontweight','b');
    end
    xlabel('Bed axial position,
zbar','color','k','fontsize',12,'fontweight','b')
    ylabel('y_{O2}','color','k','fontsize',12,'fontweight','b')
    axis([0 1 0 1.1])

    figure(13)
    plot(zbar,(1-y1bar(1,:)),zbar,(1-y1bar((nout-1)*0.2+1,:)),zbar,(1-
y1bar((nout-1)*0.4+1,:)),zbar,(1-y1bar((nout-1)*0.6+1,:)),zbar,(1-
y1bar((nout-1)*0.8+1,:)),zbar,(1-
y1bar(nout,:)),'LineWidth',2,'MarkerSize',3); %axis tight

legend('tbar=0.0','tbar=0.2','tbar=0.4','tbar=0.6','tbar=0.8','tbar=1.0
',1);
    text(.02,1.05,['\fontsize{11}d_p = ',num2str(dp),'\mum ;
\fontsize{11}L =',num2str(L),' cm ; \fontsize{11}D = ', num2str(D),'
cm'])
    if adsorptionORpurge == 111
        title('Contour plot of Nitrogen mole
fraction','color','k','fontsize',12,'fontweight','b');
    end
    if adsorptionORpurge == 222
        title('Contour plot of Nitrogen mole
fraction','color','k','fontsize',12,'fontweight','b');
    end
    xlabel('Bed axial position,
zbar','color','k','fontsize',12,'fontweight','b')
    ylabel('y_{N2}','color','k','fontsize',12,'fontweight','b')
    axis([0 1 0 1.1])

    figure(14)

plot(zbar,((Qa/(k1*rhob*L)).*n1bar(1,:)),zbar,((Qa/(k1*rhob*L)).*n1bar(
(nout-1)*0.2+1,:)),zbar,((Qa/(k1*rhob*L)).*n1bar((nout-
1)*0.4+1,:)),zbar,((Qa/(k1*rhob*L)).*n1bar((nout-
1)*0.6+1,:)),zbar,((Qa/(k1*rhob*L)).*n1bar((nout-
1)*0.8+1,:)),zbar,((Qa/(k1*rhob*L)).*n1bar(nout,:)),'LineWidth',2,'Mark
erSize',3); %axis tight

legend('tbar=0.0','tbar=0.2','tbar=0.4','tbar=0.6','tbar=0.8','tbar=1.0
',1);
    if adsorptionORpurge == 111
```

```
        title('Contour plot of adsorbed
oxygen','color','k','fontsize',12,'fontweight','b');
    end
    if adsorptionORpurge == 222
        title('Contour plot of adsorbed
oxygen','color','k','fontsize',12,'fontweight','b');
    end
    xlabel('Bed axial position,
zbar','color','k','fontsize',12,'fontweight','b')
    ylabel('n_{O2} (mmoles
O_2/g)','color','k','fontsize',12,'fontweight','b')
end
```

APPENDIX C

MATLAB PROGRAM FOR MODEL INPUTS

```
% parameters shared with the ODE routine
%
global Mg1 Mg2 Mg De1 De2 taup dYbardZbarDifferentialMethod Qa Qd rhog0
T0 n n10 n20 tbar tbara tbarp tbardep tbard nouta noutp noutdep noutd
noutcycle noutstep dzbar dtbar miu epsilon epsilonbar tc tt tstep k1 k2
k3 k4 q1 q2 Cs Cg rhob R dp L ta td tp tdep y1a y2a y1d y10 y2d Qin P0
Pa Pd Ta Td Pmax Pmin Tmax Tmin Tref Q0 kg MassAxial dtbara dtbarp
dtbardep dtbard
%
% Select differential method for dYbardZbar
dYbardZbarDifferentialMethod = 777;
% dYbardZbarDifferentialMethod = 333; 1st order (2 points) upwind
differe
% dYbardZbarDifferentialMethod = 444; 2nt order (3 points) upwind
differe
% dYbardZbarDifferentialMethod = 777; 2nd order TVD Superbee Flux
Limiter
%
% Select Mass Axial Dispersions
%
MassAxial = 881;
% Mass2=Axial = 881; Shut off mass axial dispersion
% MassAxial = 882; Turn on mass axial dispersion, need 2nd BC
%
% Select type of plots
%
choose = 2;
% choose = 1: 2D subplots of y1, y2, n1, n2, T, P
% choose = 2: Individual 2D plots of y1, y2, n1, n2, T, P
% choose = 3: Surface plots of y1, y2, n1, n2, T, P
% choose = 4: The contour plots
%
% Define number of nodes along t and along z
%
tstep = 1; % step time, sec
n = 15; % nodes along z
%
%
% Define cycles
cycle = 5; % Number of cycles
ta = 10; % adsorption time, sec
tp = 5; % pressurization time, sec
td = 10; % desorption time, sec
tdep = 5; % depressurization time, sec
tc = ta+tp+td+tdep; % cycle time, sec
tt = tc*cycle; % total time, sec
%
% Define dimensionless z and dz
%
zbarl = 0.0; % zbar lower limit, zbar = 0/L
zbaru = 1.0; % zbar upper limit, zbar = L/L
dzbar = (zbaru-zbarl)/(n-1); % zbar differential space
zbar = linspace(zbarl, zbaru, n);
%
```

```
% Define dimensionless t and dt
% Independent variable, tbar, for ODE integration
%
tbarl = 0.0; % tbar lower limit, tbar = 0/tfeed
tbaru = 1.0; % tbar upper limit, tbar = tfeed
nout = tt/tstep+1; % total nodes along t
nouta = ta/tstep+1; % nodes of adsorption step
noutd = td/tstep+1; % nodes of desorption step
noutp = tp/tstep+1; % nodes of pressurization step
noutdep = tdep/tstep+1; % nodes of depressurization step
noutcycle = tc/tstep+1; % nodes of t along a cycle
dtbara = (tbaru-tbarl)/(nouta-1); % tbar differential space when
adsorption
dtbard = (tbaru-tbarl)/(noutd-1); % tbar differential space when
desorption
dtbarp = (tbaru-tbarl)/(noutp-1); % tbar differential space when
pressurization
dtbardep = (tbaru-tbarl)/(noutdep-1); % tbar differential space when
depressurization
dtbar = (tbaru-tbarl)/(nout-1); % tbar differential space for all the
process
tbara = linspace(tbarl,dtbar*(nouta-1),nouta); % horizontal tbar when
adsorption
tbard = linspace(tbarl,dtbar*(noutd-1),noutd); % horizontal tbar when
desorption
tbarp = linspace(tbarl,dtbar*(noutp-1),noutp); % horizontal tbar when
pressurization
tbardep = linspace(tbarl,dtbar*(noutdep-1),noutdep); % horizontal tbar
when depressurization
%
% Packed bed dimensions
L = 30.48; % bed length, cm
D = 2.54; % bed diameter, cm
A = pi*(D/2)^2; % bed cross-sectional area, cm2
rhob = 1.574; % bulk density, g/cm3
%
% Adsorbent properties
%
dp = 0.100; % particle diameter, cm
epsilon = 0.51; % total column (helium) void fraction = ep x (1-e)+e
epsilonp = 0.3; % internal/intraparticle void fraction
epsilonbar = 0.3; % external/interparticle void fraction
taup = 1; % particle tortuosity factor
Cs = 0.28; % adsorbent (solid phase) heat capacity, cal/g/K
%
% Feed conditions at i = 1 (adsorption)
%                 at i = n (purge)
%
y1a = 0.21; % feed gas composition, 21% O2 + 79% N2
y2a = 0.79; % feed gas composition, 21% O2 + 79% N2
Ta = 873; % feed temperature, K
qa = 2.08; % feed mass flow rate, mmol/sec
Pa = 1.36*1013250; % pressure at i=n during adsorption, g/cm/sec2
```

```
y1d = 0; % feed gas composition, 0% O2 + 100% N2
y2d = 1; % feed gas composition, 0% O2 + 100% N2
Td = 873; % feed temperature, K
qd = 0.409; % feed mass flow rate, mmol/sec
Pd = 0.136*1013250; % pressure at i=1 during desorption, g/cm/sec2

% Bed initial conditions
y10 = 0; % saturated with 0% O2 + 100% N2
y20 = 1;
P0 = 1*1013250; % pressure after pressurization step, g/cm/sec2
T0 = 873; % temperature after pressurization step, K
%
% Langmuir isotherms of O2 and N2 on adsorbent
% n1eqm0 =
0.1895*exp(925.0/ta)*2.534*exp(2865.0/ta)*(y10)*P0/(1+2.534*exp(2865/ta
)*y10*P0);
n1eqm0 = 0;
n2eqm0 = 0;
n10 = n1eqm0; % O2 adsorbed, mmol O2/g
n20 = n2eqm0; % N2 adsorbed, mmol N2/g
%
% Gas peoperties
%
R = 8.314472*10^4; % gas constant, g.cm2/k/mmol/sec2
Cg = 0.00687; % gas phase heat capacity, cal/mmol/K
kg = 6.44e-5; % gas phase (Air at 1 atm 295K) thermal conductivity
              % cal/cm/sec/K
miu = 18.2385e-5; % air dynamic viscosity at 25 C and 1 atm, g/cm/sec
Mg1 = 0.032; % O2 molecular weight, g/mmol
Mg2 = 0.028; % N2 molecular weight, g/mmol
q1 = 3.16; % isosteric heat of adsorption of O2 on adsorbent, cal/mmol
q2 = 5.60; % isosteric heat of adsorption of N2 on adsorbent, cal/mmol
%
% Mass flux and superficial velocity
Qa = qa/A; % mass flux, mmol/cm2/sec
Qd = qd/A;
% usfeed = Qa/rhog; % superficial velocity. cm/sec
%
Q0 = 0; % without gas flux, mmol/cm2/sec
rhog0 = P0/(R*T0); % gas phase density, mmol/cm3
us0 = Qin/rhog0; % superficial velocity, cm/sec
% Mass transfer kinetic
% Gas-solid mass transfer
E1 = 0.45*q1*4184; % J/mol
E2 = 0.45*q2*4184; % J/mol
De1 = 1.61*10^(-6)*exp(-E1/8.314/298)*10^4; % O2 effective diffusivity
in adsorbent cm2/s
De2 = 1.61*10^(-6)*exp(-E2/8.314/298)*10^4; % N2 effective diffusivity
in adsorbent cm2/s

k1 = 15*De1/(dp/2)^2; % O2 overall mass transfer coefficient, sec-1
k2 = 15*De2/(dp/2)^2; % N2 overall mass transfer coefficient, sec-1
```

```
%
% Additional parameters required for proper nondimensionalization of
% dependent variables
%
Pmax = Pa; % maximum pressure, g/cm/sec2
Pmin = 0; % minimum pressure, g/cm/sec2
Tref = T0;
Tmax = Ta; % maximum temperature, K
Tmin = 273; % minimum temperature, K
```

APPENDIX D

MATLAB PROGRAM FOR ADSORPTION STEP

```
% Solve for y1, n1, n2, P, rhog, Q, us
%
function yt = PSA_adsorption(t,Y)
%
% parameters shared with the ODE routine
%
global Mg1 Mg2 De1 De2 taup dYbardZbarDifferentialMethod rhog0 T0 ncall
n dzbar dtbar epsilon epsilonbar k1 k2 rhob dp L tc tt y1a Qin Qa Pa
Pmax Pmin Tmax Tmin Tref MassAxial dtbara dtbarp dtbardep dtbard miu ta
tp td tdep
%
% preallocating
%
Y1bar = zeros(1,n);
n1bar = zeros(1,n);
n2bar = zeros(1,n);
y1bar = zeros(1,n);
Mg = zeros(1,n);
Pbar = zeros(1,n);
thetabar = zeros(1,n);
rhogbar = zeros(1,n);
n1eqmbar = zeros(1,n);
n2eqmbar = zeros(1,n);
Qbar = zeros(1,n);
usbar = zeros(1,n);
convecy1bar = zeros(1,n);
DL = zeros(1,n);
dY1bardtbar = zeros(1,n);
dn1bardtbar = zeros(1,n);
dn2bardtbar = zeros(1,n);
Yt = zeros(1,4*n);
Qin = Qa;
%
% One vector to four vectors
%
for i = 1:n
    Y1bar(i) = Y(0*n+i);
    n1bar(i) = Y(1*n+i);
    n2bar(i) = Y(2*n+i);
    Pbar(i) = Y(3*n+i);
end
for i = 1:n
    y1bar(i) = Y1bar(i)/(rhog0*L/(Qa*tt));
    Mg(i) = Mg1*y1bar(i)+Mg2*(1-y1bar(i));
end
%
% Boundary conditions after initial conditions
%
if (ncall~=0) % not initial condition
    i = 1; % Only use boundary conditions at the adsorption inlet
    y1bar(i) = y1a;
    Y1bar(i) = y1a*(rhog0*L/(Qa*tt));
end
% Formulate pre-parameters for ODEs
```

```
%
% Isobaric, Isothermal
%
for i = 1:n
    Pbar(i) = Pa/(Pmax-Pmin);
    thetabar(i) = (T0-Tref)/(Tmax-Tmin);
    rhogbar(i) = rhog0*L/(Qa*tt);
end
%
% Formulate n1eqmbar(i), n2eqmbar(i), Qbar(i), usbar(i) with initial
and
% boundary conditions
%
for i = 1:n
    py = (y1bar(i))*((Pmax-Pmin)*Pbar(i)/1013250);
    if py < 0.00013
        n1eqmbar(i) = 0;
    else
    n1eqmbar(i) = -(k1*rhob*L/Qa)*(3*0.069337*((y1bar(i))*((Pmax-
Pmin)*Pbar(i)/1013250))^(-0.10825)/(1+0.069337*((y1bar(i))*((Pmax-
Pmin)*Pbar(i)/1013250))^(-0.10825))-0.4633)/2/193.842*1000;
    end
    n2eqmbar(i) = 0;
end

if (ncall == 0)
    for i = 1:n
        Qbar(i) = Qin/Qa;
        usbar(i) = Qbar(i)/rhogbar(i);
    end
end

if (ncall ~= 0)
        for i = 1
            Qbar(i) = Qin/Qa;
            usbar(i) = Qbar(i)/rhogbar(i);
        end
        for i = 2:n
            Qbar(i) = -((n1eqmbar(i)-n1bar(i))+(n2eqmbar(i)-
n2bar(i)))*dzbar+Qbar(i-1);
            usbar(i) = Qbar(i)/rhogbar(i);
        end
end
%
% Formulate gas phase axial dispersion coefficient in mass balance, DL,
% cm2/sec
%
if MassAxial == 881
    for i = 1:n
        DL(i) = 0;
    end
end
```

```
if MassAxial == 882
        DM = (epsilon/taup)*(1/(1/De1+1/De2));
    for i = 1:n
        DL(i) = 0.7*DM +
0.5*dp*(abs(Qbar(i))*Qa)/(rhogbar(i)*(Qa*tt/L)*epsilonbar);
    end
end
%
%
% Start of 1st order (2 points) upwind difference
if dYbardZbarDifferentialMethod == 333
    %
    % Formulate convective terms for i = 3:n-2
    %
    for i = 3:n-2
        % Le = left edge of cell
        Qbar_eps_Le = (Qbar(i-1)+Qbar(i))/(2*epsilon);
        % Re = right edge of cell
        Qbar_eps_Re = (Qbar(i)+Qbar(i+1))/(2*epsilon);

        % for left edge i-1/2
        if Qbar_eps_Le >= 0
            flowdirectionLe = 1;

            ry1barLe = (y1bar(i-1)-y1bar(i-2))/(y1bar(i)-y1bar(i-1));
        elseif Qbar_eps_Le <= 0
            flowdirectionLe = -1;

            ry1barLe = (y1bar(i+1)-y1bar(i))/(y1bar(i)-y1bar(i-1));
        end

        superbeey1barLe = 0;

        fluxy1barLe = 0.5*Qbar_eps_Le*((1+flowdirectionLe)*y1bar(i-
1)+(1-flowdirectionLe)*y1bar(i))+0.5*abs(Qbar_eps_Le)*(1-
abs(Qbar_eps_Le*dtbar/dzbar))*superbeey1barLe*(y1bar(i)-y1bar(i-1));

        % for right edge i+1/2
        if Qbar_eps_Re >= 0
            flowdirectionRe = 1;

            ry1barRe = (y1bar(i)-y1bar(i-1))/(y1bar(i+1)-y1bar(i));
        elseif Qbar_eps_Re <= 0
            flowdirectionRe = -1;

            ry1barRe = (y1bar(i+2)-y1bar(i+1))/(y1bar(i+1)-y1bar(i));
        end

        superbeey1barRe = 0;
```

```
        fluxy1barRe = 0.5*Qbar_eps_Re*((1+flowdirectionRe)*y1bar(i)+(1-
flowdirectionRe)*y1bar(i+1))+0.5*abs(Qbar_eps_Re)*(1-
abs(Qbar_eps_Re*dtbar/dzbar))*superbeey1barRe*(y1bar(i+1)-y1bar(i));

        convecy1bar(i) = (fluxy1barLe-fluxy1barRe)/dzbar;
    end
    %
    % Formulate convective terms for i = 1, 2, n-1, n
    %
    for i = 1
        Qbar_eps_Le = (Qbar(i)+Qbar(i))/(2*epsilon);
        Qbar_eps_Re = (Qbar(i)+Qbar(i+1))/(2*epsilon);

        % for left edge i-1/2
         if Qbar_eps_Le >= 0
            flowdirectionLe = 1;
            ry1barLe = 1;
        elseif Qbar_eps_Le <= 0
            flowdirectionLe = -1;
            ry1barLe = 1;
        end

        superbeey1barLe = 0;

        fluxy1barLe = 0.5*Qbar_eps_Le*((1+flowdirectionLe)*y1bar(i)+(1-
flowdirectionLe)*y1bar(i))+0.5*abs(Qbar_eps_Le)*(1-
abs(Qbar_eps_Le*dtbar/dzbar))*superbeey1barLe*(y1bar(i)-y1bar(i));

        % for right edge i+1/2
        if Qbar_eps_Re >= 0
            flowdirectionRe = 1;
            ry1barRe = 0;
        elseif Qbar_eps_Re <= 0
            flowdirectionRe = -1;
            ry1barRe = (y1bar(i+2)-y1bar(i+1))/(y1bar(i+1)-y1bar(i));
        end

        superbeey1barRe = 0;

        fluxy1barRe = 0.5*Qbar_eps_Re*((1+flowdirectionRe)*y1bar(i)+(1-
flowdirectionRe)*y1bar(i+1))+0.5*abs(Qbar_eps_Re)*(1-
abs(Qbar_eps_Re*dtbar/dzbar))*superbeey1barRe*(y1bar(i+1)-y1bar(i));

        convecy1bar(i) = (fluxy1barLe-fluxy1barRe)/dzbar;
    end
    %
    for i = 2
        Qbar_eps_Le = (Qbar(i-1)+Qbar(i))/(2*epsilon);
        Qbar_eps_Re = (Qbar(i)+Qbar(i+1))/(2*epsilon);

        % for left edge i-1/2
         if Qbar_eps_Le >= 0
```

```
            flowdirectionLe = 1;
            ry1barLe = 0;
        elseif Qbar_eps_Le <= 0
            flowdirectionLe = -1;
            ry1barLe = (y1bar(i+1)-y1bar(i))/(y1bar(i)-y1bar(i-1));
        end

        superbeey1barLe = 0;

        fluxy1barLe = 0.5*Qbar_eps_Le*((1+flowdirectionLe)*y1bar(i-
1)+(1-flowdirectionLe)*y1bar(i))+0.5*abs(Qbar_eps_Le)*(1-
abs(Qbar_eps_Le*dtbar/dzbar))*superbeey1barLe*(y1bar(i)-y1bar(i-1));

        % for right edge i+1/2
        if Qbar_eps_Re >= 0
            flowdirectionRe = 1;
            ry1barRe = (y1bar(i)-y1bar(i-1))/(y1bar(i+1)-y1bar(i));
        elseif Qbar_eps_Re <= 0
            flowdirectionRe = -1;
            ry1barRe = (y1bar(i+2)-y1bar(i+1))/(y1bar(i+1)-y1bar(i));
        end

        superbeey1barRe = 0;

        fluxy1barRe = 0.5*Qbar_eps_Re*((1+flowdirectionRe)*y1bar(i)+(1-
flowdirectionRe)*y1bar(i+1))+0.5*abs(Qbar_eps_Re)*(1-
abs(Qbar_eps_Re*dtbar/dzbar))*superbeey1barRe*(y1bar(i+1)-y1bar(i));

        convecy1bar(i) = (fluxy1barLe-fluxy1barRe)/dzbar;
    end
    %
    for i = n-1
        Qbar_eps_Le = (Qbar(i-1)+Qbar(i))/(2*epsilon);
        Qbar_eps_Re = (Qbar(i)+Qbar(i+1))/(2*epsilon);

        % for left edge i-1/2
         if Qbar_eps_Le >= 0
            flowdirectionLe = 1;
            ry1barLe = (y1bar(i-1)-y1bar(i-2))/(y1bar(i)-y1bar(i-1));
        elseif Qbar_eps_Le <= 0
            flowdirectionLe = -1;
            ry1barLe = (y1bar(i+1)-y1bar(i))/(y1bar(i)-y1bar(i-1));
        end

        superbeey1barLe = 0;

        fluxy1barLe = 0.5*Qbar_eps_Le*((1+flowdirectionLe)*y1bar(i-
1)+(1-flowdirectionLe)*y1bar(i))+0.5*abs(Qbar_eps_Le)*(1-
abs(Qbar_eps_Le*dtbar/dzbar))*superbeey1barLe*(y1bar(i)-y1bar(i-1));

        % for right edge i+1/2
        if Qbar_eps_Re >= 0
```

```
            flowdirectionRe = 1;
            ry1barRe = (y1bar(i)-y1bar(i-1))/(y1bar(i+1)-y1bar(i));
        elseif Qbar_eps_Re <= 0
            flowdirectionRe = -1;
            ry1barRe = 0;
        end

        superbeey1barRe = 0;

        fluxy1barRe = 0.5*Qbar_eps_Re*((1+flowdirectionRe)*y1bar(i)+(1-
flowdirectionRe)*y1bar(i+1))+0.5*abs(Qbar_eps_Re)*(1-
abs(Qbar_eps_Re*dtbar/dzbar))*superbeey1barRe*(y1bar(i+1)-y1bar(i));

        convecy1bar(i) = (fluxy1barLe-fluxy1barRe)/dzbar;
    end
    %
    for i = n
        Qbar_eps_Le = (Qbar(i-1)+Qbar(i))/(2*epsilon);
        Qbar_eps_Re = (Qbar(i)+Qbar(i))/(2*epsilon);

        % for left edge i-1/2
         if Qbar_eps_Le >= 0
            flowdirectionLe = 1;
            ry1barLe = (y1bar(i-1)-y1bar(i-2))/(y1bar(i)-y1bar(i-1));
        elseif Qbar_eps_Le <= 0
            flowdirectionLe = -1;
            ry1barLe = 0;
        end

        superbeey1barLe = 0;

        fluxy1barLe = 0.5*Qbar_eps_Le*((1+flowdirectionLe)*y1bar(i-
1)+(1-flowdirectionLe)*y1bar(i))+0.5*abs(Qbar_eps_Le)*(1-
abs(Qbar_eps_Le*dtbar/dzbar))*superbeey1barLe*(y1bar(i)-y1bar(i-1));

        % for right edge i+1/2
        if Qbar_eps_Re >= 0
            flowdirectionRe = 1;
            ry1barRe = 1;
        elseif Qbar_eps_Re <= 0
            flowdirectionRe = -1;
            ry1barRe = 1;
        end

        superbeey1barRe = 0;

        fluxy1barRe = 0.5*Qbar_eps_Re*((1+flowdirectionRe)*y1bar(i)+(1-
flowdirectionRe)*y1bar(i))+0.5*abs(Qbar_eps_Re)*(1-
abs(Qbar_eps_Re*dtbar/dzbar))*superbeey1barRe*(y1bar(i)-y1bar(i));

        convecy1bar(i) = (fluxy1barLe-fluxy1barRe)/dzbar;
    end
```

```
    %
end % end of dYbardZbarDifferentialMethod == 333
%
%
% Start of 2nd order (3 points) upwind difference
if dYbardZbarDifferentialMethod == 444
    %
    % Formulate convective terms for i = 3:n-2
    %
    for i = 3:n-2

        % Le = left edge of cell
        Qbar_eps_Le = (Qbar(i-1)+Qbar(i))/(2*epsilon);
        % Re = right edge of cell
        Qbar_eps_Re = (Qbar(i)+Qbar(i+1))/(2*epsilon);

        % for left edge i-1/2
        if Qbar_eps_Le >= 0
            flowdirectionLe = 1;
            ry1barLe = (y1bar(i-1)-y1bar(i-2))/(y1bar(i)-y1bar(i-1));
        elseif Qbar_eps_Le <= 0
            flowdirectionLe = -1;
            ry1barLe = (y1bar(i+1)-y1bar(i))/(y1bar(i)-y1bar(i-1));
        end

        superbeey1barLe = 1;

        fluxy1barLe = 0.5*Qbar_eps_Le*((1+flowdirectionLe)*y1bar(i-
1)+(1-flowdirectionLe)*y1bar(i))+0.5*abs(Qbar_eps_Le)*(1-
abs(Qbar_eps_Le*dtbar/dzbar))*superbeey1barLe*(y1bar(i)-y1bar(i-1));

        % for right edge i+1/2
        if Qbar_eps_Re >= 0
            flowdirectionRe = 1;
            ry1barRe = (y1bar(i)-y1bar(i-1))/(y1bar(i+1)-y1bar(i));
        elseif Qbar_eps_Re <= 0
            flowdirectionRe = -1;

            ry1barRe = (y1bar(i+2)-y1bar(i+1))/(y1bar(i+1)-y1bar(i));
        end

        superbeey1barRe = 1;

        fluxy1barRe = 0.5*Qbar_eps_Re*((1+flowdirectionRe)*y1bar(i)+(1-
flowdirectionRe)*y1bar(i+1))+0.5*abs(Qbar_eps_Re)*(1-
abs(Qbar_eps_Re*dtbar/dzbar))*superbeey1barRe*(y1bar(i+1)-y1bar(i));

        convecy1bar(i) = (fluxy1barLe-fluxy1barRe)/dzbar;
    end
    %
    % Formulate convective terms for i = 1, 2, n-1, n
    %
```

```
    for i = 1
        Qbar_eps_Le = (Qbar(i)+Qbar(i))/(2*epsilon);
        Qbar_eps_Re = (Qbar(i)+Qbar(i+1))/(2*epsilon);

        % for left edge i-1/2
         if Qbar_eps_Le >= 0
            flowdirectionLe = 1;
            ry1barLe = 1;
        elseif Qbar_eps_Le <= 0
            flowdirectionLe = -1;
            ry1barLe = 1;
        end

        superbeey1barLe = 1;

        fluxy1barLe = 0.5*Qbar_eps_Le*((1+flowdirectionLe)*y1bar(i)+(1-
flowdirectionLe)*y1bar(i))+0.5*abs(Qbar_eps_Le)*(1-
abs(Qbar_eps_Le*dtbar/dzbar))*superbeey1barLe*(y1bar(i)-y1bar(i));

        % for right edge i+1/2
        if Qbar_eps_Re >= 0
            flowdirectionRe = 1;
            ry1barRe = 0;
        elseif Qbar_eps_Re <= 0
            flowdirectionRe = -1;
            ry1barRe = (y1bar(i+2)-y1bar(i+1))/(y1bar(i+1)-y1bar(i));
        end

        superbeey1barRe = 1;

        fluxy1barRe = 0.5*Qbar_eps_Re*((1+flowdirectionRe)*y1bar(i)+(1-
flowdirectionRe)*y1bar(i+1))+0.5*abs(Qbar_eps_Re)*(1-
abs(Qbar_eps_Re*dtbar/dzbar))*superbeey1barRe*(y1bar(i+1)-y1bar(i));

        convecy1bar(i) = (fluxy1barLe-fluxy1barRe)/dzbar;
    end
    %
    for i = 2
        Qbar_eps_Le = (Qbar(i-1)+Qbar(i))/(2*epsilon);
        Qbar_eps_Re = (Qbar(i)+Qbar(i+1))/(2*epsilon);

        % for left edge i-1/2
         if Qbar_eps_Le >= 0
            flowdirectionLe = 1;
            ry1barLe = 0;
        elseif Qbar_eps_Le <= 0
            flowdirectionLe = -1;
            ry1barLe = (y1bar(i+1)-y1bar(i))/(y1bar(i)-y1bar(i-1));
        end

        superbeey1barLe = 1;
```

```
        fluxy1barLe = 0.5*Qbar_eps_Le*((1+flowdirectionLe)*y1bar(i-
1)+(1-flowdirectionLe)*y1bar(i))+0.5*abs(Qbar_eps_Le)*(1-
abs(Qbar_eps_Le*dtbar/dzbar))*superbeey1barLe*(y1bar(i)-y1bar(i-1));

        % for right edge i+1/2
        if Qbar_eps_Re >= 0
            flowdirectionRe = 1;
            ry1barRe = (y1bar(i)-y1bar(i-1))/(y1bar(i+1)-y1bar(i));
        elseif Qbar_eps_Re <= 0
            flowdirectionRe = -1;
            ry1barRe = (y1bar(i+2)-y1bar(i+1))/(y1bar(i+1)-y1bar(i));
        end

        superbeey1barRe = 1;

        fluxy1barRe = 0.5*Qbar_eps_Re*((1+flowdirectionRe)*y1bar(i)+(1-
flowdirectionRe)*y1bar(i+1))+0.5*abs(Qbar_eps_Re)*(1-
abs(Qbar_eps_Re*dtbar/dzbar))*superbeey1barRe*(y1bar(i+1)-y1bar(i));

        convecy1bar(i) = (fluxy1barLe-fluxy1barRe)/dzbar;
    end
    %
    for i = n-1
        Qbar_eps_Le = (Qbar(i-1)+Qbar(i))/(2*epsilon);
        Qbar_eps_Re = (Qbar(i)+Qbar(i+1))/(2*epsilon);

        % for left edge i-1/2
         if Qbar_eps_Le >= 0
            flowdirectionLe = 1;
            ry1barLe = (y1bar(i-1)-y1bar(i-2))/(y1bar(i)-y1bar(i-1));
        elseif Qbar_eps_Le <= 0
            flowdirectionLe = -1;
            ry1barLe = (y1bar(i+1)-y1bar(i))/(y1bar(i)-y1bar(i-1));
        end

        superbeey1barLe = 1;

        fluxy1barLe = 0.5*Qbar_eps_Le*((1+flowdirectionLe)*y1bar(i-
1)+(1-flowdirectionLe)*y1bar(i))+0.5*abs(Qbar_eps_Le)*(1-
abs(Qbar_eps_Le*dtbar/dzbar))*superbeey1barLe*(y1bar(i)-y1bar(i-1));

        % for right edge i+1/2
        if Qbar_eps_Re >= 0
            flowdirectionRe = 1;
            ry1barRe = (y1bar(i)-y1bar(i-1))/(y1bar(i+1)-y1bar(i));
        elseif Qbar_eps_Re <= 0
            flowdirectionRe = -1;
            ry1barRe = 0;
        end

        superbeey1barRe = 1;
```

```
        fluxy1barRe = 0.5*Qbar_eps_Re*((1+flowdirectionRe)*y1bar(i)+(1-
flowdirectionRe)*y1bar(i+1))+0.5*abs(Qbar_eps_Re)*(1-
abs(Qbar_eps_Re*dtbar/dzbar))*superbeey1barRe*(y1bar(i+1)-y1bar(i));

        convecy1bar(i) = (fluxy1barLe-fluxy1barRe)/dzbar;
    end
    %
    for i = n
        Qbar_eps_Le = (Qbar(i-1)+Qbar(i))/(2*epsilon);
        Qbar_eps_Re = (Qbar(i)+Qbar(i))/(2*epsilon);

        % for left edge i-1/2
         if Qbar_eps_Le >= 0
            flowdirectionLe = 1;
            ry1barLe = (y1bar(i-1)-y1bar(i-2))/(y1bar(i)-y1bar(i-1));
        elseif Qbar_eps_Le <= 0
            flowdirectionLe = -1;
            ry1barLe = 0;
        end

        superbeey1barLe = 1;

        fluxy1barLe = 0.5*Qbar_eps_Le*((1+flowdirectionLe)*y1bar(i-
1)+(1-flowdirectionLe)*y1bar(i))+0.5*abs(Qbar_eps_Le)*(1-
abs(Qbar_eps_Le*dtbar/dzbar))*superbeey1barLe*(y1bar(i)-y1bar(i-1));

        % for right edge i+1/2
        if Qbar_eps_Re >= 0
            flowdirectionRe = 1;
            ry1barRe = 1;
        elseif Qbar_eps_Re <= 0
            flowdirectionRe = -1;
            ry1barRe = 1;
        end

        superbeey1barRe = 1;

        fluxy1barRe = 0.5*Qbar_eps_Re*((1+flowdirectionRe)*y1bar(i)+(1-
flowdirectionRe)*y1bar(i))+0.5*abs(Qbar_eps_Re)*(1-
abs(Qbar_eps_Re*dtbar/dzbar))*superbeey1barRe*(y1bar(i)-y1bar(i));

        convecy1bar(i) = (fluxy1barLe-fluxy1barRe)/dzbar;
    end
    %
end % end of dYbardZbarDifferentialMethod == 444
%
% Start of Superbee Flux Limiter
if dYbardZbarDifferentialMethod == 777
    %
    % Formulate convective terms for i = 3:n-2
    %
     for i = 3:n-2
```

```
        % Le = left edge of cell
        Qbar_eps_Le = (Qbar(i-1)+Qbar(i))/(2*epsilon);
        % Re = right edge of cell
        Qbar_eps_Re = (Qbar(i)+Qbar(i+1))/(2*epsilon);

        % for left edge i-1/2
        if Qbar_eps_Le >= 0
            flowdirectionLe = 1;
            ry1barLe = (y1bar(i-1)-y1bar(i-2))/(y1bar(i)-y1bar(i-1));
        elseif Qbar_eps_Le <= 0
            flowdirectionLe = -1;
            ry1barLe = (y1bar(i+1)-y1bar(i))/(y1bar(i)-y1bar(i-1));
        end

        superbeey1barLe = max(0,
max(min(1,2*ry1barLe),min(2,ry1barLe)));

        fluxy1barLe = 0.5*Qbar_eps_Le*((1+flowdirectionLe)*y1bar(i-
1)+(1-flowdirectionLe)*y1bar(i))+0.5*abs(Qbar_eps_Le)*(1-
abs(Qbar_eps_Le*dtbar/dzbar))*superbeey1barLe*(y1bar(i)-y1bar(i-1));

        % for right edge i+1/2
        if Qbar_eps_Re >= 0
            flowdirectionRe = 1;
            ry1barRe = (y1bar(i)-y1bar(i-1))/(y1bar(i+1)-y1bar(i));
        elseif Qbar_eps_Re <= 0
            flowdirectionRe = -1;

            ry1barRe = (y1bar(i+2)-y1bar(i+1))/(y1bar(i+1)-y1bar(i));
        end

        superbeey1barRe = max(0,
max(min(1,2*ry1barRe),min(2,ry1barRe)));

        fluxy1barRe = 0.5*Qbar_eps_Re*((1+flowdirectionRe)*y1bar(i)+(1-
flowdirectionRe)*y1bar(i+1))+0.5*abs(Qbar_eps_Re)*(1-
abs(Qbar_eps_Re*dtbar/dzbar))*superbeey1barRe*(y1bar(i+1)-y1bar(i));

        convecy1bar(i) = (fluxy1barLe-fluxy1barRe)/dzbar;
    end
    %
    % Formulate convective terms for i = 1, 2, n-1, n
    %
    for i = 1
        Qbar_eps_Le = (Qbar(i)+Qbar(i))/(2*epsilon);
        Qbar_eps_Re = (Qbar(i)+Qbar(i+1))/(2*epsilon);

        % for left edge i-1/2
         if Qbar_eps_Le >= 0
            flowdirectionLe = 1;
            ry1barLe = 1;
        elseif Qbar_eps_Le <= 0
```

```
            flowdirectionLe = -1;
            ry1barLe = 1;
        end

        superbeey1barLe = max(0,
max(min(1,2*ry1barLe),min(2,ry1barLe)));

        fluxy1barLe = 0.5*Qbar_eps_Le*((1+flowdirectionLe)*y1bar(i)+(1-
flowdirectionLe)*y1bar(i))+0.5*abs(Qbar_eps_Le)*(1-
abs(Qbar_eps_Le*dtbar/dzbar))*superbeey1barLe*(y1bar(i)-y1bar(i));

        % for right edge i+1/2
        if Qbar_eps_Re >= 0
            flowdirectionRe = 1;
            ry1barRe = 0;
        elseif Qbar_eps_Re <= 0
            flowdirectionRe = -1;
            ry1barRe = (y1bar(i+2)-y1bar(i+1))/(y1bar(i+1)-y1bar(i));
        end

        superbeey1barRe = max(0,
max(min(1,2*ry1barRe),min(2,ry1barRe)));

        fluxy1barRe = 0.5*Qbar_eps_Re*((1+flowdirectionRe)*y1bar(i)+(1-
flowdirectionRe)*y1bar(i+1))+0.5*abs(Qbar_eps_Re)*(1-
abs(Qbar_eps_Re*dtbar/dzbar))*superbeey1barRe*(y1bar(i+1)-y1bar(i));

        convecy1bar(i) = (fluxy1barLe-fluxy1barRe)/dzbar;
    end
    %
    for i = 2
        Qbar_eps_Le = (Qbar(i-1)+Qbar(i))/(2*epsilon);
        Qbar_eps_Re = (Qbar(i)+Qbar(i+1))/(2*epsilon);

        % for left edge i-1/2
         if Qbar_eps_Le >= 0
            flowdirectionLe = 1;
            ry1barLe = 0;
        elseif Qbar_eps_Le <= 0
            flowdirectionLe = -1;
            ry1barLe = (y1bar(i+1)-y1bar(i))/(y1bar(i)-y1bar(i-1));
        end

        superbeey1barLe = max(0,
max(min(1,2*ry1barLe),min(2,ry1barLe)));

        fluxy1barLe = 0.5*Qbar_eps_Le*((1+flowdirectionLe)*y1bar(i-
1)+(1-flowdirectionLe)*y1bar(i))+0.5*abs(Qbar_eps_Le)*(1-
abs(Qbar_eps_Le*dtbar/dzbar))*superbeey1barLe*(y1bar(i)-y1bar(i-1));

        % for right edge i+1/2
        if Qbar_eps_Re >= 0
```

```
            flowdirectionRe = 1;
            ry1barRe = (y1bar(i)-y1bar(i-1))/(y1bar(i+1)-y1bar(i));
        elseif Qbar_eps_Re <= 0
            flowdirectionRe = -1;
            ry1barRe = (y1bar(i+2)-y1bar(i+1))/(y1bar(i+1)-y1bar(i));
        end

        superbeey1barRe = max(0,
max(min(1,2*ry1barRe),min(2,ry1barRe)));

        fluxy1barRe = 0.5*Qbar_eps_Re*((1+flowdirectionRe)*y1bar(i)+(1-
flowdirectionRe)*y1bar(i+1))+0.5*abs(Qbar_eps_Re)*(1-
abs(Qbar_eps_Re*dtbar/dzbar))*superbeey1barRe*(y1bar(i+1)-y1bar(i));

        convecy1bar(i) = (fluxy1barLe-fluxy1barRe)/dzbar;
    end
    %
    for i = n-1
        Qbar_eps_Le = (Qbar(i-1)+Qbar(i))/(2*epsilon);
        Qbar_eps_Re = (Qbar(i)+Qbar(i+1))/(2*epsilon);

        % for left edge i-1/2
         if Qbar_eps_Le >= 0
            flowdirectionLe = 1;
            ry1barLe = (y1bar(i-1)-y1bar(i-2))/(y1bar(i)-y1bar(i-1));
        elseif Qbar_eps_Le <= 0
            flowdirectionLe = -1;
            ry1barLe = (y1bar(i+1)-y1bar(i))/(y1bar(i)-y1bar(i-1));
        end

        superbeey1barLe = max(0,
max(min(1,2*ry1barLe),min(2,ry1barLe)));

        fluxy1barLe = 0.5*Qbar_eps_Le*((1+flowdirectionLe)*y1bar(i-
1)+(1-flowdirectionLe)*y1bar(i))+0.5*abs(Qbar_eps_Le)*(1-
abs(Qbar_eps_Le*dtbar/dzbar))*superbeey1barLe*(y1bar(i)-y1bar(i-1));

        % for right edge i+1/2
        if Qbar_eps_Re >= 0
            flowdirectionRe = 1;
            ry1barRe = (y1bar(i)-y1bar(i-1))/(y1bar(i+1)-y1bar(i));
        elseif Qbar_eps_Re <= 0
            flowdirectionRe = -1;
            ry1barRe = 0;
        end

        superbeey1barRe = max(0,
max(min(1,2*ry1barRe),min(2,ry1barRe)));

        fluxy1barRe = 0.5*Qbar_eps_Re*((1+flowdirectionRe)*y1bar(i)+(1-
flowdirectionRe)*y1bar(i+1))+0.5*abs(Qbar_eps_Re)*(1-
abs(Qbar_eps_Re*dtbar/dzbar))*superbeey1barRe*(y1bar(i+1)-y1bar(i));
```

```
        convecy1bar(i) = (fluxy1barLe-fluxy1barRe)/dzbar;
    end
    %
    for i = n
        Qbar_eps_Le = (Qbar(i-1)+Qbar(i))/(2*epsilon);
        Qbar_eps_Re = (Qbar(i)+Qbar(i))/(2*epsilon);

        % for left edge i-1/2
         if Qbar_eps_Le >= 0
            flowdirectionLe = 1;
            ry1barLe = (y1bar(i-1)-y1bar(i-2))/(y1bar(i)-y1bar(i-1));
        elseif Qbar_eps_Le <= 0
            flowdirectionLe = -1;
            ry1barLe = 0;
        end

        superbeey1barLe = max(0,
max(min(1,2*ry1barLe),min(2,ry1barLe)));

        fluxy1barLe = 0.5*Qbar_eps_Le*((1+flowdirectionLe)*y1bar(i-
1)+(1-flowdirectionLe)*y1bar(i))+0.5*abs(Qbar_eps_Le)*(1-
abs(Qbar_eps_Le*dtbar/dzbar))*superbeey1barLe*(y1bar(i)-y1bar(i-1));

        % for right edge i+1/2
        if Qbar_eps_Re >= 0
            flowdirectionRe = 1;
            ry1barRe = 1;
        elseif Qbar_eps_Re <= 0
            flowdirectionRe = -1;
            ry1barRe = 1;
        end

        superbeey1barRe = max(0,
max(min(1,2*ry1barRe),min(2,ry1barRe)));

        fluxy1barRe = 0.5*Qbar_eps_Re*((1+flowdirectionRe)*y1bar(i)+(1-
flowdirectionRe)*y1bar(i))+0.5*abs(Qbar_eps_Re)*(1-
abs(Qbar_eps_Re*dtbar/dzbar))*superbeey1barRe*(y1bar(i)-y1bar(i));

        convecy1bar(i) = (fluxy1barLe-fluxy1barRe)/dzbar;
    end
    %
end % end of dYbardZbarDifferentialMethod == 777
%
%
% Formulate ODEs - can be used for adsorption and purge - both
directions
%
for i=1
```

```
    dY1bardtbar(i) = convecy1bar(i)-(n1eqmbar(i)-
n1bar(i))/epsilon+(epsilonbar*DL(i)*tt/(epsilon*L^2))*(Y1bar(i+2)-
2*Y1bar(i+1)+Y1bar(i))/(dzbar)^2;
end
for i=2:n-1
    dY1bardtbar(i) = convecy1bar(i)-(n1eqmbar(i)-
n1bar(i))/epsilon+(epsilonbar*DL(i)*tt/(epsilon*L^2))*(Y1bar(i+1)-
2*Y1bar(i)+Y1bar(i-1))/(dzbar)^2;
end
for i=n
    dY1bardtbar(i) = convecy1bar(i)-(n1eqmbar(i)-
n1bar(i))/epsilon+(epsilonbar*DL(i)*tt/(epsilon*L^2))*(Y1bar(n)-
2*Y1bar(n-1)+Y1bar(n-2))/(dzbar)^2;
end
%
if MassAxial == 882 % Turn on mass axial dispersion
        for i=n
            dY1bardtbar(i) = convecy1bar(i)-(n1eqmbar(i)-
n1bar(i))/epsilon + 0;
        end
end
%
for i=1:n
    dn1bardtbar(i) = k1*tt*(n1eqmbar(i)-n1bar(i));
    dn2bardtbar(i) = k2*tt*(n2eqmbar(i)-n2bar(i));
    dPbardtbar(i) = 0;
end
%
% Four vectors into one vector
%
for i = 1:n
    Yt(0*n+i) = dY1bardtbar(i);
    Yt(1*n+i) = dn1bardtbar(i);
    Yt(2*n+i) = dn2bardtbar(i);
    Yt(3*n+i) = dPbardtbar(i);
end
    Yt(0*n+1) = 0; % because Y1bar(1) = y1a*rhog(1)
%
yt=Yt';
% Increment calls to psa_1
ncall = ncall+1;
%
```

APPENDIX E

MATLAB PROGRAM FOR DESORPTION STEP

```
% Solve for y1, n1, n2, P, rhog, Q, us
%
function yt = PSA_desorption(t,Y)
%
% parameters shared with the ODE routine
%
global Mg1 Mg2 De1 De2 taup dYbardZbarDifferentialMethod rhog0 T0 ncall
Qa Qd n dzbar dtbar  epsilon epsilonbar k1 k2 k3 k4 rhob dp L y1d Qin
Pd tc tt Pmax Pmin Tmax Tmin Tref MassAxial dtbara dtbarp dtbardep
dtbard miu ta tp td tdep
%
% preallocating
%
Y1bar = zeros(1,n);
n1bar = zeros(1,n);
n2bar = zeros(1,n);
y1bar = zeros(1,n);
Mg = zeros(1,n);
Pbar = zeros(1,n);
thetabar = zeros(1,n);
rhogbar = zeros(1,n);
n1eqmbar = zeros(1,n);
n2eqmbar = zeros(1,n);
Qbar = zeros(1,n);
usbar = zeros(1,n);
convecy1bar = zeros(1,n);
DL = zeros(1,n);
dY1bardtbar = zeros(1,n);
dn1bardtbar = zeros(1,n);
dn2bardtbar = zeros(1,n);
Yt = zeros(1,4*n);
Qin = -Qd;
%
% One vector to Four vectors
%
for i = 1:n
    Y1bar(i) = Y(0*n+i);
    n1bar(i) = Y(1*n+i);
    n2bar(i) = Y(2*n+i);
    Y2bar(i) = Y(3*n+i);
end
for i = 1:n
    y1bar(i) = Y1bar(i)/(rhog0*L/(Qa*tt));
    Mg(i) = Mg1*y1bar(i)+Mg2*(1-y1bar(i));
end
%
% Boundary conditions after initial conditions
%
if (ncall~=0) % not initial condition
    y1bar(n) = y1d;
    Y1bar(n) = y1d*(rhog0*L/(Qa*tt));
end
% Formulate pre-parameters for ODEs
%
```

```
% Isobaric, Isothermal
%
for i = 1:n
    Pbar(i) = Pd/(Pmax-Pmin);
    thetabar(i) = (T0-Tref)/(Tmax-Tmin);
    rhogbar(i) = rhog0*L/(Qa*tt);
end
%
% Formulate n1eqmbar(i), n2eqmbar(i), Qbar(i), usbar(i) with initial
and
% boundary conditions
%
for i = 1:n
    py = (y1bar(i))*((Pmax-Pmin)*Pbar(i)/1013250);
    if py < 0.00013
        n1eqmbar(i) = 0;
    else
    n1eqmbar(i) = -(k1*rhob*L/Qa)*(3*0.069337*((y1bar(i))*((Pmax-
Pmin)*Pbar(i)/1013250))^(-0.10825)/(1+0.069337*((y1bar(i))*((Pmax-
Pmin)*Pbar(i)/1013250))^(-0.10825))-0.4633)/2/193.842*1000;
    end
    n2eqmbar(i) = 0;
end
if (ncall == 0)
    for i = 1:n
        Qbar(i) = Qin/Qa;
        usbar(i) = Qbar(i)/rhogbar(i);
    end
end

if (ncall ~= 0)
        for i = n
            Qbar(i) = Qin/Qa;
            usbar(i) = Qbar(i)/rhogbar(i);
        end
        for i = n-1:-1:1
            Qbar(i) = +((n1eqmbar(i)-n1bar(i))+(n2eqmbar(i)-
n2bar(i)))*dzbar+Qbar(i+1);
            usbar(i) = Qbar(i)/rhogbar(i);
        end
end
%
% Formulate gas phase axial dispersion coefficient in mass balance, DL,
% cm2/sec
%
if MassAxial == 881
    for i = 1:n
        DL(i) = 0;
    end
end

if MassAxial == 882
        DM = (epsilon/taup)*(1/(1/De1+1/De2));
```

```
    for i = 1:n
        DL(i) = 0.7*DM +
0.5*dp*(abs(Qbar(i))*Qa)/(rhogbar(i)*(Qa*tt/L)*epsilonbar);
    end
end
%
%
% Start of 1st order (2 points) upwind difference
if dYbardZbarDifferentialMethod == 333
    %
    % Formulate convective terms for i = 3:n-2
    %
    for i = 3:n-2
        % Le = left edge of cell
        Qbar_eps_Le = (Qbar(i-1)+Qbar(i))/(2*epsilon);
        % Re = right edge of cell
        Qbar_eps_Re = (Qbar(i)+Qbar(i+1))/(2*epsilon);

        % for left edge i-1/2
        if Qbar_eps_Le >= 0
            flowdirectionLe = 1;

            ry1barLe = (y1bar(i-1)-y1bar(i-2))/(y1bar(i)-y1bar(i-1));
        elseif Qbar_eps_Le <= 0
            flowdirectionLe = -1;

            ry1barLe = (y1bar(i+1)-y1bar(i))/(y1bar(i)-y1bar(i-1));
        end

        superbeey1barLe = 0;

        fluxy1barLe = 0.5*Qbar_eps_Le*((1+flowdirectionLe)*y1bar(i-
1)+(1-flowdirectionLe)*y1bar(i))+0.5*abs(Qbar_eps_Le)*(1-
abs(Qbar_eps_Le*dtbar/dzbar))*superbeey1barLe*(y1bar(i)-y1bar(i-1));

        % for right edge i+1/2
        if Qbar_eps_Re >= 0
            flowdirectionRe = 1;

            ry1barRe = (y1bar(i)-y1bar(i-1))/(y1bar(i+1)-y1bar(i));
        elseif Qbar_eps_Re <= 0
            flowdirectionRe = -1;

            ry1barRe = (y1bar(i+2)-y1bar(i+1))/(y1bar(i+1)-y1bar(i));
        end

        superbeey1barRe = 0;

        fluxy1barRe = 0.5*Qbar_eps_Re*((1+flowdirectionRe)*y1bar(i)+(1-
flowdirectionRe)*y1bar(i+1))+0.5*abs(Qbar_eps_Re)*(1-
abs(Qbar_eps_Re*dtbar/dzbar))*superbeey1barRe*(y1bar(i+1)-y1bar(i));
```

```
        convecy1bar(i) = (fluxy1barLe-fluxy1barRe)/dzbar;
    end
    %
    % Formulate convective terms for i = 1, 2, n-1, n
    %
    for i = 1
        Qbar_eps_Le = (Qbar(i)+Qbar(i))/(2*epsilon);
        Qbar_eps_Re = (Qbar(i)+Qbar(i+1))/(2*epsilon);

        % for left edge i-1/2
         if Qbar_eps_Le >= 0
            flowdirectionLe = 1;
            ry1barLe = 1;
        elseif Qbar_eps_Le <= 0
            flowdirectionLe = -1;
            ry1barLe = 1;
        end

        superbeey1barLe = 0;

        fluxy1barLe = 0.5*Qbar_eps_Le*((1+flowdirectionLe)*y1bar(i)+(1-
flowdirectionLe)*y1bar(i))+0.5*abs(Qbar_eps_Le)*(1-
abs(Qbar_eps_Le*dtbar/dzbar))*superbeey1barLe*(y1bar(i)-y1bar(i));

        % for right edge i+1/2
        if Qbar_eps_Re >= 0
            flowdirectionRe = 1;
            ry1barRe = 0;
        elseif Qbar_eps_Re <= 0
            flowdirectionRe = -1;
            ry1barRe = (y1bar(i+2)-y1bar(i+1))/(y1bar(i+1)-y1bar(i));
        end

        superbeey1barRe = 0;

        fluxy1barRe = 0.5*Qbar_eps_Re*((1+flowdirectionRe)*y1bar(i)+(1-
flowdirectionRe)*y1bar(i+1))+0.5*abs(Qbar_eps_Re)*(1-
abs(Qbar_eps_Re*dtbar/dzbar))*superbeey1barRe*(y1bar(i+1)-y1bar(i));

        convecy1bar(i) = (fluxy1barLe-fluxy1barRe)/dzbar;
    end
    %
    for i = 2
        Qbar_eps_Le = (Qbar(i-1)+Qbar(i))/(2*epsilon);
        Qbar_eps_Re = (Qbar(i)+Qbar(i+1))/(2*epsilon);

        % for left edge i-1/2
         if Qbar_eps_Le >= 0
            flowdirectionLe = 1;
            ry1barLe = 0;
        elseif Qbar_eps_Le <= 0
```

```
            flowdirectionLe = -1;
            ry1barLe = (y1bar(i+1)-y1bar(i))/(y1bar(i)-y1bar(i-1));
        end

        superbeey1barLe = 0;

        fluxy1barLe = 0.5*Qbar_eps_Le*((1+flowdirectionLe)*y1bar(i-
1)+(1-flowdirectionLe)*y1bar(i))+0.5*abs(Qbar_eps_Le)*(1-
abs(Qbar_eps_Le*dtbar/dzbar))*superbeey1barLe*(y1bar(i)-y1bar(i-1));

        % for right edge i+1/2
        if Qbar_eps_Re >= 0
            flowdirectionRe = 1;
            ry1barRe = (y1bar(i)-y1bar(i-1))/(y1bar(i+1)-y1bar(i));
        elseif Qbar_eps_Re <= 0
            flowdirectionRe = -1;
            ry1barRe = (y1bar(i+2)-y1bar(i+1))/(y1bar(i+1)-y1bar(i));
        end

        superbeey1barRe = 0;

        fluxy1barRe = 0.5*Qbar_eps_Re*((1+flowdirectionRe)*y1bar(i)+(1-
flowdirectionRe)*y1bar(i+1))+0.5*abs(Qbar_eps_Re)*(1-
abs(Qbar_eps_Re*dtbar/dzbar))*superbeey1barRe*(y1bar(i+1)-y1bar(i));

        convecy1bar(i) = (fluxy1barLe-fluxy1barRe)/dzbar;
    end
    %
    for i = n-1
        Qbar_eps_Le = (Qbar(i-1)+Qbar(i))/(2*epsilon);
        Qbar_eps_Re = (Qbar(i)+Qbar(i+1))/(2*epsilon);

        % for left edge i-1/2
         if Qbar_eps_Le >= 0
            flowdirectionLe = 1;
            ry1barLe = (y1bar(i-1)-y1bar(i-2))/(y1bar(i)-y1bar(i-1));
        elseif Qbar_eps_Le <= 0
            flowdirectionLe = -1;
            ry1barLe = (y1bar(i+1)-y1bar(i))/(y1bar(i)-y1bar(i-1));
        end

        superbeey1barLe = 0;

        fluxy1barLe = 0.5*Qbar_eps_Le*((1+flowdirectionLe)*y1bar(i-
1)+(1-flowdirectionLe)*y1bar(i))+0.5*abs(Qbar_eps_Le)*(1-
abs(Qbar_eps_Le*dtbar/dzbar))*superbeey1barLe*(y1bar(i)-y1bar(i-1));

        % for right edge i+1/2
        if Qbar_eps_Re >= 0
            flowdirectionRe = 1;
            ry1barRe = (y1bar(i)-y1bar(i-1))/(y1bar(i+1)-y1bar(i));
        elseif Qbar_eps_Re <= 0
```

```
            flowdirectionRe = -1;
            ry1barRe = 0;
        end

        superbeey1barRe = 0;

        fluxy1barRe = 0.5*Qbar_eps_Re*((1+flowdirectionRe)*y1bar(i)+(1-
flowdirectionRe)*y1bar(i+1))+0.5*abs(Qbar_eps_Re)*(1-
abs(Qbar_eps_Re*dtbar/dzbar))*superbeey1barRe*(y1bar(i+1)-y1bar(i));

        convecy1bar(i) = (fluxy1barLe-fluxy1barRe)/dzbar;
    end
    %
    for i = n
        Qbar_eps_Le = (Qbar(i-1)+Qbar(i))/(2*epsilon);
        Qbar_eps_Re = (Qbar(i)+Qbar(i))/(2*epsilon);

        % for left edge i-1/2
         if Qbar_eps_Le >= 0
            flowdirectionLe = 1;
            ry1barLe = (y1bar(i-1)-y1bar(i-2))/(y1bar(i)-y1bar(i-1));
        elseif Qbar_eps_Le <= 0
            flowdirectionLe = -1;
            ry1barLe = 0;
        end

        superbeey1barLe = 0;

        fluxy1barLe = 0.5*Qbar_eps_Le*((1+flowdirectionLe)*y1bar(i-
1)+(1-flowdirectionLe)*y1bar(i))+0.5*abs(Qbar_eps_Le)*(1-
abs(Qbar_eps_Le*dtbar/dzbar))*superbeey1barLe*(y1bar(i)-y1bar(i-1));

        % for right edge i+1/2
        if Qbar_eps_Re >= 0
            flowdirectionRe = 1;
            ry1barRe = 1;
        elseif Qbar_eps_Re <= 0
            flowdirectionRe = -1;
            ry1barRe = 1;
        end

        superbeey1barRe = 0;

        fluxy1barRe = 0.5*Qbar_eps_Re*((1+flowdirectionRe)*y1bar(i)+(1-
flowdirectionRe)*y1bar(i))+0.5*abs(Qbar_eps_Re)*(1-
abs(Qbar_eps_Re*dtbar/dzbar))*superbeey1barRe*(y1bar(i)-y1bar(i));

        convecy1bar(i) = (fluxy1barLe-fluxy1barRe)/dzbar;
    end
    %
end % end of dYbardZbarDifferentialMethod == 333
%
```

```
%
% Start of 2nd order (3 points) upwind difference
if dYbardZbarDifferentialMethod == 444
    %
    % Formulate convective terms for i = 3:n-2
    %
    for i = 3:n-2

        % Le = left edge of cell
        Qbar_eps_Le = (Qbar(i-1)+Qbar(i))/(2*epsilon);
        % Re = right edge of cell
        Qbar_eps_Re = (Qbar(i)+Qbar(i+1))/(2*epsilon);

        % for left edge i-1/2
        if Qbar_eps_Le >= 0
            flowdirectionLe = 1;
            ry1barLe = (y1bar(i-1)-y1bar(i-2))/(y1bar(i)-y1bar(i-1));
        elseif Qbar_eps_Le <= 0
            flowdirectionLe = -1;
            ry1barLe = (y1bar(i+1)-y1bar(i))/(y1bar(i)-y1bar(i-1));
        end

        superbeey1barLe = 1;

        fluxy1barLe = 0.5*Qbar_eps_Le*((1+flowdirectionLe)*y1bar(i-
1)+(1-flowdirectionLe)*y1bar(i))+0.5*abs(Qbar_eps_Le)*(1-
abs(Qbar_eps_Le*dtbar/dzbar))*superbeey1barLe*(y1bar(i)-y1bar(i-1));

        % for right edge i+1/2
        if Qbar_eps_Re >= 0
            flowdirectionRe = 1;
            ry1barRe = (y1bar(i)-y1bar(i-1))/(y1bar(i+1)-y1bar(i));
        elseif Qbar_eps_Re <= 0
            flowdirectionRe = -1;

            ry1barRe = (y1bar(i+2)-y1bar(i+1))/(y1bar(i+1)-y1bar(i));
        end

        superbeey1barRe = 1;

        fluxy1barRe = 0.5*Qbar_eps_Re*((1+flowdirectionRe)*y1bar(i)+(1-
flowdirectionRe)*y1bar(i+1))+0.5*abs(Qbar_eps_Re)*(1-
abs(Qbar_eps_Re*dtbar/dzbar))*superbeey1barRe*(y1bar(i+1)-y1bar(i));

        convecy1bar(i) = (fluxy1barLe-fluxy1barRe)/dzbar;
    end
    %
    % Formulate convective terms for i = 1, 2, n-1, n
    %
    for i = 1
        Qbar_eps_Le = (Qbar(i)+Qbar(i))/(2*epsilon);
        Qbar_eps_Re = (Qbar(i)+Qbar(i+1))/(2*epsilon);
```

```
        % for left edge i-1/2
         if Qbar_eps_Le >= 0
            flowdirectionLe = 1;
            ry1barLe = 1;
        elseif Qbar_eps_Le <= 0
            flowdirectionLe = -1;
            ry1barLe = 1;
        end

        superbeey1barLe = 1;

        fluxy1barLe = 0.5*Qbar_eps_Le*((1+flowdirectionLe)*y1bar(i)+(1-
flowdirectionLe)*y1bar(i))+0.5*abs(Qbar_eps_Le)*(1-
abs(Qbar_eps_Le*dtbar/dzbar))*superbeey1barLe*(y1bar(i)-y1bar(i));

        % for right edge i+1/2
        if Qbar_eps_Re >= 0
            flowdirectionRe = 1;
            ry1barRe = 0;
        elseif Qbar_eps_Re <= 0
            flowdirectionRe = -1;
            ry1barRe = (y1bar(i+2)-y1bar(i+1))/(y1bar(i+1)-y1bar(i));
        end

        superbeey1barRe = 1;

        fluxy1barRe = 0.5*Qbar_eps_Re*((1+flowdirectionRe)*y1bar(i)+(1-
flowdirectionRe)*y1bar(i+1))+0.5*abs(Qbar_eps_Re)*(1-
abs(Qbar_eps_Re*dtbar/dzbar))*superbeey1barRe*(y1bar(i+1)-y1bar(i));

        convecy1bar(i) = (fluxy1barLe-fluxy1barRe)/dzbar;
    end
    %
    for i = 2
        Qbar_eps_Le = (Qbar(i-1)+Qbar(i))/(2*epsilon);
        Qbar_eps_Re = (Qbar(i)+Qbar(i+1))/(2*epsilon);

        % for left edge i-1/2
         if Qbar_eps_Le >= 0
            flowdirectionLe = 1;
            ry1barLe = 0;
        elseif Qbar_eps_Le <= 0
            flowdirectionLe = -1;
            ry1barLe = (y1bar(i+1)-y1bar(i))/(y1bar(i)-y1bar(i-1));
        end

        superbeey1barLe = 1;

        fluxy1barLe = 0.5*Qbar_eps_Le*((1+flowdirectionLe)*y1bar(i-
1)+(1-flowdirectionLe)*y1bar(i))+0.5*abs(Qbar_eps_Le)*(1-
abs(Qbar_eps_Le*dtbar/dzbar))*superbeey1barLe*(y1bar(i)-y1bar(i-1));
```

```
        % for right edge i+1/2
        if Qbar_eps_Re >= 0
            flowdirectionRe = 1;
            ry1barRe = (y1bar(i)-y1bar(i-1))/(y1bar(i+1)-y1bar(i));
        elseif Qbar_eps_Re <= 0
            flowdirectionRe = -1;
            ry1barRe = (y1bar(i+2)-y1bar(i+1))/(y1bar(i+1)-y1bar(i));
        end

        superbeey1barRe = 1;

        fluxy1barRe = 0.5*Qbar_eps_Re*((1+flowdirectionRe)*y1bar(i)+(1-
flowdirectionRe)*y1bar(i+1))+0.5*abs(Qbar_eps_Re)*(1-
abs(Qbar_eps_Re*dtbar/dzbar))*superbeey1barRe*(y1bar(i+1)-y1bar(i));

        convecy1bar(i) = (fluxy1barLe-fluxy1barRe)/dzbar;
    end
    %
    for i = n-1
        Qbar_eps_Le = (Qbar(i-1)+Qbar(i))/(2*epsilon);
        Qbar_eps_Re = (Qbar(i)+Qbar(i+1))/(2*epsilon);

        % for left edge i-1/2
         if Qbar_eps_Le >= 0
            flowdirectionLe = 1;
            ry1barLe = (y1bar(i-1)-y1bar(i-2))/(y1bar(i)-y1bar(i-1));
        elseif Qbar_eps_Le <= 0
            flowdirectionLe = -1;
            ry1barLe = (y1bar(i+1)-y1bar(i))/(y1bar(i)-y1bar(i-1));
        end

        superbeey1barLe = 1;

        fluxy1barLe = 0.5*Qbar_eps_Le*((1+flowdirectionLe)*y1bar(i-
1)+(1-flowdirectionLe)*y1bar(i))+0.5*abs(Qbar_eps_Le)*(1-
abs(Qbar_eps_Le*dtbar/dzbar))*superbeey1barLe*(y1bar(i)-y1bar(i-1));

        % for right edge i+1/2
        if Qbar_eps_Re >= 0
            flowdirectionRe = 1;
            ry1barRe = (y1bar(i)-y1bar(i-1))/(y1bar(i+1)-y1bar(i));
        elseif Qbar_eps_Re <= 0
            flowdirectionRe = -1;
            ry1barRe = 0;
        end

        superbeey1barRe = 1;

        fluxy1barRe = 0.5*Qbar_eps_Re*((1+flowdirectionRe)*y1bar(i)+(1-
flowdirectionRe)*y1bar(i+1))+0.5*abs(Qbar_eps_Re)*(1-
abs(Qbar_eps_Re*dtbar/dzbar))*superbeey1barRe*(y1bar(i+1)-y1bar(i));
```

```
        convecy1bar(i) = (fluxy1barLe-fluxy1barRe)/dzbar;
    end
    %
    for i = n
        Qbar_eps_Le = (Qbar(i-1)+Qbar(i))/(2*epsilon);
        Qbar_eps_Re = (Qbar(i)+Qbar(i))/(2*epsilon);

        % for left edge i-1/2
         if Qbar_eps_Le >= 0
            flowdirectionLe = 1;
            ry1barLe = (y1bar(i-1)-y1bar(i-2))/(y1bar(i)-y1bar(i-1));
        elseif Qbar_eps_Le <= 0
            flowdirectionLe = -1;
            ry1barLe = 0;
        end

        superbeey1barLe = 1;

        fluxy1barLe = 0.5*Qbar_eps_Le*((1+flowdirectionLe)*y1bar(i-
1)+(1-flowdirectionLe)*y1bar(i))+0.5*abs(Qbar_eps_Le)*(1-
abs(Qbar_eps_Le*dtbar/dzbar))*superbeey1barLe*(y1bar(i)-y1bar(i-1));

        % for right edge i+1/2
        if Qbar_eps_Re >= 0
            flowdirectionRe = 1;
            ry1barRe = 1;
        elseif Qbar_eps_Re <= 0
            flowdirectionRe = -1;
            ry1barRe = 1;
        end

        superbeey1barRe = 1;

        fluxy1barRe = 0.5*Qbar_eps_Re*((1+flowdirectionRe)*y1bar(i)+(1-
flowdirectionRe)*y1bar(i))+0.5*abs(Qbar_eps_Re)*(1-
abs(Qbar_eps_Re*dtbar/dzbar))*superbeey1barRe*(y1bar(i)-y1bar(i));

        convecy1bar(i) = (fluxy1barLe-fluxy1barRe)/dzbar;
    end
    %
end % end of dYbardZbarDifferentialMethod == 444
%
% Start of Superbee Flux Limiter
if dYbardZbarDifferentialMethod == 777
    %
    % Formulate convective terms for i = 3:n-2
    %
     for i = 3:n-2
        % Le = left edge of cell
        Qbar_eps_Le = (Qbar(i-1)+Qbar(i))/(2*epsilon);
        % Re = right edge of cell
```

```
        Qbar_eps_Re = (Qbar(i)+Qbar(i+1))/(2*epsilon);

        % for left edge i-1/2
        if Qbar_eps_Le >= 0
            flowdirectionLe = 1;
            ry1barLe = (y1bar(i-1)-y1bar(i-2))/(y1bar(i)-y1bar(i-1));
        elseif Qbar_eps_Le <= 0
            flowdirectionLe = -1;
            ry1barLe = (y1bar(i+1)-y1bar(i))/(y1bar(i)-y1bar(i-1));
        end

        superbeey1barLe = max(0,
max(min(1,2*ry1barLe),min(2,ry1barLe)));

        fluxy1barLe = 0.5*Qbar_eps_Le*((1+flowdirectionLe)*y1bar(i-
1)+(1-flowdirectionLe)*y1bar(i))+0.5*abs(Qbar_eps_Le)*(1-
abs(Qbar_eps_Le*dtbar/dzbar))*superbeey1barLe*(y1bar(i)-y1bar(i-1));

        % for right edge i+1/2
        if Qbar_eps_Re >= 0
            flowdirectionRe = 1;
            ry1barRe = (y1bar(i)-y1bar(i-1))/(y1bar(i+1)-y1bar(i));
        elseif Qbar_eps_Re <= 0
            flowdirectionRe = -1;

            ry1barRe = (y1bar(i+2)-y1bar(i+1))/(y1bar(i+1)-y1bar(i));
        end

        superbeey1barRe = max(0,
max(min(1,2*ry1barRe),min(2,ry1barRe)));

        fluxy1barRe = 0.5*Qbar_eps_Re*((1+flowdirectionRe)*y1bar(i)+(1-
flowdirectionRe)*y1bar(i+1))+0.5*abs(Qbar_eps_Re)*(1-
abs(Qbar_eps_Re*dtbar/dzbar))*superbeey1barRe*(y1bar(i+1)-y1bar(i));

        convecy1bar(i) = (fluxy1barLe-fluxy1barRe)/dzbar;
    end
    %
    % Formulate convective terms for i = 1, 2, n-1, n
    %
    for i = 1
        Qbar_eps_Le = (Qbar(i)+Qbar(i))/(2*epsilon);
        Qbar_eps_Re = (Qbar(i)+Qbar(i+1))/(2*epsilon);

        % for left edge i-1/2
         if Qbar_eps_Le >= 0
            flowdirectionLe = 1;
            ry1barLe = 1;
        elseif Qbar_eps_Le <= 0
            flowdirectionLe = -1;
            ry1barLe = 1;
        end
```

```
        superbeey1barLe = max(0,
max(min(1,2*ry1barLe),min(2,ry1barLe)));

        fluxy1barLe = 0.5*Qbar_eps_Le*((1+flowdirectionLe)*y1bar(i)+(1-
flowdirectionLe)*y1bar(i))+0.5*abs(Qbar_eps_Le)*(1-
abs(Qbar_eps_Le*dtbar/dzbar))*superbeey1barLe*(y1bar(i)-y1bar(i));

        % for right edge i+1/2
        if Qbar_eps_Re >= 0
            flowdirectionRe = 1;
            ry1barRe = 0;
        elseif Qbar_eps_Re <= 0
            flowdirectionRe = -1;
            ry1barRe = (y1bar(i+2)-y1bar(i+1))/(y1bar(i+1)-y1bar(i));
        end

        superbeey1barRe = max(0,
max(min(1,2*ry1barRe),min(2,ry1barRe)));

        fluxy1barRe = 0.5*Qbar_eps_Re*((1+flowdirectionRe)*y1bar(i)+(1-
flowdirectionRe)*y1bar(i+1))+0.5*abs(Qbar_eps_Re)*(1-
abs(Qbar_eps_Re*dtbar/dzbar))*superbeey1barRe*(y1bar(i+1)-y1bar(i));

        convecy1bar(i) = (fluxy1barLe-fluxy1barRe)/dzbar;
    end
    %
    for i = 2
        Qbar_eps_Le = (Qbar(i-1)+Qbar(i))/(2*epsilon);
        Qbar_eps_Re = (Qbar(i)+Qbar(i+1))/(2*epsilon);

        % for left edge i-1/2
         if Qbar_eps_Le >= 0
            flowdirectionLe = 1;
            ry1barLe = 0;
        elseif Qbar_eps_Le <= 0
            flowdirectionLe = -1;
            ry1barLe = (y1bar(i+1)-y1bar(i))/(y1bar(i)-y1bar(i-1));
        end

        superbeey1barLe = max(0,
max(min(1,2*ry1barLe),min(2,ry1barLe)));

        fluxy1barLe = 0.5*Qbar_eps_Le*((1+flowdirectionLe)*y1bar(i-
1)+(1-flowdirectionLe)*y1bar(i))+0.5*abs(Qbar_eps_Le)*(1-
abs(Qbar_eps_Le*dtbar/dzbar))*superbeey1barLe*(y1bar(i)-y1bar(i-1));

        % for right edge i+1/2
        if Qbar_eps_Re >= 0
            flowdirectionRe = 1;
            ry1barRe = (y1bar(i)-y1bar(i-1))/(y1bar(i+1)-y1bar(i));
        elseif Qbar_eps_Re <= 0
```

```
            flowdirectionRe = -1;
            ry1barRe = (y1bar(i+2)-y1bar(i+1))/(y1bar(i+1)-y1bar(i));
        end

        superbeey1barRe = max(0,
max(min(1,2*ry1barRe),min(2,ry1barRe)));

        fluxy1barRe = 0.5*Qbar_eps_Re*((1+flowdirectionRe)*y1bar(i)+(1-
flowdirectionRe)*y1bar(i+1))+0.5*abs(Qbar_eps_Re)*(1-
abs(Qbar_eps_Re*dtbar/dzbar))*superbeey1barRe*(y1bar(i+1)-y1bar(i));

        convecy1bar(i) = (fluxy1barLe-fluxy1barRe)/dzbar;
    end
    %
    for i = n-1
        Qbar_eps_Le = (Qbar(i-1)+Qbar(i))/(2*epsilon);
        Qbar_eps_Re = (Qbar(i)+Qbar(i+1))/(2*epsilon);

        % for left edge i-1/2
         if Qbar_eps_Le >= 0
            flowdirectionLe = 1;
            ry1barLe = (y1bar(i-1)-y1bar(i-2))/(y1bar(i)-y1bar(i-1));
        elseif Qbar_eps_Le <= 0
            flowdirectionLe = -1;
            ry1barLe = (y1bar(i+1)-y1bar(i))/(y1bar(i)-y1bar(i-1));
        end

        superbeey1barLe = max(0,
max(min(1,2*ry1barLe),min(2,ry1barLe)));

        fluxy1barLe = 0.5*Qbar_eps_Le*((1+flowdirectionLe)*y1bar(i-
1)+(1-flowdirectionLe)*y1bar(i))+0.5*abs(Qbar_eps_Le)*(1-
abs(Qbar_eps_Le*dtbar/dzbar))*superbeey1barLe*(y1bar(i)-y1bar(i-1));

        % for right edge i+1/2
        if Qbar_eps_Re >= 0
            flowdirectionRe = 1;
            ry1barRe = (y1bar(i)-y1bar(i-1))/(y1bar(i+1)-y1bar(i));
        elseif Qbar_eps_Re <= 0
            flowdirectionRe = -1;
            ry1barRe = 0;
        end

        superbeey1barRe = max(0,
max(min(1,2*ry1barRe),min(2,ry1barRe)));

        fluxy1barRe = 0.5*Qbar_eps_Re*((1+flowdirectionRe)*y1bar(i)+(1-
flowdirectionRe)*y1bar(i+1))+0.5*abs(Qbar_eps_Re)*(1-
abs(Qbar_eps_Re*dtbar/dzbar))*superbeey1barRe*(y1bar(i+1)-y1bar(i));

        convecy1bar(i) = (fluxy1barLe-fluxy1barRe)/dzbar;
    end
```

```
    %
    for i = n
        Qbar_eps_Le = (Qbar(i-1)+Qbar(i))/(2*epsilon);
        Qbar_eps_Re = (Qbar(i)+Qbar(i))/(2*epsilon);

        % for left edge i-1/2
         if Qbar_eps_Le >= 0
            flowdirectionLe = 1;
            ry1barLe = (y1bar(i-1)-y1bar(i-2))/(y1bar(i)-y1bar(i-1));
        elseif Qbar_eps_Le <= 0
            flowdirectionLe = -1;
            ry1barLe = 0;
        end

        superbeey1barLe = max(0,
max(min(1,2*ry1barLe),min(2,ry1barLe)));

        fluxy1barLe = 0.5*Qbar_eps_Le*((1+flowdirectionLe)*y1bar(i-
1)+(1-flowdirectionLe)*y1bar(i))+0.5*abs(Qbar_eps_Le)*(1-
abs(Qbar_eps_Le*dtbar/dzbar))*superbeey1barLe*(y1bar(i)-y1bar(i-1));

        % for right edge i+1/2
        if Qbar_eps_Re >= 0
            flowdirectionRe = 1;
            ry1barRe = 1;
        elseif Qbar_eps_Re <= 0
            flowdirectionRe = -1;
            ry1barRe = 1;
        end

        superbeey1barRe = max(0,
max(min(1,2*ry1barRe),min(2,ry1barRe)));

        fluxy1barRe = 0.5*Qbar_eps_Re*((1+flowdirectionRe)*y1bar(i)+(1-
flowdirectionRe)*y1bar(i))+0.5*abs(Qbar_eps_Re)*(1-
abs(Qbar_eps_Re*dtbar/dzbar))*superbeey1barRe*(y1bar(i)-y1bar(i));

        convecy1bar(i) = (fluxy1barLe-fluxy1barRe)/dzbar;
    end
    %
end % end of dYbardZbarDifferentialMethod == 777
%
%
% Formulate ODEs - can be used for adsorption and purge - both
directions
%
for i=1
    dY1bardtbar(i) = convecy1bar(i)-(n1eqmbar(i)-
n1bar(i))/epsilon+(epsilonbar*DL(i)*tt/(epsilon*L^2))*(Y1bar(i+2)-
2*Y1bar(i+1)+Y1bar(i))/(dzbar)^2;
end
for i=2:n-1
```

```
    dY1bardtbar(i) = convecy1bar(i)-(n1eqmbar(i)-
n1bar(i))/epsilon+(epsilonbar*DL(i)*tt/(epsilon*L^2))*(Y1bar(i+1)-
2*Y1bar(i)+Y1bar(i-1))/(dzbar)^2;
end
for i=n
    dY1bardtbar(i) = convecy1bar(i)-(n1eqmbar(i)-
n1bar(i))/epsilon+(epsilonbar*DL(i)*tt/(epsilon*L^2))*(Y1bar(n)-
2*Y1bar(n-1)+Y1bar(n-2))/(dzbar)^2;
end
%
if MassAxial == 882 % Turn on mass axial dispersion
        for i = 1
            dY1bardtbar(i) = convecy1bar(i)-(n1eqmbar(i)-
n1bar(i))/epsilon + 0;
        end
end
%
for i=1:n
    dn1bardtbar(i) = k1*tt*(n1eqmbar(i)-n1bar(i));
    dn2bardtbar(i) = k2*tt*(n2eqmbar(i)-n2bar(i));
    dPbardtbar(i) = 0;
end
%
% Four vectors into one vector
%
for i = 1:n
    Yt(0*n+i) = dY1bardtbar(i);
    Yt(1*n+i) = dn1bardtbar(i);
    Yt(2*n+i) = dn2bardtbar(i);
    Yt(3*n+i) = dPbardtbar(i);
end
    Yt(0*n+n) = 0; % because Y1bar(n) = y1d*rhog(n)
%
yt=Yt';

% Increment calls to psa_1
ncall = ncall+1;
%
```

APPENDIX F

MATLAB PROGRAM FOR PRESSURIZATION STEP

```
% Solve for y1, n1, n2, P, rhog, Q, us
%
function yt = PSA_pressurization(t,Y)
%
% parameters shared with the ODE routine
%
global Mg1 Mg2 De1 De2 taup dYbardZbarDifferentialMethod rhog0 T0 ncall
n dzbar dtbar epsilon epsilonbar k1 k2 rhob dp L tc tt y1a Qin Qa Pa
Pmax Pmin Tmax Tmin Tref MassAxial dtbara dtbarp dtbardep dtbard miu ta
tp td tdep
%
% preallocating
%
Y1bar = zeros(1,n);
n1bar = zeros(1,n);
n2bar = zeros(1,n);
y1bar = zeros(1,n);
Mg = zeros(1,n);
Pbar = zeros(1,n);
thetabar = zeros(1,n);
rhogbar = zeros(1,n);
n1eqmbar = zeros(1,n);
n2eqmbar = zeros(1,n);
Qbar = zeros(1,n);
usbar = zeros(1,n);
convecy1bar = zeros(1,n);
DL = zeros(1,n);
dY1bardtbar = zeros(1,n);
dn1bardtbar = zeros(1,n);
dn2bardtbar = zeros(1,n);
Yt = zeros(1,4*n);
Qin = Qa;
%
% One vector to four vectors
%
for i = 1:n
    Y1bar(i) = Y(0*n+i);
    n1bar(i) = Y(1*n+i);
    n2bar(i) = Y(2*n+i);
    Pbar(i) = Y(3*n+i);
end
for i = 1:n
    y1bar(i) = Y1bar(i)/(rhog0*L/(Qa*tt));
    Mg(i) = Mg1*y1bar(i)+Mg2*(1-y1bar(i));
end
%
% Boundary conditions after initial conditions
%
if (ncall~=0) % not initial condition
    i = 1; % Only use boundary conditions at the adsorption inlet
    y1bar(i) = y1a;
    Y1bar(i) = y1a*(rhog0*L/(Qa*tt));
end
% Formulate pre-parameters for ODEs
```

```
%
% Isobaric, Isothermal
%
for i = 1:n
    thetabar(i) = (T0-Tref)/(Tmax-Tmin);
    rhogbar(i) = rhog0*L/(Qa*tt);
end
%
% Formulate n1eqmbar(i), n2eqmbar(i), Qbar(i), usbar(i) with initial
and
% boundary conditions
%
for i = 1:n
    py = (y1bar(i))*((Pmax-Pmin)*Pbar(i)/1013250);
    if py < 0.00013
        n1eqmbar(i) = 0;
    else
    n1eqmbar(i) = -(k1*rhob*L/Qa)*(3*0.069337*((y1bar(i))*((Pmax-
Pmin)*Pbar(i)/1013250))^(-0.10825)/(1+0.069337*((y1bar(i))*((Pmax-
Pmin)*Pbar(i)/1013250))^(-0.10825))-0.4633)/2/193.842*1000;
    end
    n2eqmbar(i) = 0;
end

if (ncall == 0)
    for i = 1:n
        Qbar(i) = Qin/Qa;
        usbar(i) = Qbar(i)/rhogbar(i);
    end
end

if (ncall ~= 0)
        for i = 1
            Qbar(i) = Qin/Qa;
            usbar(i) = Qbar(i)/rhogbar(i);
        end
        for i = 2:n
            Qbar(i) = -((n1eqmbar(i)-n1bar(i))+(n2eqmbar(i)-
n2bar(i)))*dzbar+Qbar(i-1);
            usbar(i) = Qbar(i)/rhogbar(i);
        end
end
%
% Formulate gas phase axial dispersion coefficient in mass balance, DL,
% cm2/sec
%
if MassAxial == 881
    for i = 1:n
        DL(i) = 0;
    end
end

if MassAxial == 882
```

```
        DM = (epsilon/taup)*(1/(1/De1+1/De2));
    for i = 1:n
        DL(i) = 0.7*DM +
0.5*dp*(abs(Qbar(i))*Qa)/(rhogbar(i)*(Qa*tt/L)*epsilonbar);
    end
end
%
%
% Start of 1st order (2 points) upwind difference
if dYbardZbarDifferentialMethod == 333
    %
    % Formulate convective terms for i = 3:n-2
    %
    for i = 3:n-2
        % Le = left edge of cell
        Qbar_eps_Le = (Qbar(i-1)+Qbar(i))/(2*epsilon);
        % Re = right edge of cell
        Qbar_eps_Re = (Qbar(i)+Qbar(i+1))/(2*epsilon);

        % for left edge i-1/2
        if Qbar_eps_Le >= 0
            flowdirectionLe = 1;

            ry1barLe = (y1bar(i-1)-y1bar(i-2))/(y1bar(i)-y1bar(i-1));
        elseif Qbar_eps_Le <= 0
            flowdirectionLe = -1;

            ry1barLe = (y1bar(i+1)-y1bar(i))/(y1bar(i)-y1bar(i-1));
        end

        superbeey1barLe = 0;

        fluxy1barLe = 0.5*Qbar_eps_Le*((1+flowdirectionLe)*y1bar(i-
1)+(1-flowdirectionLe)*y1bar(i))+0.5*abs(Qbar_eps_Le)*(1-
abs(Qbar_eps_Le*dtbar/dzbar))*superbeey1barLe*(y1bar(i)-y1bar(i-1));

        % for right edge i+1/2
        if Qbar_eps_Re >= 0
            flowdirectionRe = 1;

            ry1barRe = (y1bar(i)-y1bar(i-1))/(y1bar(i+1)-y1bar(i));
        elseif Qbar_eps_Re <= 0
            flowdirectionRe = -1;

            ry1barRe = (y1bar(i+2)-y1bar(i+1))/(y1bar(i+1)-y1bar(i));
        end

        superbeey1barRe = 0;

        fluxy1barRe = 0.5*Qbar_eps_Re*((1+flowdirectionRe)*y1bar(i)+(1-
flowdirectionRe)*y1bar(i+1))+0.5*abs(Qbar_eps_Re)*(1-
abs(Qbar_eps_Re*dtbar/dzbar))*superbeey1barRe*(y1bar(i+1)-y1bar(i));
```

```
        convecy1bar(i) = (fluxy1barLe-fluxy1barRe)/dzbar;
    end
    %
    % Formulate convective terms for i = 1, 2, n-1, n
    %
    for i = 1
        Qbar_eps_Le = (Qbar(i)+Qbar(i))/(2*epsilon);
        Qbar_eps_Re = (Qbar(i)+Qbar(i+1))/(2*epsilon);

        % for left edge i-1/2
         if Qbar_eps_Le >= 0
            flowdirectionLe = 1;
            ry1barLe = 1;
        elseif Qbar_eps_Le <= 0
            flowdirectionLe = -1;
            ry1barLe = 1;
        end

        superbeey1barLe = 0;

        fluxy1barLe = 0.5*Qbar_eps_Le*((1+flowdirectionLe)*y1bar(i)+(1-
flowdirectionLe)*y1bar(i))+0.5*abs(Qbar_eps_Le)*(1-
abs(Qbar_eps_Le*dtbar/dzbar))*superbeey1barLe*(y1bar(i)-y1bar(i));

        % for right edge i+1/2
        if Qbar_eps_Re >= 0
            flowdirectionRe = 1;
            ry1barRe = 0;
        elseif Qbar_eps_Re <= 0
            flowdirectionRe = -1;
            ry1barRe = (y1bar(i+2)-y1bar(i+1))/(y1bar(i+1)-y1bar(i));
        end

        superbeey1barRe = 0;

        fluxy1barRe = 0.5*Qbar_eps_Re*((1+flowdirectionRe)*y1bar(i)+(1-
flowdirectionRe)*y1bar(i+1))+0.5*abs(Qbar_eps_Re)*(1-
abs(Qbar_eps_Re*dtbar/dzbar))*superbeey1barRe*(y1bar(i+1)-y1bar(i));

        convecy1bar(i) = (fluxy1barLe-fluxy1barRe)/dzbar;
    end
    %
    for i = 2
        Qbar_eps_Le = (Qbar(i-1)+Qbar(i))/(2*epsilon);
        Qbar_eps_Re = (Qbar(i)+Qbar(i+1))/(2*epsilon);

        % for left edge i-1/2
         if Qbar_eps_Le >= 0
            flowdirectionLe = 1;
            ry1barLe = 0;
        elseif Qbar_eps_Le <= 0
```

```
            flowdirectionLe = -1;
            ry1barLe = (y1bar(i+1)-y1bar(i))/(y1bar(i)-y1bar(i-1));
        end

        superbeey1barLe = 0;

        fluxy1barLe = 0.5*Qbar_eps_Le*((1+flowdirectionLe)*y1bar(i-
1)+(1-flowdirectionLe)*y1bar(i))+0.5*abs(Qbar_eps_Le)*(1-
abs(Qbar_eps_Le*dtbar/dzbar))*superbeey1barLe*(y1bar(i)-y1bar(i-1));

        % for right edge i+1/2
        if Qbar_eps_Re >= 0
            flowdirectionRe = 1;
            ry1barRe = (y1bar(i)-y1bar(i-1))/(y1bar(i+1)-y1bar(i));
        elseif Qbar_eps_Re <= 0
            flowdirectionRe = -1;
            ry1barRe = (y1bar(i+2)-y1bar(i+1))/(y1bar(i+1)-y1bar(i));
        end

        superbeey1barRe = 0;

        fluxy1barRe = 0.5*Qbar_eps_Re*((1+flowdirectionRe)*y1bar(i)+(1-
flowdirectionRe)*y1bar(i+1))+0.5*abs(Qbar_eps_Re)*(1-
abs(Qbar_eps_Re*dtbar/dzbar))*superbeey1barRe*(y1bar(i+1)-y1bar(i));

        convecy1bar(i) = (fluxy1barLe-fluxy1barRe)/dzbar;
    end
    %
    for i = n-1
        Qbar_eps_Le = (Qbar(i-1)+Qbar(i))/(2*epsilon);
        Qbar_eps_Re = (Qbar(i)+Qbar(i+1))/(2*epsilon);

        % for left edge i-1/2
         if Qbar_eps_Le >= 0
            flowdirectionLe = 1;
            ry1barLe = (y1bar(i-1)-y1bar(i-2))/(y1bar(i)-y1bar(i-1));
        elseif Qbar_eps_Le <= 0
            flowdirectionLe = -1;
            ry1barLe = (y1bar(i+1)-y1bar(i))/(y1bar(i)-y1bar(i-1));
        end

        superbeey1barLe = 0;

        fluxy1barLe = 0.5*Qbar_eps_Le*((1+flowdirectionLe)*y1bar(i-
1)+(1-flowdirectionLe)*y1bar(i))+0.5*abs(Qbar_eps_Le)*(1-
abs(Qbar_eps_Le*dtbar/dzbar))*superbeey1barLe*(y1bar(i)-y1bar(i-1));

        % for right edge i+1/2
        if Qbar_eps_Re >= 0
            flowdirectionRe = 1;
            ry1barRe = (y1bar(i)-y1bar(i-1))/(y1bar(i+1)-y1bar(i));
        elseif Qbar_eps_Re <= 0
```

```
            flowdirectionRe = -1;
            ry1barRe = 0;
        end

        superbeey1barRe = 0;

        fluxy1barRe = 0.5*Qbar_eps_Re*((1+flowdirectionRe)*y1bar(i)+(1-
flowdirectionRe)*y1bar(i+1))+0.5*abs(Qbar_eps_Re)*(1-
abs(Qbar_eps_Re*dtbar/dzbar))*superbeey1barRe*(y1bar(i+1)-y1bar(i));

        convecy1bar(i) = (fluxy1barLe-fluxy1barRe)/dzbar;
    end
    %
    for i = n
        Qbar_eps_Le = (Qbar(i-1)+Qbar(i))/(2*epsilon);
        Qbar_eps_Re = (Qbar(i)+Qbar(i))/(2*epsilon);

        % for left edge i-1/2
         if Qbar_eps_Le >= 0
            flowdirectionLe = 1;
            ry1barLe = (y1bar(i-1)-y1bar(i-2))/(y1bar(i)-y1bar(i-1));
        elseif Qbar_eps_Le <= 0
            flowdirectionLe = -1;
            ry1barLe = 0;
        end

        superbeey1barLe = 0;

        fluxy1barLe = 0.5*Qbar_eps_Le*((1+flowdirectionLe)*y1bar(i-
1)+(1-flowdirectionLe)*y1bar(i))+0.5*abs(Qbar_eps_Le)*(1-
abs(Qbar_eps_Le*dtbar/dzbar))*superbeey1barLe*(y1bar(i)-y1bar(i-1));

        % for right edge i+1/2
        if Qbar_eps_Re >= 0
            flowdirectionRe = 1;
            ry1barRe = 1;
        elseif Qbar_eps_Re <= 0
            flowdirectionRe = -1;
            ry1barRe = 1;
        end

        superbeey1barRe = 0;

        fluxy1barRe = 0.5*Qbar_eps_Re*((1+flowdirectionRe)*y1bar(i)+(1-
flowdirectionRe)*y1bar(i))+0.5*abs(Qbar_eps_Re)*(1-
abs(Qbar_eps_Re*dtbar/dzbar))*superbeey1barRe*(y1bar(i)-y1bar(i));

        convecy1bar(i) = (fluxy1barLe-fluxy1barRe)/dzbar;
    end
    %
end % end of dYbardZbarDifferentialMethod == 333
%
```

```
%
% Start of 2nd order (3 points) upwind difference
if dYbardZbarDifferentialMethod == 444
    %
    % Formulate convective terms for i = 3:n-2
    %
    for i = 3:n-2

        % Le = left edge of cell
        Qbar_eps_Le = (Qbar(i-1)+Qbar(i))/(2*epsilon);
        % Re = right edge of cell
        Qbar_eps_Re = (Qbar(i)+Qbar(i+1))/(2*epsilon);

        % for left edge i-1/2
        if Qbar_eps_Le >= 0
            flowdirectionLe = 1;
            ry1barLe = (y1bar(i-1)-y1bar(i-2))/(y1bar(i)-y1bar(i-1));
        elseif Qbar_eps_Le <= 0
            flowdirectionLe = -1;
            ry1barLe = (y1bar(i+1)-y1bar(i))/(y1bar(i)-y1bar(i-1));
        end

        superbeey1barLe = 1;

        fluxy1barLe = 0.5*Qbar_eps_Le*((1+flowdirectionLe)*y1bar(i-
1)+(1-flowdirectionLe)*y1bar(i))+0.5*abs(Qbar_eps_Le)*(1-
abs(Qbar_eps_Le*dtbar/dzbar))*superbeey1barLe*(y1bar(i)-y1bar(i-1));

        % for right edge i+1/2
        if Qbar_eps_Re >= 0
            flowdirectionRe = 1;
            ry1barRe = (y1bar(i)-y1bar(i-1))/(y1bar(i+1)-y1bar(i));
        elseif Qbar_eps_Re <= 0
            flowdirectionRe = -1;

            ry1barRe = (y1bar(i+2)-y1bar(i+1))/(y1bar(i+1)-y1bar(i));
        end

        superbeey1barRe = 1;

        fluxy1barRe = 0.5*Qbar_eps_Re*((1+flowdirectionRe)*y1bar(i)+(1-
flowdirectionRe)*y1bar(i+1))+0.5*abs(Qbar_eps_Re)*(1-
abs(Qbar_eps_Re*dtbar/dzbar))*superbeey1barRe*(y1bar(i+1)-y1bar(i));

        convecy1bar(i) = (fluxy1barLe-fluxy1barRe)/dzbar;
    end
    %
    % Formulate convective terms for i = 1, 2, n-1, n
    %
    for i = 1
        Qbar_eps_Le = (Qbar(i)+Qbar(i))/(2*epsilon);
        Qbar_eps_Re = (Qbar(i)+Qbar(i+1))/(2*epsilon);
```

```
        % for left edge i-1/2
         if Qbar_eps_Le >= 0
            flowdirectionLe = 1;
            ry1barLe = 1;
        elseif Qbar_eps_Le <= 0
            flowdirectionLe = -1;
            ry1barLe = 1;
        end

        superbeey1barLe = 1;

        fluxy1barLe = 0.5*Qbar_eps_Le*((1+flowdirectionLe)*y1bar(i)+(1-
flowdirectionLe)*y1bar(i))+0.5*abs(Qbar_eps_Le)*(1-
abs(Qbar_eps_Le*dtbar/dzbar))*superbeey1barLe*(y1bar(i)-y1bar(i));

        % for right edge i+1/2
        if Qbar_eps_Re >= 0
            flowdirectionRe = 1;
            ry1barRe = 0;
        elseif Qbar_eps_Re <= 0
            flowdirectionRe = -1;
            ry1barRe = (y1bar(i+2)-y1bar(i+1))/(y1bar(i+1)-y1bar(i));
        end

        superbeey1barRe = 1;

        fluxy1barRe = 0.5*Qbar_eps_Re*((1+flowdirectionRe)*y1bar(i)+(1-
flowdirectionRe)*y1bar(i+1))+0.5*abs(Qbar_eps_Re)*(1-
abs(Qbar_eps_Re*dtbar/dzbar))*superbeey1barRe*(y1bar(i+1)-y1bar(i));

        convecy1bar(i) = (fluxy1barLe-fluxy1barRe)/dzbar;
    end
    %
    for i = 2
        Qbar_eps_Le = (Qbar(i-1)+Qbar(i))/(2*epsilon);
        Qbar_eps_Re = (Qbar(i)+Qbar(i+1))/(2*epsilon);

        % for left edge i-1/2
         if Qbar_eps_Le >= 0
            flowdirectionLe = 1;
            ry1barLe = 0;
        elseif Qbar_eps_Le <= 0
            flowdirectionLe = -1;
            ry1barLe = (y1bar(i+1)-y1bar(i))/(y1bar(i)-y1bar(i-1));
        end

        superbeey1barLe = 1;

        fluxy1barLe = 0.5*Qbar_eps_Le*((1+flowdirectionLe)*y1bar(i-
1)+(1-flowdirectionLe)*y1bar(i))+0.5*abs(Qbar_eps_Le)*(1-
abs(Qbar_eps_Le*dtbar/dzbar))*superbeey1barLe*(y1bar(i)-y1bar(i-1));
```

```
        % for right edge i+1/2
        if Qbar_eps_Re >= 0
            flowdirectionRe = 1;
            ry1barRe = (y1bar(i)-y1bar(i-1))/(y1bar(i+1)-y1bar(i));
        elseif Qbar_eps_Re <= 0
            flowdirectionRe = -1;
            ry1barRe = (y1bar(i+2)-y1bar(i+1))/(y1bar(i+1)-y1bar(i));
        end

        superbeey1barRe = 1;

        fluxy1barRe = 0.5*Qbar_eps_Re*((1+flowdirectionRe)*y1bar(i)+(1-
flowdirectionRe)*y1bar(i+1))+0.5*abs(Qbar_eps_Re)*(1-
abs(Qbar_eps_Re*dtbar/dzbar))*superbeey1barRe*(y1bar(i+1)-y1bar(i));

        convecy1bar(i) = (fluxy1barLe-fluxy1barRe)/dzbar;
    end
    %
    for i = n-1
        Qbar_eps_Le = (Qbar(i-1)+Qbar(i))/(2*epsilon);
        Qbar_eps_Re = (Qbar(i)+Qbar(i+1))/(2*epsilon);

        % for left edge i-1/2
         if Qbar_eps_Le >= 0
            flowdirectionLe = 1;
            ry1barLe = (y1bar(i-1)-y1bar(i-2))/(y1bar(i)-y1bar(i-1));
        elseif Qbar_eps_Le <= 0
            flowdirectionLe = -1;
            ry1barLe = (y1bar(i+1)-y1bar(i))/(y1bar(i)-y1bar(i-1));
        end

        superbeey1barLe = 1;

        fluxy1barLe = 0.5*Qbar_eps_Le*((1+flowdirectionLe)*y1bar(i-
1)+(1-flowdirectionLe)*y1bar(i))+0.5*abs(Qbar_eps_Le)*(1-
abs(Qbar_eps_Le*dtbar/dzbar))*superbeey1barLe*(y1bar(i)-y1bar(i-1));

        % for right edge i+1/2
        if Qbar_eps_Re >= 0
            flowdirectionRe = 1;
            ry1barRe = (y1bar(i)-y1bar(i-1))/(y1bar(i+1)-y1bar(i));
        elseif Qbar_eps_Re <= 0
            flowdirectionRe = -1;
            ry1barRe = 0;
        end

        superbeey1barRe = 1;

        fluxy1barRe = 0.5*Qbar_eps_Re*((1+flowdirectionRe)*y1bar(i)+(1-
flowdirectionRe)*y1bar(i+1))+0.5*abs(Qbar_eps_Re)*(1-
abs(Qbar_eps_Re*dtbar/dzbar))*superbeey1barRe*(y1bar(i+1)-y1bar(i));
```

```
        convecy1bar(i) = (fluxy1barLe-fluxy1barRe)/dzbar;
    end
    %
    for i = n
        Qbar_eps_Le = (Qbar(i-1)+Qbar(i))/(2*epsilon);
        Qbar_eps_Re = (Qbar(i)+Qbar(i))/(2*epsilon);

        % for left edge i-1/2
         if Qbar_eps_Le >= 0
            flowdirectionLe = 1;
            ry1barLe = (y1bar(i-1)-y1bar(i-2))/(y1bar(i)-y1bar(i-1));
        elseif Qbar_eps_Le <= 0
            flowdirectionLe = -1;
            ry1barLe = 0;
        end

        superbeey1barLe = 1;

        fluxy1barLe = 0.5*Qbar_eps_Le*((1+flowdirectionLe)*y1bar(i-
1)+(1-flowdirectionLe)*y1bar(i))+0.5*abs(Qbar_eps_Le)*(1-
abs(Qbar_eps_Le*dtbar/dzbar))*superbeey1barLe*(y1bar(i)-y1bar(i-1));

        % for right edge i+1/2
        if Qbar_eps_Re >= 0
            flowdirectionRe = 1;
            ry1barRe = 1;
        elseif Qbar_eps_Re <= 0
            flowdirectionRe = -1;
            ry1barRe = 1;
        end

        superbeey1barRe = 1;

        fluxy1barRe = 0.5*Qbar_eps_Re*((1+flowdirectionRe)*y1bar(i)+(1-
flowdirectionRe)*y1bar(i))+0.5*abs(Qbar_eps_Re)*(1-
abs(Qbar_eps_Re*dtbar/dzbar))*superbeey1barRe*(y1bar(i)-y1bar(i));

        convecy1bar(i) = (fluxy1barLe-fluxy1barRe)/dzbar;
    end
    %
end % end of dYbardZbarDifferentialMethod == 444
%
% Start of Superbee Flux Limiter
if dYbardZbarDifferentialMethod == 777
    %
    % Formulate convective terms for i = 3:n-2
    %
     for i = 3:n-2
        % Le = left edge of cell
        Qbar_eps_Le = (Qbar(i-1)+Qbar(i))/(2*epsilon);
        % Re = right edge of cell
```

```
        Qbar_eps_Re = (Qbar(i)+Qbar(i+1))/(2*epsilon);

        % for left edge i-1/2
        if Qbar_eps_Le >= 0
            flowdirectionLe = 1;
            ry1barLe = (y1bar(i-1)-y1bar(i-2))/(y1bar(i)-y1bar(i-1));
        elseif Qbar_eps_Le <= 0
            flowdirectionLe = -1;
            ry1barLe = (y1bar(i+1)-y1bar(i))/(y1bar(i)-y1bar(i-1));
        end

        superbeey1barLe = max(0,
max(min(1,2*ry1barLe),min(2,ry1barLe)));

        fluxy1barLe = 0.5*Qbar_eps_Le*((1+flowdirectionLe)*y1bar(i-
1)+(1-flowdirectionLe)*y1bar(i))+0.5*abs(Qbar_eps_Le)*(1-
abs(Qbar_eps_Le*dtbar/dzbar))*superbeey1barLe*(y1bar(i)-y1bar(i-1));

        % for right edge i+1/2
        if Qbar_eps_Re >= 0
            flowdirectionRe = 1;
            ry1barRe = (y1bar(i)-y1bar(i-1))/(y1bar(i+1)-y1bar(i));
        elseif Qbar_eps_Re <= 0
            flowdirectionRe = -1;

            ry1barRe = (y1bar(i+2)-y1bar(i+1))/(y1bar(i+1)-y1bar(i));
        end

        superbeey1barRe = max(0,
max(min(1,2*ry1barRe),min(2,ry1barRe)));

        fluxy1barRe = 0.5*Qbar_eps_Re*((1+flowdirectionRe)*y1bar(i)+(1-
flowdirectionRe)*y1bar(i+1))+0.5*abs(Qbar_eps_Re)*(1-
abs(Qbar_eps_Re*dtbar/dzbar))*superbeey1barRe*(y1bar(i+1)-y1bar(i));

        convecy1bar(i) = (fluxy1barLe-fluxy1barRe)/dzbar;
    end
    %
    % Formulate convective terms for i = 1, 2, n-1, n
    %
    for i = 1
        Qbar_eps_Le = (Qbar(i)+Qbar(i))/(2*epsilon);
        Qbar_eps_Re = (Qbar(i)+Qbar(i+1))/(2*epsilon);

        % for left edge i-1/2
         if Qbar_eps_Le >= 0
            flowdirectionLe = 1;
            ry1barLe = 1;
        elseif Qbar_eps_Le <= 0
            flowdirectionLe = -1;
            ry1barLe = 1;
        end
```

```
        superbeey1barLe = max(0,
max(min(1,2*ry1barLe),min(2,ry1barLe)));

        fluxy1barLe = 0.5*Qbar_eps_Le*((1+flowdirectionLe)*y1bar(i)+(1-
flowdirectionLe)*y1bar(i))+0.5*abs(Qbar_eps_Le)*(1-
abs(Qbar_eps_Le*dtbar/dzbar))*superbeey1barLe*(y1bar(i)-y1bar(i));

        % for right edge i+1/2
        if Qbar_eps_Re >= 0
            flowdirectionRe = 1;
            ry1barRe = 0;
        elseif Qbar_eps_Re <= 0
            flowdirectionRe = -1;
            ry1barRe = (y1bar(i+2)-y1bar(i+1))/(y1bar(i+1)-y1bar(i));
        end

        superbeey1barRe = max(0,
max(min(1,2*ry1barRe),min(2,ry1barRe)));

        fluxy1barRe = 0.5*Qbar_eps_Re*((1+flowdirectionRe)*y1bar(i)+(1-
flowdirectionRe)*y1bar(i+1))+0.5*abs(Qbar_eps_Re)*(1-
abs(Qbar_eps_Re*dtbar/dzbar))*superbeey1barRe*(y1bar(i+1)-y1bar(i));

        convecy1bar(i) = (fluxy1barLe-fluxy1barRe)/dzbar;
    end
    %
    for i = 2
        Qbar_eps_Le = (Qbar(i-1)+Qbar(i))/(2*epsilon);
        Qbar_eps_Re = (Qbar(i)+Qbar(i+1))/(2*epsilon);

        % for left edge i-1/2
         if Qbar_eps_Le >= 0
            flowdirectionLe = 1;
            ry1barLe = 0;
        elseif Qbar_eps_Le <= 0
            flowdirectionLe = -1;
            ry1barLe = (y1bar(i+1)-y1bar(i))/(y1bar(i)-y1bar(i-1));
        end

        superbeey1barLe = max(0,
max(min(1,2*ry1barLe),min(2,ry1barLe)));

        fluxy1barLe = 0.5*Qbar_eps_Le*((1+flowdirectionLe)*y1bar(i-
1)+(1-flowdirectionLe)*y1bar(i))+0.5*abs(Qbar_eps_Le)*(1-
abs(Qbar_eps_Le*dtbar/dzbar))*superbeey1barLe*(y1bar(i)-y1bar(i-1));

        % for right edge i+1/2
        if Qbar_eps_Re >= 0
            flowdirectionRe = 1;
            ry1barRe = (y1bar(i)-y1bar(i-1))/(y1bar(i+1)-y1bar(i));
        elseif Qbar_eps_Re <= 0
```

```
            flowdirectionRe = -1;
            ry1barRe = (y1bar(i+2)-y1bar(i+1))/(y1bar(i+1)-y1bar(i));
        end

        superbeey1barRe = max(0,
max(min(1,2*ry1barRe),min(2,ry1barRe)));

        fluxy1barRe = 0.5*Qbar_eps_Re*((1+flowdirectionRe)*y1bar(i)+(1-
flowdirectionRe)*y1bar(i+1))+0.5*abs(Qbar_eps_Re)*(1-
abs(Qbar_eps_Re*dtbar/dzbar))*superbeey1barRe*(y1bar(i+1)-y1bar(i));

        convecy1bar(i) = (fluxy1barLe-fluxy1barRe)/dzbar;
    end
    %
    for i = n-1
        Qbar_eps_Le = (Qbar(i-1)+Qbar(i))/(2*epsilon);
        Qbar_eps_Re = (Qbar(i)+Qbar(i+1))/(2*epsilon);

        % for left edge i-1/2
         if Qbar_eps_Le >= 0
            flowdirectionLe = 1;
            ry1barLe = (y1bar(i-1)-y1bar(i-2))/(y1bar(i)-y1bar(i-1));
        elseif Qbar_eps_Le <= 0
            flowdirectionLe = -1;
            ry1barLe = (y1bar(i+1)-y1bar(i))/(y1bar(i)-y1bar(i-1));
        end

        superbeey1barLe = max(0,
max(min(1,2*ry1barLe),min(2,ry1barLe)));

        fluxy1barLe = 0.5*Qbar_eps_Le*((1+flowdirectionLe)*y1bar(i-
1)+(1-flowdirectionLe)*y1bar(i))+0.5*abs(Qbar_eps_Le)*(1-
abs(Qbar_eps_Le*dtbar/dzbar))*superbeey1barLe*(y1bar(i)-y1bar(i-1));

        % for right edge i+1/2
        if Qbar_eps_Re >= 0
            flowdirectionRe = 1;
            ry1barRe = (y1bar(i)-y1bar(i-1))/(y1bar(i+1)-y1bar(i));
        elseif Qbar_eps_Re <= 0
            flowdirectionRe = -1;
            ry1barRe = 0;
        end

        superbeey1barRe = max(0,
max(min(1,2*ry1barRe),min(2,ry1barRe)));

        fluxy1barRe = 0.5*Qbar_eps_Re*((1+flowdirectionRe)*y1bar(i)+(1-
flowdirectionRe)*y1bar(i+1))+0.5*abs(Qbar_eps_Re)*(1-
abs(Qbar_eps_Re*dtbar/dzbar))*superbeey1barRe*(y1bar(i+1)-y1bar(i));

        convecy1bar(i) = (fluxy1barLe-fluxy1barRe)/dzbar;
    end
```

```
    %
    for i = n
        Qbar_eps_Le = (Qbar(i-1)+Qbar(i))/(2*epsilon);
        Qbar_eps_Re = (Qbar(i)+Qbar(i))/(2*epsilon);

        % for left edge i-1/2
         if Qbar_eps_Le >= 0
            flowdirectionLe = 1;
            ry1barLe = (y1bar(i-1)-y1bar(i-2))/(y1bar(i)-y1bar(i-1));
        elseif Qbar_eps_Le <= 0
            flowdirectionLe = -1;
            ry1barLe = 0;
        end

        superbeey1barLe = max(0,
max(min(1,2*ry1barLe),min(2,ry1barLe)));

        fluxy1barLe = 0.5*Qbar_eps_Le*((1+flowdirectionLe)*y1bar(i-
1)+(1-flowdirectionLe)*y1bar(i))+0.5*abs(Qbar_eps_Le)*(1-
abs(Qbar_eps_Le*dtbar/dzbar))*superbeey1barLe*(y1bar(i)-y1bar(i-1));

        % for right edge i+1/2
        if Qbar_eps_Re >= 0
            flowdirectionRe = 1;
            ry1barRe = 1;
        elseif Qbar_eps_Re <= 0
            flowdirectionRe = -1;
            ry1barRe = 1;
        end

        superbeey1barRe = max(0,
max(min(1,2*ry1barRe),min(2,ry1barRe)));

        fluxy1barRe = 0.5*Qbar_eps_Re*((1+flowdirectionRe)*y1bar(i)+(1-
flowdirectionRe)*y1bar(i))+0.5*abs(Qbar_eps_Re)*(1-
abs(Qbar_eps_Re*dtbar/dzbar))*superbeey1barRe*(y1bar(i)-y1bar(i));

        convecy1bar(i) = (fluxy1barLe-fluxy1barRe)/dzbar;
    end
    %
end % end of dYbardZbarDifferentialMethod == 777
%
%
% Formulate ODEs - can be used for adsorption and purge - both
directions
%
for i=1
    dY1bardtbar(i) = convecy1bar(i)-(n1eqmbar(i)-
n1bar(i))/epsilon+(epsilonbar*DL(i)*tt/(epsilon*L^2))*(Y1bar(i+2)-
2*Y1bar(i+1)+Y1bar(i))/(dzbar)^2;
end
for i=2:n-1
```

```
    dY1bardtbar(i) = convecy1bar(i)-(n1eqmbar(i)-
n1bar(i))/epsilon+(epsilonbar*DL(i)*tt/(epsilon*L^2))*(Y1bar(i+1)-
2*Y1bar(i)+Y1bar(i-1))/(dzbar)^2;
end
for i=n
    dY1bardtbar(i) = convecy1bar(i)-(n1eqmbar(i)-
n1bar(i))/epsilon+(epsilonbar*DL(i)*tt/(epsilon*L^2))*(Y1bar(n)-
2*Y1bar(n-1)+Y1bar(n-2))/(dzbar)^2;
end
%
if MassAxial == 882 % Turn on mass axial dispersion
        for i=n
            dY1bardtbar(i) = convecy1bar(i)-(n1eqmbar(i)-
n1bar(i))/epsilon + 0;
        end
end
%
for i=1:n
    dn1bardtbar(i) = k1*tt*(n1eqmbar(i)-n1bar(i));
    dn2bardtbar(i) = k2*tt*(n2eqmbar(i)-n2bar(i));
end
%
dz = L/(n-1);
m = 0.0175e-4;
c = 0.15e-4;
kp1 = m*(1-epsilon)*rhob/epsilon^3/dp;
kp2 = c*(1-epsilon)^2*miu/epsilon^3/dp^2;
K = 1e-7;
for i=1
    dPbardtbar(i) = K/miu/epsilon*ta*(Pbar(i+2)*(Pbar(i+2)-Pbar(i+1))-
Pbar(i)*(Pbar(i+1)-Pbar(i)))*(Pmax-Pmin)/(dz)^2;
end
for i=2:(n-1)
    dPbardtbar(i) = K/miu/epsilon*ta*(Pbar(i+1)*(Pbar(i+1)-Pbar(i))-
Pbar(i-1)*(Pbar(i)-Pbar(i-1)))*(Pmax-Pmin)/(dz)^2;
end
for i=n
    dPbardtbar(i) = K/miu/epsilon*ta*(Pbar(i)*(Pbar(i)-Pbar(i-1))-
Pbar(i-1)*(Pbar(i)-Pbar(i-1)))*(Pmax-Pmin)/(dz)^2;
end
%
dPbardtbar(1) = 0;
%
% Four vectors into one vector
%
for i = 1:n
    Yt(0*n+i) = dY1bardtbar(i);
    Yt(1*n+i) = dn1bardtbar(i);
    Yt(2*n+i) = dn2bardtbar(i);
    Yt(3*n+i) = dPbardtbar(i);
end
    Yt(0*n+1) = 0; % because Y1bar(1) = y1a*rhog(1)
%
yt=Yt';
```

```
% Increment calls to psa_1
ncall = ncall+1;
%
```

APPENDIX G

MATLAB PROGRAM FOR DEPRESSURIZATION STEP

```
% Solve for y1, n1, n2, P, rhog, Q, us
%
function yt = PSA_depressurization(t,Y)
%
% parameters shared with the ODE routine
%
global Mg1 Mg2 De1 De2 taup dYbardZbarDifferentialMethod rhog0 T0 ncall
Qa Qd n dzbar dtbar  epsilon epsilonbar k1 k2 k3 k4 rhob dp L y1d Qin
Pd tc tt Pmax Pmin Tmax Tmin Tref MassAxial dtbara dtbarp dtbardep
dtbard miu ta tp td tdep
%
% preallocating
%
Y1bar = zeros(1,n);
n1bar = zeros(1,n);
n2bar = zeros(1,n);
y1bar = zeros(1,n);
Mg = zeros(1,n);
Pbar = zeros(1,n);
thetabar = zeros(1,n);
rhogbar = zeros(1,n);
n1eqmbar = zeros(1,n);
n2eqmbar = zeros(1,n);
Qbar = zeros(1,n);
usbar = zeros(1,n);
convecy1bar = zeros(1,n);
DL = zeros(1,n);
dY1bardtbar = zeros(1,n);
dn1bardtbar = zeros(1,n);
dn2bardtbar = zeros(1,n);
Yt = zeros(1,4*n);
Qin = -Qd;
%
% One vector to four vectors
%
for i = 1:n
    Y1bar(i) = Y(0*n+i);
    n1bar(i) = Y(1*n+i);
    n2bar(i) = Y(2*n+i);
    Pbar(i) = Y(3*n+i);
end
for i = 1:n
    y1bar(i) = Y1bar(i)/(rhog0*L/(Qa*tt));
    Mg(i) = Mg1*y1bar(i)+Mg2*(1-y1bar(i));
end
%
% Boundary conditions after initial conditions
%
if (ncall~=0) % not initial condition
    y1bar(n) = y1d;
    Y1bar(n) = y1d*(rhog0*L/(Qa*tt));
end
% Formulate pre-parameters for ODEs
%
```

```
% Isobaric, Isothermal
%
for i = 1:n
    thetabar(i) = (T0-Tref)/(Tmax-Tmin);
    rhogbar(i) = rhog0*L/(Qa*tt);
end
%
% Formulate n1eqmbar(i), n2eqmbar(i), Qbar(i), usbar(i) with initial
and
% boundary conditions
%
for i = 1:n
    py = (y1bar(i))*((Pmax-Pmin)*Pbar(i)/1013250);
    if py < 0.00013
        n1eqmbar(i) = 0;
    else
    n1eqmbar(i) = -(k1*rhob*L/Qa)*(3*0.069337*((y1bar(i))*((Pmax-
Pmin)*Pbar(i)/1013250))^(-0.10825)/(1+0.069337*((y1bar(i))*((Pmax-
Pmin)*Pbar(i)/1013250))^(-0.10825))-0.4633)/2/193.842*1000;
    end
    n2eqmbar(i) = 0;
end

if (ncall == 0)
    for i = 1:n
        Qbar(i) = Qin/Qa;
        usbar(i) = Qbar(i)/rhogbar(i);
    end
end

if (ncall ~= 0)
        for i = n
            Qbar(i) = Qin/Qa;
            usbar(i) = Qbar(i)/rhogbar(i);
        end
        for i = n-1:-1:1
            Qbar(i) = +((n1eqmbar(i)-n1bar(i))+(n2eqmbar(i)-
n2bar(i)))*dzbar+Qbar(i+1);
            usbar(i) = Qbar(i)/rhogbar(i);
        end
end
%
% Formulate gas phase axial dispersion coefficient in mass balance, DL,
% cm2/sec
%
if MassAxial == 881
    for i = 1:n
        DL(i) = 0;
    end
end

if MassAxial == 882
        DM = (epsilon/taup)*(1/(1/De1+1/De2));
```

```
    for i = 1:n
        DL(i) = 0.7*DM +
0.5*dp*(abs(Qbar(i))*Qa)/(rhogbar(i)*(Qa*tt/L)*epsilonbar);
    end
end
%
%
% Start of 1st order (2 points) upwind difference
if dYbardZbarDifferentialMethod == 333
    %
    % Formulate convective terms for i = 3:n-2
    %
    for i = 3:n-2
        % Le = left edge of cell
        Qbar_eps_Le = (Qbar(i-1)+Qbar(i))/(2*epsilon);
        % Re = right edge of cell
        Qbar_eps_Re = (Qbar(i)+Qbar(i+1))/(2*epsilon);

        % for left edge i-1/2
        if Qbar_eps_Le >= 0
            flowdirectionLe = 1;

            ry1barLe = (y1bar(i-1)-y1bar(i-2))/(y1bar(i)-y1bar(i-1));
        elseif Qbar_eps_Le <= 0
            flowdirectionLe = -1;

            ry1barLe = (y1bar(i+1)-y1bar(i))/(y1bar(i)-y1bar(i-1));
        end

        superbeey1barLe = 0;

        fluxy1barLe = 0.5*Qbar_eps_Le*((1+flowdirectionLe)*y1bar(i-
1)+(1-flowdirectionLe)*y1bar(i))+0.5*abs(Qbar_eps_Le)*(1-
abs(Qbar_eps_Le*dtbar/dzbar))*superbeey1barLe*(y1bar(i)-y1bar(i-1));

        % for right edge i+1/2
        if Qbar_eps_Re >= 0
            flowdirectionRe = 1;

            ry1barRe = (y1bar(i)-y1bar(i-1))/(y1bar(i+1)-y1bar(i));
        elseif Qbar_eps_Re <= 0
            flowdirectionRe = -1;

            ry1barRe = (y1bar(i+2)-y1bar(i+1))/(y1bar(i+1)-y1bar(i));
        end

        superbeey1barRe = 0;

        fluxy1barRe = 0.5*Qbar_eps_Re*((1+flowdirectionRe)*y1bar(i)+(1-
flowdirectionRe)*y1bar(i+1))+0.5*abs(Qbar_eps_Re)*(1-
abs(Qbar_eps_Re*dtbar/dzbar))*superbeey1barRe*(y1bar(i+1)-y1bar(i));
```

```
        convecy1bar(i) = (fluxy1barLe-fluxy1barRe)/dzbar;
    end
    %
    % Formulate convective terms for i = 1, 2, n-1, n
    %
    for i = 1
        Qbar_eps_Le = (Qbar(i)+Qbar(i))/(2*epsilon);
        Qbar_eps_Re = (Qbar(i)+Qbar(i+1))/(2*epsilon);

        % for left edge i-1/2
         if Qbar_eps_Le >= 0
            flowdirectionLe = 1;
            ry1barLe = 1;
        elseif Qbar_eps_Le <= 0
            flowdirectionLe = -1;
            ry1barLe = 1;
        end

        superbeey1barLe = 0;

        fluxy1barLe = 0.5*Qbar_eps_Le*((1+flowdirectionLe)*y1bar(i)+(1-
flowdirectionLe)*y1bar(i))+0.5*abs(Qbar_eps_Le)*(1-
abs(Qbar_eps_Le*dtbar/dzbar))*superbeey1barLe*(y1bar(i)-y1bar(i));

        % for right edge i+1/2
        if Qbar_eps_Re >= 0
            flowdirectionRe = 1;
            ry1barRe = 0;
        elseif Qbar_eps_Re <= 0
            flowdirectionRe = -1;
            ry1barRe = (y1bar(i+2)-y1bar(i+1))/(y1bar(i+1)-y1bar(i));
        end

        superbeey1barRe = 0;

        fluxy1barRe = 0.5*Qbar_eps_Re*((1+flowdirectionRe)*y1bar(i)+(1-
flowdirectionRe)*y1bar(i+1))+0.5*abs(Qbar_eps_Re)*(1-
abs(Qbar_eps_Re*dtbar/dzbar))*superbeey1barRe*(y1bar(i+1)-y1bar(i));

        convecy1bar(i) = (fluxy1barLe-fluxy1barRe)/dzbar;
    end
    %
    for i = 2
        Qbar_eps_Le = (Qbar(i-1)+Qbar(i))/(2*epsilon);
        Qbar_eps_Re = (Qbar(i)+Qbar(i+1))/(2*epsilon);

        % for left edge i-1/2
         if Qbar_eps_Le >= 0
            flowdirectionLe = 1;
            ry1barLe = 0;
        elseif Qbar_eps_Le <= 0
```

```
            flowdirectionLe = -1;
            ry1barLe = (y1bar(i+1)-y1bar(i))/(y1bar(i)-y1bar(i-1));
        end

        superbeey1barLe = 0;

        fluxy1barLe = 0.5*Qbar_eps_Le*((1+flowdirectionLe)*y1bar(i-
1)+(1-flowdirectionLe)*y1bar(i))+0.5*abs(Qbar_eps_Le)*(1-
abs(Qbar_eps_Le*dtbar/dzbar))*superbeey1barLe*(y1bar(i)-y1bar(i-1));

        % for right edge i+1/2
        if Qbar_eps_Re >= 0
            flowdirectionRe = 1;
            ry1barRe = (y1bar(i)-y1bar(i-1))/(y1bar(i+1)-y1bar(i));
        elseif Qbar_eps_Re <= 0
            flowdirectionRe = -1;
            ry1barRe = (y1bar(i+2)-y1bar(i+1))/(y1bar(i+1)-y1bar(i));
        end

        superbeey1barRe = 0;

        fluxy1barRe = 0.5*Qbar_eps_Re*((1+flowdirectionRe)*y1bar(i)+(1-
flowdirectionRe)*y1bar(i+1))+0.5*abs(Qbar_eps_Re)*(1-
abs(Qbar_eps_Re*dtbar/dzbar))*superbeey1barRe*(y1bar(i+1)-y1bar(i));

        convecy1bar(i) = (fluxy1barLe-fluxy1barRe)/dzbar;
    end
    %
    for i = n-1
        Qbar_eps_Le = (Qbar(i-1)+Qbar(i))/(2*epsilon);
        Qbar_eps_Re = (Qbar(i)+Qbar(i+1))/(2*epsilon);

        % for left edge i-1/2
         if Qbar_eps_Le >= 0
            flowdirectionLe = 1;
            ry1barLe = (y1bar(i-1)-y1bar(i-2))/(y1bar(i)-y1bar(i-1));
        elseif Qbar_eps_Le <= 0
            flowdirectionLe = -1;
            ry1barLe = (y1bar(i+1)-y1bar(i))/(y1bar(i)-y1bar(i-1));
        end

        superbeey1barLe = 0;

        fluxy1barLe = 0.5*Qbar_eps_Le*((1+flowdirectionLe)*y1bar(i-
1)+(1-flowdirectionLe)*y1bar(i))+0.5*abs(Qbar_eps_Le)*(1-
abs(Qbar_eps_Le*dtbar/dzbar))*superbeey1barLe*(y1bar(i)-y1bar(i-1));

        % for right edge i+1/2
        if Qbar_eps_Re >= 0
            flowdirectionRe = 1;
            ry1barRe = (y1bar(i)-y1bar(i-1))/(y1bar(i+1)-y1bar(i));
        elseif Qbar_eps_Re <= 0
```

```
            flowdirectionRe = -1;
            ry1barRe = 0;
        end

        superbeey1barRe = 0;

        fluxy1barRe = 0.5*Qbar_eps_Re*((1+flowdirectionRe)*y1bar(i)+(1-
flowdirectionRe)*y1bar(i+1))+0.5*abs(Qbar_eps_Re)*(1-
abs(Qbar_eps_Re*dtbar/dzbar))*superbeey1barRe*(y1bar(i+1)-y1bar(i));

        convecy1bar(i) = (fluxy1barLe-fluxy1barRe)/dzbar;
    end
    %
    for i = n
        Qbar_eps_Le = (Qbar(i-1)+Qbar(i))/(2*epsilon);
        Qbar_eps_Re = (Qbar(i)+Qbar(i))/(2*epsilon);

        % for left edge i-1/2
         if Qbar_eps_Le >= 0
            flowdirectionLe = 1;
            ry1barLe = (y1bar(i-1)-y1bar(i-2))/(y1bar(i)-y1bar(i-1));
        elseif Qbar_eps_Le <= 0
            flowdirectionLe = -1;
            ry1barLe = 0;
        end

        superbeey1barLe = 0;

        fluxy1barLe = 0.5*Qbar_eps_Le*((1+flowdirectionLe)*y1bar(i-
1)+(1-flowdirectionLe)*y1bar(i))+0.5*abs(Qbar_eps_Le)*(1-
abs(Qbar_eps_Le*dtbar/dzbar))*superbeey1barLe*(y1bar(i)-y1bar(i-1));

        % for right edge i+1/2
        if Qbar_eps_Re >= 0
            flowdirectionRe = 1;
            ry1barRe = 1;
        elseif Qbar_eps_Re <= 0
            flowdirectionRe = -1;
            ry1barRe = 1;
        end

        superbeey1barRe = 0;

        fluxy1barRe = 0.5*Qbar_eps_Re*((1+flowdirectionRe)*y1bar(i)+(1-
flowdirectionRe)*y1bar(i))+0.5*abs(Qbar_eps_Re)*(1-
abs(Qbar_eps_Re*dtbar/dzbar))*superbeey1barRe*(y1bar(i)-y1bar(i));

        convecy1bar(i) = (fluxy1barLe-fluxy1barRe)/dzbar;
    end
    %
end % end of dYbardZbarDifferentialMethod == 333
%
```

```
%
% Start of 2nd order (3 points) upwind difference
if dYbardZbarDifferentialMethod == 444
    %
    % Formulate convective terms for i = 3:n-2
    %
    for i = 3:n-2

        % Le = left edge of cell
        Qbar_eps_Le = (Qbar(i-1)+Qbar(i))/(2*epsilon);
        % Re = right edge of cell
        Qbar_eps_Re = (Qbar(i)+Qbar(i+1))/(2*epsilon);

        % for left edge i-1/2
        if Qbar_eps_Le >= 0
            flowdirectionLe = 1;
            ry1barLe = (y1bar(i-1)-y1bar(i-2))/(y1bar(i)-y1bar(i-1));
        elseif Qbar_eps_Le <= 0
            flowdirectionLe = -1;
            ry1barLe = (y1bar(i+1)-y1bar(i))/(y1bar(i)-y1bar(i-1));
        end

        superbeey1barLe = 1;

        fluxy1barLe = 0.5*Qbar_eps_Le*((1+flowdirectionLe)*y1bar(i-
1)+(1-flowdirectionLe)*y1bar(i))+0.5*abs(Qbar_eps_Le)*(1-
abs(Qbar_eps_Le*dtbar/dzbar))*superbeey1barLe*(y1bar(i)-y1bar(i-1));

        % for right edge i+1/2
        if Qbar_eps_Re >= 0
            flowdirectionRe = 1;
            ry1barRe = (y1bar(i)-y1bar(i-1))/(y1bar(i+1)-y1bar(i));
        elseif Qbar_eps_Re <= 0
            flowdirectionRe = -1;

            ry1barRe = (y1bar(i+2)-y1bar(i+1))/(y1bar(i+1)-y1bar(i));
        end

        superbeey1barRe = 1;

        fluxy1barRe = 0.5*Qbar_eps_Re*((1+flowdirectionRe)*y1bar(i)+(1-
flowdirectionRe)*y1bar(i+1))+0.5*abs(Qbar_eps_Re)*(1-
abs(Qbar_eps_Re*dtbar/dzbar))*superbeey1barRe*(y1bar(i+1)-y1bar(i));

        convecy1bar(i) = (fluxy1barLe-fluxy1barRe)/dzbar;
    end
    %
    % Formulate convective terms for i = 1, 2, n-1, n
    %
    for i = 1
        Qbar_eps_Le = (Qbar(i)+Qbar(i))/(2*epsilon);
        Qbar_eps_Re = (Qbar(i)+Qbar(i+1))/(2*epsilon);
```

```
        % for left edge i-1/2
         if Qbar_eps_Le >= 0
            flowdirectionLe = 1;
            ry1barLe = 1;
        elseif Qbar_eps_Le <= 0
            flowdirectionLe = -1;
            ry1barLe = 1;
        end

        superbeey1barLe = 1;

        fluxy1barLe = 0.5*Qbar_eps_Le*((1+flowdirectionLe)*y1bar(i)+(1-
flowdirectionLe)*y1bar(i))+0.5*abs(Qbar_eps_Le)*(1-
abs(Qbar_eps_Le*dtbar/dzbar))*superbeey1barLe*(y1bar(i)-y1bar(i));

        % for right edge i+1/2
        if Qbar_eps_Re >= 0
            flowdirectionRe = 1;
            ry1barRe = 0;
        elseif Qbar_eps_Re <= 0
            flowdirectionRe = -1;
            ry1barRe = (y1bar(i+2)-y1bar(i+1))/(y1bar(i+1)-y1bar(i));
        end

        superbeey1barRe = 1;

        fluxy1barRe = 0.5*Qbar_eps_Re*((1+flowdirectionRe)*y1bar(i)+(1-
flowdirectionRe)*y1bar(i+1))+0.5*abs(Qbar_eps_Re)*(1-
abs(Qbar_eps_Re*dtbar/dzbar))*superbeey1barRe*(y1bar(i+1)-y1bar(i));

        convecy1bar(i) = (fluxy1barLe-fluxy1barRe)/dzbar;
    end
    %
    for i = 2
        Qbar_eps_Le = (Qbar(i-1)+Qbar(i))/(2*epsilon);
        Qbar_eps_Re = (Qbar(i)+Qbar(i+1))/(2*epsilon);

        % for left edge i-1/2
         if Qbar_eps_Le >= 0
            flowdirectionLe = 1;
            ry1barLe = 0;
        elseif Qbar_eps_Le <= 0
            flowdirectionLe = -1;
            ry1barLe = (y1bar(i+1)-y1bar(i))/(y1bar(i)-y1bar(i-1));
        end

        superbeey1barLe = 1;

        fluxy1barLe = 0.5*Qbar_eps_Le*((1+flowdirectionLe)*y1bar(i-
1)+(1-flowdirectionLe)*y1bar(i))+0.5*abs(Qbar_eps_Le)*(1-
abs(Qbar_eps_Le*dtbar/dzbar))*superbeey1barLe*(y1bar(i)-y1bar(i-1));
```

```
        % for right edge i+1/2
        if Qbar_eps_Re >= 0
            flowdirectionRe = 1;
            ry1barRe = (y1bar(i)-y1bar(i-1))/(y1bar(i+1)-y1bar(i));
        elseif Qbar_eps_Re <= 0
            flowdirectionRe = -1;
            ry1barRe = (y1bar(i+2)-y1bar(i+1))/(y1bar(i+1)-y1bar(i));
        end

        superbeey1barRe = 1;

        fluxy1barRe = 0.5*Qbar_eps_Re*((1+flowdirectionRe)*y1bar(i)+(1-
flowdirectionRe)*y1bar(i+1))+0.5*abs(Qbar_eps_Re)*(1-
abs(Qbar_eps_Re*dtbar/dzbar))*superbeey1barRe*(y1bar(i+1)-y1bar(i));

        convecy1bar(i) = (fluxy1barLe-fluxy1barRe)/dzbar;
    end
    %
    for i = n-1
        Qbar_eps_Le = (Qbar(i-1)+Qbar(i))/(2*epsilon);
        Qbar_eps_Re = (Qbar(i)+Qbar(i+1))/(2*epsilon);

        % for left edge i-1/2
         if Qbar_eps_Le >= 0
            flowdirectionLe = 1;
            ry1barLe = (y1bar(i-1)-y1bar(i-2))/(y1bar(i)-y1bar(i-1));
        elseif Qbar_eps_Le <= 0
            flowdirectionLe = -1;
            ry1barLe = (y1bar(i+1)-y1bar(i))/(y1bar(i)-y1bar(i-1));
        end

        superbeey1barLe = 1;

        fluxy1barLe = 0.5*Qbar_eps_Le*((1+flowdirectionLe)*y1bar(i-
1)+(1-flowdirectionLe)*y1bar(i))+0.5*abs(Qbar_eps_Le)*(1-
abs(Qbar_eps_Le*dtbar/dzbar))*superbeey1barLe*(y1bar(i)-y1bar(i-1));

        % for right edge i+1/2
        if Qbar_eps_Re >= 0
            flowdirectionRe = 1;
            ry1barRe = (y1bar(i)-y1bar(i-1))/(y1bar(i+1)-y1bar(i));
        elseif Qbar_eps_Re <= 0
            flowdirectionRe = -1;
            ry1barRe = 0;
        end

        superbeey1barRe = 1;

        fluxy1barRe = 0.5*Qbar_eps_Re*((1+flowdirectionRe)*y1bar(i)+(1-
flowdirectionRe)*y1bar(i+1))+0.5*abs(Qbar_eps_Re)*(1-
abs(Qbar_eps_Re*dtbar/dzbar))*superbeey1barRe*(y1bar(i+1)-y1bar(i));
```

```
        convecy1bar(i) = (fluxy1barLe-fluxy1barRe)/dzbar;
    end
    %
    for i = n
        Qbar_eps_Le = (Qbar(i-1)+Qbar(i))/(2*epsilon);
        Qbar_eps_Re = (Qbar(i)+Qbar(i))/(2*epsilon);

        % for left edge i-1/2
         if Qbar_eps_Le >= 0
            flowdirectionLe = 1;
            ry1barLe = (y1bar(i-1)-y1bar(i-2))/(y1bar(i)-y1bar(i-1));
        elseif Qbar_eps_Le <= 0
            flowdirectionLe = -1;
            ry1barLe = 0;
        end

        superbeey1barLe = 1;

        fluxy1barLe = 0.5*Qbar_eps_Le*((1+flowdirectionLe)*y1bar(i-
1)+(1-flowdirectionLe)*y1bar(i))+0.5*abs(Qbar_eps_Le)*(1-
abs(Qbar_eps_Le*dtbar/dzbar))*superbeey1barLe*(y1bar(i)-y1bar(i-1));

        % for right edge i+1/2
        if Qbar_eps_Re >= 0
            flowdirectionRe = 1;
            ry1barRe = 1;
        elseif Qbar_eps_Re <= 0
            flowdirectionRe = -1;
            ry1barRe = 1;
        end

        superbeey1barRe = 1;

        fluxy1barRe = 0.5*Qbar_eps_Re*((1+flowdirectionRe)*y1bar(i)+(1-
flowdirectionRe)*y1bar(i))+0.5*abs(Qbar_eps_Re)*(1-
abs(Qbar_eps_Re*dtbar/dzbar))*superbeey1barRe*(y1bar(i)-y1bar(i));

        convecy1bar(i) = (fluxy1barLe-fluxy1barRe)/dzbar;
    end
    %
end % end of dYbardZbarDifferentialMethod == 444
%
% Start of Superbee Flux Limiter
if dYbardZbarDifferentialMethod == 777
    %
    % Formulate convective terms for i = 3:n-2
    %
     for i = 3:n-2
        % Le = left edge of cell
        Qbar_eps_Le = (Qbar(i-1)+Qbar(i))/(2*epsilon);
        % Re = right edge of cell
```

```
        Qbar_eps_Re = (Qbar(i)+Qbar(i+1))/(2*epsilon);

        % for left edge i-1/2
        if Qbar_eps_Le >= 0
            flowdirectionLe = 1;
            ry1barLe = (y1bar(i-1)-y1bar(i-2))/(y1bar(i)-y1bar(i-1));
        elseif Qbar_eps_Le <= 0
            flowdirectionLe = -1;
            ry1barLe = (y1bar(i+1)-y1bar(i))/(y1bar(i)-y1bar(i-1));
        end

        superbeey1barLe = max(0,
max(min(1,2*ry1barLe),min(2,ry1barLe)));

        fluxy1barLe = 0.5*Qbar_eps_Le*((1+flowdirectionLe)*y1bar(i-
1)+(1-flowdirectionLe)*y1bar(i))+0.5*abs(Qbar_eps_Le)*(1-
abs(Qbar_eps_Le*dtbar/dzbar))*superbeey1barLe*(y1bar(i)-y1bar(i-1));

        % for right edge i+1/2
        if Qbar_eps_Re >= 0
            flowdirectionRe = 1;
            ry1barRe = (y1bar(i)-y1bar(i-1))/(y1bar(i+1)-y1bar(i));
        elseif Qbar_eps_Re <= 0
            flowdirectionRe = -1;

            ry1barRe = (y1bar(i+2)-y1bar(i+1))/(y1bar(i+1)-y1bar(i));
        end

        superbeey1barRe = max(0,
max(min(1,2*ry1barRe),min(2,ry1barRe)));

        fluxy1barRe = 0.5*Qbar_eps_Re*((1+flowdirectionRe)*y1bar(i)+(1-
flowdirectionRe)*y1bar(i+1))+0.5*abs(Qbar_eps_Re)*(1-
abs(Qbar_eps_Re*dtbar/dzbar))*superbeey1barRe*(y1bar(i+1)-y1bar(i));

        convecy1bar(i) = (fluxy1barLe-fluxy1barRe)/dzbar;
    end
    %
    % Formulate convective terms for i = 1, 2, n-1, n
    %
    for i = 1
        Qbar_eps_Le = (Qbar(i)+Qbar(i))/(2*epsilon);
        Qbar_eps_Re = (Qbar(i)+Qbar(i+1))/(2*epsilon);

        % for left edge i-1/2
         if Qbar_eps_Le >= 0
            flowdirectionLe = 1;
            ry1barLe = 1;
        elseif Qbar_eps_Le <= 0
            flowdirectionLe = -1;
            ry1barLe = 1;
        end
```

```
        superbeey1barLe = max(0,
max(min(1,2*ry1barLe),min(2,ry1barLe)));

        fluxy1barLe = 0.5*Qbar_eps_Le*((1+flowdirectionLe)*y1bar(i)+(1-
flowdirectionLe)*y1bar(i))+0.5*abs(Qbar_eps_Le)*(1-
abs(Qbar_eps_Le*dtbar/dzbar))*superbeey1barLe*(y1bar(i)-y1bar(i));

        % for right edge i+1/2
        if Qbar_eps_Re >= 0
            flowdirectionRe = 1;
            ry1barRe = 0;
        elseif Qbar_eps_Re <= 0
            flowdirectionRe = -1;
            ry1barRe = (y1bar(i+2)-y1bar(i+1))/(y1bar(i+1)-y1bar(i));
        end

        superbeey1barRe = max(0,
max(min(1,2*ry1barRe),min(2,ry1barRe)));

        fluxy1barRe = 0.5*Qbar_eps_Re*((1+flowdirectionRe)*y1bar(i)+(1-
flowdirectionRe)*y1bar(i+1))+0.5*abs(Qbar_eps_Re)*(1-
abs(Qbar_eps_Re*dtbar/dzbar))*superbeey1barRe*(y1bar(i+1)-y1bar(i));

        convecy1bar(i) = (fluxy1barLe-fluxy1barRe)/dzbar;
    end
    %
    for i = 2
        Qbar_eps_Le = (Qbar(i-1)+Qbar(i))/(2*epsilon);
        Qbar_eps_Re = (Qbar(i)+Qbar(i+1))/(2*epsilon);

        % for left edge i-1/2
         if Qbar_eps_Le >= 0
            flowdirectionLe = 1;
            ry1barLe = 0;
        elseif Qbar_eps_Le <= 0
            flowdirectionLe = -1;
            ry1barLe = (y1bar(i+1)-y1bar(i))/(y1bar(i)-y1bar(i-1));
        end

        superbeey1barLe = max(0,
max(min(1,2*ry1barLe),min(2,ry1barLe)));

        fluxy1barLe = 0.5*Qbar_eps_Le*((1+flowdirectionLe)*y1bar(i-
1)+(1-flowdirectionLe)*y1bar(i))+0.5*abs(Qbar_eps_Le)*(1-
abs(Qbar_eps_Le*dtbar/dzbar))*superbeey1barLe*(y1bar(i)-y1bar(i-1));

        % for right edge i+1/2
        if Qbar_eps_Re >= 0
            flowdirectionRe = 1;
            ry1barRe = (y1bar(i)-y1bar(i-1))/(y1bar(i+1)-y1bar(i));
        elseif Qbar_eps_Re <= 0
```

```
            flowdirectionRe = -1;
            ry1barRe = (y1bar(i+2)-y1bar(i+1))/(y1bar(i+1)-y1bar(i));
        end

        superbeey1barRe = max(0,
max(min(1,2*ry1barRe),min(2,ry1barRe)));

        fluxy1barRe = 0.5*Qbar_eps_Re*((1+flowdirectionRe)*y1bar(i)+(1-
flowdirectionRe)*y1bar(i+1))+0.5*abs(Qbar_eps_Re)*(1-
abs(Qbar_eps_Re*dtbar/dzbar))*superbeey1barRe*(y1bar(i+1)-y1bar(i));

        convecy1bar(i) = (fluxy1barLe-fluxy1barRe)/dzbar;
    end
    %
    for i = n-1
        Qbar_eps_Le = (Qbar(i-1)+Qbar(i))/(2*epsilon);
        Qbar_eps_Re = (Qbar(i)+Qbar(i+1))/(2*epsilon);

        % for left edge i-1/2
         if Qbar_eps_Le >= 0
            flowdirectionLe = 1;
            ry1barLe = (y1bar(i-1)-y1bar(i-2))/(y1bar(i)-y1bar(i-1));
        elseif Qbar_eps_Le <= 0
            flowdirectionLe = -1;
            ry1barLe = (y1bar(i+1)-y1bar(i))/(y1bar(i)-y1bar(i-1));
        end

        superbeey1barLe = max(0,
max(min(1,2*ry1barLe),min(2,ry1barLe)));

        fluxy1barLe = 0.5*Qbar_eps_Le*((1+flowdirectionLe)*y1bar(i-
1)+(1-flowdirectionLe)*y1bar(i))+0.5*abs(Qbar_eps_Le)*(1-
abs(Qbar_eps_Le*dtbar/dzbar))*superbeey1barLe*(y1bar(i)-y1bar(i-1));

        % for right edge i+1/2
        if Qbar_eps_Re >= 0
            flowdirectionRe = 1;
            ry1barRe = (y1bar(i)-y1bar(i-1))/(y1bar(i+1)-y1bar(i));
        elseif Qbar_eps_Re <= 0
            flowdirectionRe = -1;
            ry1barRe = 0;
        end

        superbeey1barRe = max(0,
max(min(1,2*ry1barRe),min(2,ry1barRe)));

        fluxy1barRe = 0.5*Qbar_eps_Re*((1+flowdirectionRe)*y1bar(i)+(1-
flowdirectionRe)*y1bar(i+1))+0.5*abs(Qbar_eps_Re)*(1-
abs(Qbar_eps_Re*dtbar/dzbar))*superbeey1barRe*(y1bar(i+1)-y1bar(i));

        convecy1bar(i) = (fluxy1barLe-fluxy1barRe)/dzbar;
    end
```

```
    %
    for i = n
        Qbar_eps_Le = (Qbar(i-1)+Qbar(i))/(2*epsilon);
        Qbar_eps_Re = (Qbar(i)+Qbar(i))/(2*epsilon);

        % for left edge i-1/2
         if Qbar_eps_Le >= 0
            flowdirectionLe = 1;
            ry1barLe = (y1bar(i-1)-y1bar(i-2))/(y1bar(i)-y1bar(i-1));
        elseif Qbar_eps_Le <= 0
            flowdirectionLe = -1;
            ry1barLe = 0;
        end

        superbeey1barLe = max(0,
max(min(1,2*ry1barLe),min(2,ry1barLe)));

        fluxy1barLe = 0.5*Qbar_eps_Le*((1+flowdirectionLe)*y1bar(i-
1)+(1-flowdirectionLe)*y1bar(i))+0.5*abs(Qbar_eps_Le)*(1-
abs(Qbar_eps_Le*dtbar/dzbar))*superbeey1barLe*(y1bar(i)-y1bar(i-1));

        % for right edge i+1/2
        if Qbar_eps_Re >= 0
            flowdirectionRe = 1;
            ry1barRe = 1;
        elseif Qbar_eps_Re <= 0
            flowdirectionRe = -1;
            ry1barRe = 1;
        end

        superbeey1barRe = max(0,
max(min(1,2*ry1barRe),min(2,ry1barRe)));

        fluxy1barRe = 0.5*Qbar_eps_Re*((1+flowdirectionRe)*y1bar(i)+(1-
flowdirectionRe)*y1bar(i))+0.5*abs(Qbar_eps_Re)*(1-
abs(Qbar_eps_Re*dtbar/dzbar))*superbeey1barRe*(y1bar(i)-y1bar(i));

        convecy1bar(i) = (fluxy1barLe-fluxy1barRe)/dzbar;
    end
    %
end % end of dYbardZbarDifferentialMethod == 777
%
%
% Formulate ODEs - can be used for adsorption and purge - both
directions
%
for i=1
    dY1bardtbar(i) = convecy1bar(i)-(n1eqmbar(i)-
n1bar(i))/epsilon+(epsilonbar*DL(i)*tt/(epsilon*L^2))*(Y1bar(i+2)-
2*Y1bar(i+1)+Y1bar(i))/(dzbar)^2;
end
for i=2:n-1
```

```
    dY1bardtbar(i) = convecy1bar(i)-(n1eqmbar(i)-
n1bar(i))/epsilon+(epsilonbar*DL(i)*tt/(epsilon*L^2))*(Y1bar(i+1)-
2*Y1bar(i)+Y1bar(i-1))/(dzbar)^2;
end
for i=n
    dY1bardtbar(i) = convecy1bar(i)-(n1eqmbar(i)-
n1bar(i))/epsilon+(epsilonbar*DL(i)*tt/(epsilon*L^2))*(Y1bar(n)-
2*Y1bar(n-1)+Y1bar(n-2))/(dzbar)^2;
end
%
if MassAxial == 882 % Turn on mass axial dispersion
        for i = 1
            dY1bardtbar(i) = convecy1bar(i)-(n1eqmbar(i)-
n1bar(i))/epsilon + 0;
        end
end
%
for i=1:n
    dn1bardtbar(i) = k1*tt*(n1eqmbar(i)-n1bar(i));
    dn2bardtbar(i) = k2*tt*(n2eqmbar(i)-n2bar(i));
end
%
dz = L/(n-1);
m = 0.0175e-4;
c = 0.15e-4;
kp1 = m*(1-epsilon)*rhob/epsilon^3/dp;
kp2 = c*(1-epsilon)^2*miu/epsilon^3/dp^2;
K = 1e-7;
for i=1
    dPbardtbar(i) = K/miu/epsilon*ta*(Pbar(i+2)*(Pbar(i+2)-Pbar(i+1))-
Pbar(i)*(Pbar(i+1)-Pbar(i)))*(Pmax-Pmin)/(dz)^2;
end
for i=2:(n-1)
    dPbardtbar(i) = K/miu/epsilon*ta*(Pbar(i+1)*(Pbar(i+1)-Pbar(i))-
Pbar(i-1)*(Pbar(i)-Pbar(i-1)))*(Pmax-Pmin)/(dz)^2;
end
for i=n
    dPbardtbar(i) = K/miu/epsilon*ta*(Pbar(i)*(Pbar(i)-Pbar(i-1))-
Pbar(i-1)*(Pbar(i)-Pbar(i-1)))*(Pmax-Pmin)/(dz)^2;
end
%
dPbardtbar(n) = 0;
%
% Four vectors into one vector
%
for i = 1:n
    Yt(0*n+i) = dY1bardtbar(i);
    Yt(1*n+i) = dn1bardtbar(i);
    Yt(2*n+i) = dn2bardtbar(i);
    Yt(3*n+i) = dPbardtbar(i);
end
    Yt(0*n+n) = 0; % because Y1bar(n) = y1d*rhog(n)
%
yt=Yt';
```

```
% Increment calls to psa_1
ncall = ncall+1;
%
```